De la source des tremblements de terre au risque sismique: apport de la géodésie spatiale

Raphael Grandin

Mémoire en vue d'obtenir le diplôme d'

Habilitation à Diriger des Recherches

Spécialité : **Terre, Univers, Environnement**

Université de Paris
Institut de Physique du Globe de Paris

présenté par **Raphaël GRANDIN**

From the earthquake source to seismic hazard: contribution of space geodesy

Soutenance prévue le 6 Décembre 2019 devant la commission d'examen.

Composition du jury :

Président		
XXX	XXX	XXXX
Rapporteurs		
Mme	MATHILDE CANNAT	Université de Paris, IPGP
M.	TIM WRIGHT	University of Leeds (UK)
Mme	VIRGINIE PINEL	Université Savoie Mont Blanc, ISTerre
Examinateurs		
Mme	HÉLÈNE LYON-CAEN	École Normale Supérieure de Paris
M.	STÉPHANE JACQUEMOUD	Université de Paris, IPGP
M.	YANN KLINGER	Université de Paris, IPGP
Invité		
M.	JEAN-PHILIPPE AVOUAC	CalTech, Los Angeles (USA)

Summary

The quantitative assessment of seismic hazard relies on a combination of approaches including seismology, geodesy, paleoseismology and geology. Recent advances in space geodesy have allowed for mapping the slip distribution on tectonic fault planes during and between great earthquakes. Specifically, wide-swath radar interferometry (InSAR), notably thanks to the Sentinel-1 constellation, now provide observations with short revisit intervals, making it possible to measure tectonic strain over broad areas, with a better accuracy and an improved temporal resolution. The development of methods for jointly inverting space geodetic (InSAR, optical image correlation, GNSS) and seismological data hence allows for depicting precise representations of rupture processes, and therefore to test and push the limits of existing models of earthquake cyclicity.

In order to illustrate this ongoing questioning, four case studies focusing on recent earthquakes captured by wide-swath InSAR are discussed: (a) the M7.8 2015 Gorkha himalayan earthquake, (b) the M7.8 2013 Balochistan strike-slip earthquake, (c) the M8.1+M7.6 2014 Iquique earthquake doublet on the Chile subduction and (d) the M5.8 2016 Pawnee man-induced earthquake. These examples demonstrate the relevance of seeking progress in the characterization of present-day tectonic deformation, especially in order to provide insight on interpretations of fragmentary observations of ancient earthquakes, and hence to gain a more robust appraisal of seismic hazard.

Additional progress in radar technology is expected in the coming years, bringing simultaneously high spatial resolution and high temporal resolution (notably thanks to the future NISAR mission). This progress will eventually allow for converging with independent approaches developed in the field of high resolution optical imagery (notably based on images from the Pleiades constellation). Together, these new observations will provide high definition images of deformation at very short distance from surface ruptures for future earthquakes, thereby bridging the observational gap with data acquired in the field from instantaneous or cumulative coseismic offsets.

I propose to develop the use of diverse observations – geodetic, seismological, paleoseismological, tectonic – in order to progress in the quantification of the balance between elastic and anelastic strain, in space and time, at depth and at the surface, which will require making parallel progress in mechanical modeling of coseismic deformation. As a complement, I intend to pursue my research on the topic of volcano-tectonic deformation. Jointly analyzing geodetic observations, along with teleseismic and remote sensing of volcanic activity (gas, aerosols, thermal anomalies, infrasound) will allow for characterizing, from a safe distance, the eruptive dynamics at remote and non-instrumented volcanoes, hence providing an improved understanding of hazards associated with their eruptions.

Résumé

La quantification des aléas sismiques repose sur une combinaison d'approches incluant la sismologie, la géodésie, la paléosismologie et la géologie. Les récents progrès en géodésie spatiale permettent d'accéder à la distribution de glissement fini sur les systèmes de faille pendant et entre les grands séismes. En particulier, l'interférométrie radar (InSAR) à large fauchée, notamment grâce à la constellation Sentinel-1, fournit aujourd'hui des moyens d'observation à haute fréquence de revisite, capables de mesurer des déformations tectoniques à grande échelle, avec une précision et une résolution temporelle accrues. Le développement de méthodes d'inversion conjointe des données de géodésie spatiale (InSAR, corrélation optique, GNSS) et sismologiques permet dès lors de construire une représentation précise des processus de ruptures, et ainsi de tester et repousser les limites des différents modèles existants de cycle sismique.

Afin d'illustrer ces questionnements actuels, quatre cas de séismes récents observés par l'InSAR à large fauchée sont discutés: (a) le séisme himalayen de Gorkha (M7.8, 2015), (b) le séisme décrochant du Baloutchistan (M7.8, 2013), (c) le doublet sismique d'Iquique sur la subduction chilienne (M8.1+M7.6, 2014) et (d) le séisme de Pawnee (M5.8, 2016) induit par l'activité anthropique. Ces exemples démontrent l'intérêt de progresser dans la caractérisation des déformations tectoniques actuelles, afin notamment de pouvoir mettre en perspective les observations fragmentaires associées aux séismes passés, et ainsi aboutir à une meilleure évaluation des aléas sismiques.

Des progrès supplémentaires dans les technologies radar sont anticipés pour les années à venir, permettant d'accéder simultanément à la haute résolution spatiale et à la haute résolution temporelle (notamment avec la future mission NISAR). Ces progrès permettront d'achever la convergence avec les approches développées à l'heure actuelle en imagerie optique à haute résolution (notamment avec la constellation Pleiades). Ensemble, ces nouvelles observations fourniront des images à haute définition des déformations en champ très proche des ruptures de surface des séismes à venir, faisant ainsi la jonction avec les observations de terrain de décalages cosismiques instantanés et cumulés.

Je propose de développer l'exploitation de ces observations diverses – géodésiques, sismologiques, paléosismologiques, tectoniques – dans le but de progresser dans la quantification du rapport entre déformation élastique et anélastique, dans le temps et dans l'espace, en surface et en profondeur, ce qui nécessitera d'accomplir en parallèle des progrès en modélisation mécanique de la déformation cosismique. De manière complémentaire, je compte également prolonger mes travaux portant sur les déformations volcano-tectoniques. L'analyse conjointe des observations géodésiques, télésismiques et de télédétection de l'activité volcanique de surface (gaz, aérosols, thermique, infrason) permettra de caractériser, à distance, la dynamique éruptive de volcans isolés et non-instrumentés, et ainsi de mieux comprendre les aléas associés.

Contents

Summary i

Résumé ii

I Scientific part 1

Introduction 3

1 Measuring earthquake deformation 13

2 Modeling and interpreting earthquake deformation 57

3 Implications for seismic hazard: case studies 85

Conclusion 143

Remerciements 161

II Administrative part 163

1 Curriculum Vitae 165

2 Contribution aux enseignements et à la formation 169

3 Collaborations extérieures 175

4 List of case-studies 179

5 Publications 185

Appendix 207

" Important contributions to estimating the strain buildup and the release in creep will likely come from geodetic measurements by GPS and SAR interferometry. This will take time, however modern geodetic networks will ultimately capture strain cycles. Once many case histories of strain accumulation over decades, followed by its release in tens of seconds during earthquake ruptures, have been measured, we will know more about this problem. "

Wyss & Wiemer (1999), "*How can one test the seismic gap hypothesis? The case of repeated ruptures in the Aleutians*", Pure and applied Geophysics, 155(2-4), 259-278.

Part I

Scientific part

Introduction

Background and Organization of the Report

The objective of this report is to draw a number of research directions for the coming years in the field of earthquake geodesy, seismo-tectonics and earthquake hazard assessment. Accordingly, these directions are defined on the basis of a personal research trajectory, which will be reflected by the subjectivity placed in the hierarchization of ideas and concepts.

My personal contribution to the advancement of earthquake science is organized in three directions, and the structure of the present report reflects this segmentation: (1) upstream, I work on the improvement of SAR data processing methods, by developing new methodologies to improve the quality of InSAR data processing, (2) at the modeling stage, I explore various strategies for inferring coseismic (on-fault) slip at depth based on measurements at the surface, and (3) downstream, I attempt to interpret these models within the framework of existing theories of earthquake recurrence, paying particular attention to the limits of these theories and the resulting uncertainty on our understanding of earthquake hazard and the long-term tectonic evolution of fault systems over a broad range of spatial scales (from the outcrop to the landscape).

Applications of this methodology to current problems in *volcano geodesy* represents another aspect of my research. Although many concepts developed in this report could be transposed to the field of volcano science (measurement of deformation, inverse modeling, implications for hazard), I have chosen to set this problem aside in this report. Indeed, in spite of being more accessible to direct observation because they occur at shallower depth and over longer time scales, volcanic processes involve a complex interaction between rock mechanics, thermodynamics and fluid mechanics. Understanding volcanic processes therefore requires observations and modeling approaches extending well beyond the field of geodesy. Hence, for the sake of brevity and in order to avoid an excessive fragmentation of the discussion, I have intentionally restricted this report to the field of earthquake science, as seen through the prism of space geodesy. Nonetheless, a few examples of applications of geodesy to volcanology are scattered in this report. These examples will serve to illustrate the richness of the InSAR technique, while, hopefully, breaking the monotony of the report.

In this report, recent results gained in the field of earthquake geodesy will be presented, with special emphasis on the limitations of the methodology. Accordingly, this report is mainly focused on large earthquakes (M>7), which represent the primary target of earthquake geodesy. These events are also the main source of danger for populations. On the other hand,

large earthquakes are relatively rare: a shallow earthquake of magnitude 8.0 or above occurs only once every 1–5 years. Hence, these events fall in the category of "high impact – low probability" hazards, which makes them a delicate subject of investigation. By providing a detailed description of the spatio-temporal properties of large earthquakes, space geodesy contributes to gaining a better understanding of the natural variability of these destructive events, which remains essential to better inform the population and decision-makers of the hazards they will face in the coming decades.

The first chapter presents the main techniques involved in the measurement of earthquake deformation. A special attention is given to recent advances in synthetic aperture radar interferometry (InSAR) and its future developments. The second chapter provides an overview of the methodologies for extracting information about earthquake source parameters from geodetic data. The specific challenges related to the assimilation of spaceborne imagery (whether originating from interferometry or image correlation) are treated in detail in order to identify targets for research projects aimed at improving the methodology. Finally, the third chapter brings the focus on a selected collection of recent earthquakes studied by earthquake geodesy in a variety of geodynamic contexts. For each of these events, the specific contribution of geodetic data will be presented, followed by an illustration of the salient difficulties of characterizing earthquake hazard.

Earthquake science: why do we care?

The beginning of the 21th century is characterized by a continued growth of the Earth's population. Urban centers are almost everywhere developing at high speed. This context of growing urbanization leads to an increasing vulnerability to certain types of "natural" hazards, such as floods, droughts, earthquakes, volcanic eruptions, or sea level rise [*Blaikie et al.*, 2005]. This is especially true for earthquake hazard, where the main danger comes from structural collapse. Unfortunately, areas of dense and growing population often chiefly correspond with regions of elevated seismic hazard, in particular in low-income countries [*Hough and Bilham*, 2005]. This situation is perfectly illustrated by a single fact: the three biggest urban centers in the world (Los Angeles, Tokyo, Jakarta) all fall in areas where great earthquakes (M>8) have been recorded in the historical past (Fig. 1). Recent events, such as the 2004 Sumatra earthquake (which caused >200,000 deaths, mostly resulting from the tsunami), the 2010 Haiti earthquake (which led to >100,000 fatalities, mostly due to building collapse) or the 2011 Tohoku-Oki earthquake (which was responsible for the explosion of the Fukushima nuclear plant), recall us that the worst-case scenario is not always the least likely. One must face the strong probability of seeing history repeating itself in areas as diverse as Northern India, Central America, or the metropolis of Istanbul (Fig. 2).

In parallel, a phenomenal increase in human interconnectivity is currently taking place with an exponential development of information and communication technologies. Social networks today represent a major source of real-time information in the aftermath of natural disasters. As a result, awareness of earthquake phenomena has improved in the general public, which is

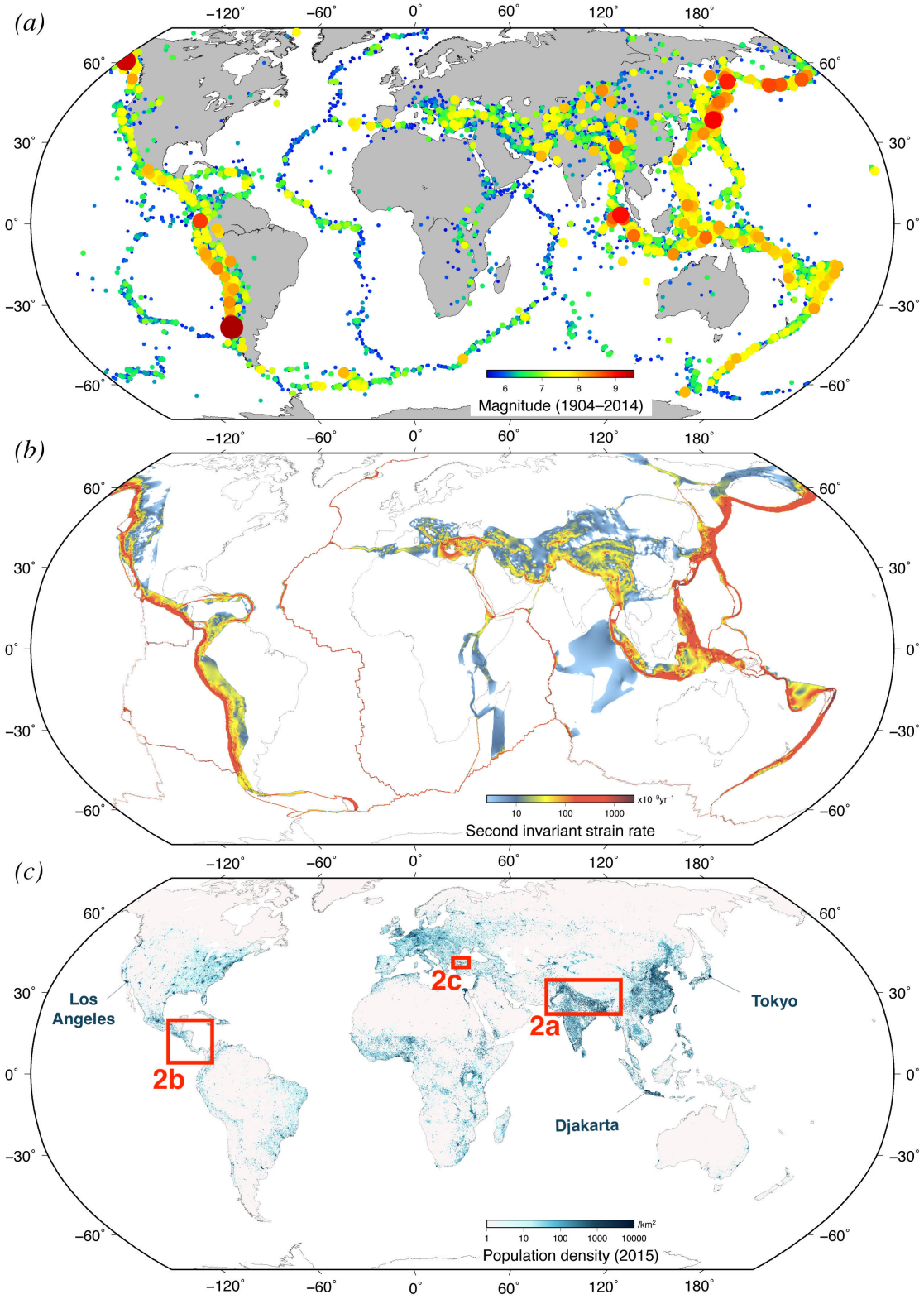

Figure 1 – (a) Global seismicity (M>5.5, 1904–2014) [source: ISC, Storchak et al., 2013]; (b) Geodetic strain rate [Kreemer et al., 2003, 2014]; (c) Population density in 2015 [source: European Commission, Joint Research Centre (JRC); Columbia University, Center for International Earth Science Information Network - CIESIN, 2015]

certainly a progress for earthquake preparedness and response management in case of a disaster [*Peary et al.*, 2012]. On the other hand, the mass of information provided by online activity provides a new tool for scientists to study the effects of earthquake shaking [e.g. *Earle*, 2010; *Bossu et al.*, 2012; *Martin et al.*, 2015]. However, a flow of incorrect or misleading news is also generated spontaneously, leading to interferences with the more reliable data coming from traditional sources of information, such as local authorities or scientists [*Vosoughi et al.*, 2018]. In such a context, better understanding earthquake phenomena, and efficiently communicating this knowledge, makes more and more sense.

The three basic questions seismologists are frequently asked, when interrogated by earthquake profanes in a context with seismological anxiety, are as follows:

- when will the next earthquake happen?
- where will it take place?
- how big is it going to be?

Unfortunately, given our present state of knowledge, answering all of these three questions with confidence remains impossible. Nevertheless, it does not mean that earthquakes cannot be anticipated.

Without going back to the story of how earthquake science was built[1], it has long been recognized that earthquake occurrence obeys certain laws: earthquakes preferentially occur in certain places, at certain times, with a certain size. First of all, small earthquakes are far more frequent than large earthquakes, giving rise to the famous Gutenberg-Richter magnitude-frequency law [*Gutenberg and Richter*, 1944]:

$$log_{10}(N) = a - bM \tag{0.1}$$

where N is the frequency of occurrence of earthquakes with magnitude greater than M. The value of a depends on the level of background seismicity, whereas the value of b remains remarkably close to 1 in almost every situation. In other words, as magnitude increases by one unit, the frequency of occurence decreases by a factor 10 (Table 1).

Furthermore, as shown in Figures 1a and 1b, earthquake rates (number of earthquakes per year, or better, the amount of earthquake energy released every year) are spatially correlated with tectonic plate boundaries. On Earth, tectonic plates move with respect to each other at rates of up to a few centimeters per year. At plate boundaries, intense deformation takes place, giving rise to sporadic earthquakes that release this accumulated strain according to one of the three standard rupture mechanisms (normal faulting for extension, reverse faulting for compression, or strike-slip faulting for transform motion). The biggest earthquakes (by far) occur offshore and at depth in subduction zone contexts, generating massive tsunamis whose effects can be anticipated to a large extent (e.g. 1960 Chile earthquake, 2004 Sumatra earthquakes, 2011 Tohoku-Oki earthquake). In contrast, continental earthquakes, albeit of more modest size, pose a significant danger because their source is located at shallower depth, sometimes striking in the heart of an urban center (e.g. 1999 Izmit earthquake, 1995 Kobe earthquake, 2016 Amatrice earthquake).

[1] The reader is referred to the concise reviews of *Ben-Menahem* [1995] and *Agnew et al.* [2002], and to the nice USGS web page gathering a timeline of the main milestones of earthquake science (`https://earthquake.usgs.gov/learn/topics/eqsci-history/eqscience-timeline.php`).

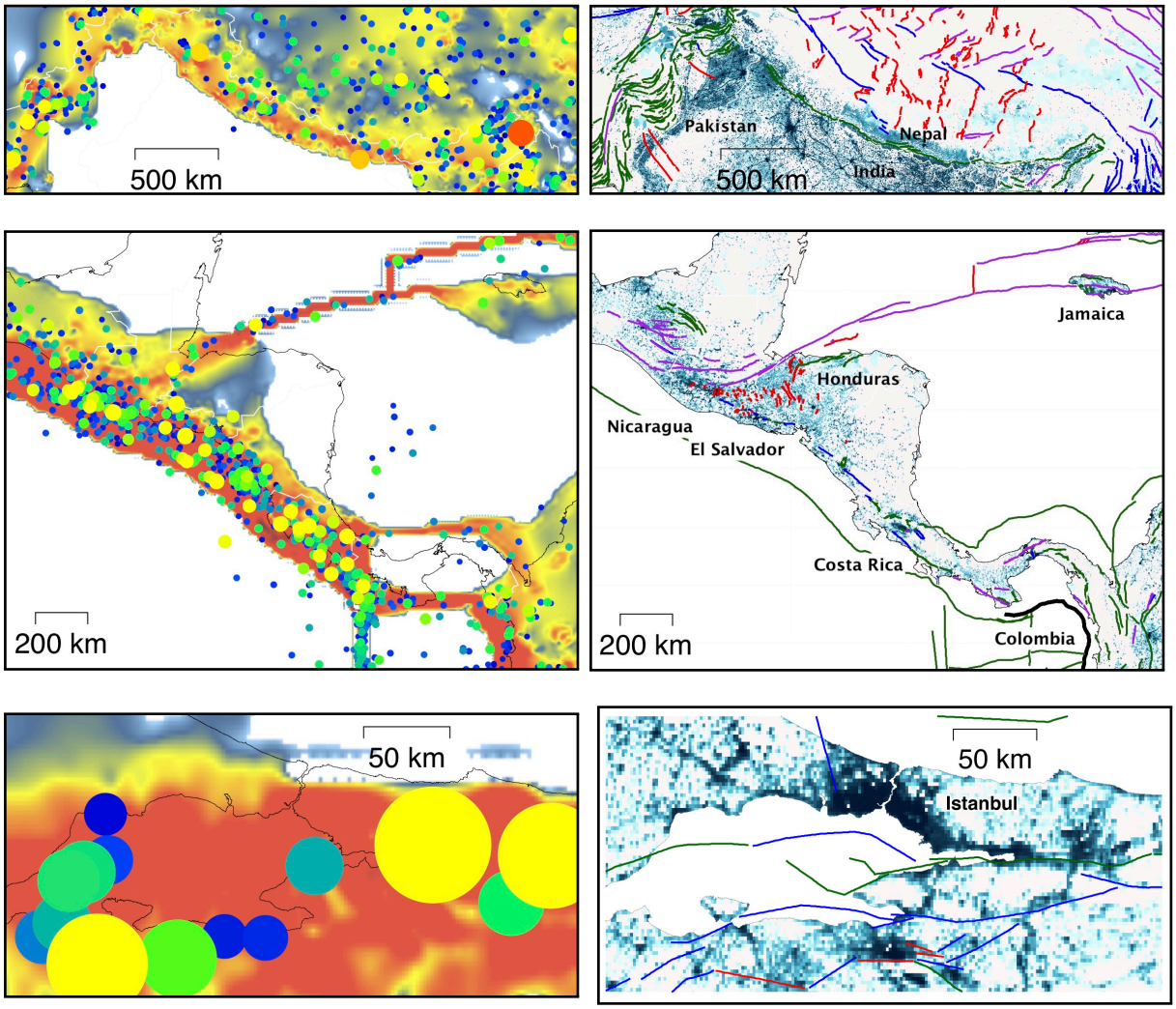

Figure 2 – Same data as in Fig. 1, for three selected regions of elevated seismic hazard. Top: India–Nepal–Pakistan. Middle: Central America. Bottom: Istanbul. Faults are from the Global Earthquake model (https://www.globalquakemodel.org/), available at https://github.com/GEMScienceTools/gem-global-active-faults

But before going further, it is worth recalling how the notion of *earthquake size* is defined. The macroscopic properties of distant seismic vibrations induced by large earthquakes (intensity, duration, frequency, direction of shaking) are usually too variable in space to be useful for the precise determination of the size of the causative earthquake. Instead, to quantify the scale of the earthquakes, seismologists use the spatial and temporal distribution of shaking and deformation to deduce the *scalar seismic moment*, defined as the product of rock rigidity μ and slip magnitude s on the fault, integrated over the fault plane Σ [*Knopoff*, 1958; *Burridge and Knopoff*, 1964; *Wyss and Brune*, 1968; *Kostrov*, 1974]:

$$M_o = \int_\Sigma \mu \; s \; \mathrm{d}A \tag{0.2}$$

Dislocation theory and indirect observations of stress changes caused by earthquakes inform us that the ratio between fault area ($A = \int_\Sigma \mathrm{d}A$) and average slip ($\bar{s}$) remains remarkably

constant across the magnitude spectrum [e.g. *Madariaga*, 1979; *Vallée*, 2013]. In other words, the broader the fault, the greater the slip (Table 1). As a consequence, the scalar moment spans a broad range of values from large to small events, which makes it inconvenient for quickly grasping the size of an earthquake. Taking the logarithm of the moment allows for building the more popular *moment magnitude scale* [*Thatcher and Hanks*, 1973; *Hanks and Kanamori*, 1979]:

$$M_w = \frac{2}{3} log_{10}\left(M_o - 9.05\right) \qquad (M_o \text{ expressed in Nm}) \qquad (0.3)$$

For small earthquakes, the seismic moment can only be determined by means of seismological measurements of the earthquake wavefield. For earthquakes smaller than $M < 6$, the ruptured area is usually just too small to be determined with accuracy, so that A remains tied with the average slip. As both slip and rupture area tend to increase with an increasing magnitude of the earthquake, larger earthquakes ($M > 6$) start to reach lengths of several kilometers or tens of kilometers. As a result of the finite speed of rupture propagation (usually smaller than but of the order of the S-waves speed, i.e. $\approx$ 2.5–3.0 km/s), the earthquake source may last for several seconds to tens of seconds. This is sufficiently long for seismologists to be able to "chop" the earthquake signal into distinct, successive time slices. As a result, details of the earthquake rupture can be distinguished (Figure 3).

Moment magnitude M_w	Scalar moment M_o	Average slip $\bar{s}$	Fault size $\sqrt{A}$	Relative frequency (events per year)
9	3×10^{22}	10 m	300 km	0.001 N
8	1×10^{21}	3 m	100 km	0.01 N
7	3×10^{19}	1 m	30 km	0.1 N
6	1×10^{18}	30 cm	10 km	N
5	3×10^{16}	10 cm	3 km	10 N

Table 1 – Relationship between earthquake size and frequency.

The accumulation of strain and its subsequent release during earthquakes has given rise to the theory of elastic rebound, first formulated by Harry Reid [*Reid*, 1910], which opens a perspective for assessing the probability of future earthquake occurrence. Earthquakes release some strain that was stored elastically by slow tectonic deformation. Since earthquakes need some time to "reload", measuring the time interval between earthquakes occurring in the past should give access to the *recurrence interval* between earthquakes. Knowing the time of the previous earthquake, then one could calculate the time left until the next event, at least in principle [e.g. *Bufe et al.*, 1977]. Unfortunately, the long time interval between large earthquakes (of the order of hundred years) makes it difficult to build a catalogue of past earthquakes, hence to evaluate this recurrence interval for damaging earthquakes. A slightly more empirical approach involves the identification of *seismic gaps*, which are locations where large earthquakes are known to have occurred in the past, but which are currently aseismic: these zones may be ripe for an imminent rupture [*McCann et al.*, 1979]. Sadly, in spite of its relative simplicity, the "seismic gap" theory has failed to pass statistical tests [*Kagan and Jackson*, 1995], suggesting that it relies on overly simplistic assumptions. Indeed, progress in the reconstruction of earthquake catalogues from paleoseismology indicates that

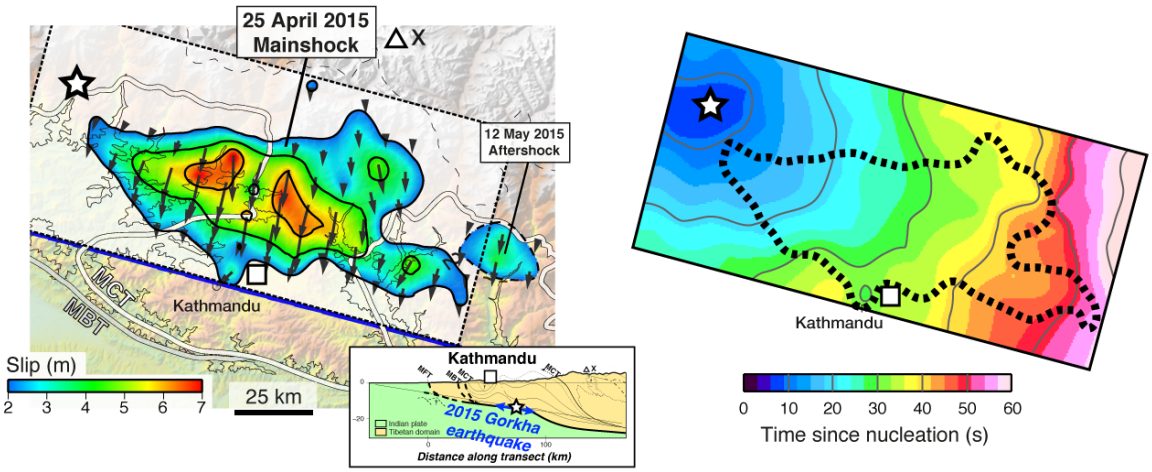

Figure 3 – Left: Slip distribution during the 2015 M_w7.9 Gorkha earthquake from joint inversion of space geodetic and seismological data. Right: Propagation of rupture front during the earthquake [modified from ***Grandin*** *et al., 2015].*

the "recurrence interval" between earthquakes can be far from periodic [e.g. *Atwater et al.*, 2003; *Ferry et al.*, 2011] (at least in certain cases), which seriously undermines the generality of the model.

The reasons for this lack of periodicity are manifold, and can be understood by examining in detail how earthquakes are distributed in space, time and as a function of their size. First, earthquakes tend to influence each other by static stress transfer at short range [*King et al.*, 1994] or as a result of dynamic stress perturbations they cause at long distance [*Parsons et al.*, 2017], which can advance or delay the occurrence of future events. More fundamentally, earthquake processes are today widely recognized as reflecting an underlying *chaotic* nature – albeit a deterministic one. In other words, earthquake nucleation and rupture propagation – hence earthquake timing, location and size – are strongly dependent on initial conditions, and hence are prone to perturbation from external factors such as surface loads [e.g. *Grollimund and Zoback*, 2001; *Saar and Manga*, 2003] or solid earth tides [e.g *Métivier et al.*, 2009]. This may seriously dampen hopes of seeing the emergence of an efficient, systematic methodology for predicting earthquakes [e.g. *Bak and Tang*, 1989; *Geller et al.*, 1997].

However, the stakes are too high to dismiss the necessity of studying earthquakes [e.g. *Stein*, 2006]. Even if the precise parameters of future earthquakes cannot yet be predicted, useful forecasts can be made by adopting a probabilistic approach [e.g. *Budnitz et al.*, 1997]. These probabilistic seismic hazard assessment (PSHA) models rely on a broad spectrum of observations of earthquake phenomena, ranging from the determination of earthquake parameters using quantitative seismological methods and state-of-the-art monitoring of present-day seismic activity, to the identification of the long-term signature of tectonic strain in the surface geomorphology and geology [e.g. *Ward*, 1994].

Studying present earthquake activity is crucial to improve hazard models, especially as recent earthquakes can be used as modern analogues of past earthquakes, which provides

an opportunity for better understanding the often incomplete paleoseismological record [e.g. *Natawidjaja et al.*, 2006; ***Grandin** et al.*, 2007b; *Garrett et al.*, 2013; *Hornblow et al.*, 2014]. A better characterization of the complexity of earthquake deformation is also essential to assess their cumulative effects in the landscapes, and to feed tectonic models with direct constraints on the mechanics of crustal faults [e.g. *Armijo et al.*, 1996; *Van der Woerd et al.*, 2002]. Furthermore, first-hand observations of modern earthquakes allow for deriving empirical laws of earthquake occurrence, such as regionalized versions of the frequency-magnitude law (Eq. 0.1), or scaling laws between earthquake parameters (e.g. slip *versus* fault length, fault length *versus* magnitude). Identification of these general laws is essential to identify the underlying physical laws governing earthquake rupture [e.g. *Kanamori and Anderson*, 1975; *Scholz*, 1982; *Ben-Zion*, 2008]. Together, a better understanding of past and present seismicity, and a better characterization of general earthquake laws, help solidify the foundations of PSHA models.

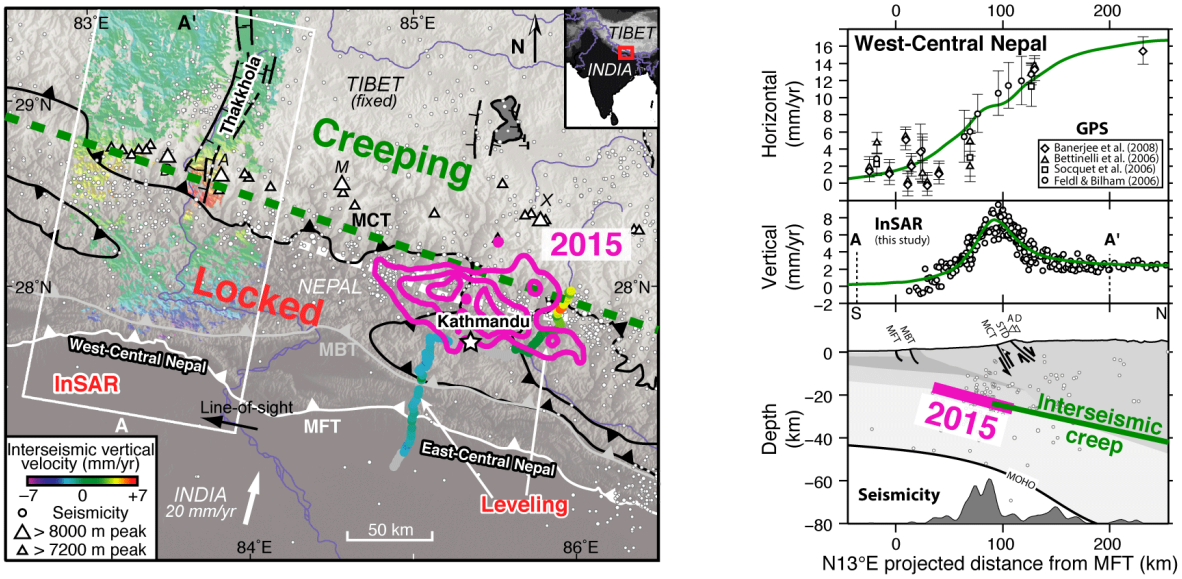

*Figure 4 – Interseismic deformation across the Himalaya in response to accumulation of slip deficit along the Main Himalayan Thrust [modified from **Grandin** et al., 2012a].*

A sub-discipline of seismology consists in studying earthquakes from a static point of view, exploiting the finite deformation that they cause, in order to deduce their characteristics. This field is called *earthquake geodesy*. The objective of earthquake geodesy is to describe, as precisely as possible, the distribution of coseismic slip, along with the geometry of the fault that ruptured during the event. The power of this approach is that it allows for determining how much of the available strain budget was released by the earthquake, and, provided that the initial budget is known, how much strain remains available for future events [*Brune*, 1968; *Kostrov*, 1974; *Shimazaki and Nakata*, 1980; *Ward*, 1998; *Tong et al.*, 2015].

Furthermore, earthquake geodesy allows for pinpointing the precise distribution of slip during earthquakes. The study of large earthquakes by geodesy demonstrates that slip is far from uniform on the fault plane (Fig. 3), which highlights the dire need for designing more physically

realistic dynamic models of earthquake nucleation, rupture propagation, segmentation and associated off-fault damage [see *Kanamori*, 2008, and references therein]. These realistic physical models are mandatory to gain a better understanding of earthquake processes, but require data to be initialized: by providing robust inference on the characteristics of coseismic slip, geodesy is one of the cornerstones of modern research in seismology.

Technical and methodological progress have also allowed geodesy to measure the very small strains that accumulate across major faults *before* and are released *just after* earthquakes. Measuring interseismic and postseismic deformation provides a direct evaluation of the degree of locking of a fault and its frictional behavior, which brings crucial constraints to fix geometric and kinematic parameters in seismic hazard models [e.g. *Segall and Harris*, 1986; *Savage and Simpson*, 1997; *Peltzer et al.*, 2001; *Wright et al.*, 2001b; *Çakir et al.*, 2003; *Johnson and Segall*, 2004; *Cavalié et al.*, 2008; *Smith-Konter et al.*, 2011; ***Grandin** et al.*, 2012a; *Chlieh et al.*, 2014] (Figure 4). Earthquake geodesy therefore helps anticipating the characteristics of future large earthquakes, which makes it a invaluable tool to better assess earthquake hazard.

Recently, the discovery of transient deformation events in a number of geodynamic contexts, such as episodic tremor and slip in subduction zones [*Rogers and Dragert*, 2003; *Vergnolle et al.*, 2010], fluid-driven creep on normal faults [*Doubre and Peltzer*, 2007], or accelerations in the creep of strike-slip faults [*Rousset et al.*, 2016a], adds a further dimension to the study of fault systems. These transient episodes of deformation may reflect a time-dependent behavior that could provide precious information about the state of stress of seismogenic faults, hence to better characterize seismic hazard as a whole.

For all these reasons, earthquake science – and in particular earthquake geodesy – is an exciting field of research. As will be explained in this report, the potential of improvement of geodetic techniques remains high, as the field is entering a mature stage. A growing set of observations suggests that earthquake deformation patterns are extremely diverse. This diversity reflects the inherent complexity of earthquake processes. We should not be discouraged by this complexity, and work harder to better understand the key ingredients that result in the "natural" disasters caused by earthquakes. If no one can predict earthquakes, it means that the future, and the surprises it will bring, cannot be predicted altogether.

Chapter 1

Measuring earthquake deformation

1.1 A century of earthquake geodesy

Permanent ground displacement caused by large earthquakes, together with other associated phenomena such as surface faulting, landslides and tsunamis, have long been observed and reported by famous geologists, including Déodat Gratet de Dolomieu (1783 Calabria earthquake Italy), Charles Darwin (1835 Conceptión earthquake, Chile), Charles Lyell (1855 Wairarapa earthquake, New Zealand) and Bunjiro Koto (1891 Mino-Owari earthquake, Nobi, Japan) [see e.g. *Sibson*, 2006; *Reitherman*, 2006]. The great M8.0 1891 Nobi earthquake was probably the first earthquake that has been captured by geodetic measurements, as the rupture zone was partly covered by a triangulation survey in 1882 *Pollitz and Sacks* [1994]. However, it is most frequently reported the very first large-scale quantitative measurement of coseismic deformation was serendipitously made in 1892. This happened in Indonesia, as an earthquake struck the strike-slip Sumatra fault during the course of a triangulation survey conducted by the Dutch colonial government [*Reid*, 1913; *Prawirodirdjo et al.*, 2000] (Fig. 1.1a).

At that time, there was no clear understanding of the phenomenon of earthquake faulting, and the theory of plate tectonics had yet to be formulated (not to mention, to be accepted). Nevertheless, geodetic surveys in areas subject to active tectonic processes expanded over much of the 20th century in response to increasing needs for precise land management information. Subsequent analysis of geodetic data spanning the time of occurence of the great 1897 Assam (India–Bangladesh) earthquake [*Oldham*, 1900; *Bilham and England*, 2001], 1906 M7.8 San Francisco (California) earthquake [*Hayford and Baldwin*, 1908; *Song et al.*, 2008] and 1923 Kanto (Japan) earthquakes [*Imamura*, 1930; *Wald and Somerville*, 1995; *Kobayashi and Koketsu*, 2005] provided the scientific community with a tool capable of appraising the broad size of areas affected by earthquake deformation, while bringing further proof in favor of the validity of the elastic rebound theory.

Continued efforts to measure deformation around the San Andreas fault system allowed for demonstrating that elastic strain was continuously building up, with only a small fraction of this strain being released by moderate earthquakes, suggesting that large earthquakes should occur in order to accommodate this deficit of strain release some time in the future [e.g. *Brune*, 1968; *Grant and Donnellan*, 1994]. Another series of earthquakes were captured by pre- and post-earthquake geodetic surveys in the 1950s, including the 1952 Kern County earthquake [e.g. *Bawden*, 2001] and the 1954 Fairview Peak-Dixie Valley earthquake sequence [e.g. *Whitten*, 1957] (the latter even occurred while geodetic surveyors were in the field, see section 3.5).

These events further demonstrated the potential of using off-fault elastic deformation to estimate coseismic slip at depth, and further highlighted the key role played by geodesy to help constrain the magnitude of large earthquakes.

Almost in parallel, volcano geodesy started to develop, in particular at Campi Flegrei (Italy), Sakura-Jima (Japan) [*Omori*, 1916, e.g.], and Kilauea (USA) [see e.g. *Dvorak and Dzurisin*, 1997]. Similarly, retrospective evaluation of these early studies of volcano deformation indicates that a consensus about the causative processes of deformation was far from being achieved. However, deformation was soon explained at first order by simple models of pressure sources embedded in a elastic medium. The interpretation of geodetic data using such simple models proved valuable to constrain the location, depth and volume change at depth [*Mogi*, 1958].

The two decades following WWII saw a technological boom that benefitted to the geophysical community in many ways. The development of the World-Wide Standard Seismological Network (WWSSN) suddenly provided a wealth of seismological data for global studies of seismic activity that definitely proved the reality of plate tectonics. About at the same time, the cold war also drove the rapid development of space research. The first, most prominent achievement of space exploration applied to earthquake science was probably the spy satellites program sent as part of the US Keyhole project initiated in the 1960s [*Cloud*, 2001]. The satellites consisted in optical devices mounted on modified intercontinental ballistic missiles. They acquired a large volume of satellite images spanning the whole globe, thanks to an amazing system involving

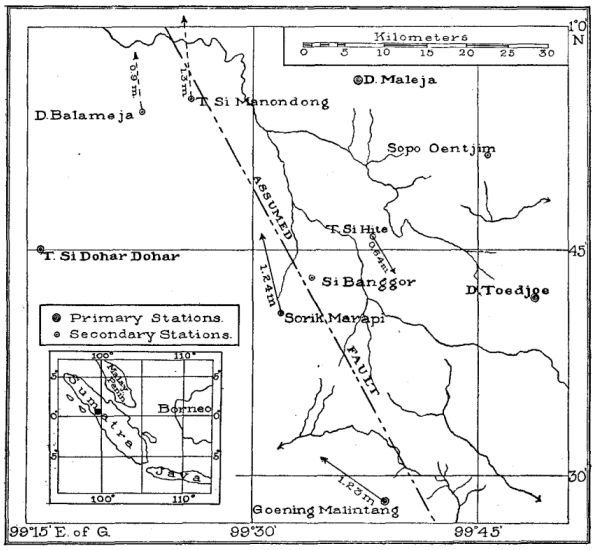

(a) 1892 M7.6 Sumatra earthquake [Reid, 1913]

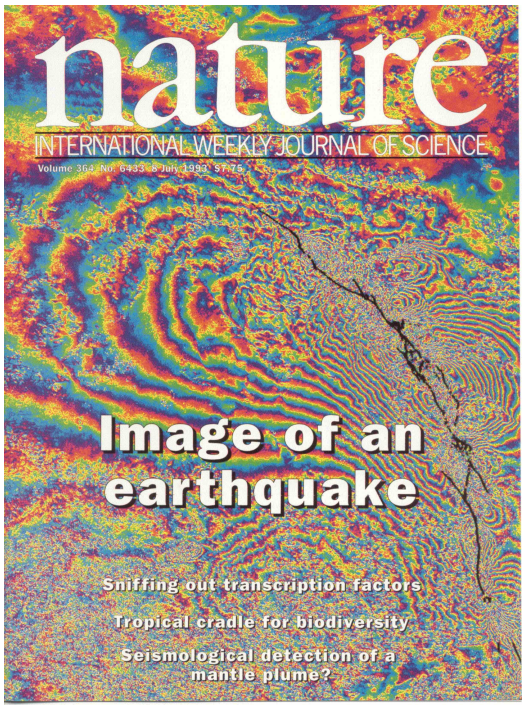

(b) 1992 M7.3 Landers earthquake [Massonnet et al., 1993]

Figure 1.1 – Two M>7 earthquakes, 100 years appart, with similar focal mechanism, represented at the same scale, illustrating the progress made over the past century in the measurement of earthquake deformation. (a) 1892 M7.6 Sumatra earthquake [Reid, 1913]. (b) 1992 M7.3 Landers earthquake [Massonnet et al., 1993].

panoramic cameras mounted on an oscillatory device to acquire high resolution stereo imagery from low earth orbit at 150-400 km altitude, and a special strategy to collect films in the sea after atmospheric reentry before the enemy could get hold of them. These images were recently declassified, and have proved exploitable to successfully measure tectonic deformation occurring in remote areas prior to the dawn of the GPS era [*Hollingsworth et al.*, 2012; *Zhou et al.*, 2016], using image correlation techniques initially developed for modern SPOT imagery [*Van Puymbroeck et al.*, 2000]. A number of other research programs were launched in the 1970s and 80s to better characterize the Earth's gravity field, officially giving birth to what is known today as space geodesy. Laser ranging of the LAGEOS satellite using various measurement sites across the globe at various epochs allowed for measuring plate motion [*Christodoulidis et al.*, 1985]. In parallel, the astronomy community provided relative measurements of the motion of tectonic plates using Very Long Baseline Interferometry, confirming these results [*Herring et al.*, 1986]. Later, the DORIS system provided another independent method to track plate motion [*Soudarin and Cazenave*, 1995].

But none of the above techniques were designed to measure the strain that has been accumulating or that is suddenly released along plate boundaries because of the sparseness of the observations. The advent of the Global Positioning System (GPS) made this objective achievable, by allowing for the deployment of – relatively – cheap and lightweight sensors with an essentially arbitrary network configuration. This quickly paved the way toward local studies of contemporaneous tectonic strain, for instance in California [*Dixon et al.*, 1991; *Feigl et al.*, 1993] or Afar [*Souriau et al.*, 1991; *Ruegg et al.*, 1993]. As part of the development and regular survey of these early networks, coseismic signals could also be measured. Among the first earthquakes captured by GPS, one may cite the 1990 M7.8 Luzon earthquake [*Silcock and Beavan*, 2001], the 1992 M7.3 Landers earthquake [*Blewitt et al.*, 1993] and the 1994 M8.1 Hokkaido-Toho-Oki earthquake [*Tsuji et al.*, 1995]. It was soon demonstrated that the GPS system was sufficiently stable and redundant that there is no need for fiducial constraints during the processing [*Blewitt et al.*, 1992], thereby allowing for the determination of absolute displacements, opening the door to a global geodetic model of present-day plate motion [e.g. *Larson et al.*, 1997]. With time, the installation of an increasing number of GPS benchmarks made it possible to broaden the scope of initially local studies, so as to capture regional deformation and refine the definition of tectonic blocks, such as in Nepal-Himalaya [*Bilham et al.*, 1997], the Caribbean [*Dixon et al.*, 1998], Japan [*Kato et al.*, 1998], South-East Asia [*Simons et al.*, 1999] or the eastern Mediterranean [*McClusky et al.*, 2000]. The deployment and expansion of permanent GPS networks across plate boundaries of special interest further enhanced the accuracy of velocity fields by allowing for a more robust mitigation of temporally uncorrelated atmospheric delays [*Bock et al.*, 1997]. This period saw the discovery – or rediscovery – of several transient phenomena, such as creep [*Duquesnoy et al.*, 1994], afterslip [*Bock et al.*, 1993; *Ruegg et al.*, 2001; *Johnson et al.*, 2006] or slow slip events (SSE) [*Rogers and Dragert*, 2003; *Vergnolle et al.*, 2010]. Coupling on currently locked fault zones derived from GPS strain measurements was more systematically assessed to better understand its relationship with seismic hazard, in particular on the world's largest megathrusts of Nepal-India [*Bilham et al.*, 1997], Japan [*Sagiya*, 1999], Sumatra [*Prawirodirdjo et al.*, 2000], Cascadia [*Miller et al.*, 2001] and Chile [*Ruegg et al.*, 2002]. The investigation of the significance of the vertical component of displacement due to tectonic processes was somehow delayed due to a lower signal-to-noise ratio and the difficulty to mitigate effects of other processes on the vertical component, such as hydrology, glacial isostatic adjustment (GIA), sea-level rise or

reference frame definition, but recent studies have attempted to integrate these measurement in tectonic coupling models [e.g. *Métois et al.*, 2012; *Fu and Freymueller*, 2012]. Finally, the development of special processing techniques dedicated to retrieving high-frequency signals, up to several Hz, from continuous high-rate GPS measurements, [*Larson et al.*, 2003], opens promising perspectives for earthquake early-warning [*Wright et al.*, 2012]. The recent detection of prompt low-frequency elastogravity signals caused by great earthquakes ahead of arrival of direct waves [*Montagner et al.*, 2016; *Vallée et al.*, 2017], and anticipated technological progress in high-precision gravity strainmeters [*Juhel et al.*, 2018], is further bridging the gap between geodesy and seismology.

Almost in parallel with the development of the GPS technique, satellites carrying radar sensors started to become available to the scientific community. The usefulness of interferometric synthetic aperture radar (InSAR) technique to measure coseismic deformation was first demonstrated by *Massonnet et al.* [1993] using the European ERS-1 satellite (Fig. 1.1b) and subsequently applied with increasing success to measure deformation from the outcrop scale to continental scale, over time intervals ranging from days to several decades. As the InSAR technique evolved, and satellites improved their imaging capabilities, the field has greatly expanded, so that InSAR data can today be accessed and processed with only minimal prior computational or geophysical training. Beyond the earthquake geodesy community, InSAR has since brought crucial observations for scientists working in a broad range of fields, from volcanology, glaciology, hydrology, landslide science, to investigations of ground deformation caused by anthropic activity in natural and urban environments. Recent trends in InSAR applied to earthquake geodesy will be reviewed in Section 1.2.

As one can realize from this brief historical account, modern ground-based geodesy has grown in parallel with the progressive understanding of the physics of active tectonic and volcanic deformation. This is no coincidence, since images of earthquake – or volcano – deformation, be it in the form of vectors scattered on a map, showing hints of the straining and warping of the Earth's surface, or even more clearly in the form of InSAR fringes that directly allow for mapping these straining regions (Fig. 1.1b), bring a vivid, compelling proof for the predominantly elastic behavior of the Earth's crust during – and, to a large extent, between – earthquakes. The ability to measure the elastic strain field of earthquakes using space geodetic techniques will naturally bring us to the question of the interpretation and modeling of these deformations, which will be the subject of the next chapter.

1.2 Interferometric Synthetic Aperture Radar (InSAR)

1.2.1 Reading list

In the following sections, we assume that the reader has a minimal background in synthetic aperture radar interferometry (InSAR), so that it is not deemed necessary to explain the basic principles of the method. For the reader who wishes to gain a deeper understanding of InSAR, the objective of the present section is to point to the main references that can introduce him/her with the key concepts, tools and applications in the field of InSAR. A number of excellent research papers, books and reviews have been written on these topics.

A list of the relevant contributions to the advancement of earthquake geodesy is provided here:

- acquisition principle and geometry of synthetic aperture radar: *Curlander and McDonough* [1991]
- digital processing: *Franceschetti and Lanari* [1999]; *Cumming and Wong* [2005]
- interferometry, principle and applications *Bamler and Hartl* [1998]; *Simons and Rosen* [2007]; *Massonnet and Souyris* [2008]; *Moreira et al.* [2013]
- phase coherence: *Zebker and Villasenor* [1992]; *Just and Bamler* [1994]
- phase filtering: *Goldstein and Werner* [1998]; *Lee et al.* [2003]; *Pinel-Puysségur et al.* [2012]; *Deledalle et al.* [2014]
- phase unwrapping techniques: *Ghiglia and Romero* [1994]; *Goldstein et al.* [1988]; *Zebker and Lu* [1998]; *Chen and Zebker* [2001]; *Hooper and Zebker* [2007]; *López-Quiroz et al.* [2009]
- tropospheric effects: *Zebker et al.* [1997]; *Hanssen* [2001]; *Li et al.* [2005]; *Doin et al.* [2009]; *Bekaert et al.* [2015b]
- ionospheric effects: *Gray et al.* [2000]; *Meyer et al.* [2006]; *Chen and Zebker* [2014]; *Gomba et al.* [2015]; *Liang et al.* [2019]
- polarimetry: *Ulaby and Elachi* [1990]; *Cloude and Pottier* [1996]; *Neumann et al.* [2009]
- multi-temporal InSAR: *Ferretti et al.* [2001]; *Berardino et al.* [2002]; *Schmidt and Bürgmann* [2003]; *Hooper et al.* [2007]; *Biggs et al.* [2007]; *Hooper* [2008]; *Ferretti et al.* [2011]; *Yan et al.* [2012]

In addition, a number of open-source softwares are available to process SAR data:

- Doris: *Kampes et al.* [2003] (`http://doris.tudelft.nl/`)
- ROI_PAC: *Rosen et al.* [2004] (`http://www.geo.cornell.edu/eas/PeoplePlaces/Faculty/matt/roi_pac.html/`)
- StamPS: *Hooper* [2008] (`https://homepages.see.leeds.ac.uk/~earahoo/stamps/`)
- NSBAS: *Doin, Guillaso, Jolivet, Lasserre, Lodge, Ducret, and* ***Grandin*** [2011]
- GMTSAR: *Sandwell et al.* [2011] (`http://topex.ucsd.edu/gmtsar/`)
- ISCE: *Rosen et al.* [2012] (`https://winsar.unavco.org/software/isce`)
- GIAnT: *Agram et al.* [2013] (`http://earthdef.caltech.edu/projects/giant/wiki`)
- Sentinel-1 toolbox (`https://sentinel.esa.int/web/sentinel/toolboxes/\unhbox\voidb@x\hbox{Sentinel-1}`)

1.2.2 InSAR: why do we need wide-swath?

Over the past 25 years, synthetic aperture radar interferometry (InSAR) has achieved spectacular success, extending the field of earthquake geodesy in an unprecedented way. Among these successes, one can cite the measurement of earthquake deformation in a variety of tectonic settings [e.g. *Massonnet et al.*, 1993; *Lasserre et al.*, 2005; ***Grandin** et al.*, 2015, 2017] (which has today, thanks to Sentinel-1, reached a point where this task is almost carried out in routine manner), as well as the characterization of transient phenomena ranging from volcanic unrest [e.g. ***Grandin** et al.*, 2010], slow-slip events (SSE) [e.g. *Cavalié et al.*, 2013] or shallow fault creep episodes [e.g. *Jolivet et al.*, 2012]. Thanks to InSAR, scientists have also been able to measure tiny strain rates associated with interseismic deformation of the upper crust in response to deep stready-state aseismic creep [e.g. *Wright et al.*, 2001b; ***Grandin** et al.*, 2012a; *Tong et al.*, 2013; *Daout et al.*, 2018].

Nevertheless, in spite of these successes, InSAR remains blind to a whole class of tectonic phenomena that have been discovered or inferred recently from GPS, seismology or laboratory experiments (Fig. 1.2). These newly discovered processes include low- and very low-frequency earthquakes (VLF), slow earthquakes and a variety of SSEs spanning a broad range of magnitudes (from M3 to M7.5) and durations (from 1 minute to 1 year). Detecting these events with InSAR would be extremely valuable to determine the actual fault area involved, hence the stress drop of these events [e.g. *Matsuzawa et al.*, 2010], which is still a subject of debate due to lack of constraints from seismology for these mostly aseismic phenomena. Also, constraining

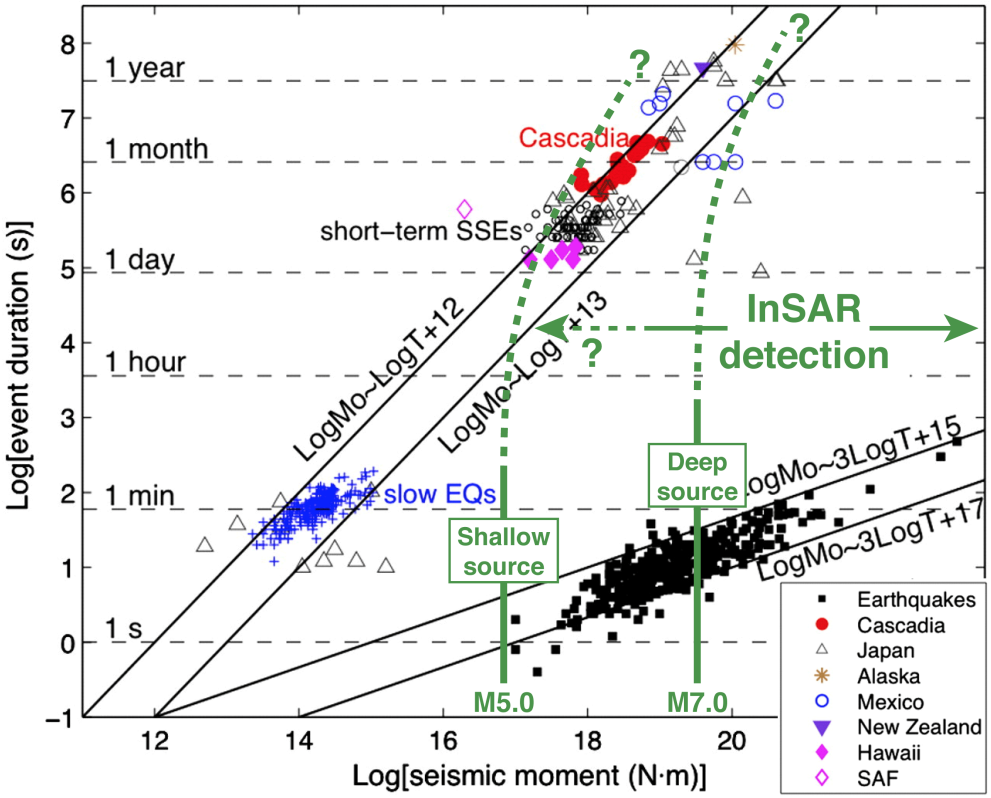

Figure 1.2 – Seismic moment versus event characteristic time of duration. Adapted from Gao et al. [2012] (see also Ide et al. [2007]; Peng and Gomberg [2010]). Annotations in green are from this study.

the slip history of the long-lasting events (namely, SSEs) would provide a better understanding of the rheological parameters that prevail within the fault zone, with potentially important implications in terms of seismic hazard assessment [e.g. *Rubin*, 2008; *Ikari et al.*, 2015].

Since most of these events occur over time scales longer than a few days, a short revisit time of the order of one day is obviously a necessary condition to avoid aliasing of the signal associated with these events. Furthermore, short revisit time should be combined with systematic acquisition capability to guarantee an homogeneous temporal sampling. These two requirements (short revisit time and global coverage during every cycle) can only met by wide-swath. Recent systems, such as the twin-satellite Sentinel-1 mission, are now capable of achieving a 6-days revisit interval in most tectonic and volcanic regions of the Earth, thanks to wide-swath acquisition modes. The main characteristics of wide-swath SAR systems will be reviewed in section 1.2.3.

Unfortunately, a short revisit is not a sufficient condition to be able to measure SSEs. Indeed, since most of these events have their sources in the deep part of fault systems (i.e. z>10–20 km), surface deformation due to SSE is particularly difficult to resolve with InSAR. In practice, this means that only the largest and/or the shallowest transients have some likelihood of detection with InSAR (Fig. 1.2).

In any case, in order to measure small strains from InSAR, it is necessary to mitigate atmospheric noise that often dominates the signal by one order of magnitude or more. Tropospheric delay is classically divided in two categories: turbulent and stratified. The former prevails on short temporal and spatial scales (a few hours, a few tens of kilometers), and will remain aliased as long as observations are available only once a day. Turbulent delays are usually cancelled by averaging several acquisitions or by low-pass temporal filtering, thereby reducing the effective temporal resolution on deformation. As a consequence, with this correction strategy, there is a strong benefit in a high frequency of revisit, hence the number of acquisitions N, because the averaging process tends to increase the SNR proportionally to $\frac{1}{\sqrt{N}}$ (assuming that the source of noise is uncorrelated between the measurements).

On the other hand, so-called "stratified delays" depend on the variability of moisture, especially with elevation. They are correlated in time over much longer time scales (a few days), with a strong seasonal variability [e.g. *Doin et al.*, 2009]. In other words, atmospheric delays contain a significant power at low temporal frequency (commonly described by a flicker noise or random walk noise). As a consequence, averaging strategies may therefore become unreliable. Nevertheless, a short revisit interval allows for a better sampling of the atmospheric noise and therefore a better characterization of its statistical properties, and hence a more efficient correction [e.g. *Gong et al.*, 2015].

In summary, wide-swath allows for achieving a shorter revisit interval. Investigations of tectonic deformation using InSAR benefit from such a shorter revisit interval because of an improved capability to correct for atmospheric artifacts. Depending on the dynamics of the process, different strategies can be implemented to take advantage of a shorter revisit interval to enhance the SNR:

- **Short, pulse-like events (earthquakes)** : averaging interferograms acquired before and after the event
- **Transient signals (SSE, postseismic)** : band-pass or low-pass temporal filtering
- **Steady-state processes (interseismic)** : linear regression in time or stacking

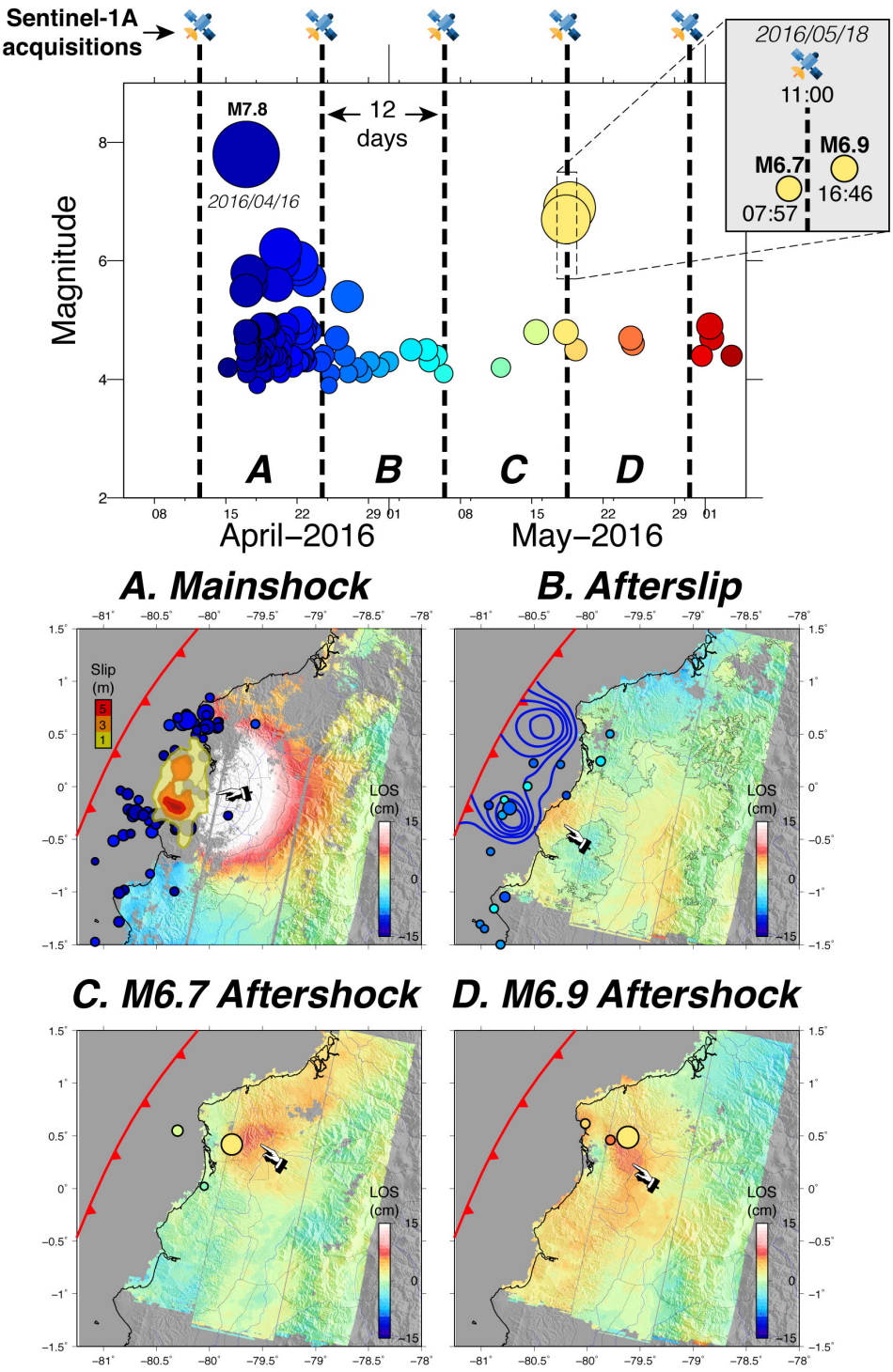

*Figure 1.3 – Deformation during and after the M7.8 16 April 2016 Pedernales captured by four consecutive 12-days Sentinel-1 interferograms. Coseismic slip model for mainshock is from Nocquet, Jarrin, Vallée, Mothes, **Grandin** et al. [2017]. Afterslip during the 30 days after the mainshock is shown with 10-cm blue contours, after Rolandone et al. [2018]. Areas of maximum deformation in the interferograms are indicated by the pointed fingers. Earthquake locations are from USGS (`https://earthquake.usgs.gov/earthquakes/search/`).*

In the specific case of postseismic deformation, a combination of different processes may occur simultaneously, such as poroelastic rebound, afterslip, viscous relaxation and occasionally energetic aftershocks [e.g. *Peltzer et al.*, 1998; *Gonzalez-Ortega et al.*, 2014; *Cheloni et al.*, 2017]. In this case, the above strategies are generally ineffective, so that atmospheric signals cannot be easily corrected. Such a complex superposition of processes with distinct temporal time scales is best analyzed by a combination of GPS (to resolve the temporal evolution of deformation) and InSAR (to map the spatial pattern of deformation) [e.g. *Klein et al.*, 2016; *Ragon et al.*, 2018a]. Enhancing the revisit frequency of SAR facilitates this combination.

Furthermore, as shown in Fig. 1.3, a short revisit interval improves chances of being able to distinguish coseismic deformation from postseismic deformation, and to isolate strong aftershocks. The strongest aftershock, according to Båth law, generally has a magnitude one degree smaller than the mainshock. Furthermore, Omori's law predicts an exponential decay of the aftershock rate. As a consequence, the bigger earthquakes have a longer aftershock sequence, and these aftershocks can be detected by InSAR. This reasoning is confirmed by facts: among the recent M>8 earthquakes captured by Sentinel-1 InSAR in the 2014–2018 period, both the 2015 Gorkha earthquake strongest aftershock (which occurred 17 days after the mainshock) and the 2016 Pedernales earthquake strongest aftershock (which occurred 32 days after the mainshock) were clearly imaged in distinct interferograms [e.g. ***Grandin** et al.*, 2015] [*Nocquet, Jarrin, Vallée, Mothes, **Grandin** et al.*, 2017]. The 2016 Pedernales earthquake is an even more special case, as the second most energetic aftershock occurred just 9 hours before the strongest aftershock. Fortunately, a Sentinel-1 image had been acquired during the 9 hours time interval (Fig. 1.3). With a 12-days revisit interval, this case represents a probability of only 3%, but systems with a 1-day revisit would make this probability rise up to 37%. This example illustrates the potential of frequent revisits to disentangle the various processes at play in the few days following major earthquakes.

Currently, as explained in section 1.2.3, widening the swath comes at the expense of temporal resolution. This compromise is acceptable when investigating processes taking place at relatively great depth, but becomes a limitation when dealing with deformation sources in the shallow sub-surface. Future systems will aim at high-resolution wide-swath (HRWS), as will be discussed in section 1.4.1.

1.2.3 Recent advances in wide-swath interferometry

For nearly two decades, the InSAR method has relied on sensors operated in the "Stripmap" mode. This mode, which is the simplest among all proposed imaging modes, consists in scanning the ground with a fixed look angle with respect to nadir, in a similar fashion as the push broom mode in optical imaging (Fig. 1.4).

The angular aperture of the radar antenna in elevation (given by the simple formula $\alpha = \lambda / L$, where λ is the wavelength, L is the antenna length in the same unit, and α is in radians) allows for achieving swath widths of the order of 100 km across-track. Given the altitude of sun-synchronous satel-

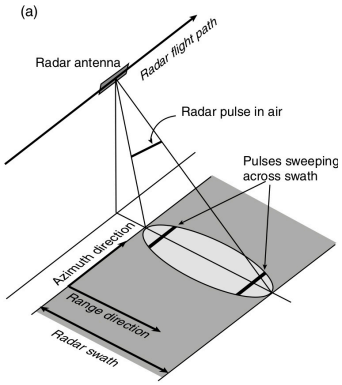

Figure 1.4 – "Stripmap" imaging method [Simons and Rosen, 2007]

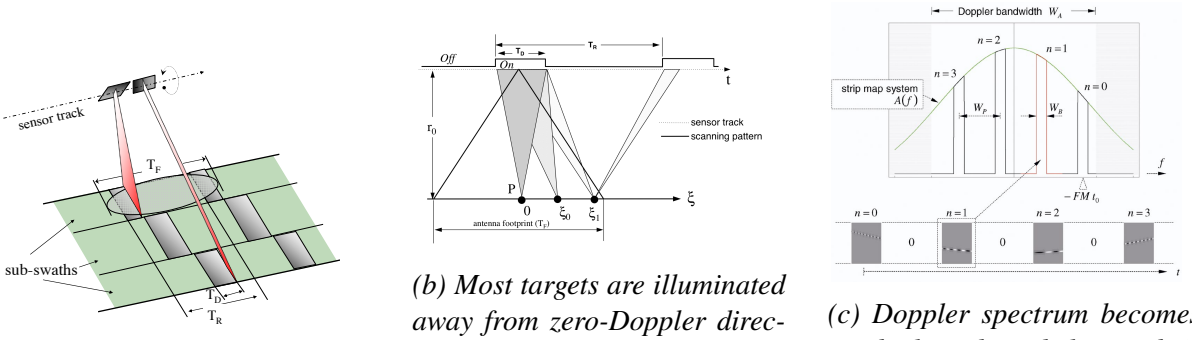

(a) ScanSAR acquisition strategy [De Zan and Guarnieri, 2006]

(b) Most targets are illuminated away from zero-Doppler direction (P, i.e. $\xi = 0$). Pixels located in burst overlaps are imaged twice (e.g. $\xi = \xi_1$) [Guarnieri and Prati, 1996]

(c) Doppler spectrum becomes comb-shaped, and the comb is centered on a frequency depending on azimuth coordinate of the targets [Holzner and Bamler, 2002]

Figure 1.5 – "ScanSAR" imaging method.

lites (600–900 km), a full Earth revolution takes ~ 1.5 hours. As a result, the total width of the regions that can be imaged in a single day cannot exceed ~ 1600 km (at the equator). Covering the full circumference of the globe therefore requires an orbital cycle of 1 month. In other words, even taking into account the limited area of tectonic deformation regions on Earth, single-satellite platforms operating in Stripmap mode cannot achieve a short revisit interval and simultaneously provide a background observation plan for the whole world.

This fundamental limitation can be circumvented by implementation of "wide-swath" mode (Fig. 1.5a). These modes take advantage of the capability of phased arrays to steer the direction of antenna radiation. By applying an appropriate delay between the radiating elements of the antenna, the radiated energy can coherently focus toward a direction that is different from the direction normal to the antenna plane[2]. A delay depending on elevation leads to a rotation of the beam in elevation (across-track), while a delay in the along-track direction allows for pointing the beam backward or forward. This "agility" allows for expanding the width of the swath by acquiring images on several sub-swaths, in a staggered manner (Fig. 1.5a).

Pulses are sent in so-called *bursts*, which consist of hundreds to a few thousand pulses sent in a fixed direction. After one burst, and after a short dead time to let the echoes from the last pulse return to the sensor, the beam can be steered in elevation, so that a distinct sub-swath is imaged (Fig. 1.5b).

After a certain amount of time during which more sub-swaths can be imaged, it becomes necessary to return to the first sub-swath and send a new burst in order to avoid gaps in the ground coverage. This is only possible, of course, because the radar antenna beam is "thick", i.e. it has a certain aperture in azimuth that results in an along-track footprint of a single pulse of the order of ~ 10 km (unlike an optical sensor). Combined with the Doppler effect, this specific feature is exploited to achieve the *synthetic aperture*.

In order to avoid any gap, any pixel should be imaged by at least one burst. If a short cycle is used, it is possible to image a given pixel several times. This number is defined as the "number of looks" of the burst mode, which is an integer greater or equal to one. Fig. 1.5c illustrates the

[2]This strategy can be interpreted as beamforming-on-transmit. See section 1.4.1 for a discussion of beamforming-on-receive modes.

Doppler spectrum of a four-look ScanSAR. However, a short cycle means more frequent cycles, hence more cumulative dead time, which explains why single-look burst-mode imaging is generally favored. This drawback has to be balanced against improved angular diversity achieved by multi-look burst-modes, as explained later.

On the other hand, maximum cycle duration is ultimately governed by the along-track length of the sub-image acquired during a single burst, and by the satellite velocity (a parameter that cannot be controlled). In the simplest scenario, the duration of the bursts – hence their along-track length – is controlled by the antenna's angular aperture in azimuth, hence by antenna size (typically $\sim$ 10 m). This specific solution corresponds to the "ScanSAR" mode. In a more complex scenario, the along-track length of burst footprint can the increased by slowly and progressively steering the antenna beam in azimuth during the course of the burst acquisition. The sweeping is done from the aft to the fore. In other words, the radar points backward at the beginning of the burst, and forward at the end. This mode is named "Terrain Observation by Progressive Scans", or "TOPS" [*De Zan and Guarnieri*, 2006] (Fig. 1.6). This strategy allows for using longer cycles, increases the Doppler frequency modulation (FM) rate (hence allowing for a higher PRF), and achieves a greater angular diversity in burst overlaps, as explained later. The Sentinel-1 satellites of the European Space Agency were the first to implement the TOPS mode as the standard acquisition mode over land (Fig. 1.7). The satellites Sentinel-1A and Sentinel-1B were launched in April 2014 and April 2016, respectively.

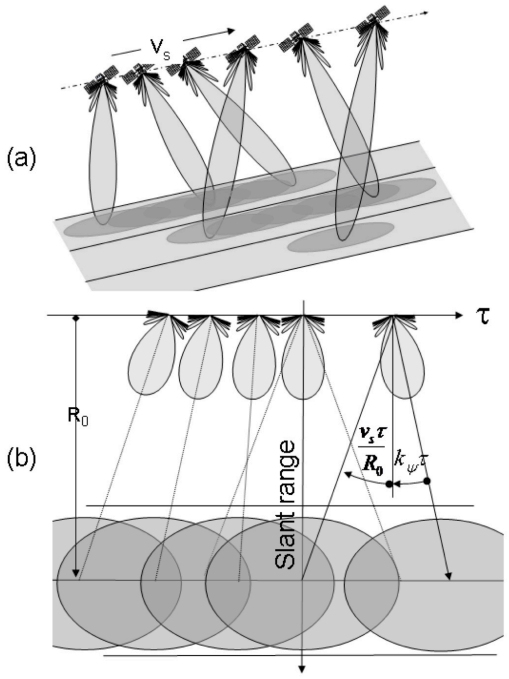

Figure 1.6 – "Terrain Observation by Progressive Scans" (TOPS) imaging mode [after De Zan and Guarnieri, 2006].

Both ScanSAR and TOPS allow for synthesizing images spanning three (or more) sub-swaths. This three-fold increase in swath width translates to an equivalent reduction in the time required to image the full globe, hence an improved revisit frequency. In turn, the fact that ground targets are only seen during a fraction of the maximum theoretical synthetic aperture duration means that the azimuth resolution will be reduced. Hence, a wide swath is obtained at the expense of azimuth resolution.

The first operational implementation of wide-swath on a spaceborne platform was achieved as part of the Shuttle Radar Topographic Mission (SRTM) in 2000 [*Rabus et al.*, 2003]. The capability to acquire 4-beam ScanSAR images spanning a 225 km-wide swath was a key requirement to make sure that the globe could be covered in the short duration of the the mission (11 days). As both antennas were carried by the same platform, perfect burst synchronization could be ensured, although processing had to deal with other problems related to platform stability during maneuvers, in addition to oscillations of the boom carrying the outboard antennas [*Hensley et al.*, 2000].

Starting with ESA's ENVISAT and JAXA's ALOS satellites, and later with CSA's RADARSAT-2 satellite and DLR's TerraSAR-X–TanDEM-X constellation, an experimental

ScanSAR mode was tested. However, it was soon recognized that a major difficulty of burst modes is the necessity to ensure a good synchronization of bursts between successive acquisitions [*Liang et al.*, 2013].

Otherwise, if bursts hit the targets with too different azimuth angles, different parts of their azimuth spectrum will be sampled, so that interferograms will become incoherent (just as standard interferometry is limited by the critical perpendicular baseline). While a controlled orbit improved the chance of getting synchronized images [*Rosich et al.*, 2007], fully solving this problem requires excellent knowledge of the location of the sensor along the track as a function of time, so that bursts can be triggered at the right time. Carrying GPS sensors on board, in combination with real-time calculation of satellite trajectory, allows for achieving this requirement. This was first done by TerraSAR-X, and almost at the same time by RADARSAT-2.

Figure 1.7 – Sentinel-1 satellite (ESA)

Another specificity of the burst modes is that the azimuth signal is no longer centered on the same Doppler centroid (DC) for all targets in a given range bin. Instead, DC drifts along the azimuth direction within each burst. The reason is that the distance between the sensor and a given target will depend, on average, on its azimuthal coordinate, whereas in Stripmap mode the average satellite-ground distance is the same for all targets in a given range bin (and close to zero-Doppler distance in the case of an unsquinted acquisition). In other words, because the beam is switched on and shut down periodically, any given target will be situated, on average, either forward or backward with respect to the zero-Doppler plane. Only for a particular azimuth coordinate will zero-Doppler be achieved, while other targets will be squinted away from zero-Doppler. As a result, the azimuth impulse response of targets will depend on their azimuthal coordinates, so that efficient azimuth compression by means of traditional focusing algorithms will leave a residual phase term superimposed on the desired phase of the target (Fig. 1.8).

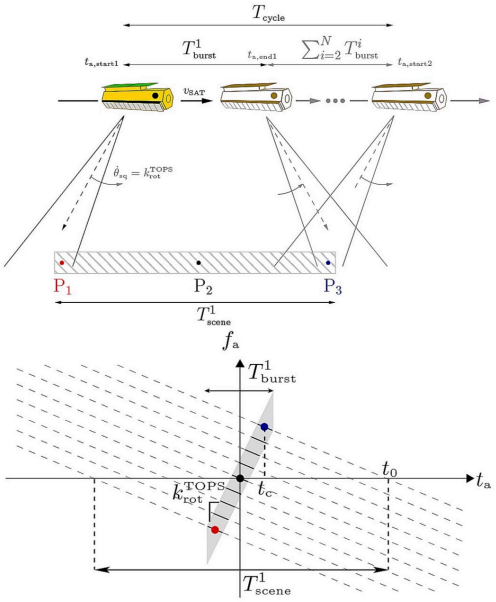

Figure 1.8 – "Wide-swath" TOPSAR imaging method [Rodriguez-Cassola et al., 2015]. In the bottom panel, oblique lines show the Doppler frequency history of targets distributed at different locations along the azimuth coordinate. The shaded region corresponds to the instantaneous azimuth bandwidth.

Due to the difficulty for most users to achieve an accurate and efficient focusing of raw data (level 0) acquired in TOPS or ScanSAR modes, space agency now supply pre-processed, focused single-look complex (SLC) images (level 1). These images are obtained after pre-processing using phase-preserving algorithms (e.g. see the IPF processor developed by MDA for Sentinel-1[3]). The user then has to correct the phase information from these images prior to ingestion into an interferometric processing chain.

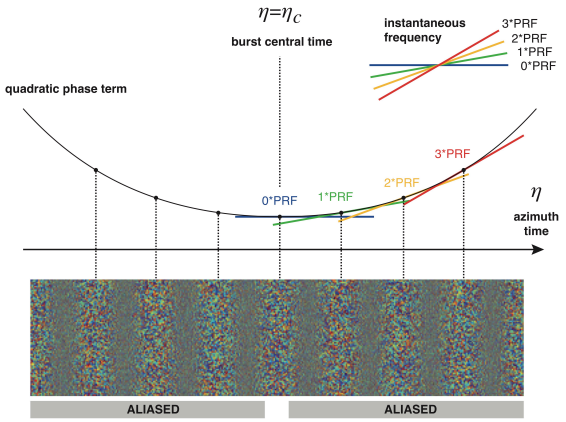

(a) Quadratic phase term in azimuth. For clarity, a small subset of an SLC image is shown here, and has been flipped 90°.

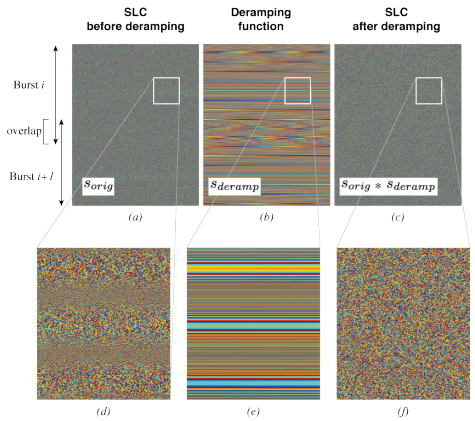

(b) Left: SLC before deramping. Middle: deramping phase screen. Right: after deramping.

*Figure 1.9 – Principe of deramping [from **Grandin**, 2015].*

The main challenge consists in removing a quadratic phase term that affects the images due to the combination of burst-mode acquisition and application of a uniform Doppler signal during azimuth focusing performed by the Agency. This quadratic phase can be visualized (Fig. 1.9a). Its expression is found as the extra exponential term in the formula of the azimuth impulse response of focused TOPS signal [e.g. *Prats et al.*, 2010; *Miranda*, 2014; ***Grandin***, 2015]:

$$s_{orig}(\eta,\tau) = A.\,\mathrm{sinc}\left(B_{eff}(\eta-\eta_0)\right) \times \exp\left\{+j\pi k_t(\tau)\left(\eta-\eta_c(\tau)\right)^2\right\} \tag{1.1}$$

where τ is range (fast) time, η is azimuth (slow) time, η_c is burst central time, η_0 is target's zero-Doppler time and k_t is Doppler centroid frequency modulation rate in the focused SLC. The cardinal sine function in the above formula means that targets are processed at their zero-Doppler location. Correction of this parasitic term involves multiplying images by a phase screen – depending on azimuth and range – equal to the complex conjugate of this exponential term, a process called "deramping" (Fig. 1.9).

The difficulty that arises from this approach is that (1) one has to "guess" the actual value of η_c and (2) the value of η_c must be determined with a great accuracy, of the order of 1/1000 pixel, to make sure high-quality interferograms can be obtained [*Prats-Iraola et al.*, 2012]. Interferograms corrected with a poor estimate of η_c will be affected by a residual phase ramp in the azimuth direction, in the form of a sawtooth pattern (Fig. 1.10a).

[3] https://sentinel.esa.int/web/sentinel/level-1-slc-processing-algorithms

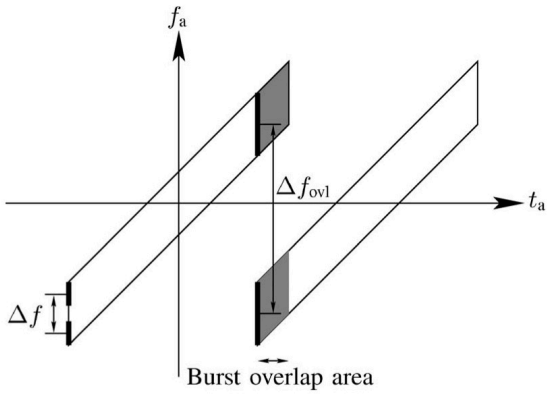

(a) Time-frequency diagram showing how the Doppler frequency difference can be measured in the burst overlap area to deduce the residual DC frequency drift affecting each burst [Prats-Iraola et al., 2012]

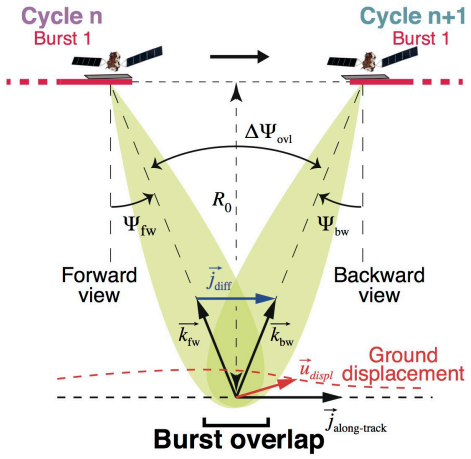

*(b) An equivalent, geometrical interpretation of spectral diversity relates the frequency difference Δf_{ovl} to horizontal motion along the satellite track [**Grandin** et al., 2016].*

Figure 1.10 – Spectral diversity.

Various strategies have been devised to compute the deramping function. A first, rough estimate of the relative values of η_c for a pair of images can be determined by means of incoherent cross-correlation of radar image amplitudes. Precise orbits can also be used to bypass this computationally demanding step. The second step, which allows for achieving the best accuracy, consists in computing backward- and forward-looking interferograms in burst overlap regions. After differencing these interferograms, a precise estimate of the coregistration error between the pair can be achieved [e.g. ***Grandin** et al.*, 2016; *Yagüe-Martínez et al.*, 2016; *Jiang et al.*, 2017]. This procedure is called "spectral diversity" [after *Scheiber and Moreira*, 2000], and is illustrated in Fig. 1.10.

The above procedure has to be applied for each burst, and for each pair of images. During experiments with real data, it was noticed that the azimuth time lag that needs to be applied to synchronize the bursts is slightly variable in azimuth and in range. A bilinear term therefore has to be included. Presumably, this additional term may originate from inaccuracies in the geometrical model [***Grandin** et al.*, 2016; *Fattahi et al.*, 2017] or from ionospheric effects [*Wang et al.*, 2017] which are notoriously known for perturbing the azimuth signal, including in C-band [*Gomba et al.*, 2017; *Liang et al.*, 2019].

An unintended capability of the TOPS mode is the measurement of ground motion along the satellite track with great accuracy, a part of the spectral diversity correction. Validation of the technique to measure coseismic deformation caused by the 2015 M_w8.3 Illapel earthquake (Chili) has demonstrated that an accuracy of the order of 10 cm can be achieved on the along-track (i.e. roughly North-South) component of ground displacement (Fig. 1.10b) [***Grandin** et al.*, 2016]. As conventional InSAR is only capable of measuring ground motion in the line-of-sight (nearly vertical) direction, the sensitivity of spectral diversity to along-track displacement provides a complementary information on ground motion that makes it possible to separate the three components of ground displacement (see Section 1.3)

To conclude, wide-swath imagery has enabled radar satellites to image the ground with a short revisit time. The Sentinel-1 system, consisting of two twin satellites, achieves a 6-day revisit time, and collects images with a swath width of 250 km. Systematic acquisitions are made over Europe, while 12-days interferometry is possible in most areas categorized as tectonic or volcanic regions [*Geudtner et al.*, 2014]. Sentinel-1 data have already allowed for measuring successfully coseismic deformation for nearly 50% of all theoretically measurable shallow M>5 earthquakes that occurred since the launch in 2014 [*Funning and Garcia*, 2017]. Using only three years of data, tests in Albania have shown that an accuracy of the order of 2-4 mm/yr can already be achieved in the measurement of continuous ground movement, such as in the Patos-Marinza area, where subsidence related to oil extraction has been detected and measured for the first time (Fig. 1.13).

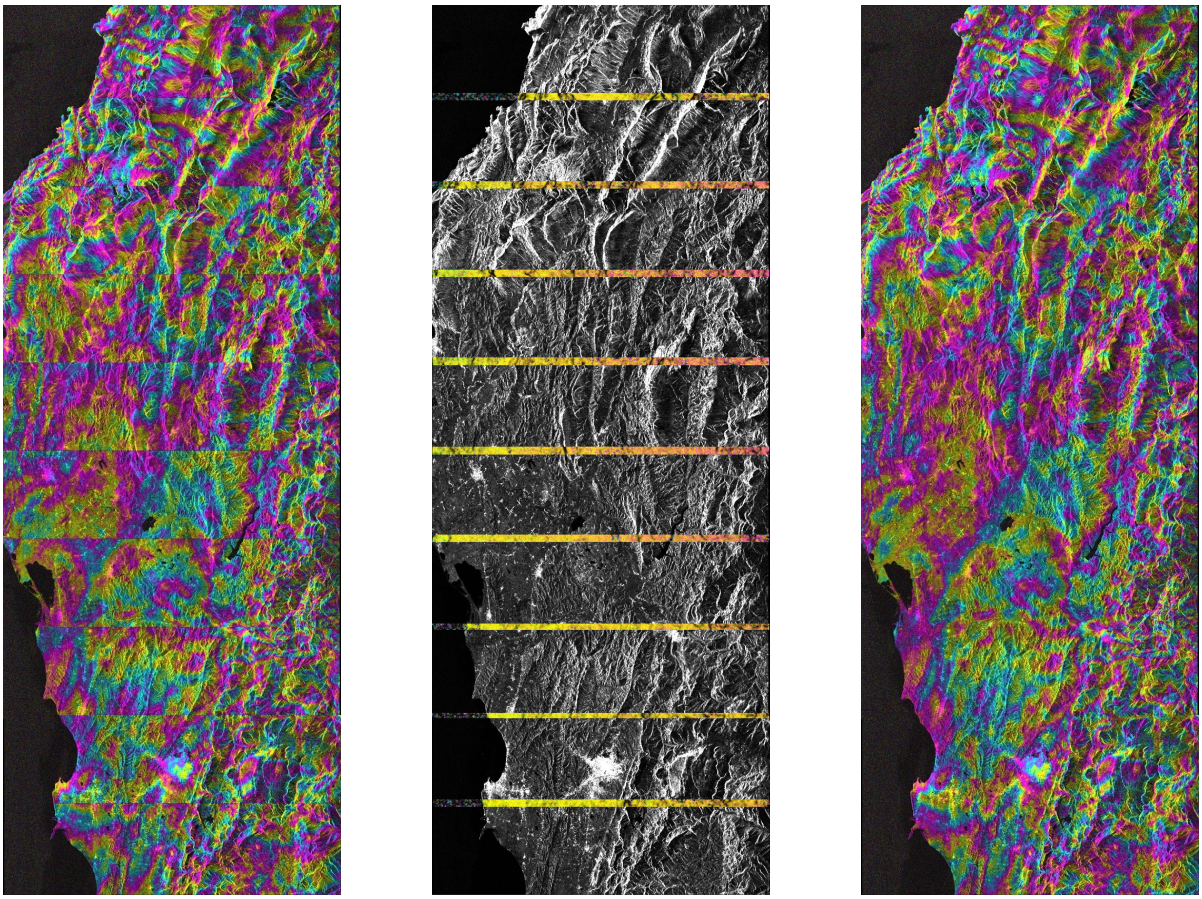

(a) Before applying spectral diversity correction.

(b) Burst-overlap interferograms.

(c) After applying spectral diversity correction.

*Figure 1.11 – Sentinel-1 interferogram covering the coastal part of Albania, illustrating the efficiency of spectral diversity correction of **Grandin** [2015] (ascending track 175; master: 2017/06/27; slave: 2017/07/03). Only one sub-swath is shown here (iw1). The covered area is approximately 80 km wide (across-track) and 200 km long (along-track). North is at the bottom.*

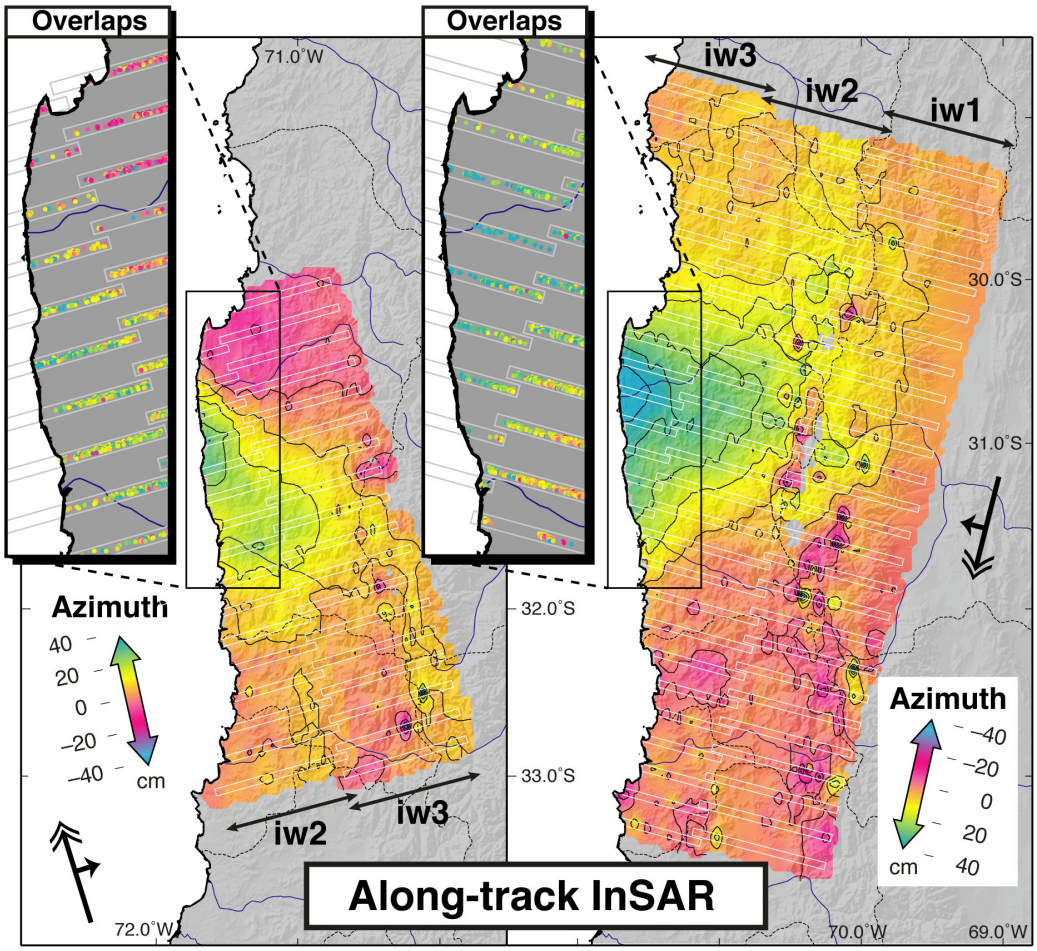

*Figure 1.12 – Along-track Sentinel-1 interferograms covering the Illapel earthquake (Chile, 16 September 2015, M_w8.3) [**Grandin** et al., 2016]. Ascending pass is to the left, descending pass to the right. Insets shows raw measurements, while main panels correspond to interpolated measurements.*

1.2.4 Multi-temporal interferometric processing

Small baseline *versus* Persistent scatterers

One strength of SAR data is the ability to accumulate stacks of images that make it possible to map deformation as a function of time. For this purpose, various strategies have been proposed, which can classically be sorted in two main categories, namely small spatial baseline subset (SBAS) [*Berardino et al.*, 2002] and persistent scatterers (PS) [*Ferretti et al.*, 2001; *Hooper et al.*, 2007].

The PS technique consists, in a stack of SAR images, in computing all the interferograms connecting the master image and all of its slaves. Hence, when N images are available, $N-1$ interferograms need to be calculated (Fig. 1.14a). In these interferograms, not all points are analyzed. Instead, only a subset of selected points are processed. These points are chosen on the basis of the stability of their phase history through time [e.g. *Ferretti et al.*, 2001; *Hooper et al.*, 2007]. Criteria on phase stability, which may include criteria on the stability of the amplitude, are used to select which pixels should be kept. Phase unwrapping, digital elevation

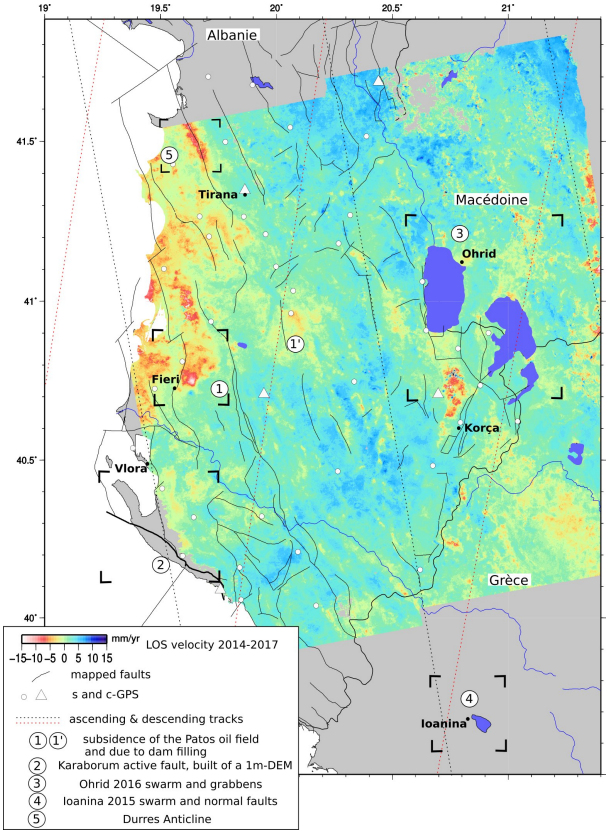

(a) Line-of-sight average velocity map for the period 2014–2017 over Albania from NSBAS processing of 109 Sentinel-1 acquisitions (ascending track 175, sub-swaths iw1 and iw2).

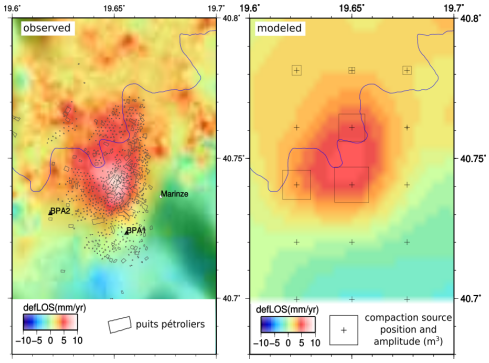

(b) Subsidence in the Patos-Marinza area due to non-conventional extraction of heavy oil. Right panel shows a first-order attempt to model subsidence using compaction sources at depth.

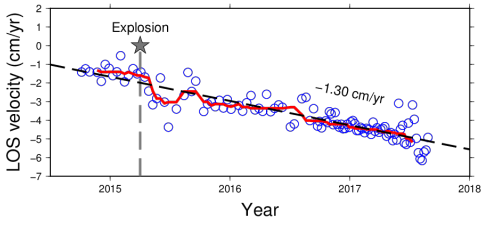

(c) Time-series of cumulative LOS displacement at the site of maximum subsidence. Star marks time of occurrence of an explosion reported at the surface.

Figure 1.13 – Surface velocity map of Albania from Sentinel-1 multi-temporal InSAR processing using NSBAS software [Métois et al., 2019].

model errors and temporal analysis are performed in a single pass, which involves solving a non-linear inverse problem. Earlier versions of the method used a prescribed temporal evolution model (e.g. linear) to determine an average velocity field, whereas more recent implementations tend to use more flexible temporal filtering strategies to determine the time history with less *a priori* [*Hooper*, 2008; *Yan et al.*, 2012]. It is believed that bright pixels, exhibiting a good phase stability through time (the so-called "persistent scatterers") represent objects with a size smaller than the resolution cell of SAR, which have a dominant contribution to the phase of the pixel. The archetype of a PS would be corner reflector surrounded by vegetation. The PS technique has achieved great success in urban areas, where the density of PS is high, but its application in regions of natural terrain with moderate coherence remains difficult. Modifications of the technique to identify groups of stable pixels, instead of individual pixels, or adapted filtering and weighting, have been proposed to overcome this limitation [*Lyons and Sandwell*, 2003; *Hooper*, 2008; *Ferretti et al.*, 2011].

The SBAS method follows a different philosophy. The idea is to compute a large number of interferograms, connecting individual acquisitions with a prescribed level of redundancy. All

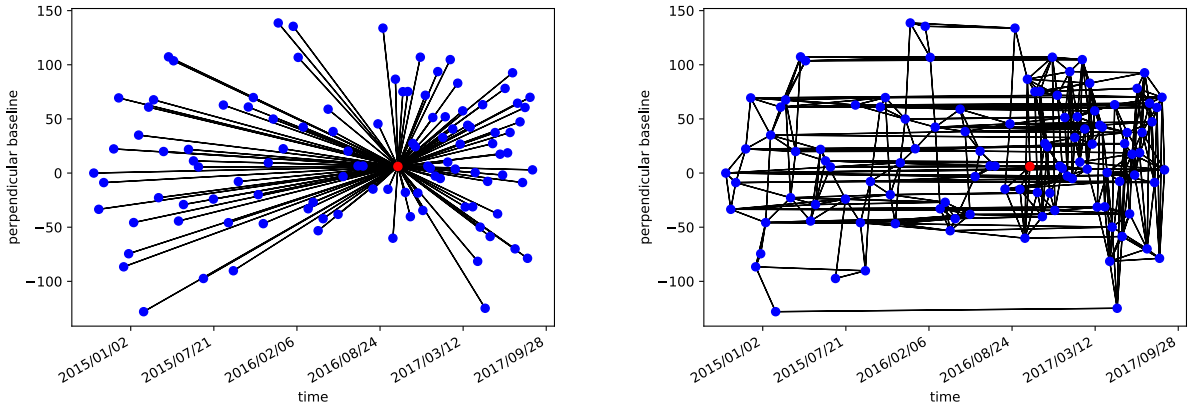

(a)
Persistent scatterers (PS)
108 interferograms

(b)
Small BAseline Subset (SBAS)
469 interferograms

Figure 1.14 – Typical interferogram network for a test Sentinel-1 dataset using the Persistent Scatterers (left) and Small BAseline Subset (SBAS) methods. Each circle represents an acquisition. X axis is time and Y axis is the perpendicular baseline. Red circle indicates the Master image. The dataset represented in this figure covers Albania and includes 109 acquisitions. The PS network consists of 108 interferograms, while the NSBAS network consists of 469 interferograms. The case shown here corresponds to the Albania dataset in Fig. 1.13.

the interferograms need to be unwrapped *a priori*, so that the temporal evolution of deformation can be determined by a simple linear inversion procedure [*Schmidt and Bürgmann*, 2003]. In order to minimize chances of unwrapping errors, only good quality interferograms are computed. The quality of interferograms, which is measured by interferometric coherence, depends on (1) the temporal separation between the acquisitions and (2) the perpendicular baseline. Hence, interferograms with a short temporal baseline or a short spatial baseline are targeted in priority (Fig. 1.14b). Additional criteria can be included to define the optimal network, such as favoring acquisitions made during the "dry" season in case of seasonal variations of interferometric coherence [***Grandin** et al.*, 2012a].

The SBAS method provides not only an average velocity map, but also the full history of pixel displacement through time (Fig. 1.15). Furthermore, the information is available for all pixels that have been successfully unwrapped throughout the stack. Temporal filtering during the inversion procedure can help separating tectonic processes, which are characterized by a slowly-varying (e.g. interseismic strain accumulation) or a stepwise contribution (e.g. coseismic deformation, as in Fig. 1.16) from signals characterized by an erratic behavior (e.g. atmosphere). Digital elevation model errors, which are proportional to the perpendicular baseline, can be estimated simultaneously.

The SBAS method is generally considered as better suited for studies of tectonic deformation over large areas, in a context of moderate to low coherence [*Hooper et al.*, 2012]. Furthermore, it has the advantage of simplicity, as the linear inversion allows for more straightforward understanding of the contribution of individual interferograms in the final product. However, a major limitation of the technique is the necessity to start with a set of unwrapped interferograms. Any unwrapping error would contaminate the inversion, and deteriorate the quality of

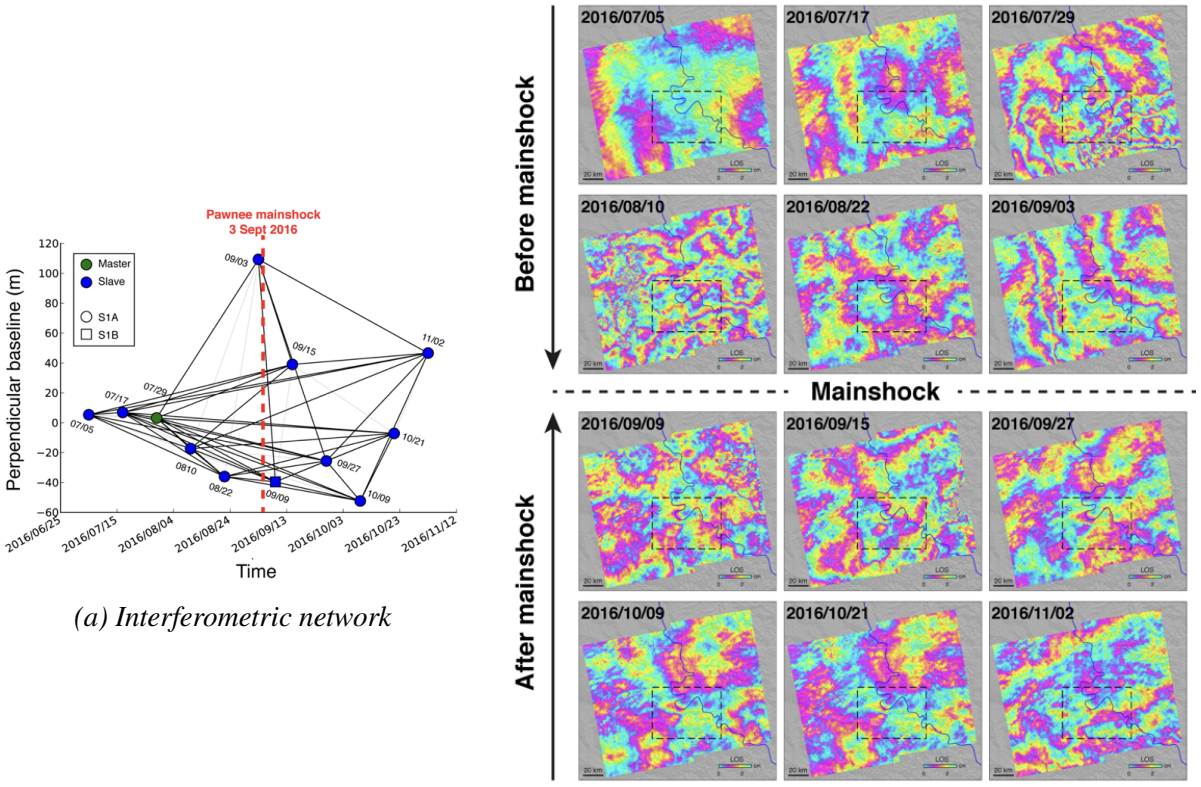

(a) Interferometric network

(b) Time-series decomposition

*Figure 1.15 – Time-series decomposition of Sentinel-1 data acquired before and after the September 2016 Pawnee earthquake [**Grandin** et al., 2017]. Left: interferogram network. Red vertical dashed line indicates the time of the earthquake. Right: interferograms corresponding to each time interval, deduced from time-series decomposition of the unwrapped interferogram network.*

the result. Unwrapping is also a challenge for PS, and the method makes it difficult to identify these errors. Hence, phase unwrapping represents a major bottleneck in multi-temporal InSAR, both for SBAS or PS.

The NSBAS processing chain

In this subsection, the specificities of the NSBAS processing chain are briefly described, with special emphasis on the methods used for correction InSAR data *prior* to unwrapping, which is the main originality and strength of NSBAS [*Doin, Guillaso, Jolivet, Lasserre, Lodge, Ducret, and **Grandin***, 2011].

Phase unwrapping consists in determining the true phase difference between any pixel and a given reference pixel whose phase is set to zero. The objective of phase unwrapping is to relieve the ambiguity on the number of 2π phase cycles (hence, the number of fringes) in the image. This problem can be interpreted as that of an integration in two dimensions. The problem is however non-trivial due to the presence of incoherent phase signals that make fringes indistinguishable, as well as inconsistencies in the phase map caused by large phase gradients in areas of rough topography or strong deformation. Early methods proposed to deal with this problem by insisting that the result should not depend on a particular choice for the starting point of the

integration path [*Goldstein et al.*, 1988; *Zebker and Lu*, 1998]. More advanced methods attempt to use cost functions and statistical approaches to determine the optimal location of phase discontinuities in areas of poor coherence [*Chen and Zebker*, 2001].

However, whichever unwrapping algorithm is chosen, the uncertainty related to potential unwrapping errors are reduced when interferometric coherence is high. The NSBAS software, developed by the ISTerre group (led by Marie-Pierre Doin, Cécile Lasserre (now at ENS Lyon) and Erwan Pathier) attempts to apply a number of corrections prior to unwrapping, in order to improve the quality of wrapped interferogram, and hence facilitate unwrapping and the subsequent SBAS analysis. This strategy is particularly relevant for C-band interferograms (such as ENVISAT or Sentinel-1) in areas of moderate coherence. The key steps include:

- spectral filter in range [*Gatelli et al.*, 1994]
- spectral diversity (for Sentinel-1) [***Grandin** et al.*, 2016] (Fig. 1.11)
- DEM error corrections [*Ducret, Doin, **Grandin**, Lasserre, and Guillaso*, 2014]
- atmospheric corrections using ERA-Interim meteorological re-analysis [*Doin et al.*, 2009] [*Jolivet, **Grandin**, Lasserre, Doin, and Peltzer*, 2011] (Fig. 1.19)

The DEM correction and spectral filter in range are especially relevant for satellites subject to broad variations in the perpendicular baseline, such as ERS, ENVISAT or ALOS-1. On the other hand, spectral diversity corrections are essential to obtain high-quality Sentinel-1 TOPS interferograms. In turn, in any situation, atmospheric corrections are becoming a standard approach to remove atmospheric fringes in areas of rough topography. Hence, these two key steps (spectral diversity and atmospheric correction) are described in detail in the following paragraphs.

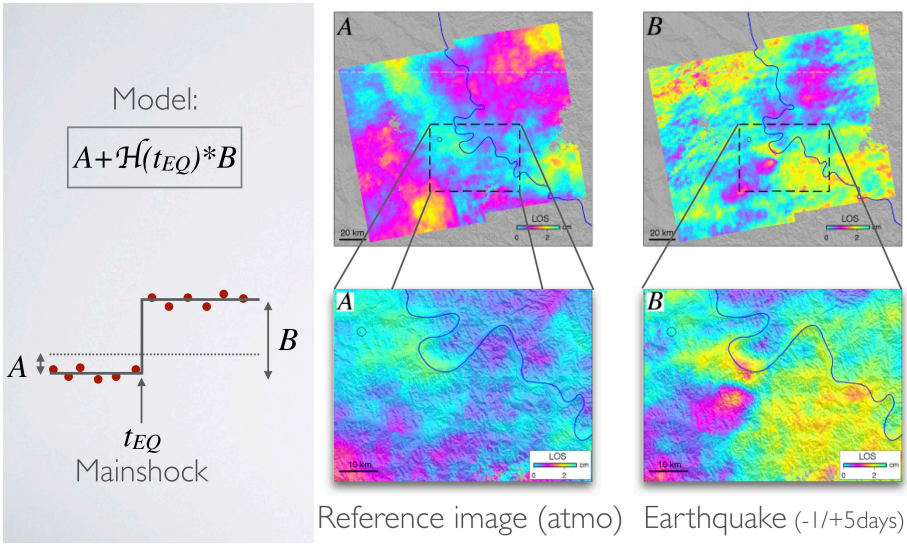

*Figure 1.16 – Separation of atmospheric signal from coseismic signal of the Pawnee earthquake [**Grandin** et al., 2017]. Starting from the phase history deduced from the interferogram time-series of Fig. 1.15, a step function was adjusted by a simple least-squares inversion for every pixel. Parameter A (constant) captures the atmospheric phase screen of the reference image, whereas B (height of the step) corresponds to the interpreted coseismic deformation. Atmospheric fluctuations in the time-series are absorbed by the residuals.*

Spectral diversity All the corrections mentioned above are applied on wrapped interferograms, in a network-consistent fashion (i.e. the value of corrected parameters for each interferogram is forced to satisfy closure on all closed loops in the image network). In particular, the spectral diversity correction implies the estimation of parameter η_c of Equation 1.1, consisting of a bilinear function of range and azimuth for each interferogram [***Grandin***, 2015; ***Grandin*** *et al.*, 2016; *Wang et al.*, 2017]. Hence, for an interferogram between acquisitions number i and j, three parameters a, b and c must be evaluated (Fig. 1.18):

$$\eta_c^{i,j} = k(a^{i,j} + b^{i,j}.x + c^{i,j}.y) \qquad (1.2)$$

where x denotes the range cell coordinate, y the azimuth cell coordinate and k is a constant set so that a is expressed in radian units.

For any closed loop between three or more acquisitions, the consistency of the retrieved values can be assessed. Fig. 1.18 shows that the observed values for parameter a are fully consistent within the interferometric network, after solving for ambiguity on its evaluation. Ambiguity arises when the "true" value of a falls beyond the $[-\pi;+\pi]$ interval. This occurs when interferograms are miregistered with an error exceeding $\sim$ 1.3 m, i.e. $\sim$ 10% of the azimuth pixel size, which is well within the capability of the cross-correlation technique [***Grandin*** *et al.*, 2016].

As shown in Fig. 1.18, a minor ambiguity can be detected and easily corrected by iterating the model. After spectral diversity correction, the residual misregistration is generally reduced by a factor $\sim$ 100, i.e. on the order of $\sim$ 1 cm, or $\sim$ 0.1% of the azimuth pixel size. Fig. 1.18 shows the excellent level of consistency across the interferometric network [see also *Fattahi et al.*, 2017]. Network consistency is also warranted with a comparable level of accuracy for factors b and c.

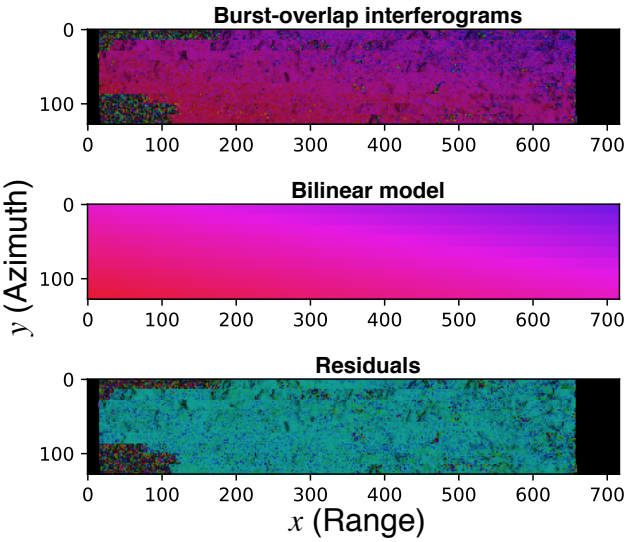

Figure 1.17 – Top: burst-overlap interferograms deduced from double-difference of forward- and backward-looking interferograms in burst overlap. The interferogram is the same as in Fig. 1.11. Middle: best fitting bilinear model. Bottom: residuals.

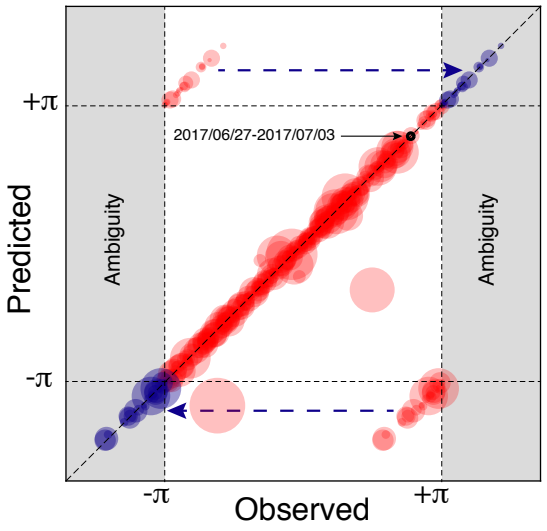

Figure 1.18 – Observed value of spectral diversity constant (term a in Equation 1.2) versus predicted value after searching for network closure and resolving ambiguity (grey bands). Each circle corresponds to an interferogram. Circles ares scaled proportionally to the uncertainty on the observed value. Blue circles represent values for which an ambiguity was detected (i.e. the observed value is incorrectly wrapped in the $[-\pi;+\pi]$ interval). Interferogram of Fig. 1.11 and 1.17 is indicated by the thick black circle.

Tropospheric delays It has been known for a long time that electromagnetic waves travel at lower speed in the atmosphere than in vacuum. In particular, in the microwave region of the spectrum, the speed of light is mainly affected by air pressure (P), air temperature (T) and air humidity (e) [e.g. *Thayer*, 1974]. The effect of spatial and temporal variations of the atmospheric delay typically manifests itself as a dependence of the retrieved interferometric phase with elevation, according to a non-trivial relation (i.e. not necessarily linear) [*Doin et al.*, 2009]. This effet has long been recognized as a major source of uncertainty when attempting to interpret interferometric fringes in terms ground deformation in regions characterized by large topographic features, such as volcanoes [e.g. *Beauducel et al.*, 2000] or mountain ranges [e.g *Elliott et al.*, 2008].

In NSBAS, the tropospheric delay can be dealt in several manners. The most promising strategy consists in using tropospheric delays predicted from meteorological information at the time of radar acquisitions. The total one-way tropospheric delay (in meters) from the satellite to a ground pixel at elevation z is given by [*Doin et al.*, 2009] [*Jolivet, **Grandin**, Lasserre, Doin, and Peltzer*, 2011]:

$$\delta \mathrm{L}^{s}_{LOS}(z) = \frac{10^{-6}}{cos(\theta)} \left\{ \frac{k_1 R_d}{g_m}(P(z) - P(z_{ref})) + \int_{z}^{z_{ref}} \left(\left(k_2 - \frac{R_d}{R_v} k_1 \right) \frac{e(z)}{T(z)} + k_3 \frac{e(z)}{T(z)^2} \right) dz \right\}, \tag{1.3}$$

where θ is the local incidence angle, $R_d = 287.05$ J.kg^{-1}.K^{-1} and $R_v = 461.495$ J.kg^{-1}.K^{-1} are respectively the dry air and water vapor specific gas constant, g_m is a weighted average of the gravity acceleration between z and z_{ref}, P is the dry air partial pressure in Pa, e is the water vapor partial pressure in Pa, and T is the temperature in K. The constants are $k_1 = 0.776$ K.Pa^{-1}, $k_2 = 0.716$ K.Pa^{-1} and $k_3 = 3.75 \cdot 10^3$ K^2.Pa^{-1}v.

The functions $P(z)$, $e(z)$ and $T(z)$ are interpolated from the meteorological re-analysis model "ERA-5" of the European Center for Medium-range Weather Forecast (ECMWF). In ERA-5, values are provided on grid nodes with a $\sim$ 25 km horizontal spacing, at different altitudes (actually, the functions must be inverted from distributions of e, T and z provided on a set of regularly spaced pressure levels). As expected, the total delay, on the order of 2 m at sea-level, decreases with increasing elevation. However, the sea-level baseline, as well as the rate of delay decrease with elevation, show significant variations in space and time. For example, Fig. 1.20 shows an example of the total delay difference computed for 6-days the interferogram of Fig. 1.19, for two points located $\sim$ 200 km apart. The shape of the two curves in Fig. 1.19 shows that (1) the total number of predicted tropospheric fringes for a topographic feature of the same height (say, 2000 m) would differ by nearly five radians, i.e. two fringes, between the two selected locations, and (2) the predicted delay at sea-level would also differ by several fringes (depending on the chosen reference altitude z_{ref} in Equation 1.3).

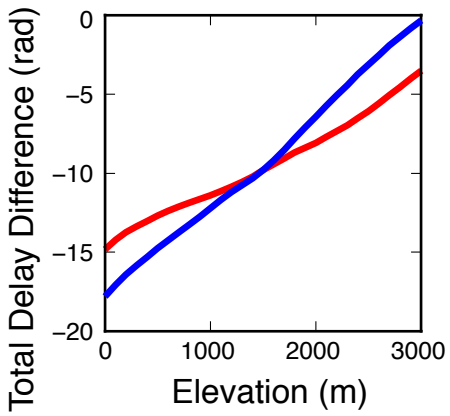

Figure 1.20 – Total (two-ways) tropospheric delay as a function of elevation for two selected locations in the interferogram of Fig. 1.19. The locations are indicated by circles in Fig. 1.19b.

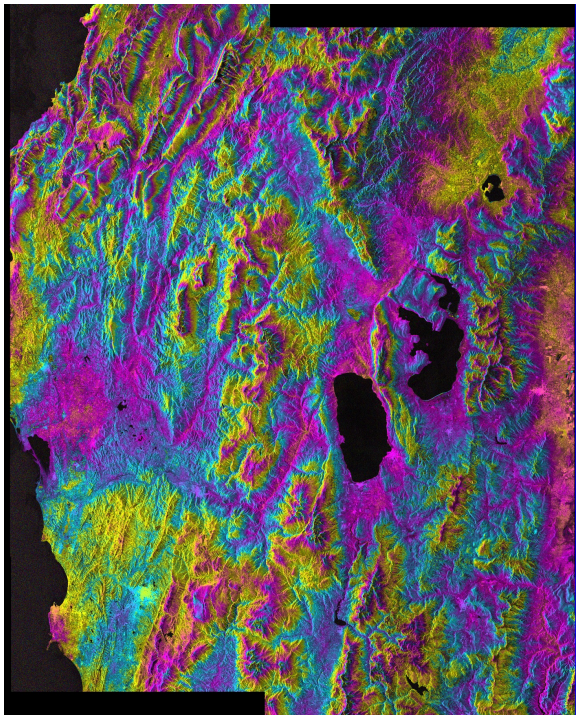

(a) Original interferogram

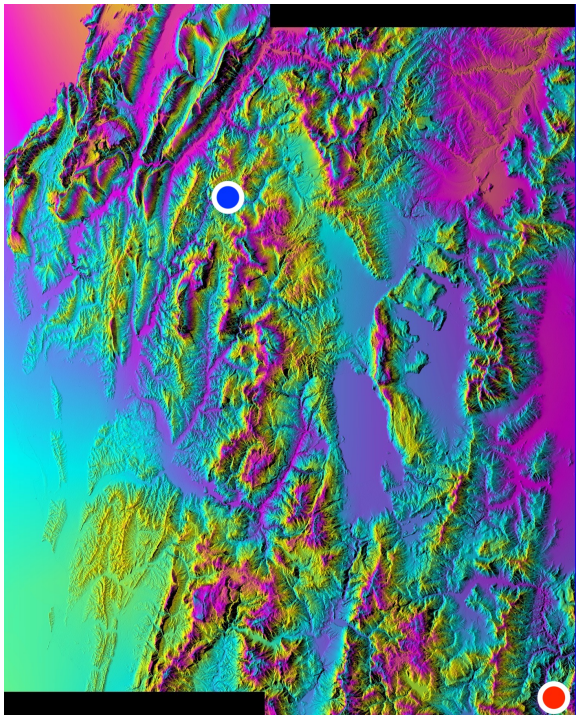

(b) Modeled atmospheric phase screen

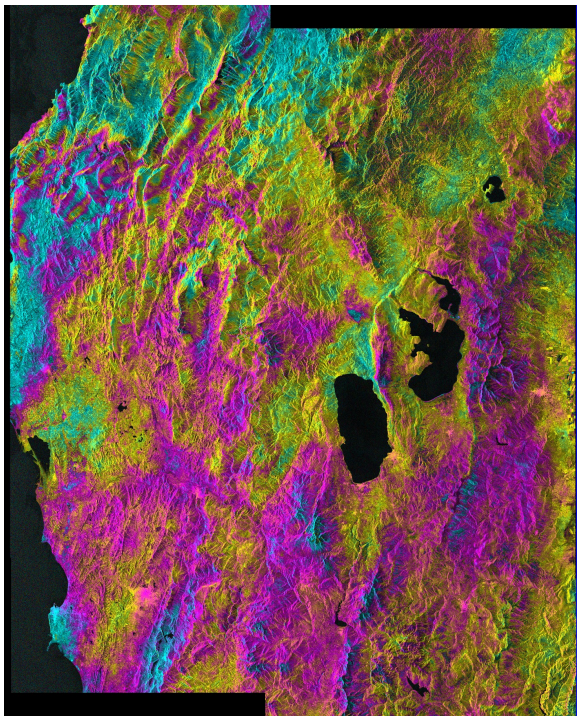

(c) Corrected interferogram (a minus b)

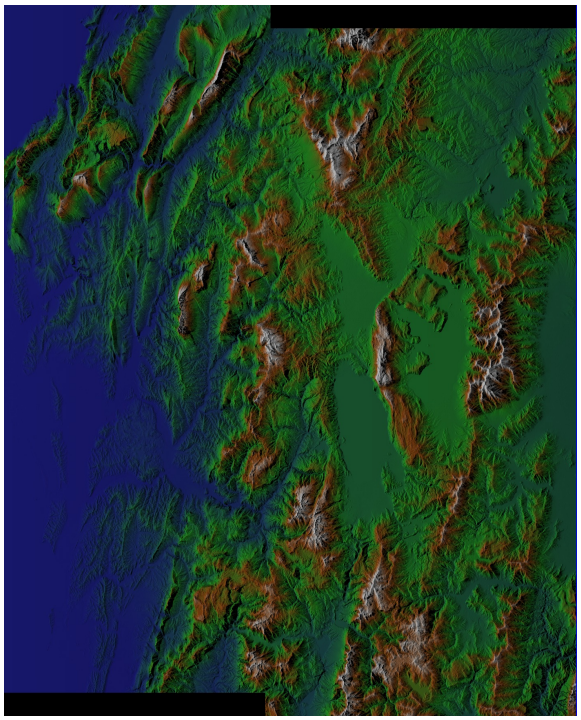

(d) Digital elevation model

*Figure 1.19 – Correction of stratified tropospheric delays using the ERA-5 meteorological analysis according to the method of Jolivet, **Grandin**, Lasserre, Doin, and Peltzer [2011] implemented in NSBAS. This Sentinel-1 interferogram covers Albania (ascending track 175; master: 2014/11/22; slave: 2014/12/04). Two sub-swaths have been assembled (iw1 and iw2). The covered area is approximately 150 km wide (across-track) and 220 km long (along-track). The elevation in the scene ranges from sea level to more than 2000 m above sea level. Blue and red dots in (b) show the location of selected ERA-5 delays shown in Fig. 1.20. North is at the bottom.*

In terms of temporal resolution, the ERA-5 model currently is currently available at 1-hour resolution, which is a significative improvement compared to the 6-hour resolution of the previous ERA-40 reanalysis. However, ERA-5 results are only available after a latency period of $\sim$ 3 months, which limits their usefulness for correcting data in real time. Near-real time solutions, such as the HRES forecasts[4] of the ECMWF, are currently considered as a surrogate for correcting InSAR data for applications requiring a rapid processing, as is done by the GACOS web service[5] [*Yu et al.*, 2018].

Phase unwrapping As a final step to interferogram processing, phase unwrapping can be performed. The traditional "branch-cut" strategy consists in propagating the fringe count across the interferogram, rounding areas of incoherent phase [*Goldstein et al.*, 1988]. Unfortunately, when coherence is poor, this method often sets aside a large fraction of the interferogram. An alternative strategy involves least-squares estimation of unwrapped phase [*Ghiglia and Romero*, 1994]. In presence of large displacement gradients, these approaches can be improved by applying prior multilooking at variable scales [*Yan et al.*, 2013]. Today, the most popular method is SNAPHU [*Chen and Zebker*, 2001], which completely unwraps interferograms by optimizing the phase jumps between the coherent regions where fringes can be unwrapped with no difficulty. However, in spite of its attractivity, this method can lead to significant errors that cannot be easily diagnosed because they tend to occur in areas of poor coherence, contrary to the "branch-cut" unwrapping errors which often produce evident spatial signatures, crossing through coherent regions. The exploitation of the redundancy offered by a network of interferograms provide an alternative approach, partially avoiding the pitfalls of SNAPHU or branch-cut techniques [*Hooper and Zebker*, 2007; *López-Quiroz et al.*, 2009; *Hussain et al.*, 2016; *Benoit et al.*, 2019].

Whichever algorithm is used for phase unwrapping, the improvement brought by NSBAS, which consists in applying a cascade of corrections prior to unwrapping, has been demonstrated by the capability of the technique to detect and measure strain accumulation in challenging environments, such as across the Main Himalayan Thrust [***Grandin** et al.*, 2012a], the Haiyuan fault [*Cavalié et al.*, 2008],the North and East Anatolian fault [*Cavalié and Jónsson*, 2014] and more recently across the Altyn Tagh fault *Daout et al.* [2018]. Other applications include the measurement of space-time evolution of subsidence in Mexico city [*López-Quiroz et al.*, 2009], vertical motion around major lake in response to temporal variations in the watermass loading [*Cavalié et al.*, 2007; *Doin et al.*, 2015], detection of creep on strike-slip faults [*Jolivet et al.*, 2012] or characterization of surface deformation due to freeze-thaw cycles affecting the permafrost [*Daout et al.*, 2017].

[4] https://www.ecmwf.int/en/forecasts/datasets/set-i

[5] http://ceg-research.ncl.ac.uk/v2/gacos/

1.3 Resolving 3D displacement

Mapping surface displacement in three dimensions facilitates interpretation

A specific characteristic of the InSAR technique is that it provides information on ground motion only for the component that is along the line-of-sight. In other words, InSAR is insensitive to displacement that takes place in the plane orthogonal to the look direction. The look direction being close to vertical (typically in the range of 30–45° with respect to nadir), the InSAR technique is approximately 1 to 2 times more sensitive to vertical displacement than to horizontal displacement. Furthermore, as SAR satellites orbit the earth in a near-polar orbit, the look direction is directed only $\approx \pm 10°$ away from the East-West direction, meaning that conventional InSAR is, by construction, least sensitive North-South displacements [in the best situation, accuracy in the N-S direction is reduced by a factor 2 w.r.t. the range direction, see *Wright et al.*, 2004]. Meanwhile, the surface displacement field during an earthquake often involves a combination of vertical and horizontal displacement, even for the most simple focal mechanisms. As a consequence of the conjunction of an oblique viewing geometry and a spatially variable ratio of horizontal:vertical displacement, a complicated fringe pattern is often observed in coseismic interferograms. This is well illustrated by the Landers earthquake (Fig. 1.1b), where several factors including uplift at the termination of a predominantly North-South oriented strike-slip fault, associated with a minor reverse component, a limited yet locally clear degree of slip partitioning, an overall curved surface trace, and the imperfect connection of multiple strands, conspired to produce a spectacularly complex interferogram.

The complexity of coseismic interferograms strongly suggests a rich underlying information content on the earthquake source. However, part of this complexity stems from the effect of the oblique projection, so that the interpretation of fringes is not straightforward. In most cases, a simple elastic model using the first order features of the source can help in understanding the shape of the fringes. Nevertheless, it is often desirable to be able to retrieve the full 3D displacement field in order to guide the interpretation of the data, especially for shallow sources of deformation.

Several methods have been proposed to reach this aim, as presented in the following paragraphs.

Combining ascending and descending InSAR

The first, obvious method is to combine ascending and descending viewing geometries. Since the two geometries are approximately symmetrical with respect to a North-South trending vertical plane, they have the same relative sensitivity to North-South displacement and vertical displacement. In other words, in-plane displacements map in the same way in the two interferograms. Under the assumption that the North-South horizontal component of displacement is not much larger than the vertical displacement, the average of the two interferograms should be approximately equal to the vertical displacement, whereas their (half) difference represents East-West displacement. Hence, one can retrieve quasi-East-West and quasi-Up-Down components of ground displacement by a simple linear combination of ascending and descending InSAR [e.g. *Fujiwara et al.*, 2000]. However, the third dimension remains unresolved with this approach.

Sub-pixel correlation of SAR images

In case of large surface displacements, it is possible to determine the motion of pixels in SAR images by means of incoherent cross-correlation [*Michel et al.*, 1999]. This technique, which is classical in optical imagery, uses the amplitude part of the master and slave images to determine motion of the pixels in images in the columns and rows directions, which in radar parlance are named the range and the azimuth directions, respectively. Depending on the coherence and the size of the subwindows used for the calculation of the correlation peak, the optimal accuracy is of the order of 10% of the size of the pixel. For a typical ENVISAT pixel (12 m ra. $\times$ 4 m az.), this means a detection threshold of the order of 1 meter, making the technique practical for large earthquakes only [e.g. *Yan et al.*, 2013]. Using only one azimuth direction deduced from SAR correlation, in combination with the two line-of-sight InSAR measurements in ascending and descending passes, the 3D displacement field can be computed [*Fialko et al.*, 2001], albeit with less accuracy on the North-South component. Even if decorrelated regions are widespread, due large displacement gradients or because of alterations of the surface causing loss of coherence, range and azimuth offsets can be used to retrieve the full 3D displacement field, as illustrated in Fig. 1.21.

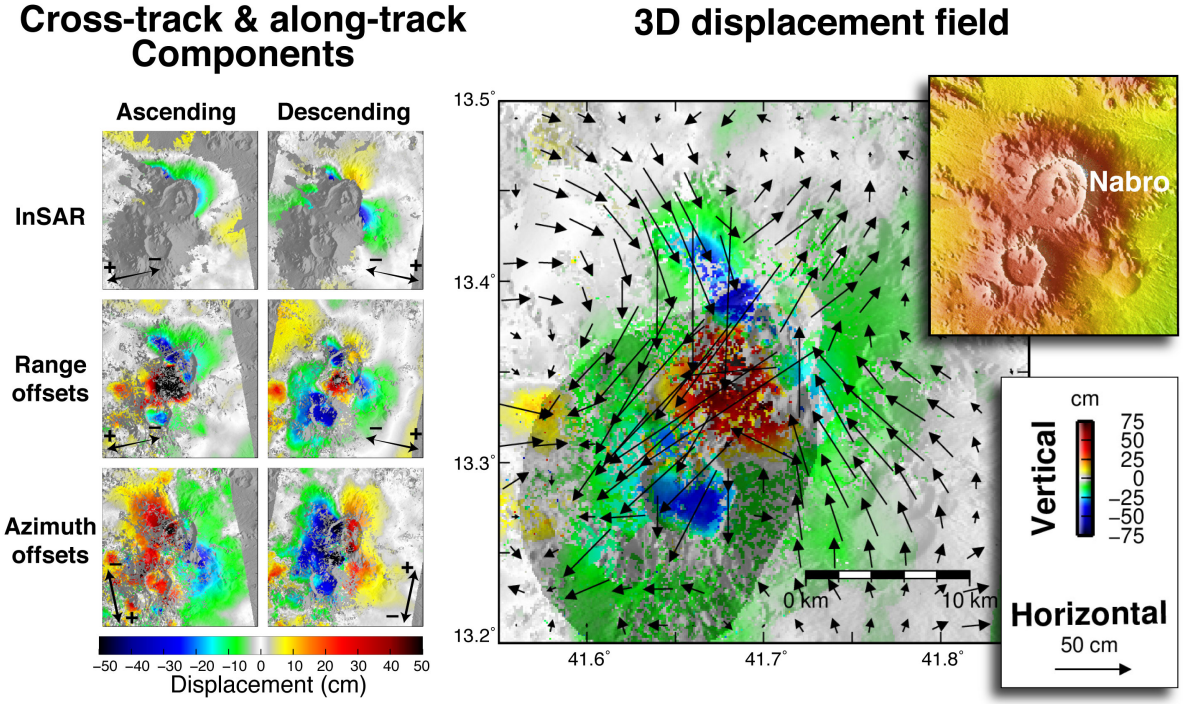

*Figure 1.21 – Static surface displacement during the Nabro eruption (Eritrea, June 2011) from TerraSAR-X data [adapted from Goitom, Oppenheimer, Hammond, **Grandin** et al., 2015]. Left panel shows the data processed according to different techniques: InSAR (top row) and sub-pixel correlation (middle row for the range component; bottom row for the azimuth component). Left columns: ascending; right column: descending. Decorrelation of InSAR data in the area of maximum deformation is not due to a high fringe rate, but rather to the presence of tephra expelled by the volcano during the eruption. The right panel shows the reconstructed 3D displacement field using these 6 components. The circular pattern exhibiting uplift (in red) is interpreted as apparent upward motion of the surface due to accumulation of tephra near the vent. Inset shows the pre-eruption topography.*

Multiple Aperture InSAR (MAI)

An alternative to cross-correlation is the so-called Multiple Aperture InSAR (MAI) method, sometimes also referred to as the split-spectrum method [*Bechor and Zebker*, 2006; *Barbot et al.*, 2008; *Jung et al.*, 2009]. The method consists in splitting the azimuth spectrum into two distinct halves prior to azimuth focusing, which allows for computing a forward- and a backward image in place of the standard image that uses the full synthetic aperture. These two images, when combined with another acquisition processed in the same way, are then used to calculate two sets of interferograms: one backward-looking interferogram and one forward-looking interferogram, each corresponding effectively to a different line-of-sight vector. For ENVISAT, the difference between the two LOS vectors is approximately half of the antenna aperture in azimuth (α), i.e.

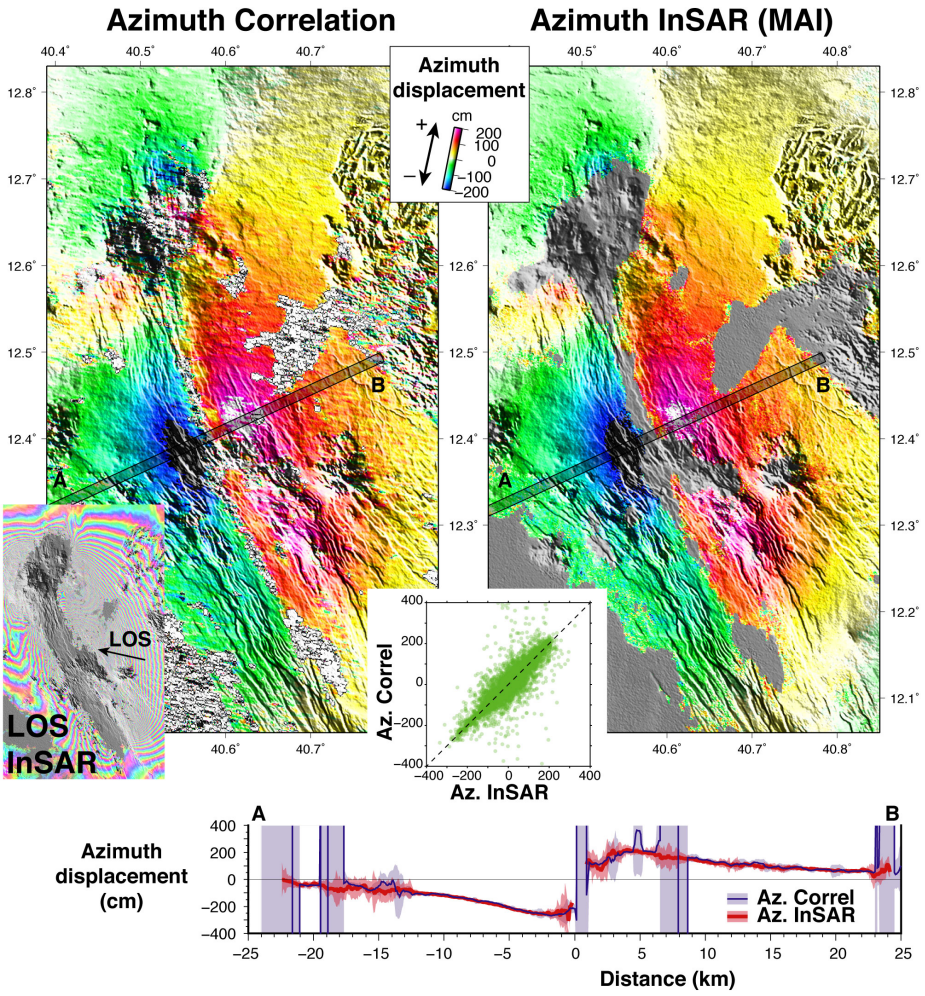

*Figure 1.22 – Azimuthal (along-track) displacement deduced from (left) image correlation and (right) Multiple Aperture InSAR, or MAI. The dataset consists of ENVISAT acquisitions spanning the September 2005 mega-dike intrusion of Manda Hararo, Ethiopia (master: 2005/05/06; slave: 2005/10/28) [**Grandin** et al., 2009]. Inset at left shows the standard line-of-sight (LOS) interferogram. Point cloud at the center shows pixelwise comparison between the two results. Graph at the bottom shows a comparison on two 2-km-wide swath profiles indicated by a grey box on the maps. Enveloppe shows the $\pm 1\sigma$ deviation from the mean, indicated by the solid curve.*

of the order of $\alpha/2 = (2\lambda/D)/2 \approx 0.3°$, where D is the antenna length in azimuth (10 m) and λ is the radar wavelength (0.056 m). The along-track component of ground motion, if not null, maps differently into these two LOS vectors, so that the difference between these interferograms carries information about this along-track displacement. Although the method also uses the phase, the sensitivity of the along-track InSAR method is typically reduced by a factor of ~ 200 compared to line-of-sight (across-track) InSAR because of the small angle between the two half-apertures. Thus, the accuracy is equivalent to that of the image correlation technique, i.e. of the order of a fraction of a pixel.

Fig. 1.22 shows a comparison of the two methods using the same input ENVISAT dataset covering the Manda Hararo mega-dike intrusion (Ethiopia). It can be seen that, similar to cross-correlation, the MAI method also fails in regions of low backscatter, hence of low coherence and low amplitude contrast. However, unlike the cross-correlation method which can retrieve displacement amplitudes that are clearly overestimated in regions of low SNR, the MAI technique is provides more stable, "smoother" results, provided InSAR coherence is sufficient (Fig. 1.22).

Split-spectrum in range

For the sake of completeness, the existence of a similar processing strategy for the range signal must be mentioned. Split-spectrum in range allows for reconstructing the motion in the line-of-sight direction with an accuracy depending on the pixel size and the interferometric coherence. In the course of the calculation, topographic effects and ionospheric effects must be corrected. This method has not been extensively used for retrieving surface deformation because it is less accurate than conventional InSAR and has a much reduced spatial resolution [see however *Jiang et al.*, 2017, for an application to the 2016 M7.1 Kumamoto earthquake using Sentinel-1 data]. It is instead increasingly used to derive ionospheric disturbances that prevail at large spatial scales [*Gomba et al.*, 2017].

Burst-overlap interferometry and spectral diversity

Unfortunately, with sensors operating in Wide-swath mode, such as Sentinel-1, the pixel size in azimuth can be greatly degraded compared to Stripmap (e.g. 4 m for Sentinel-1 Stripmap *versus* 14 m for Sentinel-1 TOPS). As a consequence, the resolution on azimuth displacement using MAI or cross-correlation is significantly reduced, hence of little practical interest. Only the range component remains measurable by cross-correlation, which due to redundancy with the standard InSAR measurement, does not add any information about the 3D displacements field. Nevertheless, it is still possible to apply a procedure similar to MAI in areas of burst overlap, following the aforedescribed “Spectral diversity” method (Fig. 1.12). This procedure allows for measuring along-track displacement in burst overlap regions with a pixelwise accuracy of the order of 10 cm, i.e. an order of magnitude better than MAI applied to Stripmap data [***Grandin et al.***, 2016]. Unfortunately, this method is only applicable in burst overlap regions, which consist in small strips, a few kilometers long in azimuth, and spanning the full width of each subswath (see insets of Fig. 1.12). In case of a complex surface displacement field, this method only provides useful measurements on a small fraction of the area of interest, typically $< 10\%$. This information may still be of interest, as it effectively mimics the presence of a continuous set of GPS sensors along a dense transect.

Nevertheless, when deformation is a smooth function of azimuth and range, interpolation between the burst overlap regions allows for estimating the full displacement field with reasonable

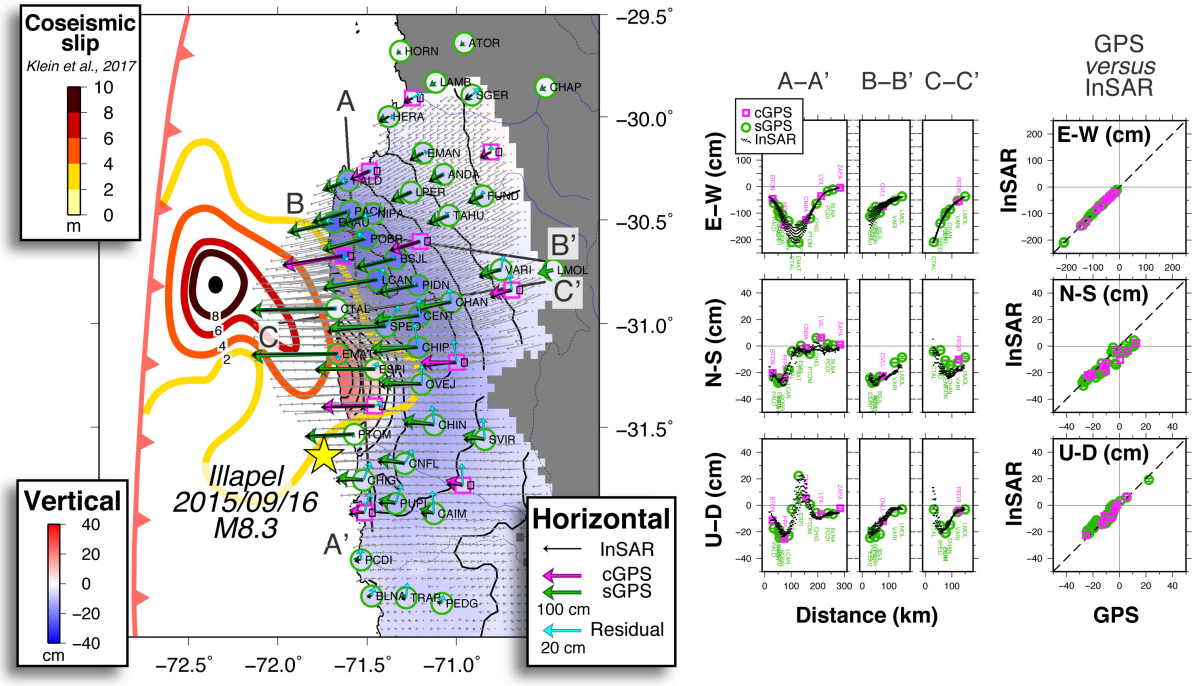

*Figure 1.23 – Three-dimensional displacement field of the 2015 Illapel earthquake from Sentinel-1 using a combination of along-track interferometry from spectral diversity shown in Fig. 1.12 and standard line-of-sight interferometry. Modified from [**Grandin** et al., 2016] using full set of co-seismic GPS vectors and slip distribution of Klein, Vigny, Fleitout, **Grandin**, Jolivet, Rivera, and Métois [2017].*

accuracy. This approach was validated in the case of the 2015 Mw8.2 Illapel earthquake (Chile) by comparing the results of the retrieved 3D displacement map against pointwise measurements by a set of continuous and campaign GPS benchmarks [***Grandin** et al.*, 2016] (Fig. 1.23). This comparison confirmed the excellent accuracy of the estimation of East-West and Vertical components (∼ 1 cm) and the good accuracy for the North-South component (∼ 10 cm). This methodology is typically relevant to quickly map the displacement field of a large subduction earthquake. In the case of the Illapel earthquake, an abrupt change from coastal subsidence to coastal uplift occurred over a distance of ∼ 100 km. This feature results from along-strike variations of the maximum depth of coseismic slip. Unfortunately, this pattern was not fully captured by continuous GPS due to the coarseness of the network. A post-earthquake GPS campaign allowed for bridging the gaps between the continuous GPS points, which required a few weeks given the size and remoteness of the region affected by deformation. In contrast, the two post-earthquake descending and ascending SAR were available respectively 11 hours and 3 days after the event. Burst-overlap interferometry is therefore adapted if one seeks to rapidly estimate the first-order features of the rupture. Therefore, this method brings a powerful solution to the lack of constraints on the 3D displacement field for regions where GPS data is scarce, such as South-West Pacific. The accuracy of the method and the fact that burst-overlap regions are frozen over the whole duration of the Sentinel-1 mission should allow for application of burst-overlap InSAR to the measurement of interseismic deformation in the near future.

Optical imagery

In spite of the advanced techniques described above, by construction, SAR imaging is not adapted to measuring horizontal motion with as much accuracy as vertical motion. Furthermore, the emergence of SAR satellites operating in wide-swath modes (ALOS-2, Sentinel-1) make the measurement of along-track displacement less accuracte, compared to previous sensors operating in Stripmap mode.

On the other hand, the geometric features of optical imagery make it more suitable to derive horizontal strain maps. Furthermore, as medium- and high-resolution optical sensors have become increasingly popular, access to these data is easier. Two classes of sensors can be used. First, medium-resolution open-access sensors of the Landsat and Sentinel-2 families provide systematic background acquisitions at 15 m and 10 m resolution, respectively. The short revisit time (5 days with S2A and S2B, 16 days with Landsat 8) allows for rapid acquisitions after an event, while maximizing chances to get cloud-free conditions. The quasi-nadir viewing acquisition makes these data little sensitive to topography. Using Level-1 orthorectified images, horizontal displacement can be measured with an accuracy of the order of 1 meter without requiring advanced photogrammetric processing [*Champenois, Klinger,* ***Grandin*** *et al.*, 2017]. For large earthquakes, such as the 2013 M7.9 Balotchistan earthquake whose fault length is ∼ 200 km long, the wide swath of the image allows for mapping the rupture in a single pass (Fig. 1.25a). The result of pixel correlation in range from SAR images acquired in wide-swath mode, such as TerraSAR-X, can then be corrected for the effect of the project of horizontal displacement

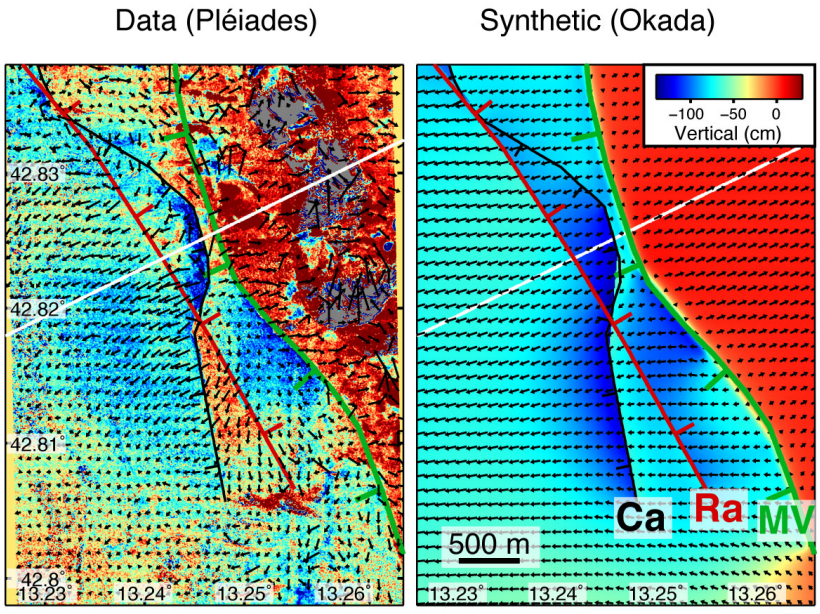

Figure 1.24 – Three-dimensional displacement field of the 30 October 2016 M6.5 Norcia earthquake (Italy). Left panel shows the full displacement field derived from Pléiades imagery. Right panel is a synthetic displacement field computed from joint inversion of ALOS-2 InSAR data and 3D Pléiades data using an elastic halfspace approach and a complex source model involving multiple faults. Note that the image covers an area of ∼ 4 km side length only, while the fault involved in the earthquake is ∼ 20 km long. From Delorme, ***Grandin****, Klinger et al. [2019].*

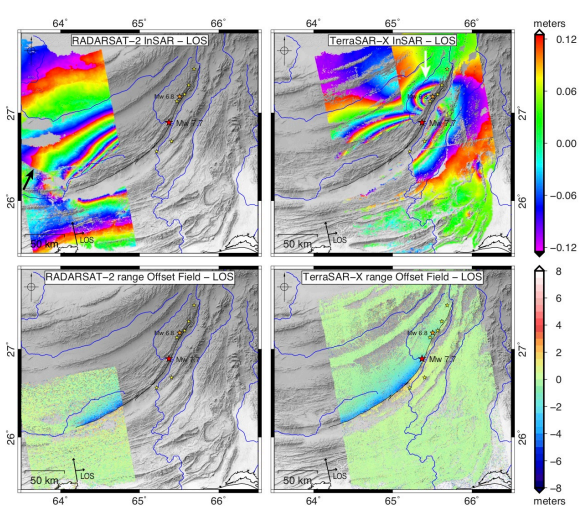

(a) SAR data

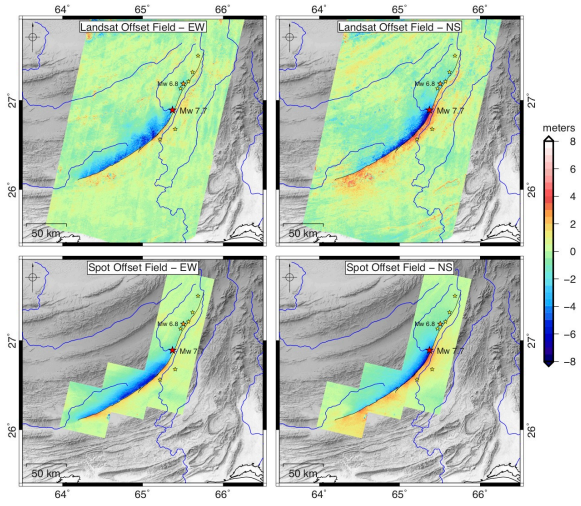

(b) Optical data

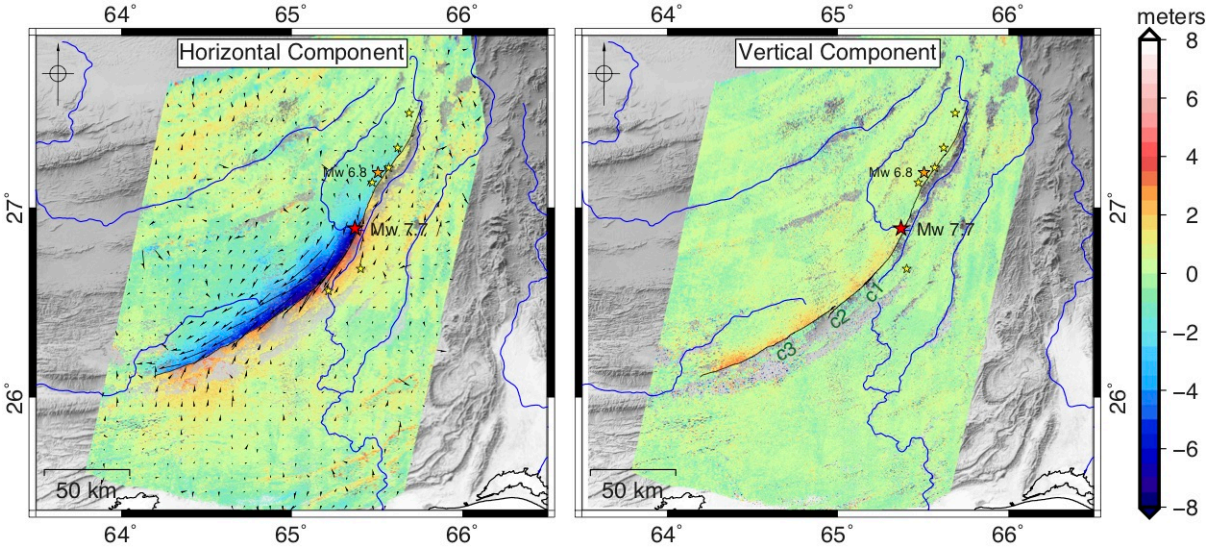

(c) 3D decomposition

*Figure 1.25 – Three-dimensional surface displacement field of the 2013 M7.9 Balotchistan earthquake (Pakistan). Top panels show the coverage from individual datasets, consisting SAR (left) and optical imagery (right). In the bottom panel, the left panel shows the horizontal displacement field derived from Landsat 8 and SPOT-5 imagery. Right panel shows the vertical displacement field computed from correlation of TerraSAR-X ScanSAR data in the range direction, after correcting for the contribution of horizontal displacement from the left panel. Note that the image covers a ∼ 200 km-wide strip. [From Lauer, **Grandin**, and Klinger, 2019].*

onto the oblique line-of-sight, thereby allowing for the restitution of vertical displacement with a similar accuracy (Fig. 1.25b).

Another class of optical sensors are carried by high-resolution optical satellites, which achieve for metric to sub-metric pixel size. The Pléiades system, consisting in two satellites, currently achieves the best performance, while allowing for easy access for public scientific institutions in France. Its main originality lies in its capability to rotate during the course of an overpass, thereby allowing for capturing several images of the same target with different viewing angles. The standard products offered by the system include stereo pairs, or tri-stereo triplets. The latter consists in a stereo pair with a B/H ratio preselected according to user requirements, and complemented by a third nadir image. This configuration is optimal for restituting topography with a high resolution. However, agility comes at the price of variability of acquisition geometry, which requires advanced photogrammetric procedures to allow for precise orthorectification and multi-temporal processing of stack of images [e.g. *Rupnik et al.*, 2016; *Labarre et al.*, 2019]. The efficiency of the technique is such that it can resolve the 3D displacement field at very high spatial resolution (of the order of $\sim$ 1 m), high accuracy (of the order of $\sim$ 40 cm and $\sim$ 20 cm for absolute vertical and horizontal displacement, respectively, and of the order of $\sim$ 10 cm for relative displacement across a surface rupture in all three dimensions). Furthermore, this method does not require the integration of SAR data, which in any event do not allow for achieving such a high level of performance. This optical-only approach is particularly suited to the study of complex deformation in the near field of shallow surface ruptures [e.g. *Vallage, Klinger,* ***Grandin*** *et al.*, 2015]. This is demonstrated in Fig. 1.24 in the case of the 30 October 2016 M6.5 Norcia earthquake (Italy), where pre- and post-earthquakes Pléiades have been processed according to the following procedure: (1a) computation of pre- and post-earthquakes DEMs, (1b) DEM differencing to resolve the vertical component of displacement, (2a) orthorectification of pre- and post-earthquake images, (2b) dense correlation of orthorectified images to calculate horizontal displacements.

1.4 Outlook

1.4.1 Future SAR constellations

To meet constraints in terms of interferometric coherence, most of the planned HRWS systems will use long-wavelength carrier frequency (Figure 1.26). The L-band, in particular, is a good compromise between resolution, coherence and can be efficiently corrected against ionospheric disturbances using split-spectrum techniques [*Gomba et al.*, 2017]. However, L-band sensors require larger antennas to compensate for the lower resolution entailed by the broader beam aperture due to a larger wavelength. As a result, long-wavelength systems are not adapted for ultra-high-resolution imaging, except when used in very special modes such as the costly Spotlight mode (i.e. costly in terms of storage, downlink resources and in-orbit time and energy consumption). At the other end of the spectrum (so to speak), short wavelength systems (such as TerraSAR-X and COSMO-SkyMed) are capable of producing extremely detailed images of the Earth's surface. In Stripmap mode, resolution reaches a few meters, whereas Spotlight modes (Sliding or Staring) can achieve a pixel size as small as $\sim$ 0.3 m [*Kraus et al.*, 2016].

However, in spite of these astounding capabilities, X-band systems have always suffered from the limited size of images acquired in a single pass (of the order of 30 km swath width in

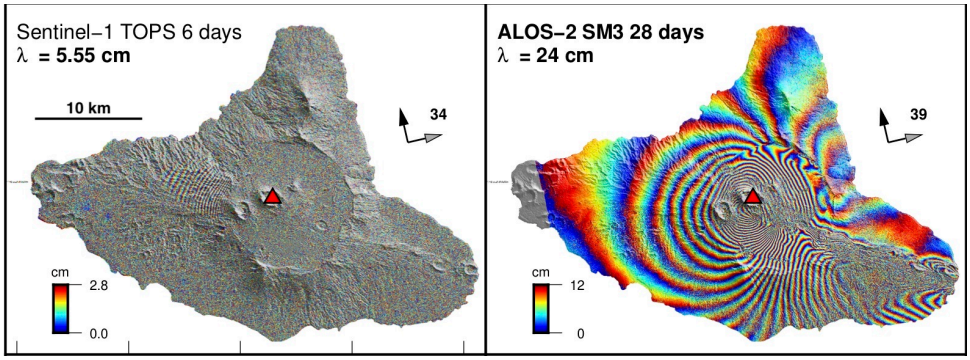

*Figure 1.26 – December 2018 eruption and dike intrusion at Ambrym (Vanuatu), as seen by C-band Sentinel-1 (left) and L-band ALOS-2 InSAR (right), showing the superiority of L-band in case of large deformation and dense vegetation cover. Adapted from Shreve, **Grandin** et al. [2019]. Image drafted by F. Delgado.*

Stripmap). As a result, the actual repeat interval between acquisitions is generally of the order of one or several months, except for a small set of pre-defined targets where the satellite is tasked to acquire images at every pass. Therefore, this high-spatial resolution capability contradicts the high-temporal resolution requirement that today represents a standard of Earth Observation. To circumvent this limitation, constellations consisting of a small number of units can cut the revisit time by a factor two to four (depending on the number of satellites). Furthermore, interoperable satellites allow for an improved redundancy and therefore less vulnerability to system malfunction or unavailability. The COSMO-SkyMed system, in particular, consisting of four satellites, has already demonstrated the capability to monitor ground motion at high-temporal and high-spatial resolutions, with promising applications in volcanology (Fig. 1.27). On the other hand, the TanDEM-X system, a companion of the TerraSAR-X satellite, does not provide an improved revisit time (except if one considers the doubling of data acquisition capabilities granted by the availability of a second satellite), but rather uses its bistatic capability to provide non-standard interferometric modes [*Rodriguez-Cassola et al.*, 2012]. Among its spectacular achievements, the TSX-TDX mission has already allowed for producing an extremely detailed global digital elevation model that has updated the now-aging SRTM dataset [*Zink et al.*, 2014].

In the coming years, a boom in the deployment of SAR satellites will take place, with the launch of several constellations:

- The C-band Sentinel-1 constellation, operational since 2016, consisting of two units with a 180° orbital phasing difference, allows for 6 days revisit time in any given acquisition geometry (or ∼ 1–4 days when ascending and descending passes are combined).
- The X-band PAZ satellite[6], launched in February 2018, has expanded the TerraSAR-X – TanDEM-X constellation, decreasing the revisit time from 11 days to 6 days.
- The L-band SAOCOM constellation[7] (Argentina Space Agency), whose first unit was launched on 8 October 2018, follows the same strategy, with two satellites so as to reach an 8 days revisit interval (Fig. 1.28a).
- The C-band RADARSAT constellation[8] (Canadian Space Agency), launched on 12 June

[6] https://directory.eoportal.org/web/eoportal/satellite-missions/p/paz
[7] https://directory.eoportal.org/web/eoportal/satellite-missions/s/saocom
[8] http://www.asc-csa.gc.ca/eng/satellites/radarsat/default.asp

2019, will use a slightly different approach, with three satellites orbiting in the same orbital plane, 30 minutes apart, which will allow for achieving a 1000 km-wide swath, hence a revisit time of 4 days, at medium resolution (∼ 50 m) [*Thompson*, 2015; *Doyon et al.*, 2018].

- The X-band COSMO-Skymed Second Generation (Italian Space Agency) [9] will include two satellites (launch of first unit planned for November 2019), reaching a 8 days revisit interval for interferometry, but with an improved agility (both at payload and platform levels) which will allow for a daily or even sub-daily imaging capability [*Calabrese et al.*, 2015].

We note that the above-mentioned satellite missions are all government-run. This is explained by the fact that, despite a long-recognized strategic interest for SAR imaging (in particular to image targets over vast, remote areas, such as oceans or polar regions), the complexity and cost of a spaceborne SAR mission could only, until recently, be taken over by the public sector (in the broad sense of the term). But things are changing fast. Similarly to the tendency witnessed with optical sensors, new concepts aiming at bringing global daily coverage with high-resolution SAR imaging are emerging in the private sector. These concepts involve companies anticipating commercial applications of the SAR technology, which has hitherto been essentially restricted to scientific and military applications. However, unlike optical sensors, SAR satellites cannot be easily downsized due to the constraints imposed by electrical power requirements, since large solar panels and high capacity batteries are required to operate active radar antennas, especially when operating in traditional pulsed modes. Furthermore, antenna size has to be kept relatively large to ensure sufficient azimuth resolution and avoid ambiguities.

Nevertheless, with progresses in technology, strategies aiming at enhancing the revisit time by sending a large number of low-cost radar microsatellites have recently emerged [e.g. *Saito*

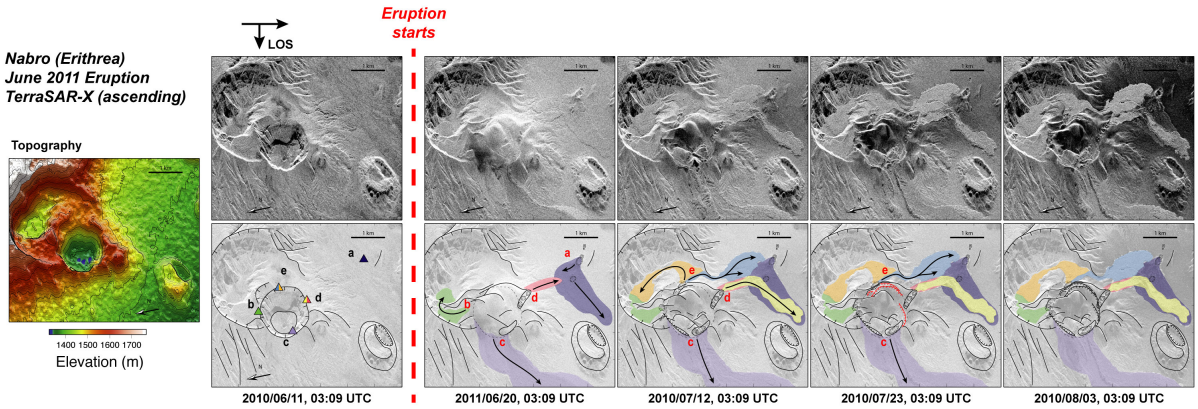

Figure 1.27 – June 2011 eruption of Nabro volcano (Eritrea) captured by short-revisit TerraSAR-X images. Upper row shows SAR images in radar geometry, where advancement of lava flows and topographic changes due to infill by volcanic material are highlighted by variations in intensity of backscattered signal. Lower row shows the same images, where the successive generations of lava flows are identified by distinct colors. Image to the left is pre-eruptive topography in radar geometry (simulation). In all panels, the satellite track is located along the upper edge of the image to emulate a perspective view such that it becomes intelligible to human perception of terrain shape.

[9] https://www.asi.it/sites/default/files/attach/evento/02_asi_workshop_15-11-2017_csg_state_of_art_technologies_final.pdf

et al., 2017]. Several concepts are currently under consideration. They all share similar characteristics, namely (1) X-band, (2) low mass, of the order of 100 kg, (2) medium resolution, of the order of 2–3 m, and (3) short revisit time, of the order of 1 day. To meet these constraints, a constellation of SAR satellites will be orbiting on several orbital planes rotated with respect to each other, not necessarily in sun-synchronous configurations. The most advanced project to date is the ICEYE project[10], which has already sent its first experimental unit in orbit, ICEYE-X1, in February 2018 (Fig. 1.28b), followed by ICEYE-X2 in September 2018. A total of 18 units are planned to be operational by 2020. Similar, albeit less advanced projects, include Capella Space[11], Umbra-lab [12], Urthecast's OptiSAR, [13] and FalconSAR and DragonSAR, by Space Advisory Company[14]. The viability of these projects will obviously depend on the market's interest, measured in terms of funds raised to cover the investments of research, development and operation of this new generation of commercial SAR systems[15].

1.4.2 High-resolution wide-swath

Whether they be operated in Stripmap, ScanSAR, TOPS or Spotlight modes, first- and second-generation SAR satellites are all faced with a fundamental theoretical limitation. Indeed, the ratio between the swath width W_g and the azimuth resolution δ_{az} is bounded to a maximum value of $\approx 19 \times 10^3$ [*Gebert et al.*, 2009]. In other words, all of these satellites have to trade azimuth resolution against swath width. The reason for this limitation is that improving the azimuth resolution requires an increase of the PRF, which in turn causes a shortening of the

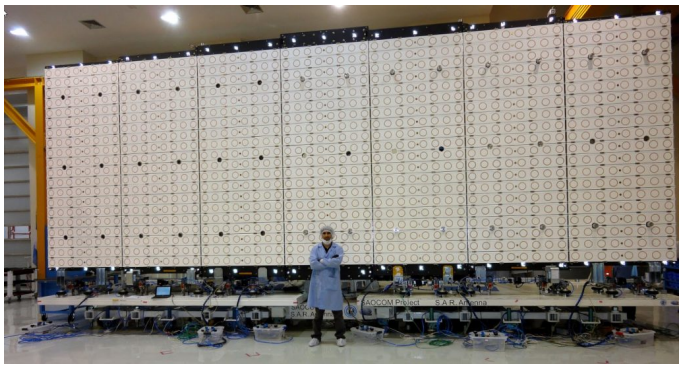

(a) The L-band antenna of SAOCOM-1A (CONAE), with an area of 35 m^2, will radiate a peak power of 3.1 kW. The satellite weights a total of 3000 kg.

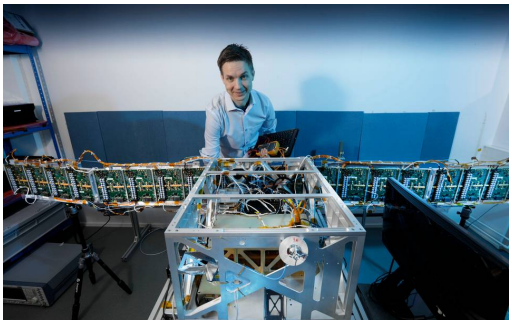

(b) ICEYE co-founder Pekka Laurila photographed with a full-scale model of the ICEYE-X1 satellite. The deployable antenna ICEYE-X1 has a total length of 3.25 meters, while the satellite weights only 70 kg.

Figure 1.28 – Contrasting approaches behind the designs of two SAR satellites launched in 2018.

[10] https://www.iceye.com/
[11] https://www.capellaspace.com/
[12] https://umbralab.com/
[13] https://www.urthecast.com
[14] http://www.spaceadvisory.com/products/satellites/falconsar/
[15] http://syntheticaperturеradar.com/new-space-disruption-iceye-umbra-lab-and-capella-space/

time window available for reception between the pulses, hence leading to range ambiguity that limits the swath width. The Spotlight mode of TerraSAR-X ($W_g = 10$ km; $\delta_{az} = 1$ m) and the ScanSAR mode of ALOS-2 ($W_g = 350$ km; $\delta_{az} = 30$ m) represent two end-member modes that fall close to this theoretical limit.

Breaking the W_g/δ_{az} bound is mandatory to simultaneously achieve short revisit time (which requires a wide swath, as explained in Section 1.2.2) and fine spatial resolution. This requires a complete change in paradigm in the concept of SAR design. Today, the most promising strategies to achieve high-resolution wide-swath (HRWS) imaging can be organized in three main categories, which as not mutually exclusive:

- **Digital beamforming-on-receive** allow for using a prescribed part of the received signal in space and in time as it sweeps through the antenna, so as to focus the source of the echoes on a narrow set of targets. When applied in the elevation dimension, this technique mitigates range ambiguity. The SweepSAR method [*Freeman et al.*, 2009] will be the first beamforming-on-receive method to be implemented on a SAR satellite, with the future NISAR ("Nasa-ISRO-SAR") mission[16] (Fig. 1.29). The satellite will include a 12-m diameter deployable reflector antenna and two phased array feeds operating independently in L- and S-bands. Furthermore, it will operate in L- and S-bands, with a carrier bandwidth featuring a main carrier band and a secondary band, shifted in frequency, that will allow for correcting the effects of ionospheric dispersion that disturb in low-frequency radar. Similarly, the ALOS-4 satellite, the successor of ALOS-2, will use digital beamforming techniques and a dual-frequency L-band radar to achieve a broader swath than ALOS-2, while keeping the same resolution specifications [*Motohka et al.*, 2018].
- **Multiple input multiple output (MIMO)** further makes use of several sub-antennas (that can belong to the same physical antenna) that operate independently on distinct elevation channels to achieve the simultaneous acquisition of several Stripmap-like images on a set of adjacent sub-swaths [*Krieger*, 2014]. In order to avoid confusion between echoes received at the same time but originating from distinct channels, **waveform encoding** is implemented according to orthogonality criteria (either by means of a time-shift or a frequency-shift) so that matched filtering in range effectively suppresses the undesired echoes.
- **Variable Pulse Repetition Interval (PRI)** allows for moving the location of the blind range bins that naturally emerge when the PRI is fixed, so that a continuous image is produced. When combined with **multiple channels in azimuth**, this approach allows for sampling echoes independently of the PRI, thereby achieving an improved azimuth resolution. The latter mode is called "Staggered SAR" [*Villano et al.*, 2014; *Queiroz de Almeida*, 2018], and is currently considered as the potential acquisition mode for the future TanDEM-L mission[17].

Provided substantial investments are made by space agencies, these advanced SAR systems will further boost the range of applications of the InSAR technique. For instance, a 350 km-wide swath would allow for a repeat cycle of 8 days. A constellation consisting of 8 satellites would cut the repeat cycle down to 1 day. Operating such a satellite in multichannel staggered SAR would allow for 3 m azimuth resolution, while the range resolution can be adjusted through the chirp bandwidth down to a similar value.

[16] https://nisar.jpl.nasa.gov

[17] http://www.dlr.de/hr/en/desktopdefault.aspx/tabid-8113/

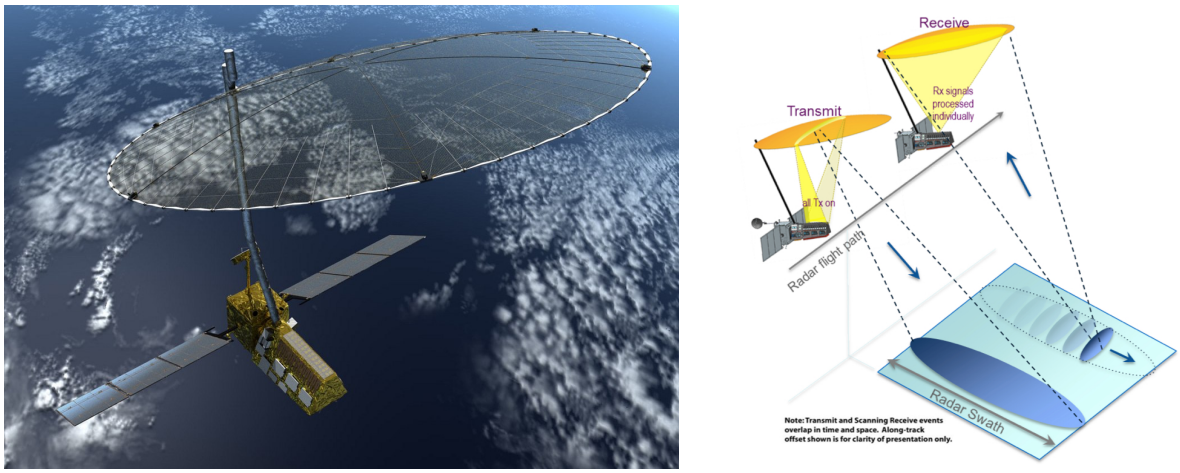

Figure 1.29 – Left: artist concept of the NISAR satellite. Right: SweepSAR acquisition mode. The full antenna feed is used to transmit a fan-shaped beam, while a sliding part of the feed is used during receive in order to focus the reception of echoes originating from a narrow range bin. Figure taken from https://nisar.jpl.nasa.gov/. *See also animation at* https://nisar.jpl.nasa.gov/technology/sweepsar/.

Research directions

SAR imaging, and in particular InSAR, is becoming more and more popular. In turn, if users were provided by raw data only, the obvious complexity in the processing of these new acquisition modes would certainly hinder this democratization. Space agencies have anticipated this problem, and it is likely that these new data will be made available in SLC format to most users, after a standard phase-preserving pre-processing has been performed. This policy has already been followed with the TerraSAR-X and Sentinel-1 satellites, whose products are available in SLC by default. In case of Sentinel-1 TOPS and TerraSAR-X ScanSAR images, the SLCs had to be further pre-processed by the users to achieve high-quality interferograms (see section 1.2.3). Next-generation SAR system will certainly be delivered along with high-quality processing tools, in the form of pre-processed products or on-demand processing chains available to all. For instance, the NISAR science team is already planning to deliver wrapped interferograms, either registered on standard range-azimuth grid or geocoded, that can be readily ingested in any standard InSAR processing chain, relieving users from the burden of correlation, focusing and interferometric combination. Correction of ionospheric disturbances will be further eliminated on-the-fly thanks to the dual-band acquisition.

As a result of this general trend, several research directions could be followed, hereafter listed by increasing order of difficulty:

- focus on post-processing of massive stacks of InSAR data, by focusing efforts on (1) the improvement of coherence and accuracy through improved phase filtering and unwrapping [e.g. ***Grandin** et al.*, 2012a], more advanced corrections of atmospheric and ionospheric disturbances [e.g. *Liang et al.*, 2019], a better understanding of mechanisms of phase misclosure [*De Zan et al.*, 2015], etc, (2) the development of efficient and reliable phase unwrapping algorithms, coupled with post-processing methods to correct for residual unwrapping errors [e.g. *Benoit et al.*, 2019], (3) the implementation of novel techniques to extract the full spatial and temporal information content of interferogram stacks,

which should be achieved with a reduced computational time, hence involving a certain degree of data reduction [e.g. *Shirzaei*, 2015; *Jolivet and Simons*, 2018].

- propose new methods of processing advanced SAR modes in order to extract a deformation signal in a way that may have not been imagined in the original system design, as new acquisition modes open the door for opportunistic utilization of the raw data. For instance, high resolution wide swath SAR imaging will provide the opportunity for a renewed impetus for the development of multiple aperture InSAR (MAI, see Fig. 1.22) [e.g. ***Grandin** et al.*, 2016].
- make use of one or several low-cost, passive companions that could take advantage from the main satellite to simultaneously compute a bistatic or multistatic dataset, thereby expanding the geometric, radiometric, resolution and spectral capabilities of the system [e.g. *Runge et al.*, 2002; *Krieger and Moreira*, 2003].Concepts currently in discussion include SESAME, StereoSAR (companions of Sentinel-1) and SAOCOM-CS (companion of SAOCOM-1b) [*Hanssen et al.*, 2015; *Rott et al.*, 2017; *Giudici et al.*, 2018].
- investigate the possibility to deploy swarms of radar nano-satellites that could cooperate to form large synthetic aperture arrays, with potentially new capabilities that could not be achieved by single-platform SAR missions [e.g. *Engelen et al.*, 2012; *Wye and Lee*, 2016].

1.4.3 Optical imagery

A growing offer in high-resolution optical imagery

Accordingly, a major limitation of optical imagery is the lack of visibility in the presence of clouds. Nevertheless, this drawback is balanced by the rapid expansion of observation capabilities as more and more sensors are sent in orbit, both by space agencies and private companies. The former category includes the Sentinel-2 and Landsat satellites, which provide timely and reliable information about surface changes. The great number of applications of these data, both for commercial and public purposes, have made them standard satellite products, which means that they will certainly be maintained, replaced, and probably expanded and improved in the coming decades. But the most promising trend comes from the latter category, which includes the Pléiades satellite, as well as satellites operated by the DigitalGlobe company. These high- and very-high resolution satellites include the "Ikonos", "QuickBird", "WorldView" and "GeoEye" families, with a resolution better than 50 cm. However, unlike the Pléiades imagery which is accessible thanks to contracts passed between the French state and the operator (Airbus Defense and Space), imagery from DigitalGlobe remain expensive for scientists.

The recent, and still ongoing deployment of medium-resolution "Planet Scope" (2–4m) and "Dove" high-resolution (80 cm) nanosatellite constellations (operated by the Planet Labs company), orbiting in very-low Earth orbit ($\sim$ 400 km) which allows for an exceptionally short revisit time of 1 day, seems to represent a game changer that could significantly alter the traditional business model in the domain [see *Gómez Ferreras*, 2017, for a comparison of the economic models of DigitalGlobe and Planet Labs] (Fig. 1.30a). These products are accessible at no cost for scientists through a dedicated Education and Research program [18] [see e.g. *Kääb et al.*, 2017, for a study of coseismic deformation during the 2016 M7.8 Kaikōura earthquake, NZ].

[18] https://www.planet.com/markets/education-and-research/

(a) Planet Labs CEO Will Marshall comparing his company's Dove cubesat to a traditional satellite during a TED Talk. Credit: Steve Jurvetson. (From http://spacenews.com/planet-labs-announces-95-million-investment/)

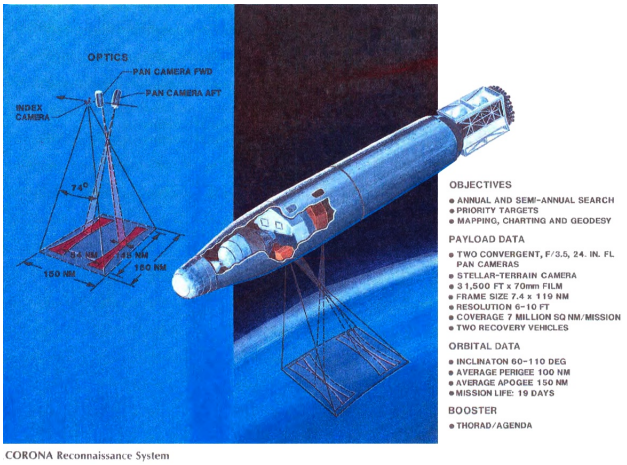

CORONA Reconnaissance System

(b) Artist concept of the Corona Reconnaissance System, version KH-4B (1967–1972). (From https://en.wikipedia.org/wiki/Corona_(satellite))

Figure 1.30

The WorldView Legion 6-satellites constellation of Digital Globe[19], to be launched in 2021, the follow-up Pleaides NEO mission[20] of Airbus, consisting of 4 satellites expected to be launched between 2020 and 2022, and the micro-satellite constellation CO3D[21], planned for 2023 and fully dedicated to stereoscopic imaging, will further increase the offer in high-resolution imaging, and will certainly provide new opportunities in the exploitation of optical imagery for Solid Earth applications.

In comparison with SAR imagery, another advantage of optical imagery is its ability to work in inter-operability. In other words, it is possible to cross-correlate optical image acquired by very different systems, including aerial photographs and satellite images acquired by different sensors and taken from very different angles. Of course, as geometrical and radiometric differences become increasingly significant between the images, this task can become challenging. Future trends in optical imaging will certainly focus in the estimation of refined geometric models of sensors in order to enable a common referencing of images originating from a variety of sources. This will allow for taking advantage of multiple observations with short revisit time in a given area of interest, thereby achieving high-temporal resolution on deformation. Candidate processes whose study could benefit from this kind of approach include the estimation of rapid afterslip following a shallow continental earthquake, or the real-time 3D monitoring of lava flows. Furthermore, the use of legacy satellite imagery from early Landsat and SPOT programs, or even from the recently declassified US-owned spy-satellite "Keyhole" program, could allow for going back in time as early as the 1960s or 1970s (Fig. 1.30b). This could make it possible to study earthquakes that occurred in the pre-InSAR era, i.e. before $\sim$ 1995, or detect

[19] http://spacenews.com/in-buying-digitalglobe-mda-ensures-ssl-will-build-just-disclosed-\worldview-legion-constellation/

[20] https://www.intelligence-airbusds.com/en/8671-pleiades-neo-trusted-intelligence

[21] https://www.airbus.com/newsroom/press-releases/en/2019/07/airbus-to-develop-co3d-earth-observation-programme-for-cnes.html

shallow surface deformation that have been steadily accumulating over the past 40–50 years in response to shallow fault creep, such as on the North Anatolian Fault, the Chaman Fault or the San Andreas Fault.

Better data require better models

High-resolution optical images will soon be available with shorter revisit intervals, which will make it possible to capture the coseismic deformation field in areas of large deformation with great detail by combining several sensors and/or several acquisition geometries (instead of single-geometry images available from medium-resolution satellites such as Landsat or Sentinel-2). These high-resolution images will provide a direct access to on-fault slip across surface ruptures of continental earthquakes, as well as the measurement of off-fault coseismic strain within the few hundred meters from the fault trace.

However, as technical difficulties behind the computation of these detailed geodetic observations are currently being polished, the main challenge may be in the process of shifting from the measurement step toward the modeling step.

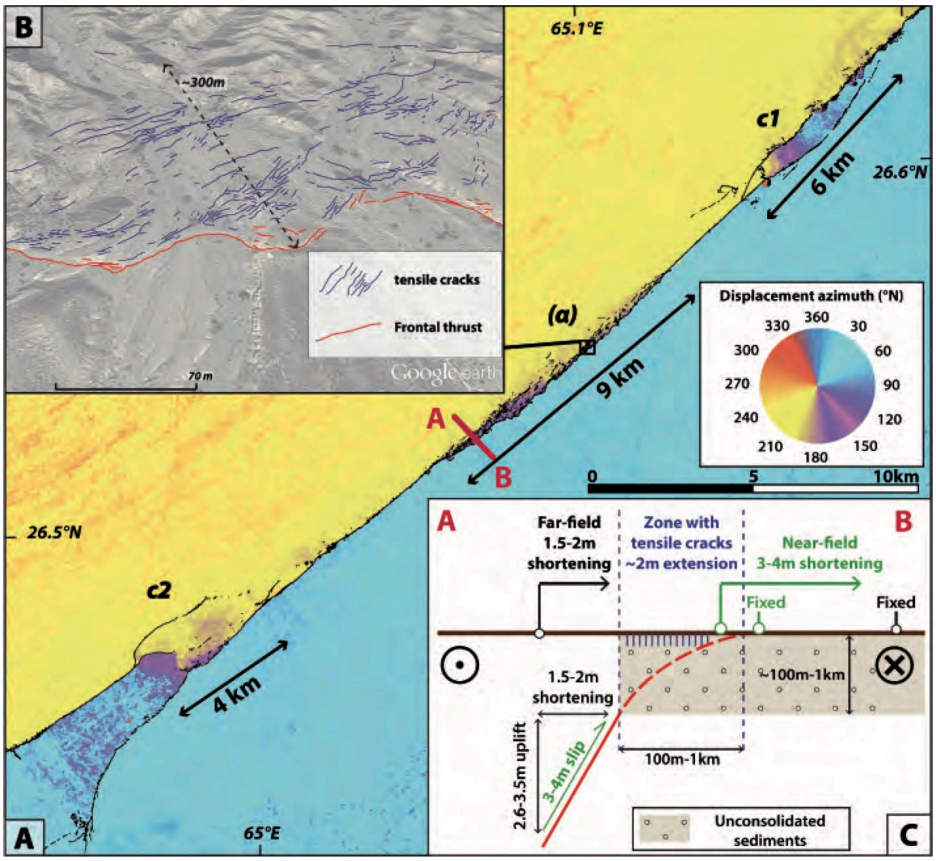

*Figure 1.31 – Near-field horizontal displacement for the 2013 M7.8 Balochistan earthquake from SPOT-5 data (resolution: 2.5 m) [Vallage, Klinger, **Grandin** et al., 2015]. Inset at the upper left corner shows distributed cracks in the hanging wall of the NW-dipping fault. Inset at the lower right corner shows the interpretation of the very-near-field excess of fault-perpendicular displacement observed across the fault.*

Two recent studies illustrate what could become a standard in the coming decade, and the challenges that these new observations will bring:

- deformation across the surface rupture of the 2013 M7.8 Balochistan earthquake [*Vallage, Klinger, **Grandin** et al.*, 2015] (Fig. 1.31) shows a variable degree of partitioning, associated with abrupt broadening and splitting of the rupture trace on several distinct fault strands, typical of transpressional ruptures. As a result, triple junctions, associated with rotations, prevail in the very near-field of the rupture trace (a few hundred meters from the fault). However, surprinsingly, off-fault deformation reveals a substantial "excess" of shortening directly across the fault (as would be observed in the field), compared to relative displacement in the far-field (a few kilometers from the fault, as would be observed by GPS or InSAR). This excess cannot be explained by a simple elastic effect. Although interpretation is non-unique, this observation may indicate the existence of sharp changes in the fault geometry at shallow depth (i.e. shallower than 1 km), combined with a conservation of the magnitude of the slip vector [*Vallage, Klinger, **Grandin** et al.*, 2015].

- deformation in the very-near-field of the 2016 M6.5 Norcia earthquake [*Delorme, **Grandin**, Klinger et al.*, 2019] (Fig. 1.32) exhibits a remarkable degree of complexity. During this normal-faulting event, several fault strands are activated, giving rise to a horst-and-graben deformation pattern. However, horizontal deformation displays sharp gradients in the few hundred meters away from the ruptures. If interpreted in the framework of elasticity, these deformation indicate substantial geometrical complexities on the fault planes and/or abrupt changes in the slip vector magnitude at shallow depth (shallower than 0.5 km).

These two examples illustrate that, as one gets closer and closer to coseismic surface ruptures, deformation may become increasingly complex. Additional examples of extreme complexity of the deformation field in the near-field of surface-rupturing earthquake, as revealed by high-resolution optical imagery or LIDAR data, include the 2010 M7.2 El Mayor earthquake [*Oskin et al.*, 2012] and the 2016 M7.8 Kaikōura earthquake [*Hamling et al.*, 2017; *Klinger et al.*, 2018]. This complexity was largely overlooked by prior studies that relied only on SAR, because SAR interferometry measurements fail in areas of intense deformation, whereas SAR image correlation generally lacks sufficient spatial resolution and accuracy to capture this complexity. Conversely, this complexity has long been recognized by earthquake geologists investigating earthquake deformation immediately after earthquakes in the field, but could not be quantitatively assessed by standard observation methods, even when aerial or satellite imagery was available to map the ruptures in great detail [e.g. *Philip and Meghraoui*, 1983; *Lyon-Caen et al.*, 1988; *Crone et al.*, 1987; *Caskey et al.*, 1996; *Klinger et al.*, 2005; *Jacques et al.*, 2011].

Bridging the observational gap between on-fault coseismic slip measured in the field – reflecting plastic deformation – and off-fault deformation measured from InSAR – reflecting an elastic behavior – calls for a new modeling approach capable of simultaneously accounting for a number of phenomena that all prevail in the shallow subsurface, including: (1) elasticity, (2) plastic strain / damage / fracturing, (3) gravitational body forces, (4) lithological layering, (5) dynamic stress pulses. Computational tools such as discrete element methods may provide a flexible approach to tackle some of these issues. Applying these advanced methods to the understanding of novel on- and off-fault deformation data captured by high-resolution sensors will provide clues on their relative importance. This research direction may have far-reaching

implications on the re-interpretation of on-fault slip and off-fault deformation data acquired in the field (either coseismically, in paleoseismic trench, or from offset geological features), and eventually on previous estimations of repeat times of large earthquakes and the geological slip rates of faults.

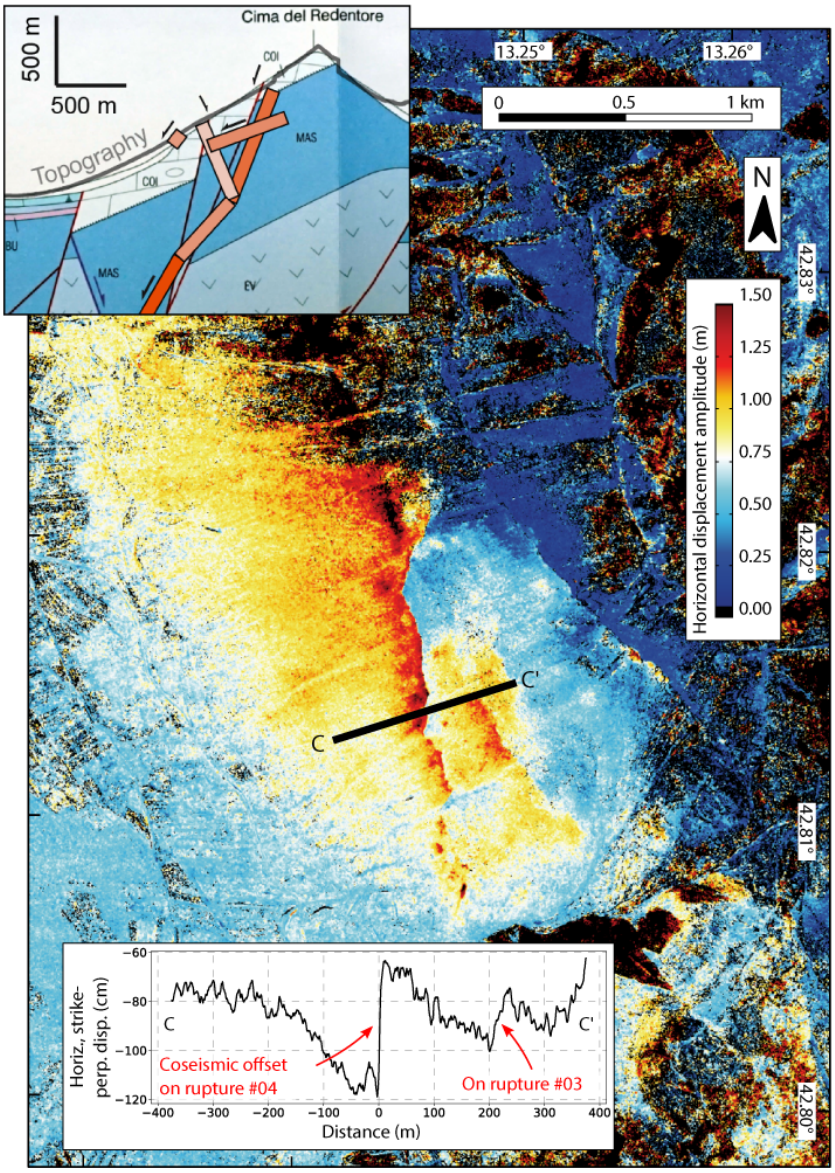

*Figure 1.32 – Near-field horizontal displacement for the 2016 M6.5 Norcia earthquake from Pleiades data (resolution: 0.6 m) [Delorme, **Grandin**, Klinger et al., 2019]. Inset at the upper left corner shows the inferred fault geometry at depth, compared with sub-surface geology.*

Chapter 2

Modeling and interpreting earthquake deformation

2.1 From surface strain to slip at depth

Geodesy focuses on the precise positioning of points on or above the Earth surface. On the other hand, geology deals with understanding of processes taking place in the Earth's interior. A similar dichotomy arises in the study of earthquakes. Earthquake geodesy provides constraints on the motion of the Earth's surface (and generally, everywhere except on the fault surface – see previous section), whereas earthquake geology attempts to determine the slip that took place on the fault itself. Bridging the gap between the two approaches – going from strain (or displacement, or tilt) at the surface, to slip at depth – requires finding the solution of an inverse problem. The two main ingredients of a slip inversion are the forward model (which allows for predicting displacement or strain from a given set of parameters describing the source), and an inversion procedure.

The absolute necessity of carrying out an inversion is particularly clear when working with InSAR. Indeed, InSAR provides line-of-sight range change measurements, sampled regularly in two spatial dimensions (along-track and across-track). Therefore, interferograms are often rich in detail and complexity, which clearly indicates the high information content carried by these data (as discussed in the previous chapter). However, the fringe pattern alone is difficult to interpret because the combined effects of planar strain, tilt and rotations cannot be disentangled [*Peltzer et al.*, 1994; *Price and Sandwell*, 1998].

Only in rare instances can one avoid the necessity of using a computational model of deformation (even a simple one) to reproduce the basic features of the fringe pattern [e.g. for shallow landslides, where InSAR provides a direct information about basal slip, see *Schlögel et al.*, 2015]. In most cases, the elastic strain measured at distance from the fault is only indirectly related to sub-surface slip [*Tarantola et al.*, 1979], which requires performing an inversion.

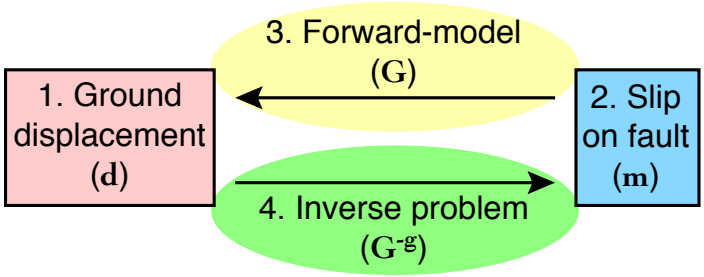

Figure 2.1 – Classical description of the static slip inversion problem.

The standard procedure for solving a static slip inverse problem can be broken down into four distinct steps (Fig. 2.1):

1. data pre-processing
2. fault setup
3. forward problem calculation
4. inversion

The aim of static slip inversion is to determine fault slip at depth, using geodetic data acquired at the surface as an input, and assuming a certain form of prior knowledge on the forward problem. More precisely, the (forward) relationship between slip at depth and displacement at the surface is supposed to be known (section 2.2). Furthermore, a minimum knowledge of the characteristic of the source is usually available, either derived from field observations, seismology, neotectonics, paleoseismology, or prior experience of similar phenomena.

Unfortunately, such a problem is often ill-posed, in the sense that several, distinct slip models may yield very similar displacement distribution at the surface [e.g. *Freund and Barnett*, 1976; *King and Wesnousky*, 2007]. Similarly, relatively different Earth models can yield slightly different results, which may as well be explained by differences in the slip distribution. If these difference are within the uncertainty of the measurements, which is often the case, it will not be possible to distinguish between alternative models solely on the basis of goodness of fit to the data. Furthermore, the dataset often consists of several types of data, with different sensitivities, spatial sampling and accuracies. These data must be weighted appropriately to extract the best of them, which is not straightforward. Finally, constraints on the choice of a particular fault model are often imposed by the inversion algorithm itself, and *vice versa*. The "art" of slip inversion therefore involves many subtleties, and is thus prone to many pitfalls.

In this section, the successive steps leading to the resolution of the problem of static slip inversion are described, emphasizing the importance of several key steps and assumptions that can harm the final result if they are overlooked.

2.2 Forward model

2.2.1 Elastic, homogeneous, isotropic halfspace

Before diving into the details of inverse problem theory, one needs to have a forward model at hand. Displacement and strain at the Earth's surface in response to slip on a buried fault was solved by various authors, following the dislocation approach of Volterra [see *Segall*, 2010, and references therein]. The most popular set of equation is from *Okada* [1985], which corresponds to a rectangular dislocation of arbitrary geometry (albeit with a horizontal upper edge) embedded in a homogeneous, isotropic elastic half-space (earlier solutions from *Mansinha and Smylie* [1971] derived from *Maruyama* [1964], and *Savage and Hastie* [1966], yield identical predictions, but did not include the tensile case). A similar solution exists for triangular elements [*Comninou and Dundurs*, 1975; *Meade*, 2007; *Nikkhoo and Walter*, 2015].

For volcano applications, an equivalently popular model providing analytical expressions of surface deformation in response to subsurface pressure changes is the "Mogi" model of *Mogi* [1958] (previously proposed in *Anderson* [1936]), which consists in an isotropic point pressure source embedded in an homogeneous, isotropic elastic half-space. The Okada model has become the standard approach for modeling tensile cracks (vertical dikes or horizontal sills),

gaining further popularity. However, the complexity of sources of volcano deformation has however made it necessary to use more complex models (prolate spheroid shaped [*Yang and Davis*, 1988], penny-shaped crack [*Sun*, 1969], finite spherical [*McTigue*, 1987]; [see *Lisowski*, 2007; *Segall*, 2010, and references therein]). A recent model involving compound dislocations allows for generalizing these pressure sources, while adding an extra degree of freedom to Okada's model for planar sources [*Nikkhoo et al.*, 2016].

Since the classical solution of Okada is extremely well documented[22], it is more useful to discuss of its limitations, and on the potential consequences of these limitations when attempting to extract information about coseismic deformation data. This is the objective of the present section. The problem of volcanic deformation is not addressed specifically in the following, but the main shortcomings would also apply.

2.2.2 Elastic heterogeneity

The fact that the homogeneous-elastic forward model has been so extensively used suffices to demonstrate its success in providing a pragmatic and efficient tool for interpretation of geodetic data by the geologist. However, some authors have pointed out that the effects of elastic heterogeneity, due to layering or lateral variations in material properties, may be important in order to interpret second-order features of coseismic deformation [e.g. *Du et al.*, 1994; *Cattin et al.*, 1999; *Masterlark*, 2003; *Fialko*, 2004; *Hearn and Bürgmann*, 2005; *Dong et al.*, 2014]. Unfortunately, the same authors admit that information about the lateral and vertical variations of elastic properties is often uncertain. Enhancing the realism of the model is therefore achieved at the expense of an increased number of unknowns. This approach may be mandatory to accurately model far-field deformation in response to great megathrust earthquakes (M>8.5) such as the 2004 Sumatra earthquake [*Masterlark and Hughes*, 2008], the 2010 Maule earthquae [*Pollitz et al.*, 2011] or the 2011 Tohoku-Oki earthquake [*Zhou et al.*, 2012]. However, for continental earthquakes of moderate size, where optimization of the fault geometry is often required, the supplementary computational burden involved in calculating deformation in a non-homogeneous, non-isotropic medium is often deemed prohibitive.

Fig. 2.2 illustrates the effect of elastic layering on the predicted surface displacement field, using the slip distribution of the 2015 M_w7.9 Gorkha earthquake of ***Grandin** et al.* [2015] as a test case. The increase in the stiffness of rocks with depth produces a significant difference in the horizontal *versus* vertical decay of deformation away from the source at distances comparable with the depth to the most significant stiffness contrast. The fault lies at a depth of $\sim$ 15 km, and has a dip of 7°. Two different forward models are compared: (1) homogeneous, isotropic, linear, Poissonian ($\nu = 0.25$) model using *Okada* [1985]'s equations, and (2) a layered, elastic model using [*Zhu and Rivera*, 2002]'s method and an elastic structure derived from seismological analysis of ***Grandin** et al.* [2015]. This comparison shows two differences:

- The first difference is with the horizontal:vertical ratio at the location of peak uplift (which matches with the location of peak southward horizontal displacement) captured by continuous GPS station *KKN4*. For the same amount of uplift, the layered model predicts $\sim$ 15 % more southward displacement than the homogeneous model. Since this difference occurs at the site where maximum displacement is measured, such a small relative

[22] Okada's paper is cited 4,500 times according to Google Scholar.

difference maps into a significant absolute difference in the residuals, especially if the $\mathcal{L}_2$-norm metric is used to quantify the misfits (see section 2.3).

- The second difference is observed in the far-field, where displacement attenuates more rapidly away from the source for the layered model than for the homogeneous model, due to increase of rock stiffness with depth, as already noticed by *Rybicki* [1971] or *Ma and Kusznir* [1994]. As a result, inversions using a layered elastic space tend to predict more slip at depth than for homogeneous halfspaces [*Simons et al.*, 2002, e.g.]. This is particularly true for the vertical component, which is generally better captured by InSAR than by GPS. This effect is most pronounced for sources with a strong component of horizontal slip [*Pollitz*, 1996].

As a consequence of these differences, slip inversions using a forward model that includes layering tend to deepen the slip distribution, compared to a homogeneous case [*Savage*, 1998; *Simons et al.*, 2002]. The implication is critical when the coseismic slip model is subsequently employed to initialize postseismic deformation models in attempts to investigate the relative importance of afterslip *versus* viscous relaxation [*Kreemer et al.*, 2006; *Zhao et al.*, 2017]. Indeed, a deeper coseismic source will lead to stress changes occurring at greater depth, hence in regions of potentially lower viscosity, which could excite viscous relaxation more efficiently. Hence, a stiffer viscosity would be required, whereas producing the same amount of postseismic deformation with a "shallow" slip model deduced would require a more compliant viscosity. Similarly, stress-driven afterslip models strongly rely on the down-dip contour of the coseismic slip distribution, which is highly sensitive to the type of elastic model used in the coseismic slip inversion, as well as on the inversion procedure itself [see *Klein, Vigny, Fleitout,* ***Grandin****, Jolivet, Rivera, and Métois*, 2017, and references therein].

Another kind of heterogeneity arises from the *lateral* changes in elastic properties. These heterogeneity chiefly prevail across large fault systems, in particular megathrusts and large strike-slip faults, because cumulative geological offset allows for juxtaposing blocks of material with potentially very different material properties. In contrast to vertically stratified media, approximate analytic solutions are generally impractical for laterally variable distributions of elastic parameters. The question of brittle rupture on bimaterial interface has received substantial attention from seismologists [e.g. *Ampuero and Ben-Zion*, 2008], but paradoxically less so from geodesists. A simple analytic model is available for predicting the relative displacement across a vertical strike-slip fault separating two media of distinct rigidity, and slipping below a certain locking depth [*Le Pichon et al.*, 2005]. Applications of this model to interseismic deformation captured by GPS or InSAR across the San Andreas Fault and the Altyn Tagh fault [*Jolivet et al.*, 2008, 2009] show that the asymmetry in the velocity profiles can be explained by a rigidity contrast (of a factor two or more) across the fault. An alternative interpretation for asymmetric deformation across faults involves the introduction of a slightly non-vertical fault geometry, which can explain the data equally well, without the necessity of invoking rigidity contrasts [*Fialko*, 2006]. Surprisingly, few examples of a asymmetric material properties are reported for coseismic data, possibly suggesting that coseismic modeling approaches (generally based on Okada's equations) tend to systematically interpret asymmetry in terms of an asymmetric (non-vertical) fault than in terms heterogeneous material properties. This situation may represent a case of epistemic error, due to a trade-off between material properties and fault geometry, similar to the one existing between slip and fault dip, described by *Ragon et al.* [2018b]. Nevertheless, the actual solution may fall in between the two end-member models (heteroge-

neous elastic model only *versus* dipping faults only) [see *Chéry*, 2008, and references thererin]. More accurate GPS data (i.e. longer time-series), a denser spatial resolution of measurements (thanks to InSAR) and more efficient modeling approaches [e.g. *Barbot et al.*, 2009] may be the key toward determining the relative likelihood of these conflicting models.

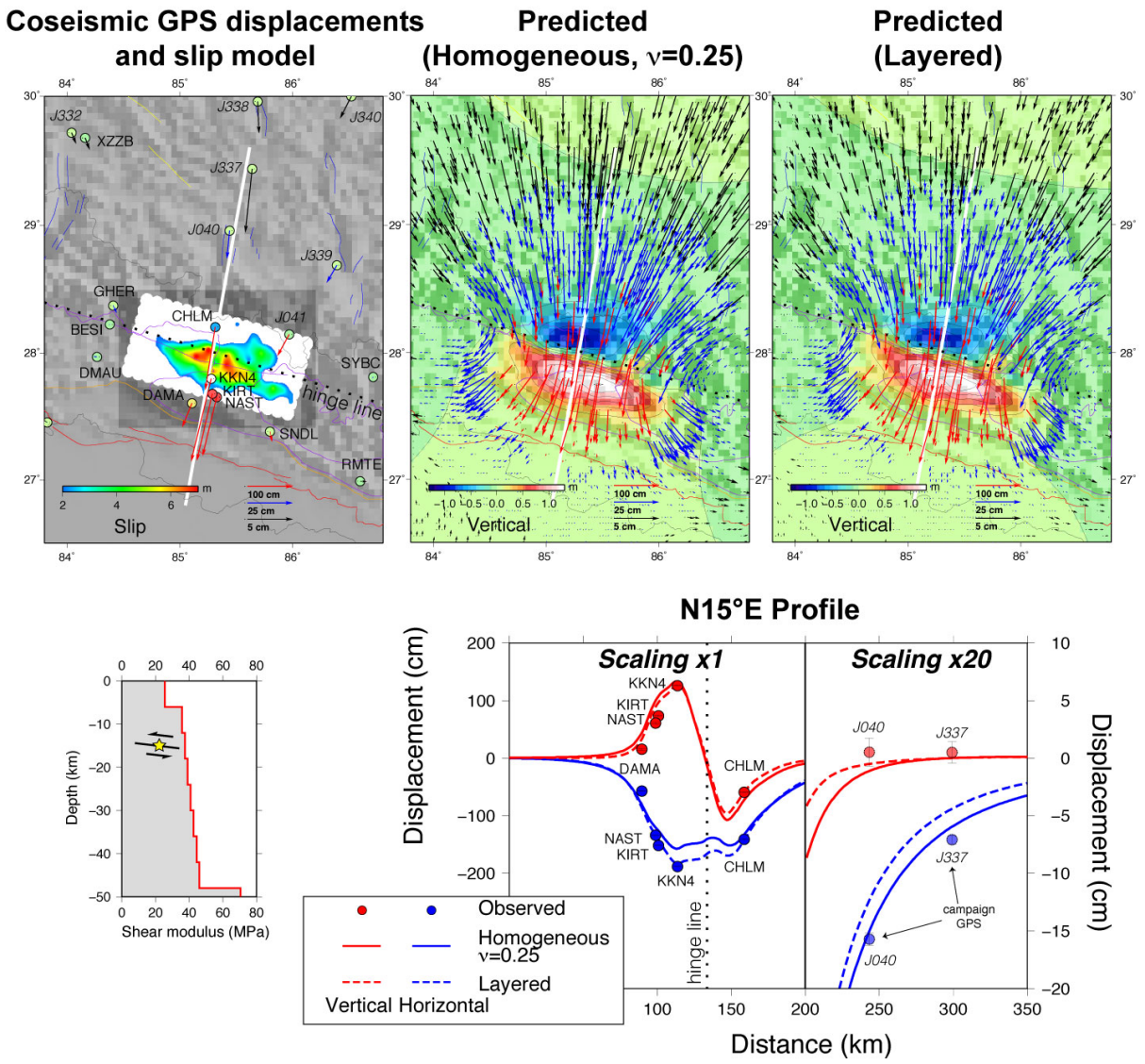

Figure 2.2 – Observed and predicted 3D displacement field during the Gorkha earthquake computed from the slip model of ***Grandin*** *et al. [2015] using homogeneous elastic half-space (plain line) [Okada, 1985] and a layered half-space (dashed line) [Zhu and Rivera, 2002]. The synthetics were computed using the CSI program (R. Jolivet, ENS). GPS data is from Galetzka et al. [2015] for Nepal and Wu et al. [2016] for Tibet (campaign sites have a code of the form JXXX). Note that Tibetan GPS stations were not available at the time when the slip model was computed. White line on the maps indicates the profile shown in the lower right panel.*

2.2.3 Topographic effects

Another caveat of the popular homogeneous isotropic halfspace analytic solutions is that they fail to account for the effect of topography, which have long been recognized as potentially significant [e.g. *McTigue and Mei*, 1981]. Taking full account of the topography requires the use of the computationally expensive finite element method [e.g. *Russo et al.*, 1997; *Trasatti et al.*, 2003], or the less computationally demanding boundary element method [e.g. *Cayol and Cornet*, 1998]. Approximate analytic solutions have shown that the effect of topography on strain, tilt and displacement are proportional to the local slope [*Meertens and Wahr*, 1986; *McTigue and Segall*, 1988]. Topography therefore produces a sensible effects in volcanic contexts, where steep slopes ($> 20°$) often prevail.

Availability of InSAR data on the flanks of Mount Etna has clearly shown that accounting for topography better explains the fringe pattern on the flanks and summit of the volcano than the standard Mogi model [e.g. *Williams and Wadge*, 1998; *Cayol and Cornet*, 1998]. A number of approximate analytical solutions have been proposed to account for the effect of topography, but with limited popularity in the community. An exception is the station correction method of [*Williams and Wadge*, 1998], which consists in accounting for variation of the station-source distance induced by a variable topography by modifying the source depth in the classical Mogi solution. This simple method yields surprisingly good results on Mount Etna while obviating the need for increasing the forward model complexity.

On the other hand, in tectonic contexts, slopes are generally more gentle, which makes the effect of topography less evident [*Mctigue and Stein*, 1984]. Nevertheless, the first order lesson that can be learned from the volcano studies listed above is that the effect of topography remains insignificant as long as the ratio H/Z between the source depth H and the receiver relative elevation Z (defined as the difference between the receiver elevation and the "average" elevation in the area) remains large.

Accordingly, the evaluation of the quantity Z depends on the spatial scale of interest. At short spatial wavelength ($<$ a few km), topographic slopes can be steep, giving rise to local slope effects that can be relatively well reproduced using the station correction method of *Williams and Wadge* [1998], as shown by *Tinti and Armigliato* [2002] and *Armigliato and Tinti* [2003] in the cases of the 1976 Friuli earthquake and 1980 Irpinia earthquakes. Fortunately, these effects cancel out at large scale ($>$ a few tens of kilometers). An exception may be the Gorkha earthquake, where the prominent Himalayan topography leads to an average slope of 2–5° towards the south above the causative, north-dipping fault. This sloping topography would be expected to produce an apparent rotation of the fault plane by an equivalent amount, if the surface was incorrectly supposed to be flat (which is an assumption made in most studies). However, uncertainty on the actual dip angle of the fault is of the same order, which is probably the reason why this question has attracted little attention [***Grandin** et al.*, 2015; *Wang and Fialko*, 2015; *Elliott et al.*, 2016; *Tung and Masterlark*, 2016].

Similarly, quantity H may also become small as the fault gets close to the surface, or even equal to zero for a surface rupture (this situation rarely occurs in volcanology, fortunately). Hence, *Thompson and Meade* [2018] have pointed that the effect of topography may become significant for a vertical strike-slip fault rupturing the surface in a location of steep fault-perpendicular slope. According to *Thompson and Meade* [2018], ignoring the effect of topography when inverting for coseismic slip could lead to a fictitious shallow slip deficit [e.g. *Fialko et al.*, 2005] in the final slip distribution.

Another case where the effect of topography should be considered is the 2016 Norcia earthquake. As illustrated in Fig. 2.3, the Norcia earthquake ruptured the surface on at least three sub-parallel normal fault strands, producing a complex pattern of vertical deformation [*Delorme, **Grandin**, Klinger et al.*, 2019]. Furthermore, the local topographic slope in the area is as steep as 25° on average. At depth, the three faults are believed to connect, but failing to account for the steep surface slopes makes it impossible to properly describe this connection. As a consequence, it has become necessary to rotate the coordinate system in order to take into

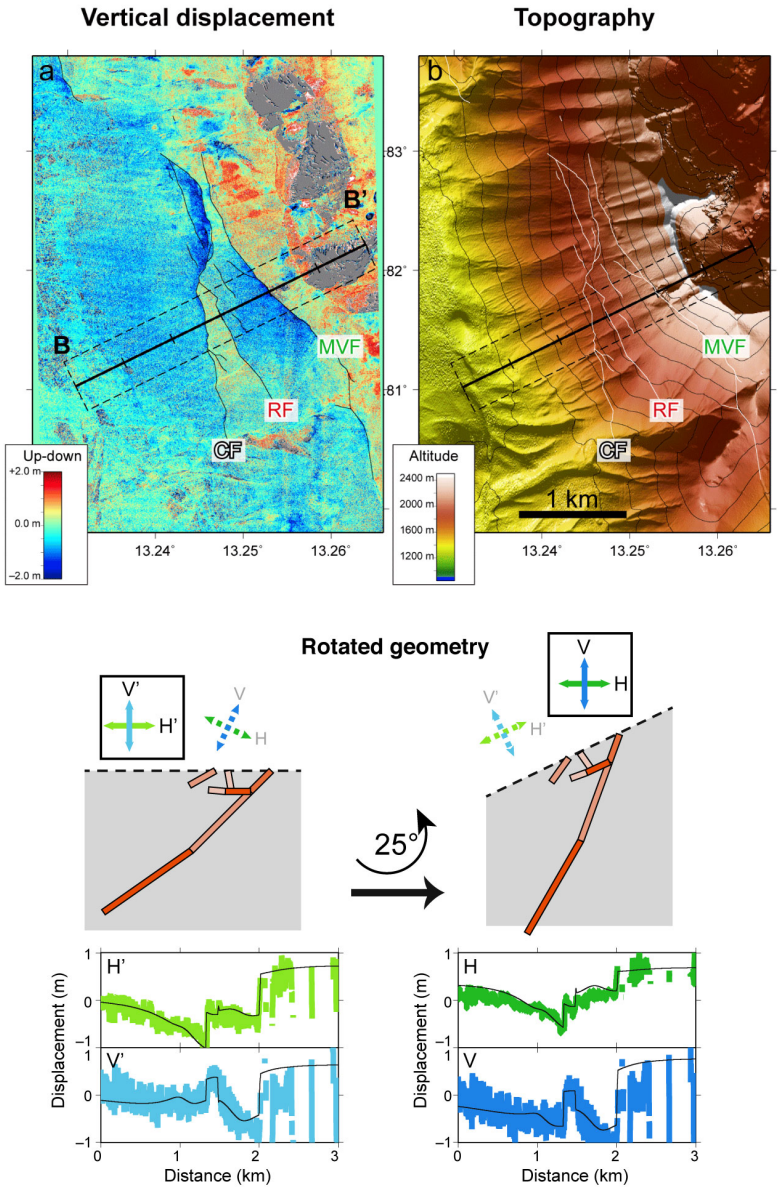

*Figure 2.3 – Top left: vertical displacement field in the area of surface ruptures of the 2016 Norcia earthquake, from differencing of pre- and post-earthquake Pleiades-derived DEMs. Top right: pre-earthquake topography. Bottom: a rotation of the coordinate system is required (a) to account for the effect of the topographic slope of the free-surface and (b) to properly describe the fault geometry at depth [Delorme, **Grandin**, Klinger et al. 2019].*

account (a) the sloping free surface and (b) the correct angle made by the faults with respect to this free surface. Unfortunately, deformation at broader scale cannot be correctly described by this rotated model, which currently poses a difficulty for including this correction in a rigorous static slip inversion incorporating jointly near-field data (optical image correlation) and far-field data (GPS, InSAR). In the coming years, as more systematic coverage of surface ruptures by high-resolution imagery will become available, the necessity of properly handling the effect of near-fault topography will become more patent.

2.3 Constraining the seismic moment

The simplest information that can be determined for an earthquake is its size, which is expressed as its seismic moment. The scalar moment M_o of the (double-couple) seismic source is defined as:

$$M_o = \int_\Sigma \mu(A) s(A)\, \mathrm{d}A \tag{2.1}$$

where s is the magnitude of slip on the fault plane Σ, μ is the shear modulus, or modulus of rigidity, and $\mathrm{d}A$ is an infinitesimal part of the fault plane surface. Seismology can determine M_o directly from the amplitude of seismic waves, after correcting for the effects of source radiation pattern, rupture directivity and seismic wave propagation [*Aki and Richards*, 1980]. On the other hand, provided the shear modulus remains relatively constant on the fault plane (see section 2.2), geodesy can only provide information about the product of slip and slip area, a quantity called "potency", $P_o = \int_\Sigma s(A)\, \mathrm{d}A$ [e.g *Heaton and Heaton*, 1989]. Seismic potency (or moment) being a zero-frequency characteristic of the earthquake source (hence the subscript "o"), the measurement of static displacements or strains is directly sensitive to this physical quantity.

Assuming that source location and mechanism are already known, the geodetic potency P_o can be determined with a good confidence using only a handful of geodetic measurements (strain or displacement) [e.g. *Wyatt*, 1988; *Amoruso et al.*, 2004]. This property is illustrated in Fig. 2.4, where Monte-Carlo sampling of fault parameters of the 2019 M8.0 Lagunas earthquake (Peru) shows the stability of the Potency (orange curve), independently of oscillations in other parameters (including the source depth).

However, it is important to consider the spatial distribution of geodetic measurements in such an analysis. Indeed, as discussed in section 2.2, changing the assumptions on the forward model changes the horizontal:vertical displacement ratio both in the near- and far-field, leading to overestimation or underestimation on the magnitude of slip, and hence on the computation of the potency.

More importantly, in case of an earthquake being captured by a GPS network, a few benchmarks can be located very close to the causative fault. This was the case, for instance, during the 2010 M7.0 Haiti earthquake, as shown in Fig. 2.5. In particular, one GPS benchmark (DFRT) sits right on the fault trace, exactly in the area where surface rupture was thought to have best chances to have occurred based on the gradient in surface displacement in the InSAR data [see *Bilham and Fielding*, 2013].

Surface rupture did not happen during the Haiti earthquake, but GPS benchmark DFRT still recorded a coseismic displacement of ~0.7 m. At first sight, this may sound like a good news, indicating that the earthquake source will be very well constrained. But in fact, quoting

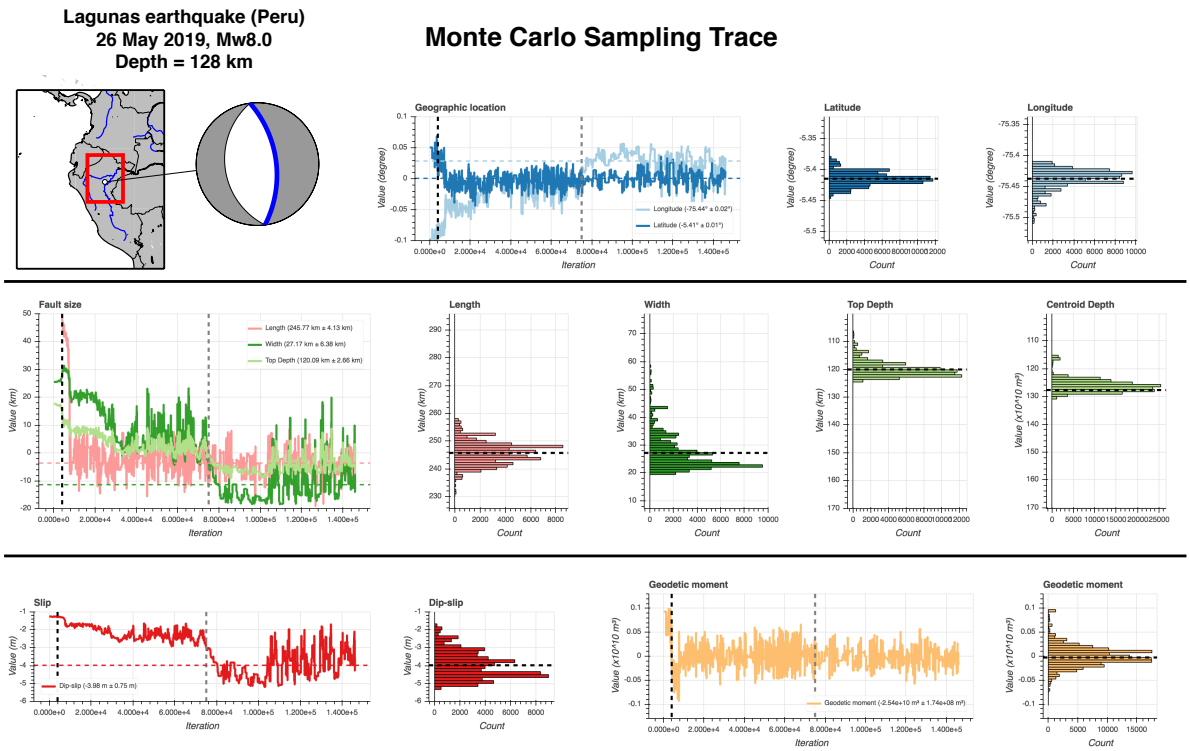

(a) Monte Carlo exploration of fault parameters for the 26 May 2019 Lagunas (Peru) earthquake. Colored curves show the trace of Monte Carlo Markov Chain sampling chain. In spite of an evident trade-off between fault width (dark green) and slip (red), the geodetic moment (yellow) remains remarkably stable throughout the exploration. Model vector length: 9 rows (longitude, latitude, depth, width, length, slip, 3 InSAR reference constants). Data vector length: 1335 rows (123 GPS vectors, 966 InSAR LOS points). Forward model: Okada [1985]. Number of iterations: 150,000. Software: Classic Slip inversion / PyMC version 2. Runtime: 3157 seconds on a single CPU (Intel Core i7 3GHz).

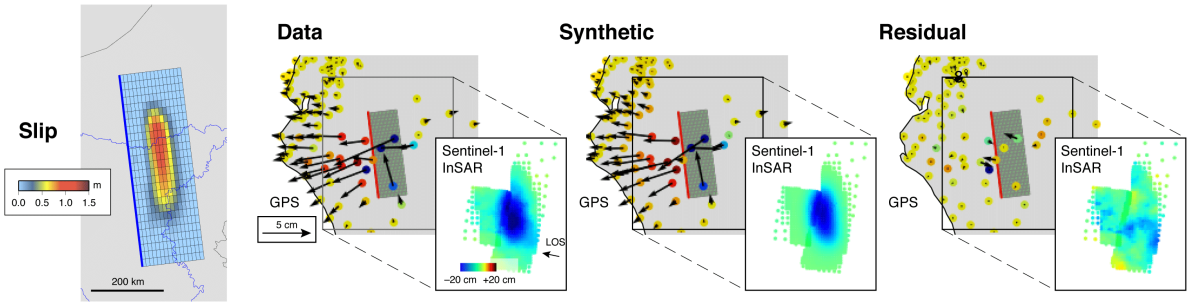

(b) Slip model, and observed, predicted and residual surface displacement from GPS and InSAR data.

Figure 2.4 – Bayesian inversion of source model of the 26 May 2019 M8.0 Lagunas (Peru) intermediate depth earthquake.

an anonymous colleague when discussing of the relevance of very-near-field measurements (whether geodetic or seismological), "*How can a mosquito say that he is biting a mouse or an elephant when he has his nose stuck on its victim's back?*".

Similarly, using synthetic tests for a potential 2004 Parkfield-like rupture, *Ziv, Doin, and* ***Grandin*** [2013] demonstrated that GPS stations located too close to an earthquake fault are prone to a very heterogeneous resolution on fault slip, leading them to be extraordinarily sensitive to slip only on a small portion of the fault plane. As these near-field stations are often those where maximum coseismic displacement has been recorded, the overall misfit to the data is dominated by potential difficulties to fit these particular stations with a low level of relative residual (i.e. relative to displacement magnitude). Due to this difficulty, site DFRT has always been poorly fit in the most slip inversions of the Haiti earthquake [*Calais et al.*, 2010; *Meng et al.*, 2012] [*Saint Fleur, Feuillet,* ***Grandin*** *et al.*, 2015], so that it was eventually discarded in a subsequent slip inversion *Symithe et al.* [2013]. In fact, the most suitable stations to determine the seismic potency are the ones that are located in the mid-field of the source, i.e. at a distance larger but of the order of the size of the source *Ziv et al.* [2013].

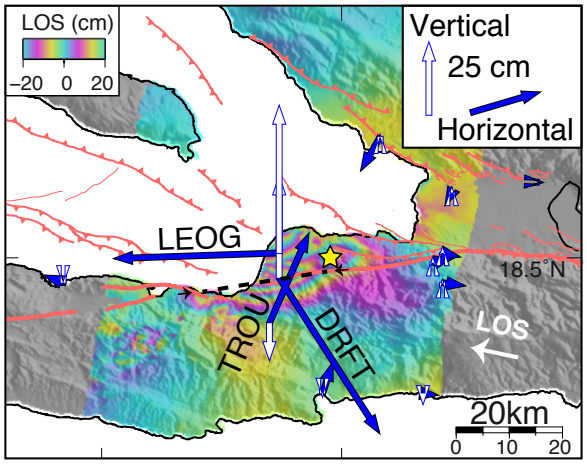

Figure 2.5 – Coseismic GPS data for 2010 M7.0 Haiti earthquake (from Saint Fleur, Feuillet, ***Grandin*** *et al. [2015], using vectors published by Calais et al. [2010]) superimposed on ALOS-2 InSAR data. Dashed line indicates surface trace of the causative fault.*

Nevertheless, let us not throw the baby out with the bathwater. As shown in Fig. 2.6 for the case of the 2016 Mw6.5 Norcia earthquake (Italy), GPS data acquired in the very-near-field may still be intelligible, as long as the full complexity of the fault geometry is taken into account. In particular, the rotation of vectors, or lateral variations in the vertical component of displacement over short distances are diagnosis of changes in the slip distribution at shallow depth, due to the partitioning of deformation on several branches, or the proximity of a sinuous surface rupture. The improvement of our capability to measure very-near-field deformation will therefore require a complexification of fault models at shallow depth. In cases when this complexity is not the main subject of attention, very-near-field data should be ignored. However, in order to be fully logical, one should refrain in such cases from interpreting the shallow distribution of slip derived from the inversion. In particular, investigating the pending question of the significance of the so-called "shallow slip deficit" phenomenon [*Fialko et al.*, 2005], requires the integration of geodetic data very close to the fault, which is difficult when using only InSAR (as in Fig. 2.6a). Using optical imagery (as in Fig. 2.6b) can provide a better resolution of shallow slip, which has been shown to lead to a reduction of the shallow slip deficit effect [*Xu et al.*, 2016].

Coming back to the distinction between seismic moment and seismic potency, an important difference should be kept in mind when attempting to compare geodetically determined moments from the seismic moments estimated from seismology. Indeed, if one sets aside for a moment the previous discussion about the spatial distribution of elastic parameters (is it homogeneous or not?), one key characteristic of elastic-halfspace forward models used in geodesy is

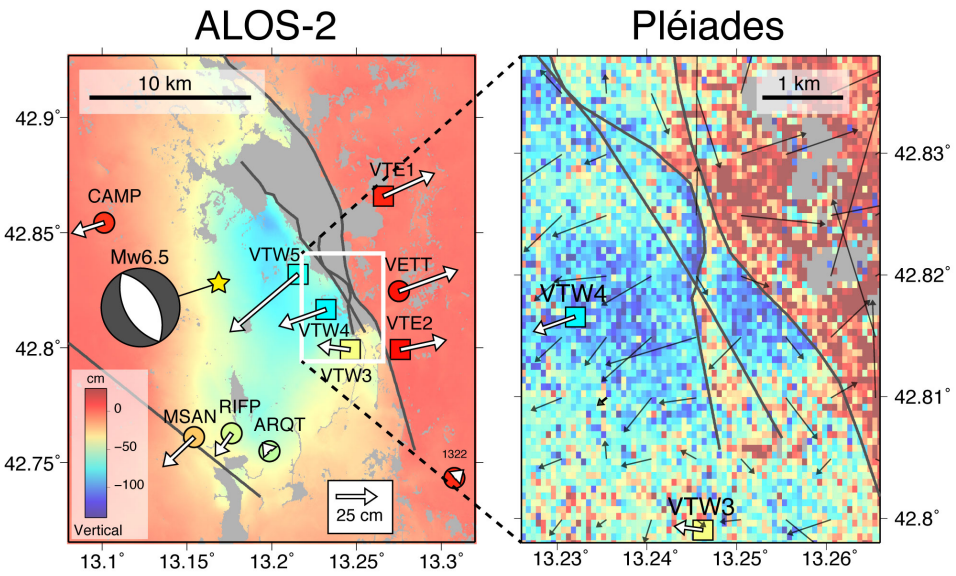

*Figure 2.6 – Geodetic dataset for the 2016 M6.5 Norcia earthquake [Delorme, **Grandin**, Klinger et al., 2019]. Left panel show the vertical displacement derived from ALOS-2 InSAR and the GPS data. Right panel shows data in the very-near-field of the surface rupture, from Pléiades (thin black vectors) and GPS (thick white vectors). GPS data is from RING network (circles, `ftp://gpsfree.gm.ingv.it/amatrice2016/static/Cosismico_30Oct2016_GPS_GdL_V1.dat`) and [De Guidi et al., 2017] (squares).*

that their predictions depend only on one elastic parameter. In particular, predictions from homogeneous models depend only on the Poisson ratio, and are insensitive to the absolute value of the shear modulus μ in Equation 2.1 [*Converse and Comninou*, 1975; *Masterlark*, 2003]. Converting geodesic potency into a seismic moment therefore requires multiplication by a shear modulus whose value can be uncertain by a factor ~ 2 (especially when dealing with interfaces separating materials with different rigidities, such as subduction planes separating a stiff oceanic plate from a more compliant oceanic block [e.g. *Ampuero and Dahlen*, 2005]). As a consequence, matching seismic moment derived from geodesy with seismic moment determined from seismology is subject to substantial uncertainty.

An implication of this difficulty is that the determination of the amount of aseismic slip that accompanies offshore ruptures (e.g. in a subduction setting) is fundamentally subject to large uncertainty. A combination of additional factors can conspire to further increase this difficulty:

- due to the offshore location of the event, the data is acquired in the far-field, leading to a low SNR;
- azimuthal coverage of the data is limited, which combined with imprecise earthquake location, leads to a trade-off between distance (epicentral distance and hypocentral depth) and potency;
- GPS stations occasionally fall within nodal directions of focal mechanisms, leading to a small displacement signal (e.g. 16 March 2013 Iquique "precursor", discussed in Sec-

tion 3.3 [e.g. *Ruiz, Metois, Fuenzalida, Ruiz, Leyton,* ***Grandin****, Vigny, Madariaga, and Campos*, 2014] [*Bedford et al.*, 2015]).

This being said, the exploitation of permanent GPS time-series from a network of instruments in the context of an underlying transient deformation (e.g. postseismic or SSEs), aiming at quantifying the seismic-to-aseismic ratio in the total slip budget of plate interfaces, is providing encouraging results, especially when the seismological and geodetic informations are considered jointly. Currently, this is only possible in areas of relatively fast deformation, and requires a good network (e.g. Chile, Mexico, Japan, California). In particular, matched filters attempting to detect small signals buried in the noise of GPS signals provide an opportunity to expand the catalogue of detected earthquakes from geodesy beyond on M>6 class. Comparison with catalogues of earthquakes and micro-earthquakes will, perhaps, allow for achieving a closure of the slip budget on the interface in periods devoid of large earthquakes (i.e. during interseismic, postseismic, SSEs) [e.g. *Frank*, 2016; *Rousset et al.*, 2017]. Such combined geodetic-seismological approaches should be systematically advocated.

A potential way to further improve estimates of seismic moment from geodesy would be to combine GPS and InSAR measurements with tilt measurements from long-base tiltmeters [e.g. *Boudin et al.*, 2008]. Unfortunately, although detection of coseismic "steps" has been reported by such instruments, the usefulness of tiltmeters to measure permanent coseismic tilt has been hampered so far by the difficulty to properly model the non-linear response of the surrounding fractured, fluid-filled host rock mass [e.g. *McHugh and Johnston*, 1977; *Zadro and Braitenberg*, 1999]. Although improvements in the technology of tiltmetry – in particular the development of optical tiltmeters [e.g. *Chawah et al.*, 2015] – should provide more robust estimate of the actual tilt experienced by the instruments, investigations of site effects will likely remain a difficult (but necessary) field of investigation. The issue of non-linear site response may be circumvented by deploying a large number of instruments and checking *a posteriori* for the compatibility of observations with the linear elasticity hypothesis. Accordingly, this would require the availability of low-cost sensors, which still seems far from being achieved.

2.4 The "inverse problem" problem

2.4.1 Principle

In general, as long as the problem can expressed in an explicit form (which is usually the case in Earth Sciences), one can write the forward problem as:

$$d = g(m) \tag{2.2}$$

where d is a point in the observation space (or data space) $\mathcal{D}$, m is a point in the model space $\mathcal{M}$, and g is a function that maps the parameter space onto the data space. In the matter that interests us, the function g describes how slip on a fault at depth will produce a certain displacement of the Earth surface, assuming a certain Earth model. The Earth model characteristics (elastic thickness, viscosity, etc) can also be included in the parameter list, as is done for determining mechanical parameters involved in postseismic relaxation [e.g. *Vergnolle et al.*, 2003; *Bruhat et al.*, 2011; *Doin et al.*, 2015; *Klein et al.*, 2016] or to study the characteristics of elastic heterogeneities in coseismic deformation data [*Du et al.*, 1994; *Fialko*, 2004; *Barbot et al.*, 2009]. However, they are generally held fixed when studying coseismic deformation (see Section 2.2

for a discussion of the importance of the forward model). Hence, the parameter space consists of a set of slip vectors or slip values (if the rake is fixed), whereas the data space consists of observed displacements (in the form of 3D vectors, or projection of these vectors onto a line-of-sight vector or a baseline vector). The two spaces $\mathcal{D}$ and $\mathcal{M}$, or manifolds, are therefore naturally described as vector spaces.

A simple approach for solving inverse problems can be described as follows:

> "*I suggest that the setting, in principle, for an inverse problem should be as follows: use all available a priori information to sequentially create models of the system, potentially an infinite number of them. For each model, solve the forward modelling problem, compare the predictions to the actual observations and use some criterion to decide if the fit is acceptable or unacceptable, given the uncertainties in the observations and, perhaps, in the physical theory being used. The unacceptable models have been falsified, and must be dropped. The collection of all the models that have not been falsified represent the solution of the inverse problem.*" [*Tarantola*, 2006]

This statement highlights the importance of treating all uncertainties as a part of the problem (including uncertainty on our physical theory) while integrating all possible prior information within the inversion procedure itself. Unfortunately, in spite of its simplicity and generality, this approach is not necessarily tractable from a computational point of view because it requires to describe the shape of the parameter space, which is potentially high-dimensional. In practice, solving an inverse problem often corresponds to find "the" vector in the parameter space that best matches our observations and, if possible, identify the degree of variability of this vector given a possible set of errors on our observations and models.

Therefore, assuming this simplified approach, solving the inverse problem corresponds to finding the vector $\hat{\mathbf{m}}$ in the parameter space that maximizes the likelihood function [e.g *Tarantola and Valette*, 1982b]:

$$\hat{\mathbf{m}} = \underset{\mathbf{m}}{\arg\max}\,\{\mathcal{P}(\mathbf{m}|\mathbf{d})\} = \underset{\mathbf{m}}{\arg\max}\,\left\{\mathcal{P}(\mathbf{d}|\mathbf{m})\mathcal{P}_m(\mathbf{m})\right\} = \underset{\mathbf{m}}{\arg\max}\,\left\{\delta(\mathbf{d}-g(\mathbf{m}))\mathcal{P}_m(\mathbf{m})\right\} \quad (2.3)$$

where $\mathcal{P}(\mathbf{m}|\mathbf{d})$ is the conditional p.d.f. of $\mathbf{m}$ given $\mathbf{d}$ (which captures our posterior estimation of this solution, including the associated uncertainty), $\mathcal{P}(\mathbf{d}|\mathbf{m})$ is the conditional p.d.f. of $\mathbf{d}$ given $\mathbf{m}$ (which contains our understanding of the physics of the problem), and $\mathcal{P}_m(\mathbf{m})$ is the marginal density function of $\mathbf{m}$ (which describes our prior estimation of what we think may be an acceptable solution). The second equality in Equation 2.3 involves the Bayes' rule.

Linear problems are defined as the class of problems where the function g is linear, so that g can be described by its matrix representation $\mathbf{G}$ (expressed in an appropriate coordinate system in the data and parameter vector spaces), which results in the famous matrix formulation of the forward problem [e.g. *Tarantola*, 1987; *Menke*, 1989]:

$$\mathbf{d} = \mathbf{G}\mathbf{m} \quad (2.4)$$

In the matter we are focusing on, a typical linear problem consists in finding the slip distribution on a set of fault patches, given a set of displacement measurements at the surface. As long as the above problem is linear, and that the assumed variances-covariances are Gaussian (i.e. $\mathbf{m} = \mathcal{N}(m_o, C_m)$, $\mathbf{d} = \mathcal{N}(d_o, C_d)$), finding the solution to the above inverse problem is

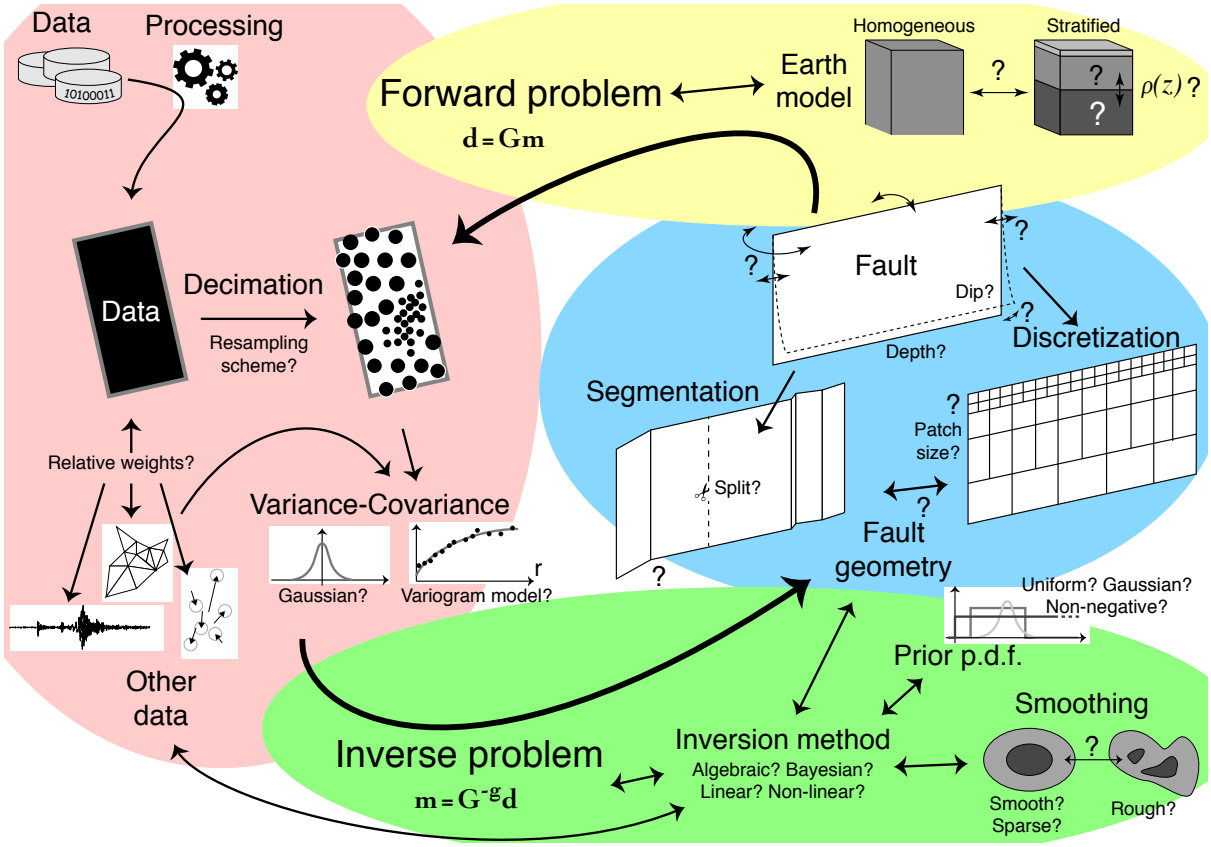

Figure 2.7 – Slip inversion as a highly non-linear inverse problem.

equivalent to searching for the "best" **m** in the least-squares sense [e.g. *Tarantola and Valette*, 1982a; *Maurer et al.*, 2017].

Progress in the understanding of inverse problem theory and improvements in computational resources have allowed for further formalizing inversion procedures. The standard methodology involves the definition of a cost function, whose minimization is sought (e.g. the norm of the residuals for the Gaussian case). Minimization can be achieved by methods belonging to two distinct classes. First, approaches pertaining to the field of linear algebra reformulate the minimization in terms of one or several matrix operations, hereafter called "algebraic". They can be extended to weakly non-linear problems by means of a linearization and an iterative procedure [*Tarantola and Valette*, 1982b]. These methods are fast and lead to a unique solution, especially when the problem is close to linear and well conditioned, which allows for inverting a large number of parameters (i.e. a large number of patches). However, they fail when the cost function has a complex shape, and it is difficult to implement sophisticated constraints on the final solution, such as restricting certain parameters to remain within given bounds.

On the other hand, in probabilistic approaches, minimization is achieved by exploration of the parameters space. Sampling of the parameter space is performed using sampling algorithms that can be iteratively search for the global minimum in the parameter space, such as Monte Carlo Markov Chains (MCMC), simulated annealing, genetic algorithm or neighbourhood algorithm [e.g. *Mosegaard and Sambridge*, 2002]. These probabilistic approaches, often also called "Bayesian", are generally more flexible because they actually consist in running

the forward problem many times, with no need for an actual "inversion" [e.g. *Mosegaard and Tarantola*, 1995; *Clarke et al.*, 1997; *Tiampo et al.*, 2000; *Fukushima et al.*, 2005; *Sudhaus and Sigurjón*, 2009; *Duputel et al.*, 2014; *Jolivet et al.*, 2015]. The prior information can be encoded as probability density functions (p.d.f.) of any kind (e.g. Gaussian, Uniform, etc) to avoid sampling regions of the parameter space that we know are not hosting the solution. By construction, they allow for assessing not only the "best model", but also the uncertainty associated with this solution, which makes it possible to determine which part of the solution is reliable, and which part should be regarded with caution. And, perhaps most importantly, non-linear problems can be easily tackled with these approaches, while allowing an assessment of trade-offs between parameters.

The two approaches (probabilistic or algebraic) are not completely orthogonal, but their philosophies are rather different. The probabilistic approach intends to find an ensemble of solutions following an "agnostic" strategy, within some reasonable constraints defined as probability density functions, using "smart-brute force". In this sense, it is in line with the recommendation of Albert Tarantola quoted above. Its main drawback is that only a limited number of parameters can be explored simultaneously, which makes this method difficult to apply to high-dimension problems (see e.g. Figure 2.4, where inverting for the optimal geometry of a single fault patch takes nearly one hour on a standard desktop computer). The exploration can nevertheless be parallelized [e.g. *Sambridge*, 1999; *Minson et al.*, 2013], but the "curse of dimensionality" still imposes a major limitation to the size of the problems that can be tackled by Bayesian approaches. The advent of the quantum computer, which may accommodate radically different algorithms capable of efficiently handling high-dimensional Bayesian optimization problems (including machine learning problems), could be a major game changer, but remains a distant dream [see *Biamonte et al.*, 2017, and references therein].

In the following section, the discussion will focus on the benefits of using the algebraic approach, in particular to gain a better understanding of the impact of various assumptions that are traditionally made during the inversion procedure. Although these methods are often criticized, they offer a number of major advantage over Bayesian approaches. First, they usually provide a reliable first-order estimation of the prime features of earthquake sources. They also allow for a fast calculation of the inverse problem, which makes them convenient to explore the effect of particular assumptions in the overall strategy of resolution of the inverse problem (e.g. fault geometry, data decimation, relative weights), and hence to question these assumptions. Finally, as defining the prior information that should be injected in a Bayesian inversion can be tricky, and in any case generally involves a degree of subjectivity that is often overlooked [e.g. *Scales and Snieder*, 1997]. Application of algebraic approaches should not be disregarded on the basis of them not being "rigorous", because they merely represent a special case of Bayesian inversion where prior p.d.f. is Gaussian – which is often a not too unreasonable assumption.

2.4.2 Solution of the linear inverse problem

Here, the matrix $\mathbf{G}$ is an $m \times n$ matrix (i.e. m rows, n columns), not necessarily square. The number of columns of $\mathbf{G}$ is n, which equals the size of the $\mathbf{m}$ vector. It can be chosen arbitrarily, from 1 (one patch, one slip component) up to any large number (several sub-faults, many patches, three slip components).

On the other hand, the number of rows of $\mathbf{G}$ is m, which equals the size of the $\mathbf{d}$ vector, and is dictated by the number of available observations. Prior to the development of GPS

and InSAR in the late 1990s, observations of static deformation induced by earthquakes were scarce, and in any case, were restricted to a few tens or hundreds of points at most. These data came in the form of triangulation-trilateration (sometimes pre-processed as displacement vectors) or leveling data acquired during surveys carried out along roads. Hence, availability of measurements was essentially conditioned by accessibility, yielding only a limited sampling of the actual strain field (section 3.5). Due to the limitations of these datasets, static slip inversions had to remain simple, in the sense that the number of inverted parameters could not be increased indefinitely, at the risk of seeing the problem become unstable. As a consequence, early attempts to solve static slip problems focused on the determination of a small number of parameters [e.g. *Jungels and Frazier*, 1973; *Thatcher*, 1975; *Tarantola et al.*, 1979]. However, setting length($\mathbf{m}$) = dim($\mathcal{M}$) = $n \leq m$ = dim($\mathcal{D}$) = length($\mathbf{d}$) does not guarantee that the optimal solution will be obtained, because of the sparseness of observations, which results in a heterogeneous resolution (see section 2.3).

A counter-intuitive approach to avoid this problem is to voluntarily choose a large number of parameters (such that dim($\mathcal{M}$) > dim($\mathcal{D}$)), making the problem underdetermined. In the context of static slip inversion, this is achieved by dividing the fault plane into many smaller sub-faults [e.g. *Ward and Barrientos*, 1986]. From a linear algebra point of view, this situation yields an infinite number of exact solutions composed of the sum of a particular vector and an extra vector belonging to the null space of $\mathbf{G}$ [e.g. *Backus and Gilbert*, 1967; *Parker*, 1977; *Ward and Valensise*, 1989]. This indetermination is not a desirable effect, because it brings in extra terms that cannot be resolved by the data. However, among these solutions, the minimum norm solution $\hat{\mathbf{m}}_{\text{MMN}}$ is the exact solution closest to $\mathbf{m} = \mathbf{0}_{\mathcal{M}}$ (using the euclidian distance), which is naturally the least affected by excessive oscillations in the solutions. It is straightforward to verify that its expression is:

$$\hat{\mathbf{m}}_{\text{MMN}} = \mathbf{G}^t \left(\mathbf{G}\mathbf{G}^t\right)^{-1} \mathbf{d} = \mathbf{G}^{\dagger}\mathbf{d} \tag{2.5}$$

where $\mathbf{G}^{\dagger}$ is the right Moore-Penrose inverse (as $\mathbf{G}\mathbf{G}^{\dagger} = \mathbf{I}_m$). This solution is unique [*Jackson*, 1972].

Unfortunately, in the underdetermined case, this approach suffers from a serious limitation, because the data vector is fit perfectly, whatever its erroneous content. As a result, the inversion procedure attempts to explain small errors in the observations by adjusting the model accordingly. This issue is illustrated by the example of Fig. 2.2, where observations (and predictions) of vertical displacement of the Gorkha earthquake for sites in Tibet are close to zero. A small error in the observed displacement would require a large change in the modeled potency to match these observations.

This problem can be tackled by accounting for observation errors in the problem. These can be managed rigorously by recasting the cost function in terms of reduced χ^2 statistics. More precisely, instead of minimizing $\mathbf{e}^t\mathbf{e}$, the minimization must be sought on $\mathbf{e}^t\mathbf{C}_d\,\mathbf{e}$ [*Jackson*, 1972], which is equivalent to rewriting the forward problem as $\mathbf{C}_d^{1/2}\mathbf{d} = \mathbf{C}_d^{1/2}\mathbf{G}\mathbf{m}$. In the simplest formulation, $\mathbf{C}_d$ is diagonal, with terms equal to the inverse of the variance σ_i^2 of each d_i (i.e. $\mathbf{C}_d = diag(1/\sigma_1^2, 1/\sigma_2^2, \ldots, 1/\sigma_n^2)$) [e.g. *Kaula*, 1966; *Fialko*, 2004]. A more advanced approach consists in filling off-diagonal terms using a covariance model estimated by analyzing noise auto-correlation in the data [*Jordan and Franklin*, 1971; *Lohman and Simons*, 2005; *Sudhaus and Sigurjón*, 2009]. In practice, $\mathbf{C}_d$ then acts as a linear transformation whose effect is to introduce relative weights between observations. However, if $\mathbf{C}_d$ includes small values on the

diagonal (i.e. if some observations have a large variance), then the problem can become ill-conditioned, leading to further instability of the result.

Under these circumstances, $\mathbf{G}\mathbf{G}^t$ in Equation 2.5 may not be inversible. A workaround is to use the singular value decomposition (SVD) of matrix $\mathbf{G}$, which always exists whatever the dimensions of $\mathbf{G}$, is given by [e.g. *Jackson*, 1972; *Matsu'ura*, 1977a]:

$$\mathbf{G} = \mathbf{U}\mathbf{D}\mathbf{V}^t \tag{2.6}$$

where $\mathbf{U}$ and $\mathbf{V}$ are semi-orthogonal matrixes (i.e. such that $\mathbf{U}\mathbf{U}^t = \mathbf{I}_n$ and $\mathbf{V}^t\mathbf{V} = \mathbf{I}_m$) containing the eigenvectors of $\mathbf{G}\mathbf{G}^t$ and $\mathbf{G}^t\mathbf{G}$, respectively, and $\mathbf{D}$ $m \times n$ matrix (i.e. same dimensions as $\mathbf{G}$), containing on its diagonal non-negative, real eigenvalues of $\mathbf{G}$, also called its *singular* values. The singular values are usually ordered such that $\lambda_1 \geq \lambda_2 \geq \ldots \geq \lambda_n$. The *rank* of $\mathbf{G}$ is equal to the number of non-zero singular values. The ratio λ_1/λ_n defines the *condition number* of $\mathbf{G}$. A large condition number means that the matrix is close to being singular.

Applying SVD to $\mathbf{G}^t$ yields $\mathbf{G}^t = \mathbf{U}\mathbf{D}\mathbf{V}^t$, so that $\mathbf{G} = \mathbf{V}\mathbf{D}^t\mathbf{U}^t$. The approximate solution for $\mathbf{G}^\dagger$ (Equation 2.5) is then given by:

$$\hat{\mathbf{m}}_{\text{MMN}} \approx \left(\mathbf{U}\mathbf{D}_o^{-1}\mathbf{V}^t\right)\mathbf{d} \quad \text{where :} \quad diag\left\{\mathbf{D}_o^{-1}\right\} = \begin{cases} 1/\lambda_i & \text{if } \lambda_i > t \\ 0 & \text{otherwise} \end{cases} \tag{2.7}$$

where t is a small threshold, for instance $t = 10^{-12}\lambda_{\max}$.

Similarly, when the problem is overdetermined (i.e. $n < m$), and assuming the matrix $\mathbf{G}^t\mathbf{G}$ is non-singular (i.e. $\mathbf{G}$ has full rank), the least-squares solution $\hat{\mathbf{m}}_{\text{LSQ}}$ is unique, and can be found by minimization of the $\mathcal{L}_2$ of residuals $\mathbf{e} = \mathbf{d} - \mathbf{G}\mathbf{m}$, which yields:

$$\hat{\mathbf{m}}_{\text{LSQ}} = \left(\mathbf{G}^t\mathbf{G}\right)^{-1}\mathbf{G}^t\mathbf{d} = \mathbf{G}^\dagger\mathbf{d} \tag{2.8}$$

where $\mathbf{G}^\dagger$ is the left Moore-Penrose inverse (as $\mathbf{G}^\dagger\mathbf{G} = \mathbf{I}_n$).

Again, if $\mathbf{G}^t\mathbf{G}$ is ill-conditioned or singular (i.e. $\mathbf{G}$ is rank deficient), then it is not possible to calculate $\left(\mathbf{G}^t\mathbf{G}\right)^{-1}$, but the SVD of $\mathbf{G}$ (taking $\mathbf{G} = \mathbf{U}\mathbf{D}\mathbf{V}^t$ this time) still offers an approximate solution for $\mathbf{G}^\dagger$ (Equation 2.8):

$$\hat{\mathbf{m}}_{\text{LSQ}} \approx \left(\mathbf{V}\mathbf{D}_o^{-1}\mathbf{U}^t\right)\mathbf{d} \quad \text{where :} \quad diag\left\{\mathbf{D}_o^{-1}\right\} = \begin{cases} 1/\lambda_i & \text{if } \lambda_i > t \\ 0 & \text{otherwise} \end{cases} \tag{2.9}$$

where t is a small threshold.

To mitigate the issue of ill-conditioning, the so-called *truncated SVD* method can then be used. It consists in gradually incorporating only the most significant eigenvalues-eigenvectors in the solutions and testing their significance in terms of fit to the data (accordingly, the fit will not be exact anymore) [e.g. *Wiggins*, 1972; *Jackson*, 1972; *Harris and Segall*, 1987; *Thatcher et al.*, 1997; *Gallovič and Ampuero*, 2015]. This way, only the meaningful features of the slip distribution are restituted, at the cost of risking an underestimation of slip in regions of poor resolution (i.e. at depth, or in areas not covered by geodetic data). A similar approach consists in working on the diagonalized version of $\mathbf{G}^t\mathbf{G}$ (which is positive-definite, hence always diagonalizable with real, positive eigenvalues) a procedure called "spectral expansion" [*Gilbert*, 1971; *Parker*, 1977; *Xu et al.*, 2017].

2.4.3 Incorporating InSAR data in static slip inversions: challenges and opportunities

Although in practice the above methods are not used anymore in the field of static slip inversion, they still bear an interest in that they allow for understanding the structure of the inverse problem, and provide useful tools to estimate the degree of resolution and "constraintness" of a particular problem. As already stated, earlier studies relied on a limited number of observations, so that the main question was whether the problem was under- or over-determined, or, more accurately, under- or over-constrained [e.g. *Jackson*, 1972; *Tarantola and Valette*, 1982a]. The advent of InSAR has somehow changed this situation, as InSAR data carries a large number of observations in a single image.

However, these observations are highly redundant, which calls for some kind of reduction, or decimation. Decimation of InSAR data is usually performed using a quadtree algorithm, where cell size is determined according to a variety of criteria such as the curvature of the displacement field (second-order spatial derivative) [*Simons et al.*, 2002], the RMS scatter about the mean [*Jónsson et al.*, 2002], the model resolution [*Lohman and Simons*, 2005] or the distance to the fault trace [***Grandin** et al.*, 2009], as in Fig. 2.8 ; [see also *Miyashita and Matsu'ura*, 1978, for an early attempt to reduce a spatially dense geodetic data set].

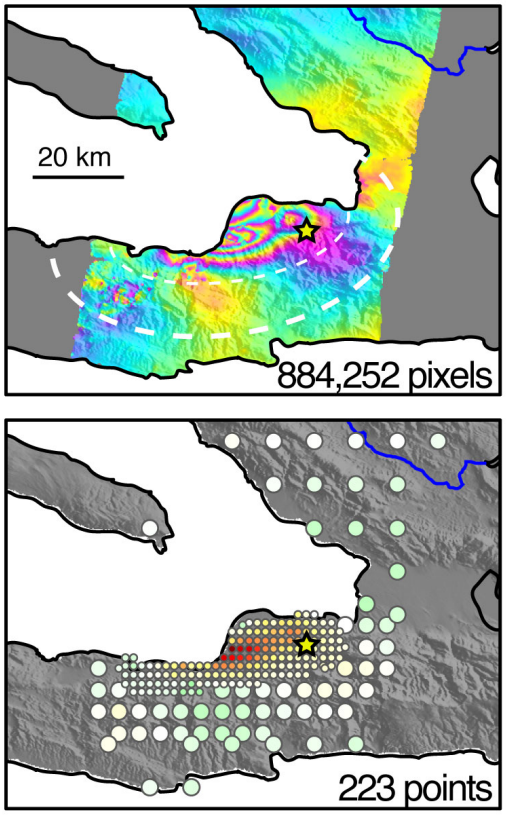

*Figure 2.8 – Downsampling of InSAR data for the Haiti earthquake [Saint Fleur, Feuillet, **Grandin** et al., 2015]. Here, the level of downsampling depends on the distance from the fault trace. Three distance bins are defined, each corresponding to a fixed downsampling rate. White dashed lines in upper panel show the location of the three distance bins. In this case, downsampling achieves a reduction of the number of points by a factor ~ 4000.*

Even after applying moderate decimation to the InSAR dataset, the richness of InSAR information instantly makes the problem overdetermined, in the sense that line-of-sight displacements sampled on thousands of pixels can be dumped in the **d** vector. From a linear algebra point of view, as long as the problem is overdetermined, the problem can be easily solved by classical least-squares (Equation 2.8).

Nevertheless, a question that immediately arises is the problem of weighting different data points that are potentially affected by a different degree of noise or uncertainty. This problem is often encountered when inverting jointly GPS and InSAR data, or, worse, when inverting seismological and geodetic data. The common practice consists in performing several inversions using each dataset separately, in order to identify the resolution provided by each dataset, and then attempt for a fusion of the different datasets by adjusting the weights between them [*Delouis et al.*, 2002, e.g.]. This

last step often involves a degree of arbitrariness.

However, prior to running these final models with many patches, the issue of the optimal fault geometry has to be resolved (this issue also applies to the Bayesian approach). With the large number of observations provided by InSAR, it is possible to split the fault into an even larger number of patches, which can be distributed homogeneously on the fault, or defined in a "smarter" way, by accounting for the variable resolution on the fault plane: patches can be made smaller in well-resolved parts of the fault plane, whereas poorly resolved regions should be described by larger patches [see e.g. *Page et al.*, 2009; *Barnhart and Lohman*, 2010] (Fig. 2.9). This way, ill-conditioning can be mitigated.

Accordingly, a bigger **d** is an incentive for attempting the inversion on a bigger **m**. Ideally, the size of **m** should be fixed rigorously to capture just as much complexity as is contained in the data [see e.g. *Sambridge et al.*, 2006]. However, the problem of ill-posedness never fully vanishes. Indeed, determining the slip distribution of even the best observed earthquake is generally ambiguous, in that one can easily find relatively different slip models that can yield a very similar displacement field at the surface, hence achieving a nearly identical fit to the data [e.g. *Mavko*, 1981; *Tong et al.*, 2015].

Tackling the issue of ill-posedness (as well as ill-conditioning) classically involves the ad-

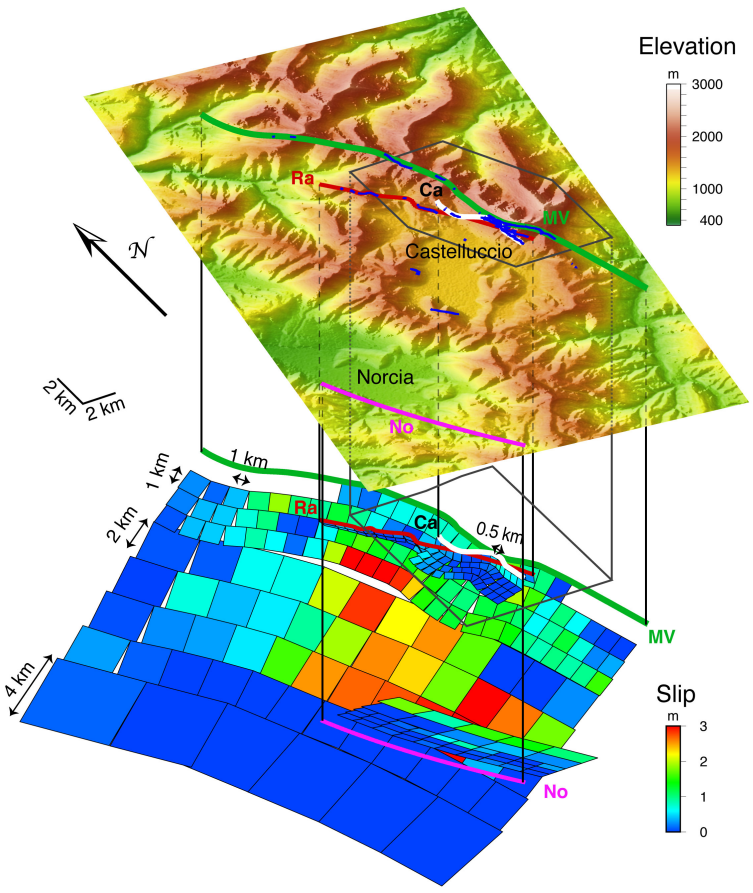

*Figure 2.9 – Discretization of multiple fault planes as a function of depth and as a function of resolution (from [Delorme, **Grandin**, Klinger et al. 2019]). See Fig. 2.6 for a detailed view of deformation in the area of reported surface ruptures (in blue on the map).*

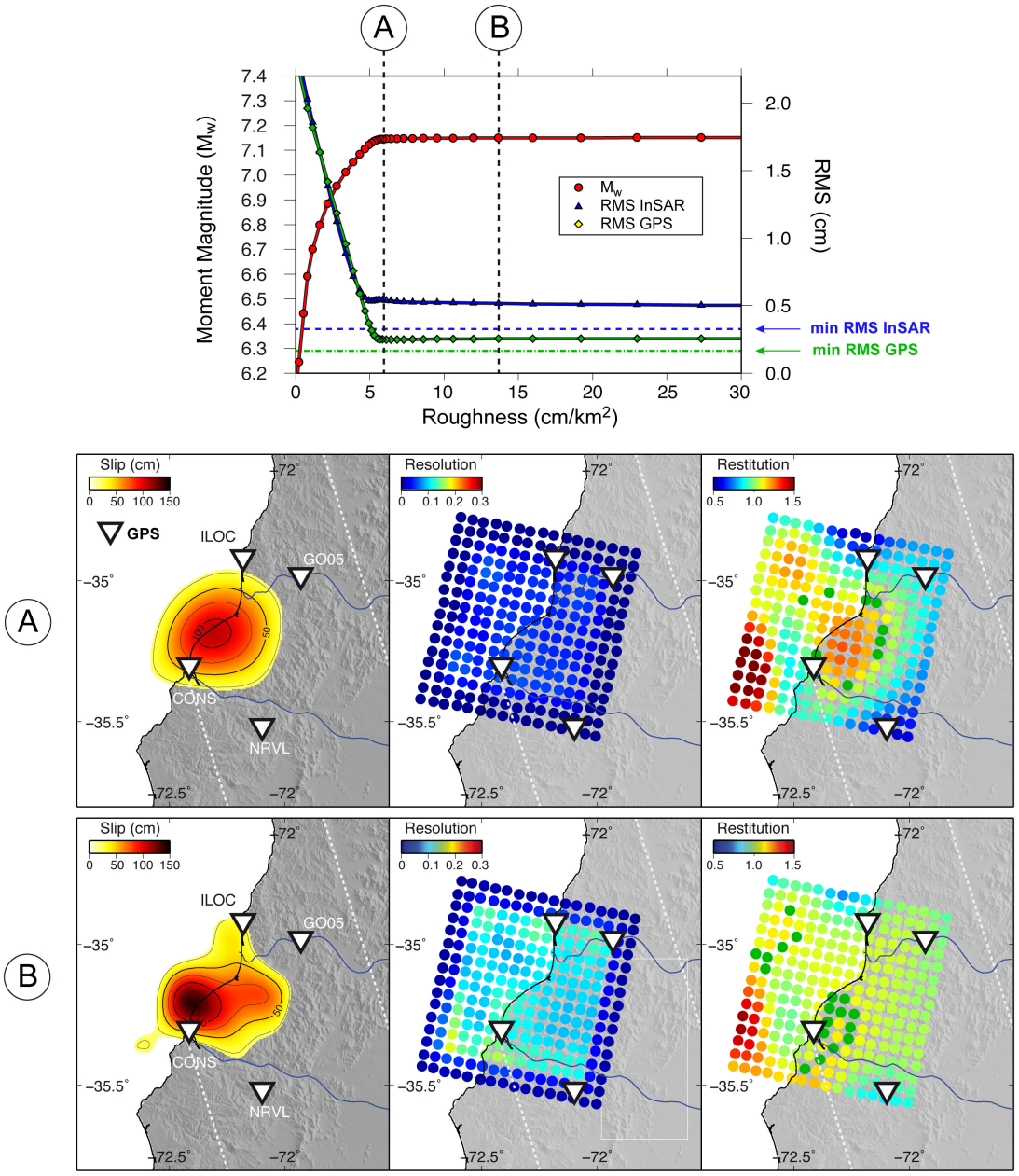

Figure 2.10 – Joint inversion of GPS and InSAR data for 25 March 2012, Mw7.0 Constitución earthquake (largest aftershock of the 2010 Mw8.8 Maule earthquake). Upper panel shows an L-curve exploration of data misfit versus roughness of slip distribution. Blue and yellow curves represent the RMS residual of InSAR and GPS data, respectively. Red curve displays the seismic moment, which is shown to remain stable even for rough models, as discussed in Section 2.3. Bottom panel shows two solutions obtained in the exploration, with nearly identical fit to the data. Inverted white triangles show the location of GPS stations. A: smooth model ; B: rough model. The middle and right columns show two different representations of the model resolution matrix **R** *(Equation 2.13) The middle column shows the diagonal terms of* **R**, *whereas the right column is the restitution, i.e. the sum of the rows of* **R**. *Modified from [Ruiz,* ***Grandin*** *et al., 2013].*

dition of Tichonov regularization terms in the cost function, in the form of the $\mathcal{L}_2$ norm of the solution (so-called "damping", [e.g. *Leão and Silva*, 1989; *Wald and Heaton*, 1994; *Klein et al.*, 2017]) or of its higher-order spatial derivatives (gradient, Laplacian, etc, [e.g. *Segall and Harris*, 1986; *Jónsson et al.*, 2002; *Simons et al.*, 2002; *Fialko*, 2004; *Maerten et al.*, 2005; ***Grandin et al.***, 2009]):

$$\hat{\mathbf{m}} = \min_{\mathbf{m}} \left\{ ||\mathbf{d} - \mathbf{G}\mathbf{m}||_2 + \alpha ||\nabla^2 \mathbf{m}||_2 \right\} \tag{2.10}$$

The meta-parameter α allows for "tuning" the degree of smoothness of the solution, usually following an "L-curve" approach to explore the trade-off between misfit and solution roughness [e.g. *Segall and Harris*, 1987] (Fig. 2.10), although other techniques such as Akaike's Bayesian Information Criterion (ABIC) [*Yabuki and Matsu'Ura*, 1992; *Fukahata and Wright*, 2008] or ${}_j\mathcal{R}_i$ [*Barnhart and Lohman*, 2010] may provide more rigorous methodologies to define the optimal value of α. The geodetic moment, which is simply the sum of slip on all patches (weighted by their area), can also be included as a constraint satisfying linearity. However, such an approach is generally inefficient because the geodetic moment is already relatively well determined using only a small set of geodetic displacement measurements (see section 2.3).

Alternatively, implicit regularization can also be enforced by including covariance terms in the variance-covariance matrix on the model $\mathbf{C}_m$, hence modifying the simple least-squares solution formula (Equation 2.8) [*Tarantola*, 1987; *Radiguet et al.*, 2011].

$$\begin{aligned} \hat{\mathbf{m}} &= \mathbf{m}_o + \left(\mathbf{G}^t \mathbf{C}_d^{-1} \mathbf{G} + \mathbf{C}_m^{-1}\right)^{-1} \mathbf{G}^t \mathbf{C}_d^{-1} (\mathbf{d} - \mathbf{G}\mathbf{m}_o) \\ &= \mathbf{m}_o + \mathbf{C}_m \mathbf{G}^t \left(\mathbf{G}\mathbf{C}_m\mathbf{G}^t + \mathbf{C}_d\right)^{-1} (\mathbf{d} - \mathbf{G}\mathbf{m}_o) \end{aligned} \tag{2.11}$$

where $\mathbf{m}_o$ is a vector describing any prior information on our model. In this formulation, covariances between patches in $\mathbf{m}$ can be specified using a Gaussian [e.g. *Tarantola and Valette*, 1982b] or a Laplace distribution [e.g. *Lohman and Simons*, 2005] parametrized by the relative distance between the m_i patches. This ensures that the square matrix $\mathbf{C}_m$ is positive-definite, hence inversible [*Armstrong and Jabin*, 1981], while injecting some spatial dependence between the model parameters.

Whichever resolution method is picked among the abovedescribed approaches, the solution of the inverse problem can be written:

$$\hat{\mathbf{m}} = \mathbf{G}^{-g}\mathbf{d} \tag{2.12}$$

where $\mathbf{G}^{-g}$ is the generalized inverse. However, this matrix can be explicitly calculated only in the case of a linear problem (e.g. $\mathbf{G}^{-g} = \left(\mathbf{G}^t\mathbf{G}\right)^{-1}\mathbf{G}^t$ in Equation 2.8, or $\mathbf{G}^{-g} = \left(\mathbf{G}^t\mathbf{C}_d^{-1}\mathbf{G} + \mathbf{C}_m^{-1}\right)^{-1}\mathbf{G}^t\mathbf{C}_d^{-1}$ in Equation 2.11), whereas it remains tied to the $\mathbf{d}$ vector in other formulations of the inverse problem solution. Nevertheless, even if the chosen inversion method is not actually linear, it may be helpful to compute $\mathbf{G}^{-g}$ because this matrix informs on the *resolution matrix* $\mathbf{R}$ [*Backus and Gilbert*, 1968; *Tarantola and Valette*, 1982a]:

$$\mathbf{R} = \mathbf{G}^{-g}\mathbf{G} \tag{2.13}$$

This square matrix has a size equal to the length of the $\mathbf{m}$ vector. Two different representations of the resolution matrix can be made: either its diagonal or the sum of its rows, the latter being called the *restitution* [*Page et al.*, 2009] (Fig. 2.10).

Alternative regularization strategies, which lead to a break-down of linearity, include:

- the implementation of non-negative constraints:

$$\hat{\mathbf{m}} = \min_{\mathbf{m}} \; ||\mathbf{d} - \mathbf{G}\mathbf{m}||_2, \text{ subject to } m_i \geq 0, \; \forall i \in [|0, n|] \tag{2.14}$$

  for instance to prevent left-lateral slip when the causative fault is known to be right-lateral [e.g. *Hartzell and Heaton*, 1983; *Du et al.*, 1992; *Arnadóttir and Segall*, 1994]. This approach can also be used to define bounds on the rake angle (e.g. to force the rake to be within $\pm 15°$ of a prescribed rake angle) by using a non-orthogonal basis for slip description (instead of the usual decomposition of slip into two orthogonal strike-slip and dip-slip components) [e.g. *Saint Fleur, Feuillet, **Grandin** et al.*, 2015; *Delorme, **Grandin**, Klinger et al.*, 2019]. Formally, this kind of problem falls in the category of *linear programming*. This approach is generally very efficient in terms of regularization because geodetic data are very sensitive to the potency, which is equal (in first approximation) to the algebraic sum of slip magnitude on all faults involved in the model: bounding the direction of slip

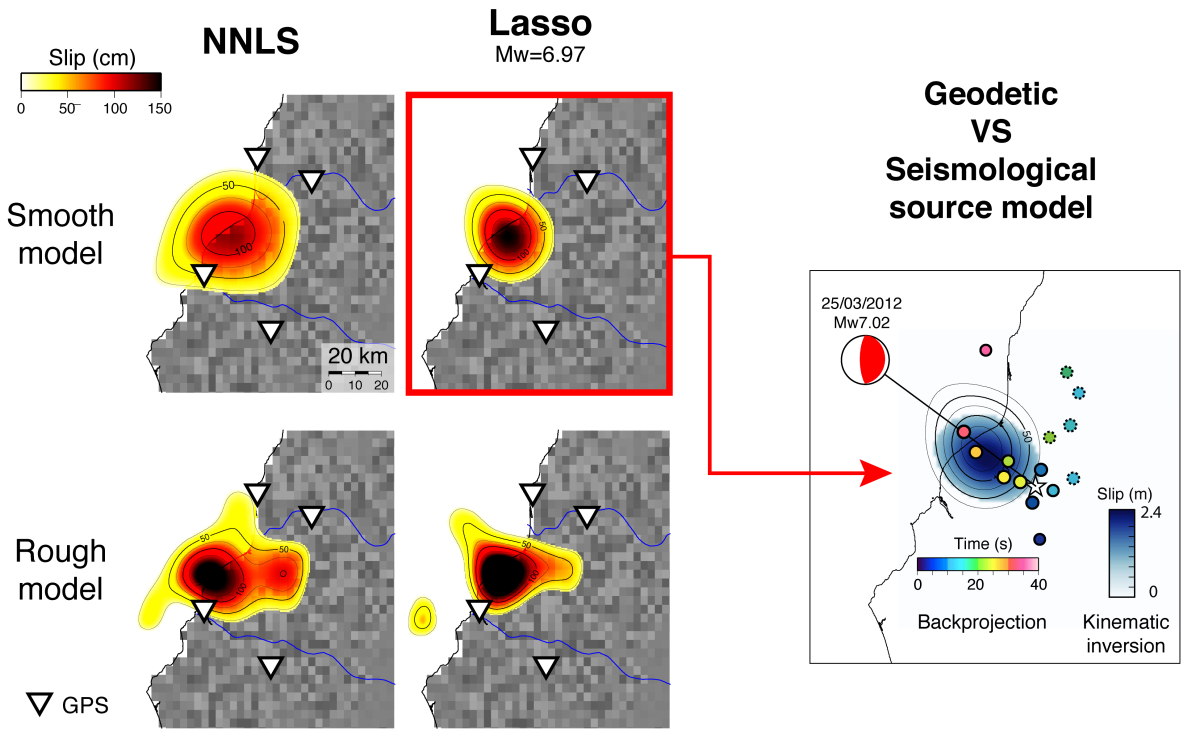

*Figure 2.11 – Variability of slip models for the Maule aftershock depending on the amount of smoothing, for two inversion methods (see Fig. 2.10). All solution lead to equivalent fit to the data. The upper and middle rows show a comparison of slip models obtained using non-negativity constraints (left, Equation 2.14) versus prescribed seismic moment enforced by $\mathcal{L}_1$ metric using the Lasso algorithm (right, Equation 2.15). Upper and middle rows show different degrees of model roughness. Lower panel compares the solution derived from GPS and InSAR (contours) against a solution deduced from strong-motion records (in blue). Color circles indicate the space-time distribution of sources of high frequency radiation detected during the rupture by backprojection of seismic energy. Modified from [Ruiz, **Grandin** et al., 2013].*

effectively prevents unphysical oscillatory distribution of slip on the fault plane, although some authors argue that such negative or oscillatory features may diagnose a poorly conditioned problem and should therefore not be forcefully discarded [*Yagi and Fukahata*, 2011]. In general, inequality constraints are achieved by iterative algorithms, such as the gradient method [e.g. *Ward and Barrientos*, 1986; *De Natale and Pingue*, 1991] or the augmented Lagrangian method [e.g. *Cayol et al.*, 2014], which makes them computationally intensive. The original algorithm allowing for non-negativity constraints by *Lawson and Hanson* [1974] has long been implemented in Matlab [23] and Python. A more recent, faster implementation has been reported by *Bro and De Jong* [1997].

- constraints on the seismic moment using the $\mathcal{L}_1$ norm, instead of the $\mathcal{L}_2$ norm, to minimize the influence of patches with low resolution:

$$\hat{\mathbf{m}} = \min_{\mathbf{m}} \; ||\mathbf{d} - \mathbf{G}\mathbf{m}||_2, \text{ subject to } \sum_{i=1}^{n} |m_i| \leq M_o \tag{2.15}$$

  Using the $\mathcal{L}_1$ norm avoids a tendency of the $\mathcal{L}_2$ norm to exclude scenarios with localized, extreme values (Fig. 2.11). Hence, the $\mathcal{L}_1$ metric favors "sparse", compact slip solutions, which may be argued as not totally unphysical, for instance in the case of the 2011 M9.0 Tohoku (Japan) [e.g. *Evans and Meade*, 2012]. Since the $\mathcal{L}_1$ norm is not differentiable, the problem becomes non-linear, but remains *convex*, which allows for finding a solution through a variety of methods [*Boyd and Vandenberghe*, 2004]. An efficient algorithm to solve this particular problem is the "Lasso" (Least Absolute Shrinkage and Selection Operator) [*Tibshirani*, 1996], which is both available for Matlab and Python.

- mechanical contraints, in the form of a prescribed stress distribution that forces the slip distribution to remain kinematically compatible, hence smooth, for example by means of a Boundary Element Model (BEM) tied to the inversion procedure [e.g. *Sun et al.*, 2011; *Maerten et al.*, 2005]. This approach has also been developed to cases of volcanic deformation, especially dyke or sill intrusions, whose lateral variations in opening are interpreted as reflecting lateral contrasts in driving pressure [e.g. *Fukushima et al.*, 2005; *Yun et al.*, 2006]. Finding the optimal pressure/stress distribution given a fixed dyke/fault geometry is still a linear problem, whereas searching the optimal fault/dyke geometry turns the problem into a non-linear one. Coupling with algorithms allowing for non-negativity constraints is also possible, e.g. to avoid reverse slip or interpenetration of fractures [*Maerten et al.*, 2010; *Cayol et al.*, 2014]. This approach places a lot of importance in the definition of the geometry, which greatly controls the deformation pattern, given simple stress boundary conditions, whereas standard approaches of the slip inversion problem assume that most of the complexity in the deformation stems from variable slip/opening on dislocations having a relatively simple geometry. As a consequence, BEM approaches are expected to yield a lower fit compared to mechanically unconstrained inversions [e.g. *Herbert et al.*, 2014], which should be considered as the price to pay to obtain a more realistic solution from a mechanical point of view.

- definition of a small number of empirical hyper-parameters that allow for constructing spatially complex slip distributions, such as the "control points" in the kinematic inver-

[23] See interesting narrative of the algorithm implementation at `https://blogs.mathworks.com/loren/2006/12/12/brief-history-of-nonnegative-least-squares-in-matlab/`

sions of *Causse et al.* [2017], or the geometric parameters of an elliptical crack as in the dynamic inversion of *Ruiz and Madariaga* [2011]. So far, these approaches have not been fully explored in the context of static slip inversions.

Unfortunately, the problem cannot always be treated as linear. The most common source of non-linearity stems from the necessity to simultaneously estimate fault slip and fault geometry. Indeed, changing the fault dip, location or depth dramatically changes the distribution of surface displacements in a manner that can be highly non-linear. As a result, the inversion procedure generally follows a succession of steps [e.g. *Matsu'ura*, 1977a,b; *Ward and Barrientos*, 1986; *Funning et al.*, 2007; ***Grandin** et al.*, 2010]:

1. data decimation, based on previous knowledge of fault location;
2. non-linear inversion using fixed slip dislocations, to determine the fault geometry;
3. discretization of the fault plane into a large number of smaller sub-faults;
4. linear inversion of slip distribution on the fault plane.

The non-linear problem of finding the best geometry can be tackled using several approaches, including quasi-Newton iterative algorithm [*Tarantola and Valette*, 1982a] or Monte Carlo methods [e.g. *Amoruso et al.*, 1998; *Funning et al.*, 2005]. All of these methods are however limited in the number of parameters that can be inverted, which restricts their application to simple fault geometries. Alternatively, defining new geometrical parameters, such as fault skewness or fault curvature, as is done by *Fukushima et al.* [2005], allows for keeping a small number of parameters while simultaneously allowing for describing relatively complex geometries.

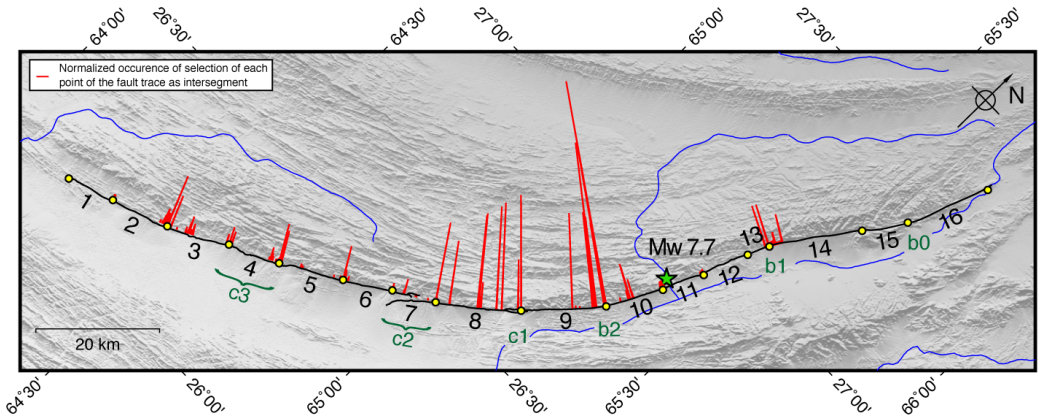

*Figure 2.12 – Optimization of the fault geometry along-strike by piecewise linear fitting of the fault trace using an unknown number N of sub-segments [from Lauer, **Grandin**, and Klinger, 2019]. For each tested value of N, the algorithm searches for the best set of connected segments that closely match the fault trace. The resulting connections are collected and represented as a histogram along the fault trace. For a broad range of values for N, a stable set of points representing breaks in the fault trace are identified. These points can then be selected as intersegments in order to decrease the number of unknown in the subsequent optimization of fault geometry.*

For faults that break the surface, attaching the dislocations to the fault trace already provides a strong constraint that limits the number of non-linear parameters. The fault can be discretized into a certain number of sub-faults, not necessarily with uniform size, in order to capture the first- or second-order features of the rupture [e.g. *Pritchard et al.*, 2002; *Barnhart and Lohman*, 2010]. The discretization involves a certain degree of arbitrariness, but automatic approaches have been proposed, such as the $\mathcal{L}_1$ trend filtering method [*Klinger*, 2010; *Lauer, **Grandin**, and Klinger*, 2019] (Figure 2.12). However, for earthquakes with no surface rupture, it is often difficult to identify the fault geometry due to limited resolution at depth. For instance, ambiguity between the two possible conjugate planes cannot always be resolved using InSAR, even for relatively shallow ruptures [e.g. *Pinel-Puysségur, **Grandin**, Bollinger et al.*, 2014]. In case of a sequence of earthquakes, it is reasonable to assume that the later events were triggered by the previous shocks by static stress transfer. With this assumption, the most likely fault geometry can be determined by analyzing Coulomb Stress changes on the second fault caused by slip on the first fault (Fig. 2.13).

Unfortunately, in the above 4-steps procedure, epistemic uncertainty is not always propagated correctly from the first to the last step, as discussed by *Duputel et al.* [2014] concerning uncertainty on Earth's elastic model, and by *Ragon et al.* [2018b] concerning uncertainty on fault geometry. More specifically, underestimating the uncertainty or the bias inherited from a particular choice of fault geometry may lead to serious misinterpretations, since any complexity in the data is first interpreted as a result of fault geometry (step 2), and, only in a subsequent

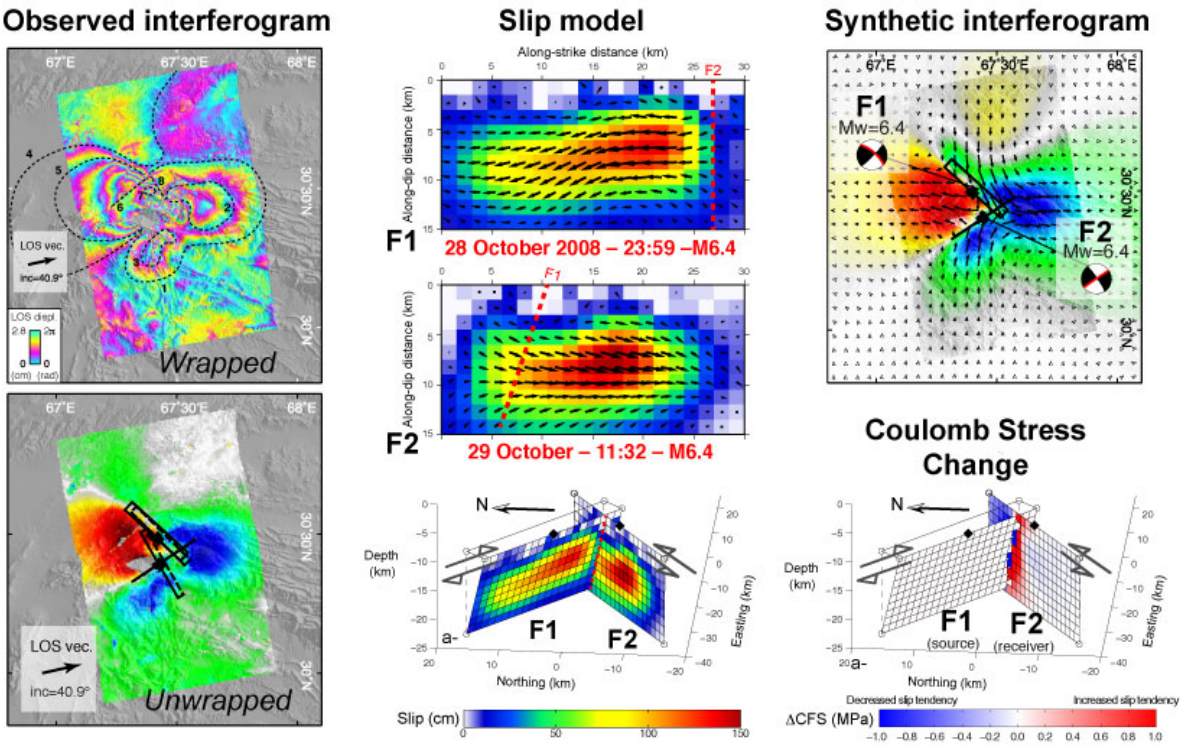

*Figure 2.13 – ALOS interferogram covering the 2008 Ziarat earthquake sequence [modified from Pinel-Puysségur, **Grandin**, Bollinger et al., 2014].*

step (step 4), as a result of slip distribution. In other words, if the "real" fault geometry is simple and if the "real" slip distribution is complex, then this approach may incorrectly attribute the cause of the data variability to the complexity of the fault geometry and deduce that the slip distribution is smooth. Unfortunately, this approach is difficult to avoid, as many recent intermediate and large magnitude continental earthquakes, such as the 1992 Landers, 1999 Hector Mine, 2013 Balotchistan, 2016 Kaikōura or 2016 Norcia earthquakes [*Xu et al.*, 2016] [*Vallage, Klinger,* ***Grandin*** *et al.*, 2015] [*Hamling et al.*, 2017] [*Delorme,* ***Grandin****, Klinger et al.*, 2019] are characterized by excessively complex rupture geometries, involving changes in dip and strike both along-dip and along-strike, as well as branching between several fault strands. An alternative procedure, which would allow for reversing the logic (possibly by iterating between fault geometry non-linear optimization and slip distribution linear inversion, as attempted in *Fukuda and Johnson* [2010] and *Tung and Masterlark* [2018a]), remains to be invented.

2.5 Summary: the blindspots of static slip inversion using InSAR

- **Forward problem** In most situations, faults are assumed to be embedded in a linear elastic homogeneous isotropic halfspace. Departure from this idealized situation may bias the final slip model, both in terms of fault geometry, slip distribution and slip magnitude. Vertical stratification of elastic properties play a role when considering shallow-dipping dip-slip faults, whereas lateral variations of rigidity may be subject to a trade-off against fault dip for nearly vertical strike-slip faults. Topographic effects may also influence deformation in the immediate surrounding of surface ruptures when they occur in steeply sloping areas.

- **InSAR data decimation** The objective of InSAR data decimation is to redistribute the weights within the dataset in order to decrease the number of data points, while retaining the same information content. Several issues may appear: (1) difficulty to balance the relative weight of far-field *versus* near-field data, leading to over- or under-fitting, and heterogeneous resolution on the fault plane, (2) information loss in the near-field due to complexity of deformation within the fault zone, which can reach several hundred meters.

- **Data weighting** The sensitivity of each data set is difficult to quantify. This difficulty can be concealed by the use of covariance matrixes, which, at the end of the day, act as weighting operators within each dataset as well as between the datasets. However, filling the covariance matrixes requires some pre-processing, and is therefore not free of bias (selection of a region with no deformation, estimation of noise through variogram calculation and fitting by an empirical model).

- **Fault discretization** The fault geometry that is known to the inversion is full condensed into to model vector ($\mathbf{m}$). However, the true fault is often complex, with multiple branches, a wavy trace and roughness up to some undetermined scale. This complexity is well captured by the data at shallow depth, but its extension at depth is poorly constrained. Variable patch size is desirable, with smaller patches near the surface and close to complexities. However, adjusting the discretization of the fault involves some arbitrary choice.

Furthermore, the fault geometry (dip, depth, strike) has a non-linear effect on the data vector, so that it requires re-running the Greens function calculation and inversion.

- **Optimal fault geometry** The optimal fault geometry is usually explored assuming a small number of patches, hence a simplified slip distribution. In a second step, this geometry is fixed, an inversion is carried out on a large number of patches, but a reappraisal of the fault geometry optimization is usually not made, hence possibly introducing epistemic errors.

- **Smoothing** The maximum degree of roughness in a slip inversion is largely governed by the data resolution, but does not preclude the existence of roughness at smaller scale, below the resolution threshold. In any case, smoothness is often considered uniformly smooth in slip inversions. Evidence for a great variability of slip at the surface could suggest that if the same slip roughness prevailed at depth, then it would always be filtered out by the elastic crust, so that slip roughness retrieved by the inversion would underestimate the actual slip roughness. However, on-fault and off-fault physical and chemical conditions are highly variable with depth, so that slip could also be smoother at depth than in the shallow sub-surface.

- **Inversion procedure** The computational cost of Bayesian (MCMC-like) methods may hamper a full appraisal of the actual sensitivity of the inversion to the data itself, as well as all other modeling assumptions that are necessary for setting up the problem. On the other hand, linear inversion methods are incapable of ingesting non-trivial prior p.d.f.s, and can be caught in local mimima.

2.6 Outlook

A simple conclusion can be drawn from the discussion developed in this chapter. The main advantage of the algebraic approach is to provide a fast and comprehensive solution to inverse problems. However, its application becomes increasingly complex in situations of non-linearity and heterogeneity of datasets. Furthermore, it requires making strong assumptions about prior information (in particular prior uncertainty on data and model are Gaussian). Finally, it does not provide a convenient method to explore the range of posterior models that reasonably fit the data (beyond the "best" model). On the other hand, the Bayesian approach provides a more flexible framework, capable of accounting for uncertainty on the data, the model and our physical laws. Its main disadvantage is its computational cost. In the future, a range of strategies to accelerate the calculation of the inverse problem may be explored, exploiting different directions:

- use of Graphics Processing Unit (GPU) to accelerate data-parallel computations whose burden is dominated by arithmetic operations [*Jolivet et al.*, 2014; *Masuti et al.*, 2014]

- extension of linear inversion techniques to truncated multivariate Gaussian priors, in order to allow for fast inversions using non-negativity or bounded constraints [*Nocquet*, 2018]

- coupling of computationally-efficient eXtended Finite-element Methods (XFEM), which are specifically adapted to crack problems [*Bodart et al.*, 2016], with adapted optimization strategies.

Chapter 3

Implications for seismic hazard: case studies

The aim of this chapter is to illustrate how space geodetic measurements of earthquake deformation contribute to a better understanding of the difficult concepts that prevail in the field of seismic hazard assessment. Instead of conducting a general discussion of this extremely broad topic, the choice has been made to highlight a limited number of recent earthquakes that have been captured by space geodesy. Starting from the measurements, the slip distributions derived from inverse modeling will analyzed. These results will be progressively put in perspective, taking into account the specific geodynamic context surrounding each of these case studies. The objective is to show that each earthquake allows for illuminating a specific limit in the current debate about models of earthquake occurrence.

3.1 The 2015 M7.9 Gorkha earthquake, Nepal

Not (yet) the big one?

3.1.1 A long expected continental megathrust earthquake

It has long been recognized that the mountain belt separating India and Eurasia is subject to shortening, with velocity boundary conditions of $\sim$ 40 mm/yr in the North-South direction, as part of a collision that started around 50 Ma [*Molnar and Tapponnier*, 1975; *Besse et al.*, 1984; *DeMets et al.*, 1990; *Bilham et al.*, 1997]. Approximately half of this shortening is accommodated by a complex network of crustal faults in the interior and on the edges of the Tibetan plateau, while the remaining $\sim$ 20 mm/yr appears to be accommodated directly across the Himalayan range[*Tapponnier et al.*, 1982; *Armijo et al.*, 1986; *Avouac and Tapponnier*, 1993; *Calais et al.*, 2006a; *Wright et al.*, 2004b].

The Himalayan megathrust being a unique geological object, it has been the subject of so much attention by so many geoscientists that it is impossible to summarize the state of our knowledge on this system without having to focus on a series of key facts and concepts[24]. The Himalayan range is supported by the largest continental thrust on Earth, the Main Himalayan Thrust (MHT). Geodesy (first ground-based, then space-based) has demonstrated that full locking of the plate interface across the MHT is currently taking place over a strike-perpendicular width of $\sim$ 100 km, from the trace of the Main Frontal thrust (MFT), up to approximately the location of the high peaks of the Himalaya (>7000 m a.s.l.), where a narrow band of microseismicity marks the transition zone between deep stable-sliding and shallow stick-slip [*Bilham et al.*, 1997; *Lavé and Avouac*, 2001; *Bollinger et al.*, 2004; ***Grandin** et al.*, 2012a; *Stevens and Avouac*, 2015]. Tectonic strain cannot be accumulated indefinitely, and has to be released by some kind of "rapid" slip on the MHT. Hints of past earthquake ruptures have been found by analyzing historical information, as well as digging trenches at the MFT, and the result of these tremendous efforts are quite worrying (Fig. 3.1). It appears that giant earthquakes, with magnitudes greater than M8.5, and perhaps as large as M9.0, have occurred in medieval times. These magnitudes are essentially constrained by the inferred coseismic slip at the surface, which can be as large as 20 meters or more, as measured in trenches dug at the front of the MFT [*Lavé et al.*, 2005; *Kumar et al.*, 2006; *Sapkota et al.*, 2013; *Bollinger et al.*, 2014; *Roux-Mallouf et al.*, 2016; *Wesnousky et al.*, 2017]. These giant events appear to be required to ensure a closure of the seismic moment budget, given the significant rate of present-day accumulation of strain (measured by GPS) and the long quiescence interval that separates these events [*Stevens and Avouac*, 2016].

The 25 April 2015 M7.9 Gorkha earthquake struck the heart of the Himalaya, affecting what is probably the most studied portion of the megathrust. It took the life of nearly 9,900 people, injuring many more and provoking significant damage to infrastructures, both due to primary shaking, as well as induced landslides. This earthquake was not a surprise for those familiar with

[24] The current state of knowledge on seismic hazard associated with the megathrust is presented in detailed in a number of recent reviews [e.g. *Avouac*, 2015; *Bilham*, 2019].

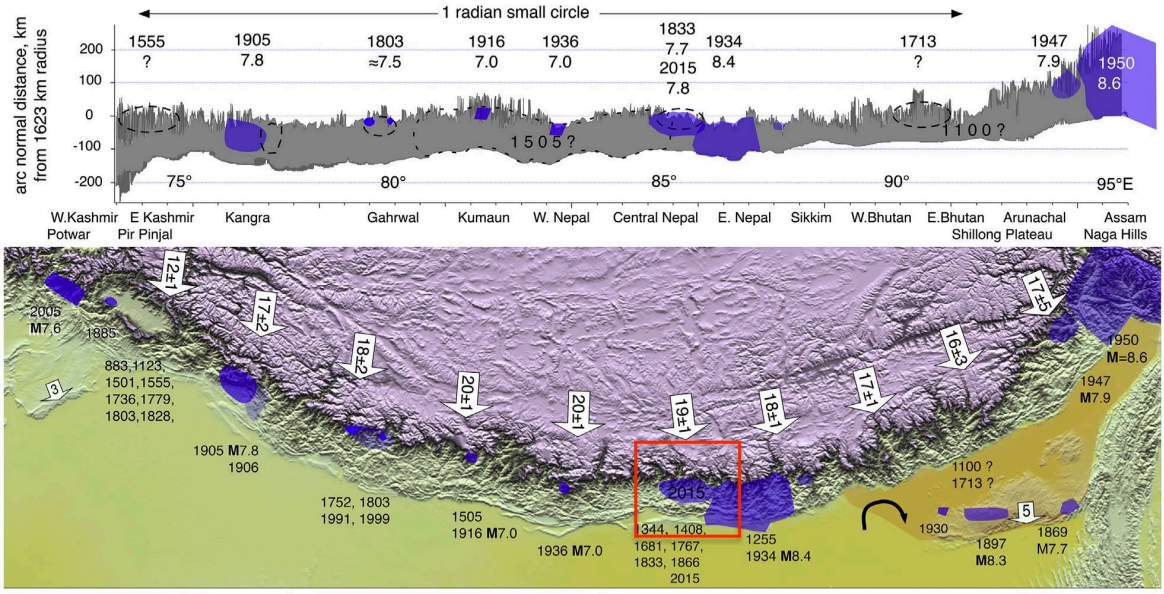

(a) Location of inferred historical earthquakes along the Himalayan arc. Adapted from [Bilham et al. 2017].

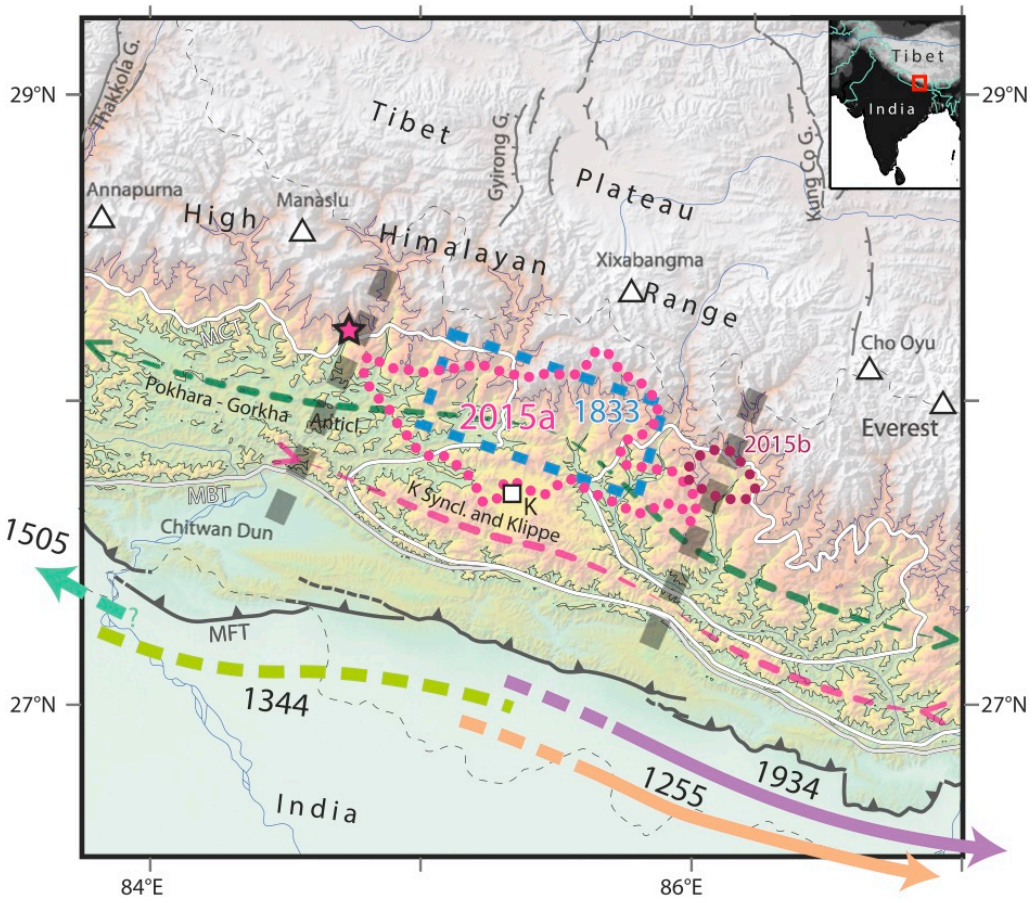

*(b) Along-strike distribution of historical earthquakes central Nepal. Location of the 2015 Gorkha earthquake is indicated by the pink contour. Adapted from [**Grandin** et al. 2015].*

Figure 3.1 – Historical seismicity along the Himalayan belt.

seismic hazard in the Himalaya. However, according to *Wyss* [2017], the predicted death toll for an earthquake of magnitude M∼8 in Kathmandu was between 21,000 and 42,000, well above the actual number of fatalities. Similarly, the total loss of fatalities resulting from a repetition of the 1934 Bilhar-Nepal earthquake if it has occurred in 2011 has been estimated to reach a number of 83,000 [*Sapkota et al.*, 2016]. Hence, the consequences of the 2015 earthquake were not as catastrophic as initially anticipated, which may suggest that our prior understanding of earthquake hazard in Nepal may need to be revised. The features of this earthquake, which were described in detail thanks to an unprecedented amount of seismological and geodetic data [e.g. *Galetzka et al.*, 2015; ***Grandin** et al.*, 2015], may provide an explanation of this apparent discrepancy.

Thanks to Sentinel-1 and ALOS-2 InSAR, it has been possible to precisely map the coseismic slip distribution of the Gorkha earthquake on the plate interface (Fig. 3.2). The results show that slip was restricted to a ∼ 120 km-long, 50 km-wide portion of the MHT. There still remains a substantial disagreement about the actual slip distribution in the down-dip part of the rupture. Some authors argue that the geodetic data require the presence of a steeper ramp near the down-dip edge of the rupture, where slip would have tapered while slightly propagating down-dip of the kink that separates the flat (up-dip) and the ramp (down-dip) [*Elliott et al.*, 2016]. On the other hand, others, using the same data, propose that geodetic data can be better explained if the contribution of a shallow steeply-dipping out-of-sequence thrust is included, in addition to the flat where most of the moment was released [*Whipple et al.*, 2016]. However, a complex slip distribution on a perfectly planar fault seems to yield a similar fit to the data [***Grandin** et al.*, 2015; *Tung and Masterlark*, 2016]. Detailed analysis of aftershock seismicity suggests that the 12 May 2015 M7.3 Kodari aftershock (in brown in Fig. 3.1b) occurred at greater depth than other earthquakes occurring at the same distance from the MFT near the main slip patch of the Gorkha earthquake, indicating that along-strike changes in the geomety of the MHT may be significant, which further complicates the analysis and may partly explain the apparent disagreement between these previous studies [*Baillard et al.*, 2017]. This controversy illustrates the difficulty to pinpoint the actual geometry, kinematics and coordinates of buried active faults from observations acquired at the surface (geodesy, seismology), at least when these faults do not reach the surface. A similar ambiguity on the detailed geometry of a shallow-dipping fault plane prevails for the slow-slip events occurring on the Guererro gap of the Mexico subduction [*Radiguet et al.*, 2012].

Nevertheless, in spite of the significant coseismic slip (peaking at ∼ 7 meters), geodetic data clearly show that the earthquake failed to rupture the 50 km most frontal part of the MHT, and did not propagate laterally beyond the longitudinal interval spanned by the Kathmandu klippe. The southern termination of the earthquake may be due to the existence of structural barriers, in the form of a transition from a flat to a ramp, that could not be overcome by the rupture front [*Hubbard et al.*, 2016]. Similarly, contours of the 2015 Gorkha earthquake slip distribution shows that the event matches with a re-entrant of the main structural features affecting the upper plate (Fig. 3.1b). This coincidence has been proposed to stem from the presence of significant along-strike structural changes within the upper plate associated with variations of the MHT geometry [*Hubbard et al.*, 2016; *Baillard et al.*, 2017] and/or lateral variations in sediment thickness covering the downgoing Indian plate [*Fan and Shearer*, 2015; *Denolle et al.*, 2015], that would have limited rupture propagation (grey dashed lines in Fig. 3.1b,a). Large earthquakes (M>8) that occurred in the past ∼500 years also appear to have been limited along-strike around the same longitude [*Bilham and Ambraseys*, 2005; *Wesnousky et al.*, 2017],

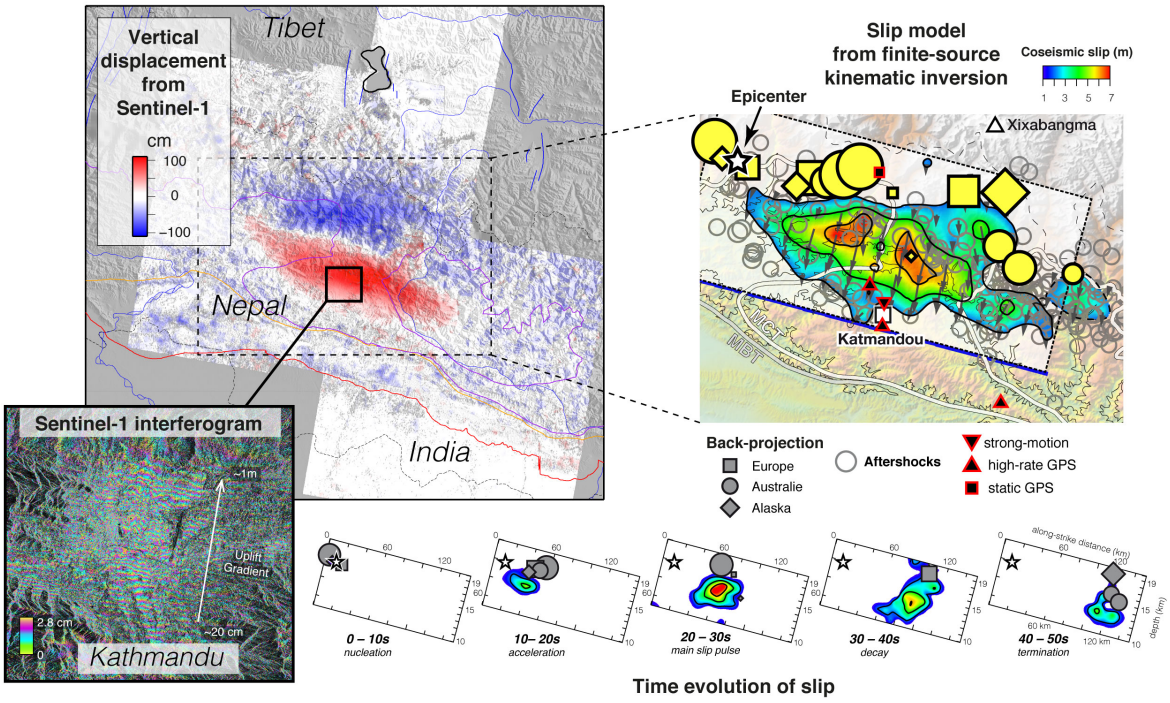

Figure 3.2 – Rupture process of the Gorkha earthquake from InSAR, GPS and seismological data [adapted from ***Grandin*** *et al., 2015]. Upper left panel shows the vertical displacement field induced by the earthquake (red: uplift; blue: subsidence). Upper right panel shows the slip distribution of the earthquake. Yellow symbols indicate points of high-frequency radiation deduced from back-projection at teleseismic distance. Lower panel shows the rupture propagation of the earthquake.*

suggesting that the structural anomaly may mark its imprint onto the seismic segmentation of the megathrust. Unfortunately, structural anomalies are ubiquitous along the whole Himalayan arc, so that the actual difficulty lies in the hierarchization of these complexities, and the eventual identification of first-order discontinuities that could maintain their influence over many seismic cycles.

Seismological data acquired at teleseismic distance indicates that the rupture occurred somehow "smoothly" from West to East, i.e. exhibiting little acceleration or deceleration during the rupture (besides the starting and stopping phase toward rupture ends). Coherent high-frequency radiation was detected down-dip of the rupture, along the transition zone, but the core of the rupture seems to have primarily radiated low frequencies. These spectral and directivity features, combined with the site effects of the Kathmandu basin that acted as a low-pass filter, likely explain the limited number of casualties by collapse of small-size buildings, in spite of the relatively large magnitude and unfavorable location of the earthquake. Another factor that played in favor of a limited death toll was the date of occurrence: the earthquake struck on a Saturday, around noon, when people were outside of the houses.

3.1.2 So? Expected, or unexpected?

The 2015 Gorkha earthquake illustrates perfectly a major shortcoming of the attempts to quantitatively characterize seismic hazard in this region. To put it in simple words, the problem can be summarized as follows. We know that (1) the area is accumulating strain, (2) huge earthquakes M>8.5 occurred in the past, rupturing long portions of the megathrust, up to the surface and (3) intermediate-size earthquakes (7<M<8.5) occur infrequently, but rupture only part of the megathrust, sometimes failing to reach the surface, such as the 1833 or 2015 earthquakes in the Kathmandu area [*Bollinger et al.*, 2016]. What we do not know is (1) what will be the size of the next event, and, of course, (2) when it will occur. We can say that the upper limit for the magnitude of a large earthquake is quite high (perhaps as large as M=9), and that so much slip deficit has accumulated since the previous great earthquakes that the "the big one is overdue"[25] [e.g. *Wesnousky et al.*, 2017; *Bilham et al.*, 2017].

Unfortunately, this information is not very useful for a country such as Nepal, with limited resources and which faces many other challenges. On one hand, the relatively limited level

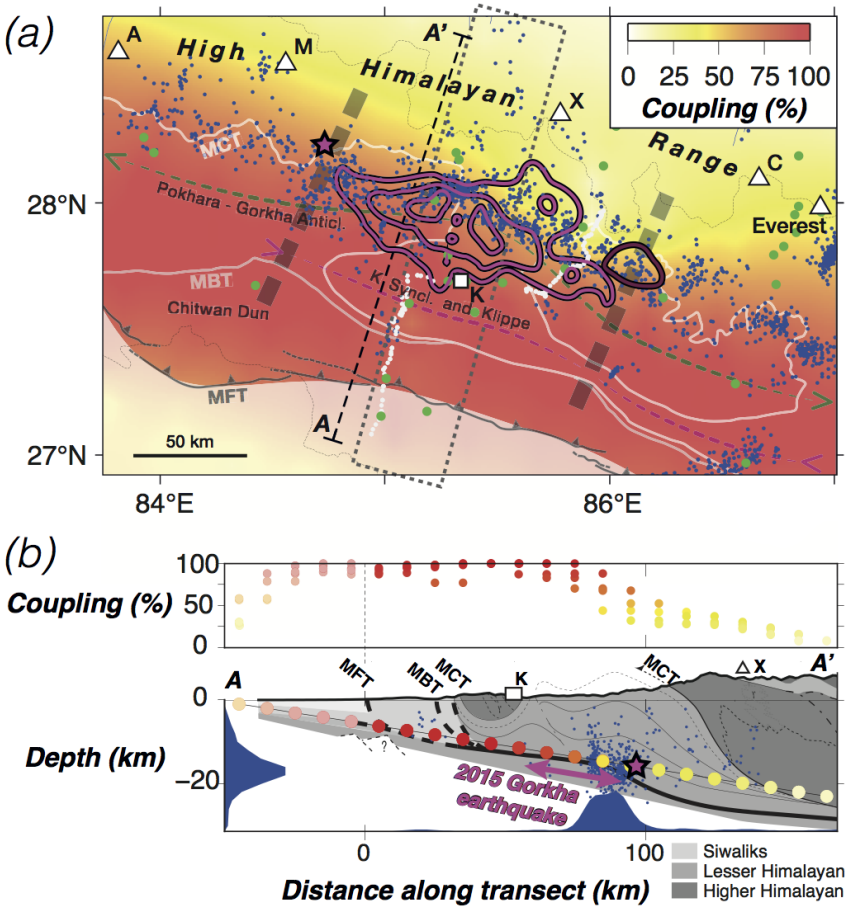

Figure 3.3 – Interseismic coupling on the MHT and slip distribution of the 25 April 2015 M7.9 Gorkha earthquake (purple) and its 12 May 2015 M7.3 aftershock (brown) [adapted from ***Grandin*** *et al., 2015].*

[25] The same somehow misleading statement applies to the San Andreas fault, as explained by Susan Hough in her book "*Predicting the unpredictable*" [*Hough*, 2016].

of damage sustained by the capital city of Kathmandu (for the reasons given earlier) could be considered as a relief. The downside, however, is that this experience may give a false impression of safeness. Such an underestimation of the hazard related to future events may not be limited to the layman, but could also percolate into seismic hazard assessments. Indeed, one can argue that the 2015 Gorkha earthquake may actually represent an outlier, in that it *would* have led to many more disastrous effects on local populations (1) if the earthquake had occurred during the night (although the correlation between time-of-day and fatality rate is sometimes questioned [e.g. *Allen et al.*, 2009]), (2) if the high-frequency radiation had been different (e.g. stronger high-frequency radiation, leading to stronger effects on unsafe small one- to two-stories dwellings), this parameters being strongly dependent on the depth of the event, an extreme case being a surface-rupturing earthquake, (3) if the directivity had been different (i.e. if radiation had been focused toward Kathmandu, instead of away from it), and, of course, (4) if the magnitude had been higher. In the above list, for past earthquakes, point (1) is usually known, point (3) is extremely difficult to assess for a pre-instrumental earthquake [e.g. ***Grandin** et al.*, 2007a], point (2) is impossible to constrain, and point (4) is precisely the main unknown which one is left to estimate based on macroseismic reports [e.g. *Martin et al.*, 2015].

Because we have been able to depict the very particular characteristics of the 2015 Gorkha earthquake, we can reconsider this event as an illustration of the difficulty to constrain the magnitude of past blind earthquakes based entirely on macroseismic observations [e.g. *Johnston*, 1996]. Indeed, the inherent variability in spectral, spatial and temporal properties of earthquake ruptures leads to a high uncertainty in ground motion prediction, irrespective of other knowable

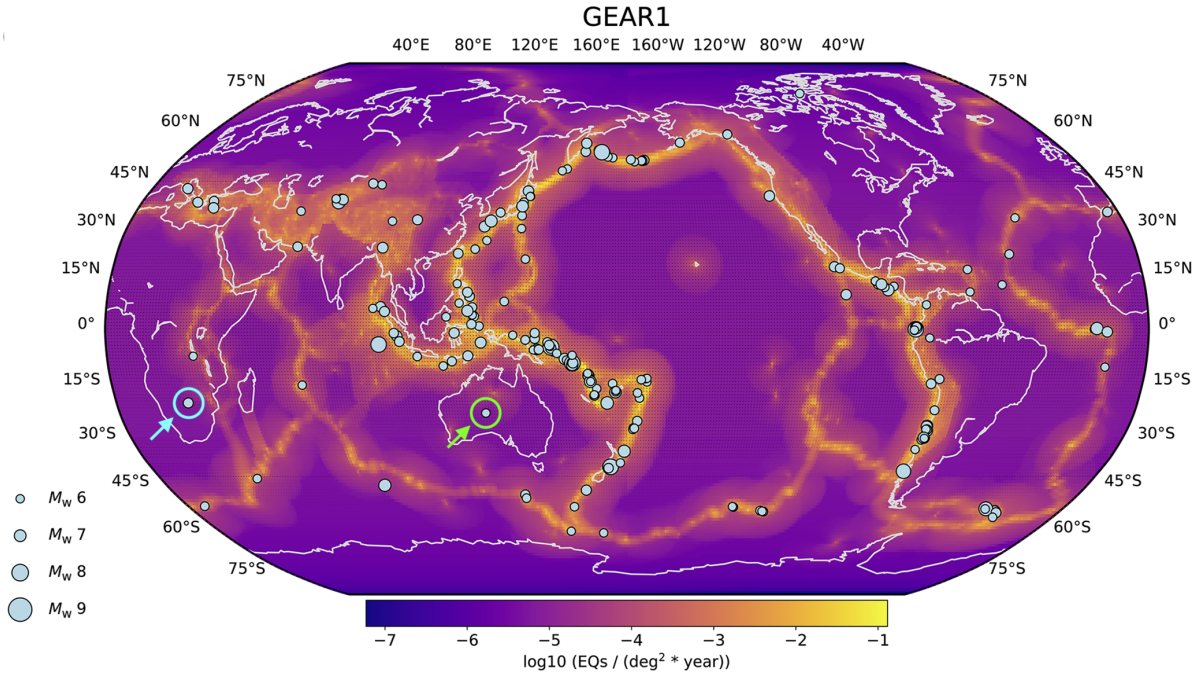

Figure 3.4 – Forecast map of M_w>5.95 earthquake rates by the GEAR1 model [Bird et al., 2015] for the period 1 October 2015 – 7 September 2017. A retrospective recount of actual earthquakes occurring in the prospective period is overlaid as blue circles [modified from Strader et al., 2018]. The 2017 Botswana and 2016 Petermann Range earthquakes are circled in cyan and green, respectively.

parameters commonly introduced in the analysis, such as seismic wave attenuation, site effects, construction vulnerability or time of day. The difficult task of disentangling this variability entirely provides a justification for the approach adopted by the SHAKEMAP project, which aims at systematically reassessing the macroseismic effects of recent instrumental earthquakes, for which all these contributions can be deconvolved *Allen et al.* [2009]. For past historical earthquakes, favorable site effects prevailing in Katmandu, combined with the sampling bias introduced by the fact that the overwhelming majority of information comes from the capital city of Kathmandu, whereas coverage from the rest of the country is sparser, further complicates the analysis.

By a symmetrical effect, a similar difficulty arises when attempting to determine the magnitude of large historical earthquakes in areas devoid of intermediate-size instrumental earthquakes. A perfect illustration of this difficulty is the Levant fault, where no M>5.2 instrumental earthquake has been recorded, the largest earthquake in the area being the M7.3 1995 Gulf of Aqaba earthquake and its largest aftershock (with M5.6) [*Klinger et al.*, 1999; *Ataeva et al.*, 2015], which occurred offshore and to the south of the Levant fault. On the other hand, historical [*Ambraseys*, 2009] and paleoseismological [*Lefevre et al.*, 2018] inference suggest the occurrence of large earthquakes in the past millenium. A crucial unknown is the magnitude that should be ascribed to an inferred rupture that took place in the 8th century AD. The rupture length seems to be well constrained, reaching $\sim$ 200 km. However, two problems need to be solved to estimate the magnitude of the earthquake(s) responsible for this rupture:

- Did this rupture occur in a single M$\sim$8 earthquake, or in a sequence of several (2 or 3?) M$\sim$7 events [*Ambraseys*, 2009; *Lefevre et al.*, 2018]?
- How do we use the locking depth deduced from present-day GPS measurements [*Le Beon et al.*, 2008] and/or scaling relationships [*Wells and Coppersmith*, 1994] to convert this 200 km (or 100 km or 66 km) length into a moment magnitude, hence, into a coseismic slip?
- Based on assumptions on the segmentation of the fault zone, how do we check whether past earthquakes have always "respected" this segmentation of the fault zone, i.e. have only ruptured individual segments in full, and never partially?

Because large event such as the 8th century AD earthquake(s) are rare, these assumptions have a strong influence on the maximum magnitude in the composite instrumental / historical / paleoseismological earthquake catalogue, hence on the inferred seismic hazard in the area [*Marti*, 2018]. The situation only gets worse in intraplate contexts, where instrumental seismicity is close to zero, where paleoseismological constraints are fragmentary, where historical information are thin, and, what is more, where our understanding of the mechanism responsible for these earthquakes is at best rudimentary [e.g. *Calais et al.*, 2016] (see Section 3.4).

In a recent controversy, *Stein et al.* [2012] and *Frankel* [2013] have argued about the false sense of confidence conveyed by seismic hazard maps [see also *Lacassin and Lavelle*, 2016, for a more fundamental questioning of the PSHA rationale *versus* identification of worst-case scenarios]. *Stein et al.* [2012] correctly point that recent earthquakes, leading to a high death toll, such as the M9.2 2004 Sumatra, the M8.1 2008 Wenchuan, the M7.3 2010 Haiti and the M9.0 2011 Tohoku earthquakes, have forced to revisit the basic assumptions used to build hazard maps, meaning that these earthquakes were off the spectrum of anticipated earthquakes based on pre-event hazard maps. The 2015 Gorkha earthquake, as a "negative outlier" – in the sense

that it led to less casualties that initially expected, although predictions of the death toll of a future earthquake in such a context of rapidly growing urban population should be regarded with caution [e.g. *Bilham and Hough*, 2006; *Sapkota et al.*, 2016] – should complement this list.

Incorporating geodetic strain rates into hazard models that usually rely primarily on seismic catalogues, is a first step to address seismic hazard in Nepal and elsewhere [e.g. *Bird et al.*, 2015; *Strader et al.*, 2018; *Wang et al.*, 2019a] (Fig. 3.4). However, as pointed by *Stein and Stirling* [2015], such maps are still prone to significant uncertainty caused by observational blind spots, including:

- the maximum magnitude of earthquakes when extrapolating the frequency-magnitude law determined from a catalogue containing only low magnitude events;
- the impact of assumptions in the distinction between mainshocks and aftershocks, which is a pre-requisite to build a declustered catalogue;
- the difficulty to estimate meaningful seismicity and deformation rates in plate interiors.

Although some researchers are willing to throw out the baby with the bathwater [e.g. *Kossobokov and Nekrasova*, 2012; *Mulargia et al.*, 2017], a critical re-appraisal of a previous forecast that performed poorly is, arguably, a sign of good health for such a young science as probabilistic seismic hazard assessment (PSHA). Recent fails, such as the 2017 M_w6.5 Moiyabana earthquake (Botswana) [*Kolawole et al.*, 2017] or the 2016 M_w6.0 Petermann Range earthquake (Australia) [*Wang et al.*, 2019b] (highlighted in Fig. 3.4) – fortunately in areas of low population density (Fig. 1) – illustrate the difficulty of forecasting moderate-sized earthquakes in continental interiors. These two events correspond to the reactivation of ancient faults affecting the basement (respectively of Paleoproterozoic and Proterozoic ages). These unexpected events will remain difficult to anticipate, because they fall in low probability regions, but have a relatively moderate magnitude, hence a relatively "short" recurrence interval. Hence, in a region of low seismicity, recognizing the signs of a recent earthquake rupture in the paleoseismic record may be crucial – possibly more helpful than building general-purpose seismic hazard maps, even if based on seismological and geodetic data – to provide safe recommendation for the construction of sensitive infrastructure, such as nuclear plants.

3.2 The 2013 M7.8 Balochistan earthquake, Pakistan

An outlier in scaling relationships?

3.2.1 Seismotectonic context and data analysis

Contrary to the 2015 Gorkha (Nepal) earthquake (Section 3.1), the 24 September 2013 M7.8 earthquake was a rather unexpected event. This large earthquake occurred close to, but not exactly on the plate boundary between the Indian plate and the Eurasian plate. More precisely, the earthquake nucleated at the southern tip of the Chaman fault, one of the main strike-slip faults that accommodate the ~ 15 mm/yr sinistral strain between Eurasia and India, along the eastern border of the Makran accretionary wedge [*Szeliga et al.*, 2012; *Byrne et al.*, 1992] (Fig. 3.5).

Surprisingly, the 2013 earthquake did not propagate toward the North, where the M7.7 1935 Quetta earthquake occurred 150 km away along the Ghazaband fault. Neither did the earthquake jump on the Ornach-Nal fault, further South, to connect with the triple junction between the India, Eurasia and Arabia plates. Instead, the earthquake broke a fault strand, previously known as the Hoshab fault, belonging to the Makran ranges [*Lawrence et al.*, 1981]. The Hoshab fault has a markedly curved surface trace, and the 2013 earthquake seems to have followed for ~ 200 km this curved structure from its northernmost tip (where it merges into the Chaman–Ghazaband–Ornach-Nal en échelon system), down to a section where the Hoshab fault makes a >45° angle with the strike of the Chaman transform fault. In the area where slip seems to have stopped, the Hoshab fault delineates the contact between a flat alluvial plain to the south and a mountain range where Paleogene to early Miocene sedimentary series, perched ~ 1000 m above the plain, are heavily eroded (the Kech band) [*Ellouz-Zimmermann et al.*, 2007]. The whole area stands above a décollement buried at ~ 12 km depth that connects with the active Makran front, offshore to the South, where the great M8.1 1945 earthquake is believed to have taken place. Therefore, although large earthquakes were anticipated in the area [e.g. *Bilham and Hough*, 2006], the fault activated in 2013 was not the obvious candidate for the next earthquake: too much in the interior of the accretionary prism to be still active, too far the West and too oblique to belong to the Chaman transform system.

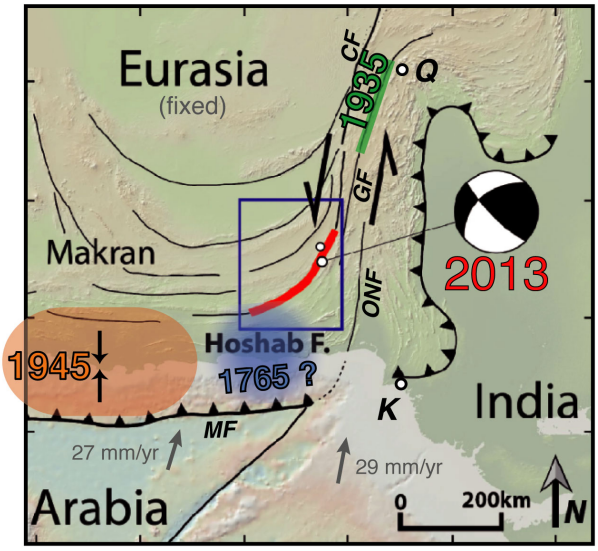

Figure 3.5 – Location and size of M8.1 1945 and M7.5(?) 1765 earthquakes are from Byrne et al. [1992]. For the 1945 earthquake, intensity 5 isoseismals are used as a proxy of the rupture area. Location of the M7.7 1935 Quetta earthquake is from Fattahi et al. [2015], after Engdahl [2002]. K: Karachi (population: 15–20 million) Q: Quetta (population: 1 million). CF: Chaman fault. GF: Ghazaband fault. ONF: Ornach-Nal fault. MF: Makran front.

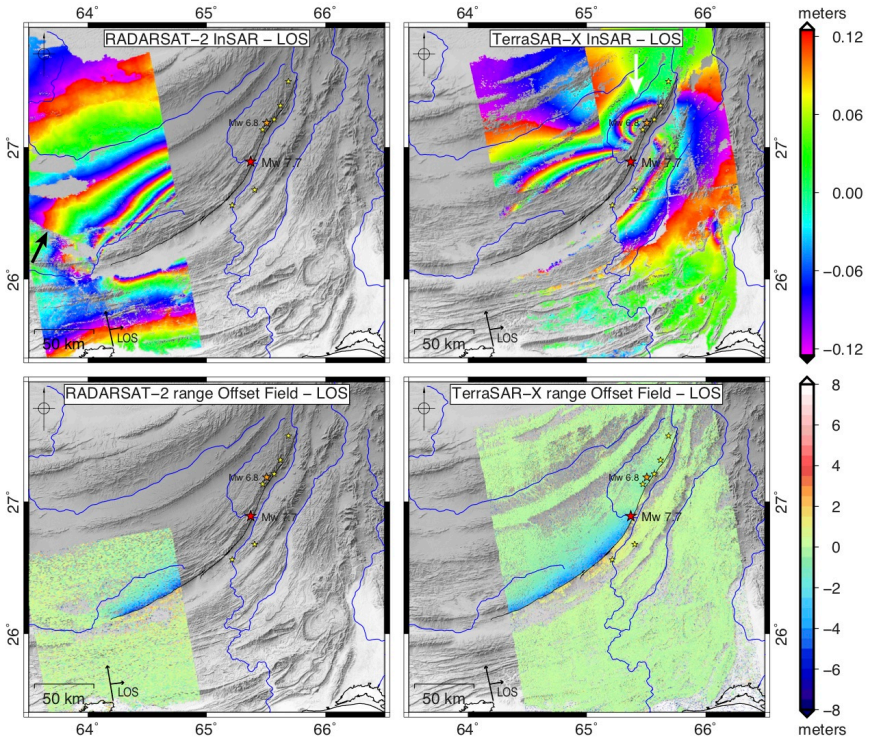

Figure 3.6 – SAR image coverage of the Balochistan earthquake by RADARSAT-2 (left) and TerraSAR-X (right), processed using InSAR (top) and range correlation (bottom).

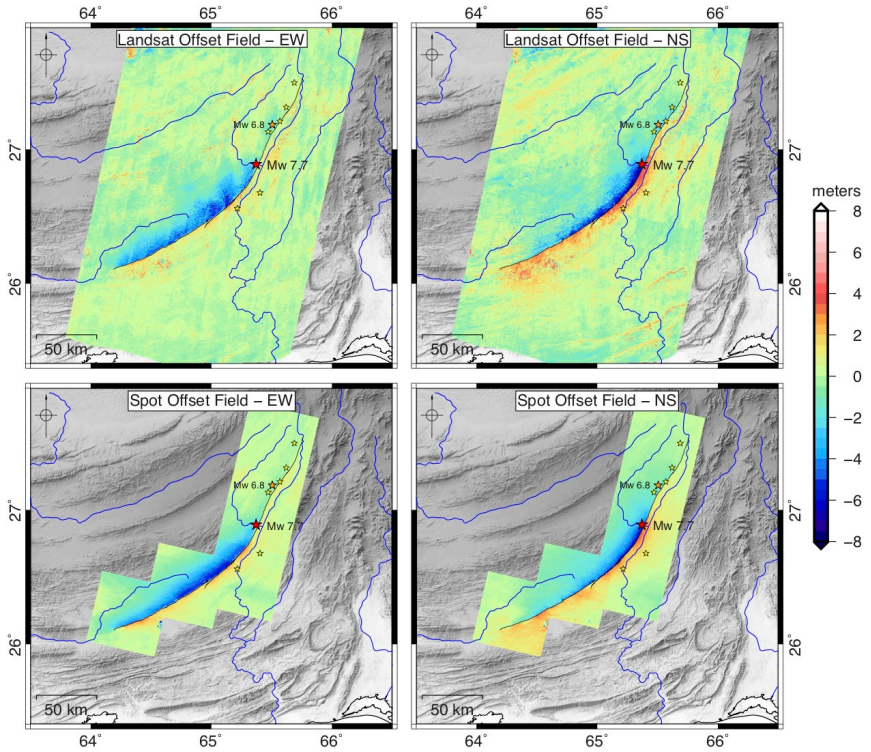

Figure 3.7 – Optical image coverage of the Balochistan earthquake from Landsat (top) and SPOT (bottom) processed using sub-pixel correlation.

The part of the world that was hit by the 24 September 2013 M7.8 earthquake is remote, both for climatic and political reasons. This has three consequences. First, little is known about the past behavior of the Hoshab fault, as geological and paleoseismological constraints are difficult to acquire without the possibility to physically access to the fault. Second, the number of casualties caused by the large earthquake was likely limited[26] for an earthquake of this magnitude, and in any case was not associated with a broad press coverage. Hence, this earthquake raised little interest in the general public. The third consequence is the lack of near-field geodetic or seismological observations, due to difficult access to the area. Fortunately, the area being essentially desertic, space geodesy is a convenient tool to study the earthquake. However, this event occurred during an unfavorable period for InSAR. Indeed, the ENVISAT and ALOS-1 satellites had been decommissioned the previous year, and the Sentinel-1 and ALOS-2 satellites were not to be launched until the next year. The coverage by Radarsat-2 was limited to the southern tip of the earthquake, while TerraSAR-X Stripmap data only covered a narrow ($\sim$ 30 km-wide) band of terrain crossing the rupture. The only choice left to study this earthquake with InSAR was TerraSAR-X data acquired in ScanSAR mode in the years prior to the event. A request was therefore sent to DLR to acquire a new acquisition that would be synchronized with the previous one. After several iterations with DLR, the coverage was finally complete in December 2013.

Development of a specific method to handle ScanSAR data was then carried out [***Grandin***, 2014], which eventually resulted in a complete InSAR coverage of the event. In addition to ScanSAR InSAR, range offsets were computed from sub-pixel correlation of SLC images (Section 1.3), providing a complement to the InSAR measurement close to the fault, where the high fringe rate prevented any unwrapping (Fig. 3.6). On the other hand, in spite of the large magnitude of slip, the coarse azimuthal correlation of TerraSAR-X ScanSAR, combined with unfavorable orientation of the fault, precluded any meaningful measurement of azimuth offsets. Nevertheless, in parallel to the exploitation of radar imagery, high-resolution optical imagery was processed to retrieve a detailed map of horizontal displacements [*Vallage, Klinger,* ***Grandin*** *et al.*, 2015] (Fig. 3.7). The combined radar-optical dataset provides the first complete coverage of the three-dimensional surface displacement induced by the 2013 Balochistan earthquake (Fig. 1.25).

This exceptional geodetic coverage shows that slip during the 2013 earthquake was predominantly strike-slip over the full length of the rupture, peaking at $\sim$ 11 meters just 50 km to the south of the epicenter, and remaining over 6 meters throughout. Reverse slip starts to increase progressively toward the southern tip of the fault, reaching 4 meters near the termination of the fault, where obliquity with respect to the Chaman fault is maximum (Fig. 3.8). A static slip inversion of the earthquake (carried out by Benjamin Lauer during his PhD research project) reveals that slip is mostly concentrated near the surface (depth $<$ 5 km). Furthermore, the first northern half of the rupture seems to have been predominantly strike-slip, with an average of $\sim$ 10 m, until a geometric complexity was reached (c2 in Fig. 3.8). Further south, the strike-slip components decreases steadily, whereas a significant reverse component of $\sim$ 3 m becomes visible.

[26] A total of 825 fatalities was reported on 1 October 2013 in the Pakistanese press: https://web.archive.org/web/20131004042227/http://www.nation.com.pk/pakistan-news-newspaper-daily-english-online/national/01-Oct-2013/balochistan-quake-toll-jumps-to-825

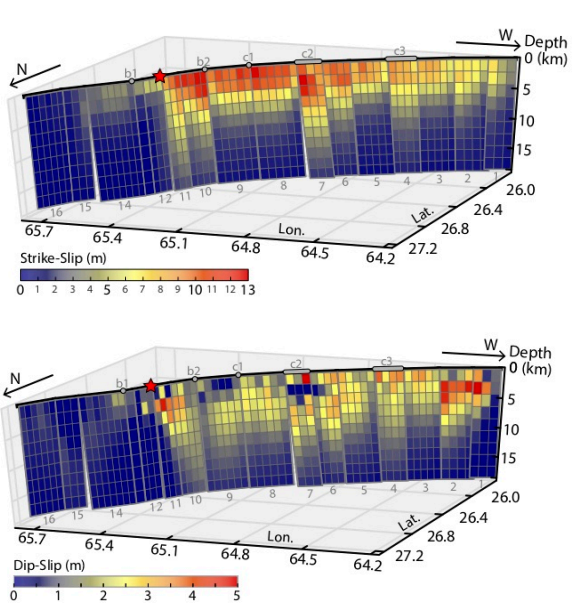

(a) From Lauer

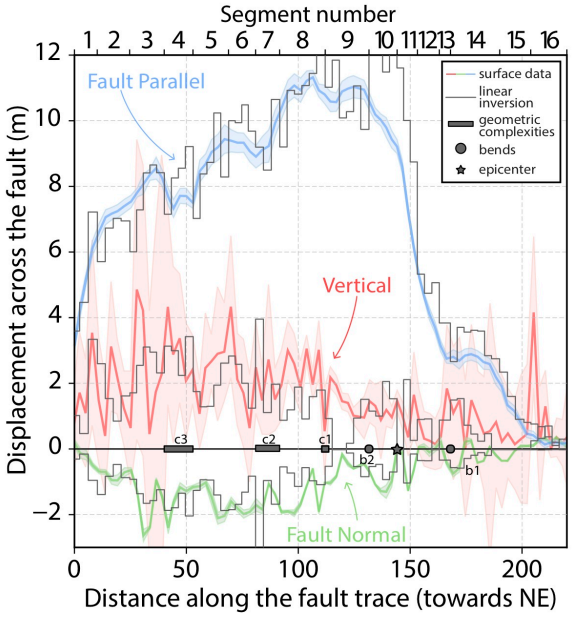

(b) From Lauer

*Figure 3.8 – Left: slip distribution at depth of the 2013 Balochistan earthquake from inversion of optical and radar imagery. Right: slip distribution at the surface deduced directly from the data (colored curves) and recovered by the slip inversion (grey histograms) [Lauer, **Grandin**, and Klinger, 2019].*

3.2.2 The "shallow slip deficit" controversy

All along the rupture, no evidence of the so-called "shallow slip deficit" [*Fialko et al.*, 2005] could be found (Fig. 3.8a). Instead, slip appears to have peaked at very shallow depth, perhaps even reaching its maximum at the surface. Such a lack of shallow slip deficit is often interpreted as a sign of "structural maturity" [*Dolan and Haravitch*, 2014]. The rationale behind this interpretation is that, as the fault slips over geological time scales, asperities on the fault plane, in the form of geometric complexities, would be smoothed over. This gradual evolution is consistent with the fact that fault trace geometries mapped in the field tend to become simpler as the fault advances toward maturity [*Stirling et al.*, 1996]. The same evolution toward a simpler fault plane geometry is inferred at depth from seismic profiles across normal fault systems [*Mansfield and Cartwright*, 1996], which is explained by a similar model of maturation by

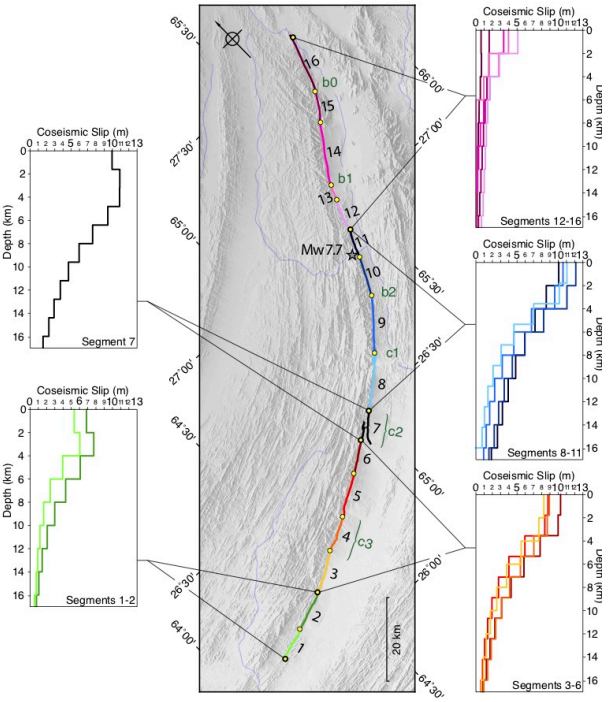

Figure 3.9 – TBW

progressive linkage of small youthful fractures into longer, more mature fault segments [*Peacock*, 2002]. As a result of this simplification of the fault geometry, coseismic slip on the fault plane should be more homogeneous for a mature fault, whereas immature faults should exhibit a more "patchy" slip distribution, introducing a discrepancy between slip at depth and slip at the surface. This view is considered by some authors as being supported by the comparison of the slip distribution at depth for of a (small) set of recent $M > 7$ earthquakes captured by space geodesy, *versus* their cumulative slip history [*Dolan and Haravitch*, 2014]. Others consider that the quantitative analysis of the morphology of fault scarps exposed at the surface in various tectonic contexts also supports the interpretation of link between fault maturity and shallow slip simplicity [*Brodsky et al.*, 2011].

Although this theory may be difficult to disprove, it has not yet grown to sufficiently high level of popularity to be considered as accepted. According to this theory, absence of shallow slip deficit during the 2013 earthquake would point to a structural maturity of the Hoshab fault. Unfortunately, information is still lacking about the potential maturity of the Hoshab fault to test this hypothesis. Nevertheless, although the relative amount of strike-slip *versus* reverse slip accumulated on the Hoshab fault is unknown, it may be noted that this fault belongs to the interior of an accretionary prism, hence may be dominated by a thrusting component. Should this possible maturity (?) on the reverse component (Mode III slip) explain the absence of shallow slip deficit on the strike-slip component (Mode II slip)? The question remains open.

Alternatively, lack of shallow slip deficit during the 2013 Balochistan earthquake, as opposed to previous earthquakes where such an observation was previously reported by some authors [*Fialko et al.*, 2005; *Fialko et al.*, 2010; *Dolan and Haravitch*, 2014] (M7.3 Landers, M7.1 Landers, M7.6 Izmit, M6.5 Bam and M7.2 El Mayor-Cucapah), may also be explained by the much larger magnitude of the earthquake, compared to cases of shallow slip deficit previously reported in the literature: intermediate to large earthquakes (M6.5-7.5) would be prone to shallow slip deficit (presumably due to off-fault plasticity that would absorb a fraction of the strain released dynamically during the earthquake) [*Kaneko and Fialko*, 2011]), whereas huge earthquakes (M∼8.0) would shatter everything up to the surface.

Recently, on methodological grounds, several studies have argued that the significance of previous claims of shallow slip deficits should be downplayed. First, *Xu et al.* [2016] have demonstrated that image correlation data covering the highly-strained region around a surface-rupturing fault provides evidence for limited shallow slip deficit. Including these data in a static slip inversion, along with InSAR, makes shallow slip deficit drop from 15–60% down to 3–19% only. The reason for this difference probably lies in the lack of resolution at shallow depth when only InSAR is taken into account, because of the clipping of InSAR where strain gets too high [e.g. ***Grandin** et al.*, 2009]. A second objection comes from the necessity to correctly account for local topography of the Earth surface when using near-field data in the inversions, which is seldom done [*Thompson and Meade*, 2018]. Failing to account for these topographic effects may lead to overestimating shallow slip

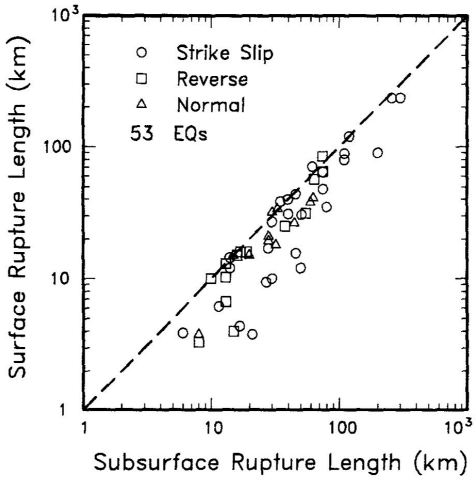

Figure 3.10 – Surface rupture length versus sub-surface rupture length. Strike-slip earthquakes are indicated by white circles.[Wells and Coppersmith, 1994]

deficit. In the same line, the presence of a compliant fault zone [as revealed directly by InSAR in the vicinity of coseismic ruptures, e.g. *Wright et al.*, 2001a], characterized by a decreased shear modulus, can also result in an underestimation of shallow slip (by as much as 20%) if a homogeneous medium is assumed during the forward model calculation [*Barbot et al.*, 2008].

The lack of any surface rupture in the famous M7.1 2010 Haiti earthquake, in spite of a peak slip reaching $\sim$ 5 meters at depth [*Saint Fleur, Feuillet, **Grandin** et al.*, 2015], clearly illustrates that slip does not systematically reach the surface. However, the question of the significance of a lack of shallow slip for surface-rupturing earthquakes remains controversial. Although it is difficult to conclude with certainty on this subject, a first-order picture seems to emerge, whereby most of the slip occurs close to the surface for strike-slip earthquakes with M>7.5–8.0, whereas smaller earthquakes are more problematic in that they can exhibit substantial slip deficit at shallow depth. The 2018 Palu earthquake provides another example of a large magnitude (M7.5) strike-slip rupture lacking shallow slip deficit [*Socquet et al.*, 2019]. Furthermore, the fault involved in the Palu earthquake is characterized by a fast slip rate (35–40 mm/yr), and the 2018 rupture propagated with a supershear velocity (>4.3 km/s) [*Bao et al.*, 2019]. These features are compatible with the idea that powerful ruptures do not generally exhibit shallow slip deficits.

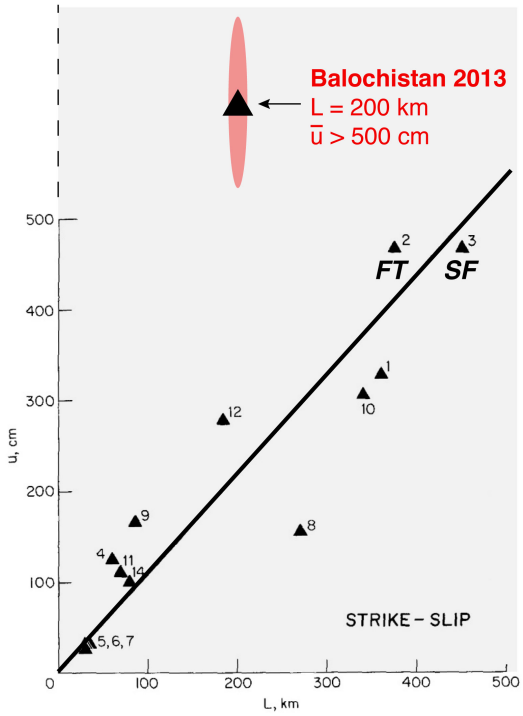

Figure 3.11 – Rupture length (L) versus mean slip ($\bar{u}$) for great strike-slip earthquakes [adapted from Scholz, 1982]. The 2013 Balochistan earthquake falls outside of the figure bounds, as indicated by the red arrows. In what follows, only the points of interest are listed. 1: Alaska 1958; 2: Fort Tejon 1857 (FT); 3: San Francisco 1906 (SF); 8: Guatemala 1976; 9: Gibbs Fault zone 1974; 10: Ercincan 1939 (Turkey); 11: Erbaa Niksar 1942 (Turkey); 12: Gerebe-Bolu 194 4(Turkey); 13: Gönen-Yenice 1953 (Turkey); 14: Mudurnu 1967 (Turkey).

Note that a similar conclusion can be drawn from the classical work of *Wells and Coppersmith* [1994], when the subsurface-to-surface rupture length is plotted (Fig. 3.10): although the correlation is unclear when all earthquakes are taken into account, the large strike-slip earthquakes with rupture length greater than 100 km seem to follow a 1:1 ratio (accordingly, this inference is based on a small number of points, and estimates of subsurface rupture length may be subject to uncertainty, especially for pre-instrumental earthquakes). Nevertheless, it suggests that above a certain magnitude, the surface rupture length provides a good indication of subsurface rupture length, which would be compatible with the lack of significance of shallow slip deficit for large strike-slip earthquakes.

If this rule-of-thumb holds approximately true, then its consequence are twofold. First, it means that the length of the surface rupture provides a reliable measurement of the total length of the underground rupture, which facilitates the assessment of rupture size of past earthquakes. Second, it means that slip at the surface provides a good proxy of slip at depth. Armed with these two assumptions, it should be only necessary to fix the maximum depth of coseismic slip to be

able to derive an estimation of the potency or the seismic moment of an earthquake. Although information on the rupture length for past earthquakes is often available (either based on reports of felt shaking, or from direct mapping of surface ruptures), the along-strike distribution of slip is rarely constrained [recent studies now emerge to improve this situation, see *Zielke et al.*, 2015, and references therein]. Yet, coseismic slip is a key ingredient to assess the slip budget of a fault based on its loading rate and the characteristics of past seismicity, thereby providing valuable constraints on the earthquake recurrence interval [e.g. *Pondard et al.*, 2007; *Wedmore et al.*, 2017; *Lefevre et al.*, 2018].

3.2.3 Slip to length ratio of the Balochistan: why such a large stress drop?

An important question then arises : can we go further, and estimate the magnitude of slip, or average slip $\bar{u}$, based on a knowledge of the rupture length L, as suggested by the nearly linear relationship between rupture length and mean slip reported by *Scholz* [1982]? Unfortunately, as shown in Fig. 3.11, when the 2013 Balochistan is plotted on the graph of *Scholz* [1982], the dot falls clearly off the chart. We note however that the relation suggested by *Scholz* [1982] is largely biased by the two Californian events (dots number 2 and 3 in Fig. 3.11), and was later challenged by several authors based on additional data and a re-evaluation of $\bar{u}$ and L [e.g. *Bodin and Brune*, 1996]. Nevertheless, even accounting for these objections, the 2013 Balochistan still remains an outlier: it is either too short, or slipped too much.

Based on this first analysis, it appears that it may be necessary to broaden the scope of the comparison if one wants to find other cases of great earthquakes sharing similar characteristics with the 2013 Balochistan earthquake. Numerous scaling relationships between earthquake parameters have been proposed in the literature [e.g. *Wells and Coppersmith*, 1994; *Shaw and Scholz*, 2001; *Romanowicz and Ruff*, 2002; *Stirling et al.*, 2002; *Manighetti et al.*, 2007; *Wesnousky*, 2008; *Hanks and Bakun*, 2008; *Leonard*, 2010]. These studies have identified that distinct behaviors may prevail depending on the tectonic regime, the size of the earthquake, the geodynamic context, the slip rate of the fault, the structural maturity of the fault, the spacing between geometrical complexities along the fault, or a combination thereof. These numerous factors seem however dominated by the geodynamic context. According to *Scholz et al.* [1986], a significant difference prevails among great strike-slip earthquakes between interplate earthquakes on one hand, and intraplate and oceanic earthquakes on the other, leading *Romanowicz and Ruff* [2002] to split strike-slip earthquakes in two distinct classes (Fig. 3.12): class A (interplate) are characterized by longer ruptures than their class B (intraplate and oceanic) counterparts. As shown in Fig. 3.12, the 2013 Balochistan earthquake falls between these two classes (see Fig. 3.12 caption), which makes its interpretation uncertain.

However, when comparing the 2013 earthquakes with other events of the class A, this first comparison suggests that the stress drop $\Delta\sigma$ (using the formula $\Delta\sigma \propto \mu(\bar{u}/l)$, where μ is the shear modulus and l is the smallest dimension of the event, i.e. its along-dip width [*Kanamori and Anderson*, 1975]) was much higher during the 2013 Balochistan earthquake than other great interplate strike-slip earthquakes listed by *Scholz* [1982] and *Bodin and Brune* [1996]. This inference is further supported by the fact that the Hoshab fault is unlikely to rupture at depths greater than 12 km, thereby precluding the existence of slip at great depth [as suggested by e.g. *Shaw and Wesnousky*, 2008; *King and Wesnousky*, 2007], thus effectively restricting the down-dip width of the fault. This high stress drop would be compatible with a long repeat time [*Kanamori and Allen*, 1986]. This is in keeping with the recurrence time of 800 years

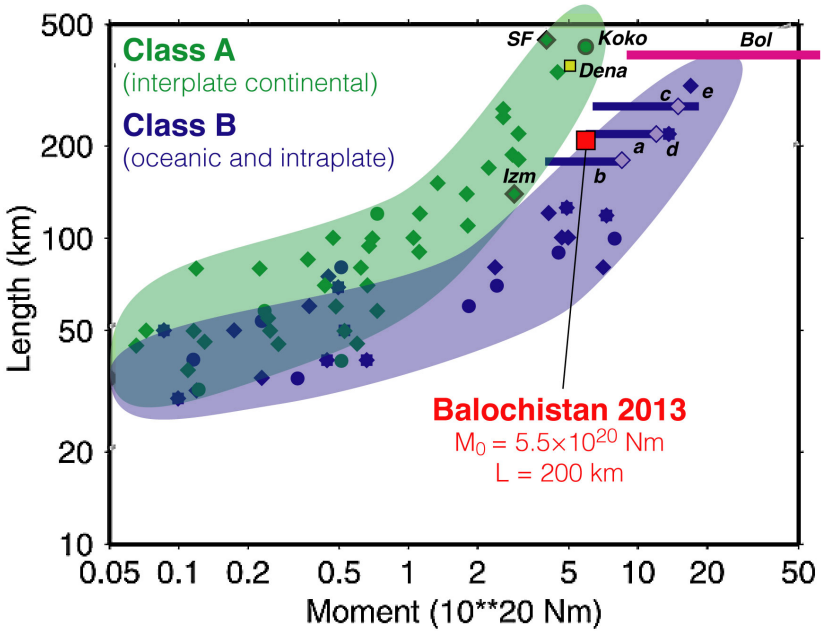

Figure 3.12 – Seismic moment versus length for strike-slip earthquakes [redrawn from Romanowicz and Ruff [2002]. Distinction between class A and B earthquakes is from Romanowicz and Ruff [2002]. SF: San Francisco 1906; Koko: Kokoxili 2001; Izm: Izmit 1999; Dena: Denali 2002; Bol: Bolnay 1905. a: Haiyuan, 1920; b: Fuyun 1931; c: Bogd 1957; d: Macquarrie Ridge 1989; e: Balleny Island 1998. Seismic moments for the 1905 Bolnay, 1920 Haiyuan, 1931 Fuyun, 1957 Bogd earthquakes have been updated based on re-evaluation of coseismic slip by Choi et al. [2018], Liu-Zeng et al. [2015], Klinger et al. [2011] and Kurtz et al. [2018], respectively. Empty diamonds are the original estimates used by Romanowicz and Ruff [2002].

estimated for the 2013 Balochistan earthquake based on a 1 cm/yr slip rate of the Hoshab fault [*Zhou et al.*, 2015]. It would also be compatible with an "intraplate" tectonic setting, prone to large stress drops (three times higher on average than interplate earthquakes, according to *Shaw and Scholz* [2001]). This is further supported by a regional analysis of corner frequencies of a large collection of global earthquakes, which indicates that large stress drops prevail in Eastern Pakistan [*Allmann and Shearer*, 2009].

Accordingly, the distinction between intra- and interplate is somehow arbitrary, as the 1920 Haiyuan earthquake, in spite of its classification in the "intraplate" category, occurred along one of the major strike-slip faults accommodating extrusion of the Tibetan plateau, just as the 2001 Kokoxili earthquake. Nevertheless, based on the above arguments, one can assert that the fault involved in the 2013 Balochistan earthquake would be closer to the "intraplate" faults that broke in large "atypical" earthquakes in the 20th century in Central and East Asia, and that form a group of events with large stress drops. Keeping the numbering of Fig. 3.12, these earthquakes include (b) the M8.0 1931 Fuyun and (c) the M8.3 1957 Gobi-Altay, which were part of a sequence of M>8 earthquake that struck Mongolia between 1905 and 1957 [*Kurushin*, 1997; *Chéry et al.*, 2001; *Klinger et al.*, 2011; *Kurtz et al.*, 2018], as well as (a) the M_s8.5 1920 Haiyuan earthquake [*Lasserre et al.*, 1999; *Liu-Zeng et al.*, 2015].

However, we note that in Fig. 3.12, the seismic moment of three large eastern-asian M~8

earthquakes (1920, 1931 and 1957) was updated, as it was initially overestimated (blue bars in Fig. 3.12). For instance, in the case of the M_s8.5 1920 Haiyuan earthquake, coseismic offsets of the order of 10 m were initially reported, based on optical images with a limited resolution. Careful analysis of well resolved data (especially LiDAR) led to the discovery of smaller offsets (5 m on average). The 10 m offsets actually reflect the cumulative effect of several earthquakes (two in this case) [*Ren et al.*, 2016]. Similar reevaluations were reported for the coseismic offsets of the 1857 Fort Tejon earthquake [*Zielke et al.*, 2012], the 1931 Fuyun earthquake [*Klinger et al.*, 2011] and the 1957 Bogd earthquake [*Kurtz et al.*, 2018]. The M8.0 1951 Damxung (Tibet) earthquake (not shown in Fig. 3.12) may also qualify in the class B category due to a large slip (up to 10 m), given a relatively short surface rupture length ($\sim$ 90 km) [*Armijo et al.*, 1989]. However, its seismic moment is uncertain (ranging between 4.0×10^{20}Nm and 36.5×10^{20}Nm [*Chen and Molnar*, 1977; *Wells and Coppersmith*, 1994]) and recent studies are lacking to confirm that estimations of surface slip are not biased towards high values due the cumulative effect of several earthquakes.

These examples illustrate how a reassessment of surface slip distribution using high resolution photographs allows for revisiting the slip distribution of past events. Conversely, detailed observations of surface slip distribution for modern earthquakes such as the 2013 Balochistan are crucial to correctly decipher the offsets caused by these older events in available satellite imagery and in the field [*Zielke et al.*, 2015].

3.2.4 Slip distribution of the Balochistan earthquake: a "smooth" event?

To go further in this discussion, we need to analyze the along-strike slip distribution of the earthquake, not just its average characteristics. In Fig. 3.13, we compare the surface slip distribution of the 2013 Balochistan earthquake with three recent earthquakes that have been studied in detail by modern space geodetic techniques: (1) the M7.8 2001 Kokoxili [*Lasserre et al.*, 2005; *Klinger et al.*, 2006; *Xu et al.*, 2006], (2) the M7.9 2002 Denali earthquake [*Wright et al.*, 2004a; *Haeussler et al.*, 2004] (3) the M7.6 1999 Izmit earthquake [*Çakir et al.*, 2003]. We note that the 24 September 2013 M7.8 earthquake is the largest continental strike-slip earthquake since these three earthquakes.

We further extend the comparison to two earthquakes that successively broke the San Andreas fault, and which were already included in Fig. 3.11: the M7.9 1857 Fort Tejon earthquake and the M7.9 1906 San Francisco earthquake (Fig. 3.14). The magnitude of these two events is poorly constrained, as it is deduced from the length of the rupture and the extrapolation of slip at depth from measurements of surface slip [*Sieh*, 1978b; *Harris and Simpson*, 1996; *Song et al.*, 2008; *Zielke et al.*, 2012]. The choice of these events was motivated by their rupture length exceeds 100 km, so that they can be safely considered width-limited. Finally, slip distribution of three M$\sim$8 earthquakes that formed a sequence of events in the first half of the 20th century in Central Asia (Mongolia) are included: the 1905 Bolnay earthquake, the 1931 Fuyun earthquake and the 1957 Bogd earthquake [*Choi et al.*, 2018; *Klinger et al.*, 2011; *Kurtz et al.*, 2018].

In spite of the limited sample size, significant differences can be noticed between these five events. All earthquakes, with the exception of the 2013 Balochistan earthquake, show significant along-strike variations in the magnitude of surface slip. Unlike other ruptures, the 2013 Balochistan exhibits a rather simple slip distribution, characterized by a peak near the center of the rupture, a steady decrease of slip away from the peak, and an abrupt decay at extremities. This shape, especially near the southern extremity where slip decreases sharply,

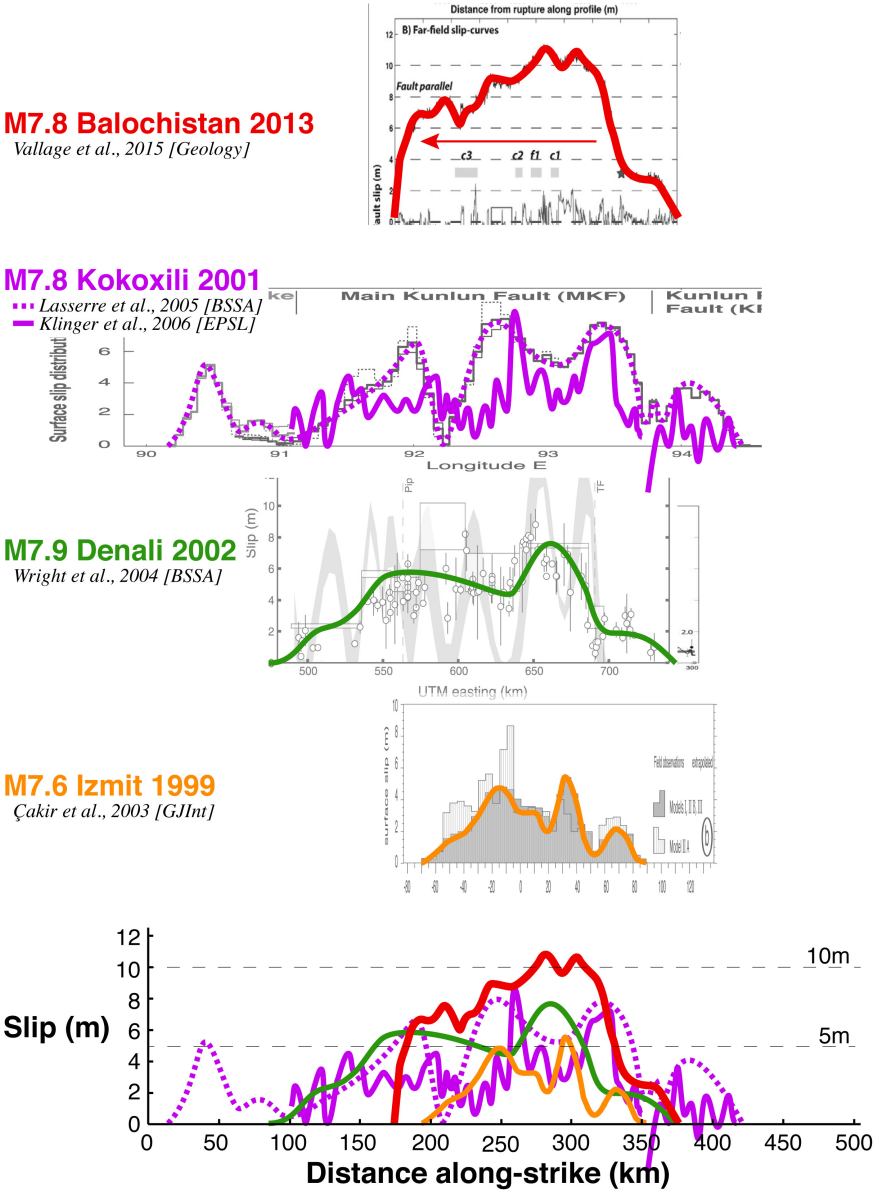

Figure 3.13 – Along-strike slip distribution of recent M7.5–8.0 strike-slip earthquakes observed by space geodesy. Only strike-slip is taken into account here. Slip has been projected along-strike for consistency. Slip distributions have been approximately aligned according to the location of the centroid. Horizontal arrow shows the direction of rupture propagation for the Balochistan earthquake.

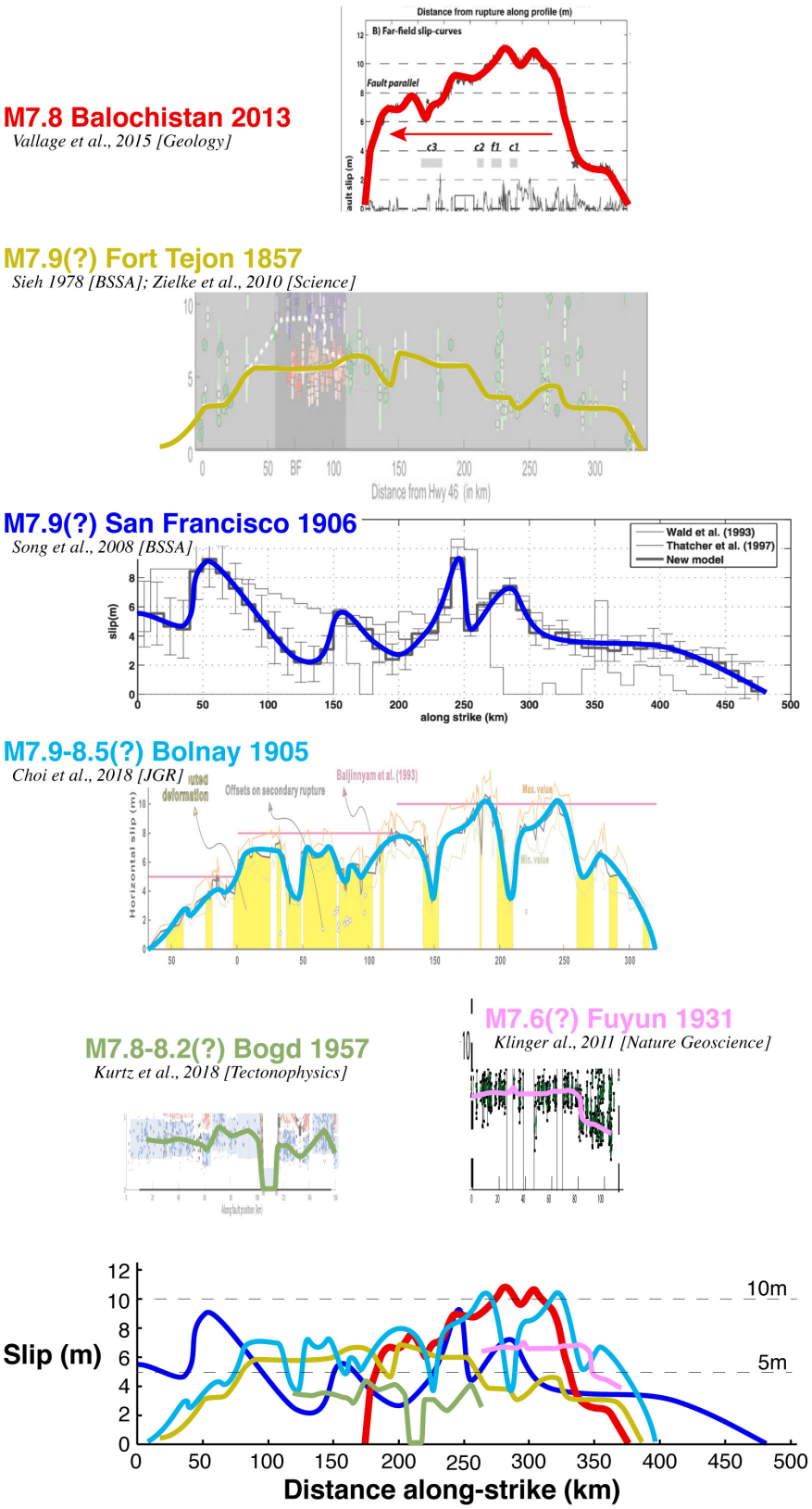

Figure 3.14 – Along-strike slip distribution of historical M7.5–8.0 strike-slip earthquakes whose slip distribution was determined by detailed mapping of coseismic offsets.

is close to the theoretical elliptical slip profile for an ideal crack in an elastic medium under uniform stress conditions [*Sneddon*, 1946; *Bürgmann et al.*, 1994]. This high slip gradient indicates a large stress concentration near the tip of the rupture [*Manighetti et al.*, 2004]. Slip at the northern limit of the earthquake appears to have been limited by the presence of the creeping section of the Chaman fault, whereas propagation toward the south was likely stopped by the excessive obliquity of the fault with respect to the surrounding stress conditions (Fig. 3.16). The absence of secondary ruptures capable of dissipating this off-fault stress is compatible with this extremely large slip gradient, whereas other ruptures in the above comparison are often associated with distributed ruptures and/or partitioning on strike-slip and thrust faults. The quality of the description of surface ruptures for other earthquakes (including the 1857 Fort Tejon rupture, reanalyzed by *Zielke et al.* [2012] using LiDAR) rules out the possibility of a spurious variability induced by measurement errors.

Based on this comparison, it appears that the earthquake that shares the most similar slip distribution with the 2013 Balochistan earthquake may be the 1857 Fort Tejon earthquake. This earthquake broke the south-central part of the San Andreas fault, whereas the 1906 earthquake later broke the northern part of the fault [*Harris and Simpson*, 1996]. Based on reports of felt foreshocks and tremors in the Parkfield area, the 1857 earthquake likely nucleated to the north of the rupture (Fig. 3.17) [*Sieh*, 1978a; *Bouchon and Aki*, 1980]. Slip quickly reached a peak of ~5 meters in the Carrizo plain, then decreased to further to the south, where slip remained approximately constant down to the rupture termination to the NE of the city of Los Angeles [*Sieh*, 1978b; *Zielke et al.*, 2012]. Similarly to the 2013 Balochistan earthquake, the 1857 Fort Tejon earthquake nucleated in a region subject to creep, started to propagate along-strike, then

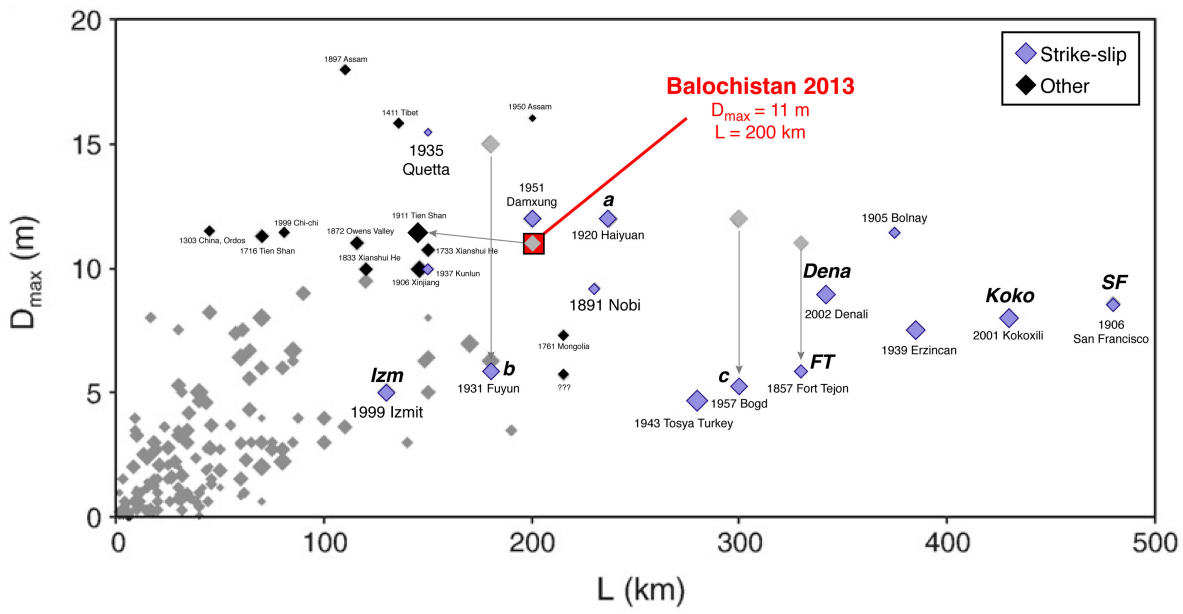

Figure 3.15 – Maximum slip inferred from surface measurements of coseismic slip versus rupture length [adapted from Manighetti et al. 2007]. Re-estimation of fault length and maximum slip for the 1911 Tien Shan earthquake is from Arrowsmith et al. [2016]. For references justifying other updates (events b, c and FT), please refer to the legend of Figure 3.12.

continued as the main fault was making a bend (the so-called "Big Bend") (Fig. 3.16). However, unlike the 2013 Balochistan earthquake, the 1857 Fort Tejon earthquake did not stop there, but instead further propagated into the Mojave area. One is tempted to imagine what would have happened to the 1857 slip profile if the earthquake had halted in the Big Bend, for instance near the branching of the Garlock Fault, where the obliquity of the SAF with respect to its average strike direction reaches its maximum. This speculative reconstruction is sketched in Fig. 3.17. Apparently, the 1857 rupture made its way across this "geometrical barrier" and halted ~ 150 km further south, at the latitude where the SAF splits into the two distinct segments of the San Bernardino and San Jacinto sections. Overcoming this barrier eventually led to a doubling of the 1857 rupture length. In the case of the 2013 Balochistan earthquake, fault obliquity monotonously increases both within and beyond the rupture trace, which is likely unfavorable for a protracted rupture. Comparing the slip distribution of the 2013 Balochistan earthquake with all earthquakes previously quoted shows that the termination of the 2013 Balochistan earthquake rupture is characterized by an extremely steep along-fault slip gradient, with slip in excess of 8 m over a length of ~ 150 km dropping down to 0 m in less than 10 km. These large gradients fall at the higher end of gradients reported by *Shaw* [2011] based on a similar dataset containing 7 earthquakes (including the 2001 Kokoxili earthquake).

The main features of the 2013 Balochistan earthquake can be summarized as: (1) extreme surface slip, (2) large stress drop, (3) large stress concentration at rupture end (especially at

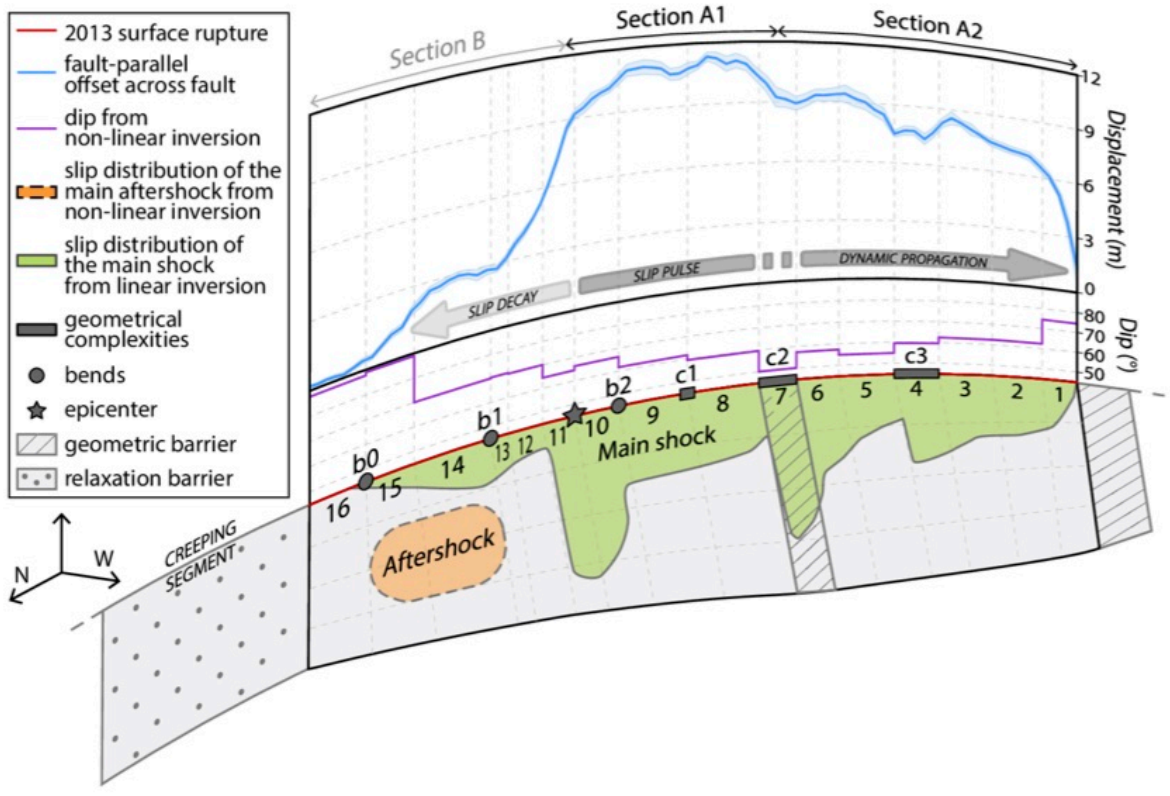

*Figure 3.16 – Relationship between coseismic slip during the 2013 Balochistan earthquake (green), geometrical barriers (dashed) and the creeping section of the Chaman fault (dotted) [from Lauer, **Grandin**, and Klinger, 2019].*

southern termination). A combination of two factors may explain these specificities: (1) an "intraplate" setting (or conversely of a low interseismic strain rate) and (2) the existence of an obstacle to a further propagation of the rupture at ~ 200 km from the nucleation point.

Incidentally, the above discussion suggests similarities between the 2013 Balochistan earthquake and 1857 Fort Tejon and the 1931 Fuyun earthquakes. It should be noted that the two latter events could be interpreted as archetypes of the so-called "characteristic earthquake" model [*Schwartz and Coppersmith*, 1984], although some authors have invoked a more conceptually nuanced model, named the "characteristic slip" model [e.g. *Sieh*, 1996; *Klinger et al.*, 2003]. According to both models, the distribution of slip at the surface would be re-iterated during every largest earthquake striking a given location. In other words, the cumulative slip accu-

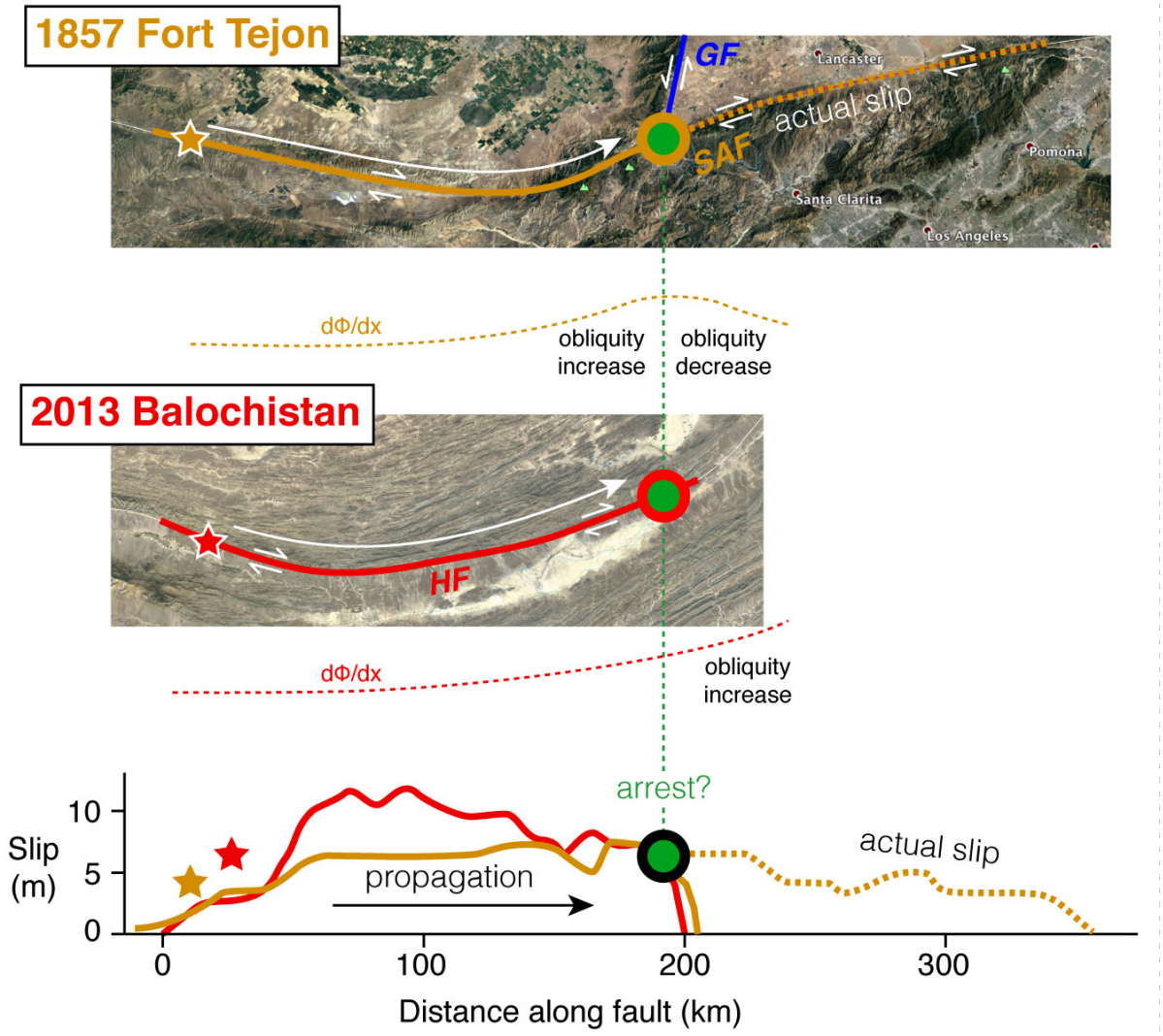

Figure 3.17 – Tentative scenario for an arrest of the 1857 Fort Tejon earthquake near the connection (in green) between the San Andreas Fault (SAF, in orange) and the Garlock Fault (GF, in blue). The slip profile and map for the Balochistan earthquake and Hoshab fault (HF, in red) have been flipped along-strike to align with the west-to-east directivity of the Fort Tejon rupture. Stars indicate the approximate nucleation point of the ruptures.

mulated since N "seismic cycles" would equal N times the slip u that occurred during the previous largest earthquake. In the characteristic earthquake model, the along-strike variability of slip is reproduced for each event, whereas this question is not addressed in the characteristic slip model. As noted by *Schwartz and Coppersmith* [1984] and further developed by *Youngs and Coppersmith* [1985], the characteristic earthquake model has profound implications on our appraisal of seismic hazard. Indeed, the characteristic earthquake model implies that (1) extreme events with large magnitude are able to break entire segments of a major fault, and that (2) smaller events are unable to alter significantly the slip distribution of these master events. Hence, the slip budget is completely dominated by the master events. This leads to a distorted frequency-magnitude distribution that does not follow the traditional logarithmic Gutemberg-Richter (GR) frequency-magnitude relationship [*Gutenberg and Richter*, 1944], a cornerstone of most seismic hazard assessment models. As a consequence of this failure of the GR, a direct implication of the characteristic earthquake model is that extrapolation of maximum magnitude from instrumental data is simply futile, which underlines the importance of gaining a better understanding of the magnitude of past earthquakes that can be deduced from paleoseismological observations [see e.g. the discussion between S. Wesnousky and Y. Kagan in *Wesnousky*, 1994; *Kagan*, 1996; *Wesnousky*, 1996, and references therein].

Leaving aside the question of whether the slip distribution of great earthquakes remains fixed during every seismic cycle, and ignoring the question of the seismic moment (both questions are not essential to the reasoning), these events of "extreme" slip bear some similarity with the great megathrust earthquakes that are known to occur on collision and subduction zones. More specifically, the 2011 Tohoku earthquake, with its huge coseismic slip (as large as 73–81 m according to some studies [e.g. *Hooper et al.*, 2013]), provides a compelling example of the existence of extremely large surface slip. Even if a posteriori analysis of GPS data suggests that the location of the Tohoku-Oki rupture may have been anticipated [e.g. *Loveless and Meade*, 2016], the magnitude of slip would have remained unexpected. The large megathrust events documented in trenches along the front of the Himalayan megathrust (with slip larger than 20 m [*Kumar et al.*, 2006]), provide yet another hint for the existence of these rare extreme events. Properly taking into account these extreme events, which, chiefly, are best documented in regions of low tectonic strain, remains a major challenge of seismic hazard assessment.

3.3 2014 M8.1 Iquique earthquake, Chile

In search for offshore earthquake transients ...

3.3.1 A double event

This earthquake is very special, for two reasons. First, it cannot be summarized as a single master event followed by its aftershock sequence. Instead, the main event consists in two earthquakes (Fig. 3.18). The M8.1 mainshock occurred on 1 April 2014, but was followed 15 hours later (on 3 April) by an M7.6 aftershock. The magnitude of this aftershock exceeds the magnitude of the mainshock minus one, thereby departing from Båth's law [*Båth*, 1965], so that these two events must be considered as forming a doublet [*Ruiz, Metois, Fuenzalida, Ruiz, Leyton, **Grandin**, Vigny, Madariaga, and Campos*, 2014] [*Duputel et al.*, 2015; *Catalán et al.*, 2015].

The earthquake doublet was studied in detail from the seismological, geodetic and tsunami point of views. In particular, the geodetic dataset for this earthquake is optimal. It consists in an InSAR coverage acquired by the TerraSAR-X satellite in ScanSAR mode, both on ascending and descending passes (Fig. 3.19a). These interferograms provide a full line-of-sight coverage onland. However, since the first post-event images were acquired after 3 April 2014, the respective contributions of the two mainshocks cannot be separated. Nevertheless, the earthquakes continuous GPS network of the IPOC[27] (Integrated Plate Boundary Observatory of Chile) consortium captured both events, providing a set of relatively dense points with three-dimensional displacements (Fig. 3.19c). Finally, sea level records from tide gauge stations maintained by SHOA[28] (Servicio Hidrográfico y Oceanográfico de la Armada) allow for measuring absolute vertical displacement at complementary locations (Fig. 3.19b).

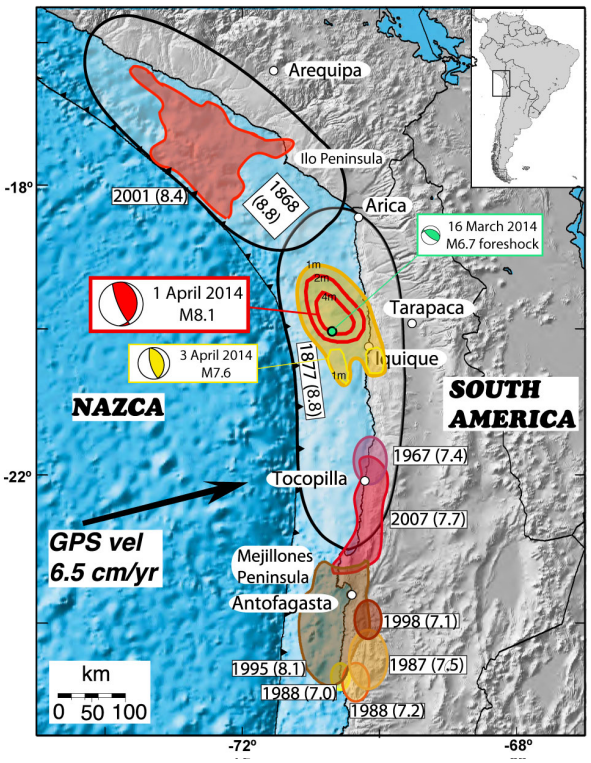

Figure 3.18 – Recent ruptures on the North Chile – South Peru megathrust interface [modified after Béjar-Pizarro et al., 2010].

These data show that the main event consists in a M8.1 earthquake that broke the offshore part of the megathrust, but did not reach the trench, as confirmed by the moderate coeval tsunami

[27] https://www.ipoc-network.org/welcome-to-ipoc/
[28] Data available from http://www.ioc-sealevelmonitoring.org/station.php?code=coqu.
[29] Software available from http://igets.u-strasbg.fr/soft_and_tool.php.

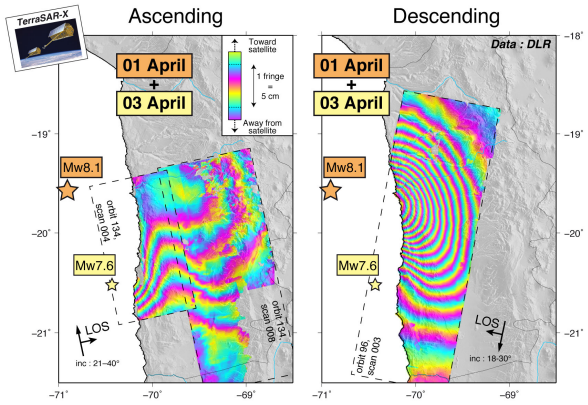

(a) *InSAR coverage of the the April 2014 Iquique doublet by the TerraSAR-X satellite. Data was acquired in ScanSAR mode. Two ScanSAR tracks were processed for the ascending pass, whereas one descending track was sufficient. Data were processed with a modified version of ROI_PAC [**Grandin**, 2014].*

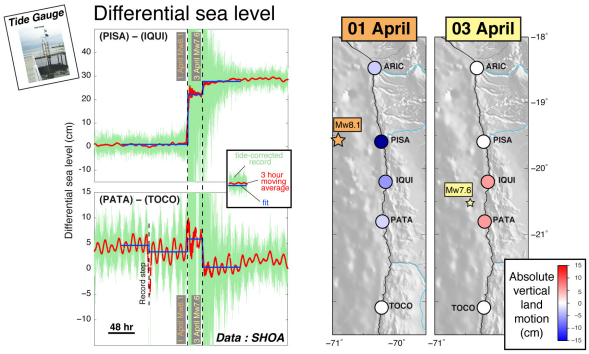

(b) *Tide gauge data for the April 2014 Iquique doublet. On the left, the difference between two pairs of records is shown, to mitigate the effect of correlated fluctuations due to regionally-coherent barometric effects. Time-series in green is corrected from tides using the software ETERNA[29] [Wenzel, 1996]. Time-series in red is the same, after applying 3-hour moving average. Time-series in blue is the best-fit for the filtered record, using a model consisting of step functions at the time of the earthquakes.*

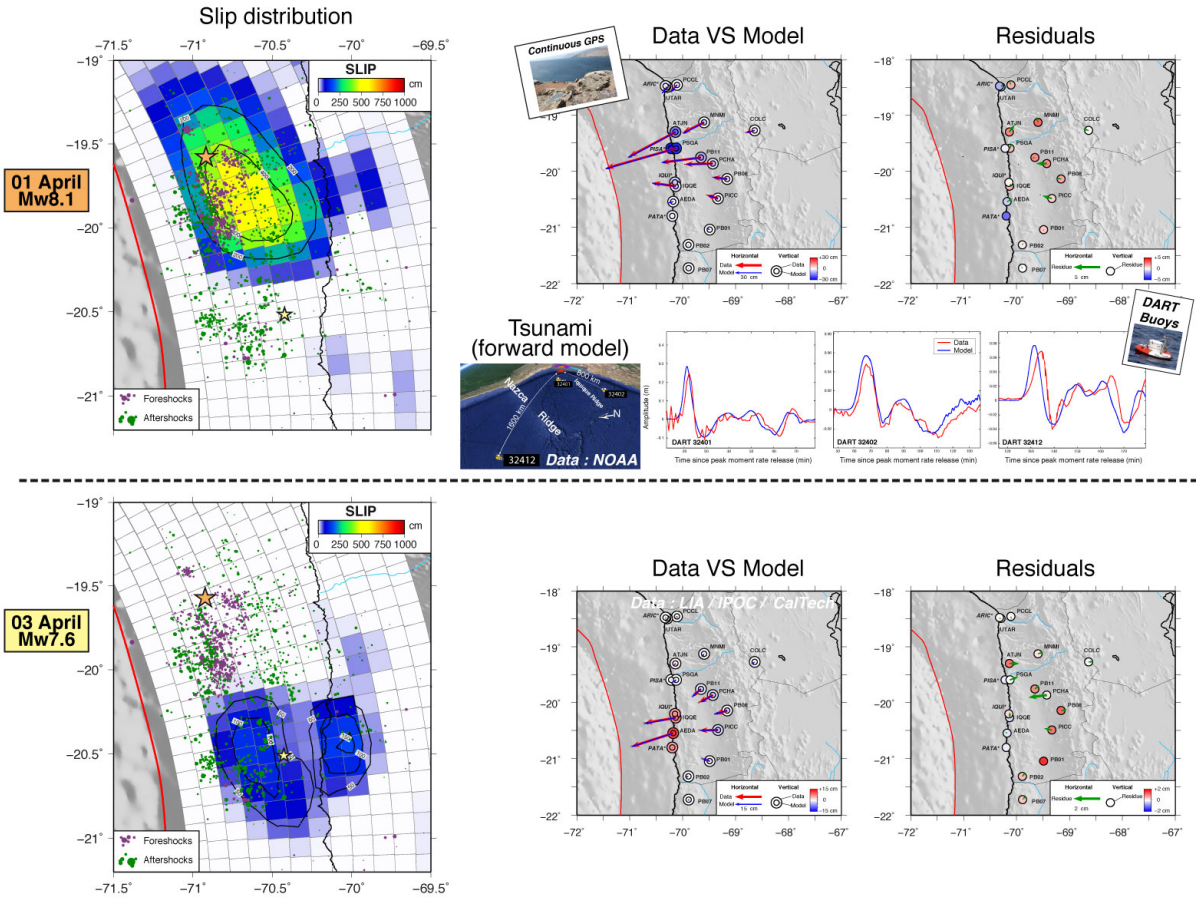

(c) *Static slip inversion of InSAR, GPS and tide gauge data for the 1 April (top) and 3 April (bottom) earthquakes. Forward modeling of tsunami waveforms at DART buoys was performed by Sébastien Allgeyer.*

Figure 3.19

(Fig. 3.19c). The second event occurred further to the south, slightly deeper, breaking the interface under the city of Iquique, the main coastal city of the area. Both of these two earthquakes were followed by aftershocks up-dip of the rupture.

In spite of their magnitudes, these two event failed to fill the seismic gap left by the giant M8.8 1877 earthquake that broke the whole megathrust interface over a length of 400 km, from the Mejillones peninsula up to Arica. A similar situation was observed further to the north in Peru, where the M8.4 2001 Arequipa earthquake broke the central part of the area ruptured during the much bigger M8.8 1868 earthquake [*Ruegg et al.*, 2001]. Such a partial rupture of a previously identified megathrust segment is reminiscent of the case of the 2015 Gorkha earthquake discussed in Section 3.1, and suggests that earthquake (and tsumami) hazard remains high in the area.

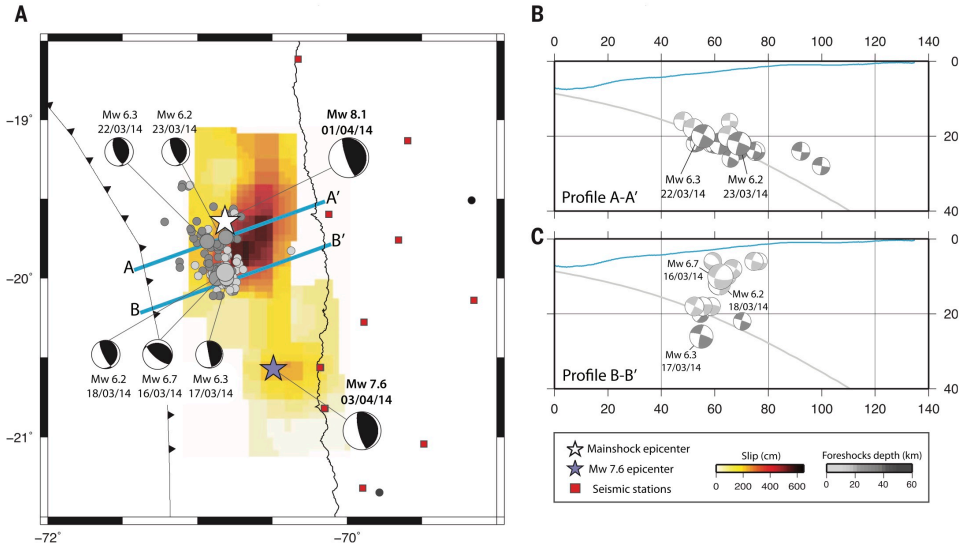

*Figure 3.20 – Relocated foreshock seismicity up-dip of the 01–03 April 2014 earthquake doublet [Ruiz, Metois, Fuenzalida, Ruiz, Leyton, **Grandin**, Vigny, Madariaga, and Campos, 2014].*

3.3.2 An aseismic precursory transient?

Besides the doublet nature of the mainshock, the most striking feature of this sequence lies in the seismicity that was recorded before the mainshock. Foreshock seismicity began attracting seismologists' attention on 16 March 2014 (i.e. two weeks before the doublet), when a relatively shallow M6.7 earthquake occurred offshore of the city of Iquique. The latter event had an "abnormal" focal mechanism, revealing reverse slip on a fault oriented at 45° to the strike of the megathrust. This upper plate event is interpreted to have occurred on a high-angle backthrust inboard of the eroded and fractured wedge overlying the megathrust interface [*León-Ríos et al.*, 2016]. In the two weeks following this "foreshock", continued seismic activity was recorded both on the interface and in the upper plate. Four earthquakes with M>6 were recorded (Fig. 3.20). Concurrently with this foreshock seismicity, a subtle trenchward displacement of GPS stations was recorded onland, reaching a maximum of ∼14 mm at Pisagua (PSGA) (Fig. 3.21a). This gradual displacement is consistent with a release of elastic strain as the plate boundary unlocked offshore of the GPS network.

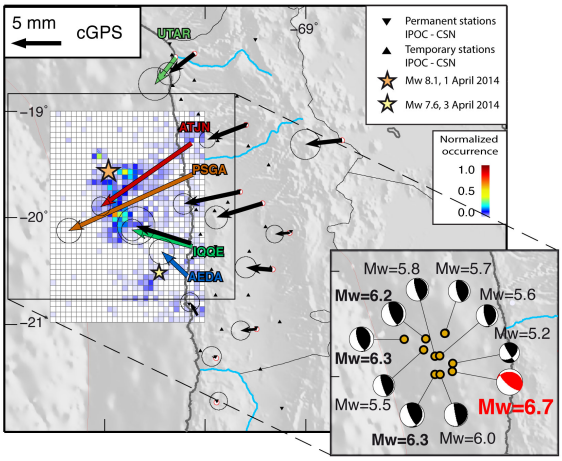

(a) *Foreshock activity in the 15 days before the 1 April 2014 Iquique earthquake and concurrent cumulative displacement at GPS stations of the IPOC network.*

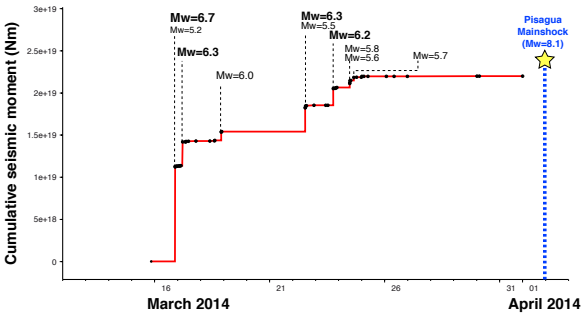

(b) *Cumulative seismic moment for the foreshocks in (a).*

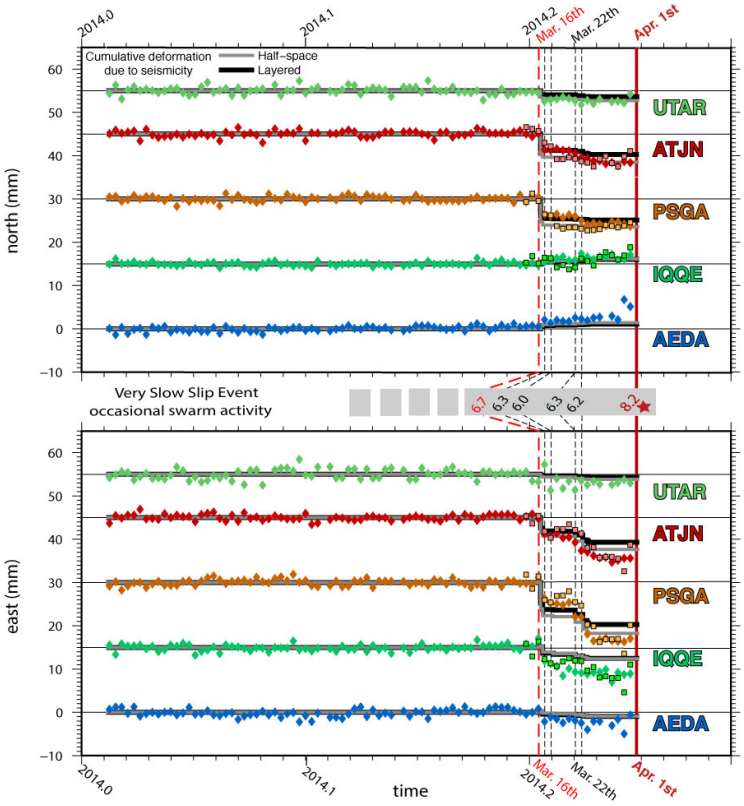

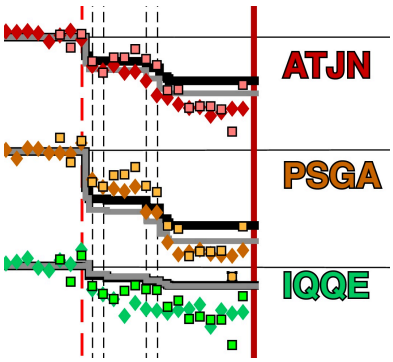

(d) *Same as (c), zoomed on the three stations showing the highest SNR on the east component. Grey and black lines are synthetic displacements computed from SSN locations and Global CMT mechanism and seismic moment using a homogeneous elastic half-space and a layered elastic half-space, respectively*

(c) *Time-series of GPS displacements for selected stations in (a). Modified from Ruiz, Metois, Fuenzalida, Ruiz, Leyton, **Grandin**, Vigny, Madariaga, and Campos [2014] after removal of a common-mode signal in the time series. Squares are common-mode-filtered time-seried from Bedford et al. [2015], for comparison.*

Figure 3.21

On the basis of these displacements, after a first-order modeling of coseismic displacements and a preliminary processing of continuous GPS, *Ruiz, Metois, Fuenzalida, Ruiz, Leyton, **Grandin**, Vigny, Madariaga, and Campos* [2014] proposed the existence of an underlying aseismic slip on the interface. On the other hand, after a thorough re-analysis of the same observations, *Bedford et al.* [2015] argued that the observed displacement could be explained by the cumulative effect of the foreshocks: according to the authors, given uncertainty on (1) GPS measurements and (2) earthquake parameter determinations (location, focal mechanism, effect of shear modulus on the conversion between potency and seismic moment), the necessity of invoking an aseismic component to account for the observed displacement cannot be established. Nevertheless, two periods of relatively small seismic moment release (18–21 March and 25–31 March, Fig. 3.21b) seem to correspond to continued displacement of GPS stations, thereby suggesting that a minor aseismic component may also coexist [*Bedford et al.*, 2015]. The same conclusion had been previously drawn by *Schurr et al.* [2014].

Independent re-processing of the common mode filtering using a principal component analysis of pre-earthquake noise in the GPS time-series (Fig. 3.21c) suggests that uncertainty on displacement during these two "quiet" time intervals is high. Comparing the two processing strategies indicates substantial differences on a day-to-day basis, although both converge to the same cumulative displacement (Fig. 3.21d). As a consequence, the precise timing of the inferred aseismic component remains uncertain, while the source location of the aseismic signal is highly ambiguous as it is essentially constrained by a handful of noisy vectors. Hence, it is almost impossible to determine whether the aseismic component (whose very existence remains unclear) occurred at the same time and location as the foreshocks, or if it happened closer to the trench or even at greater depth, near the transition zone.

Still, additional evidence points to an abnormal behavior of the megathrust prior to the 2014 Iquique sequence, even before the 16 March foreshock. *Socquet et al.* [2017] reported on a similar transient displacement in the year preceding the 2014 sequence, with maximum trenchward

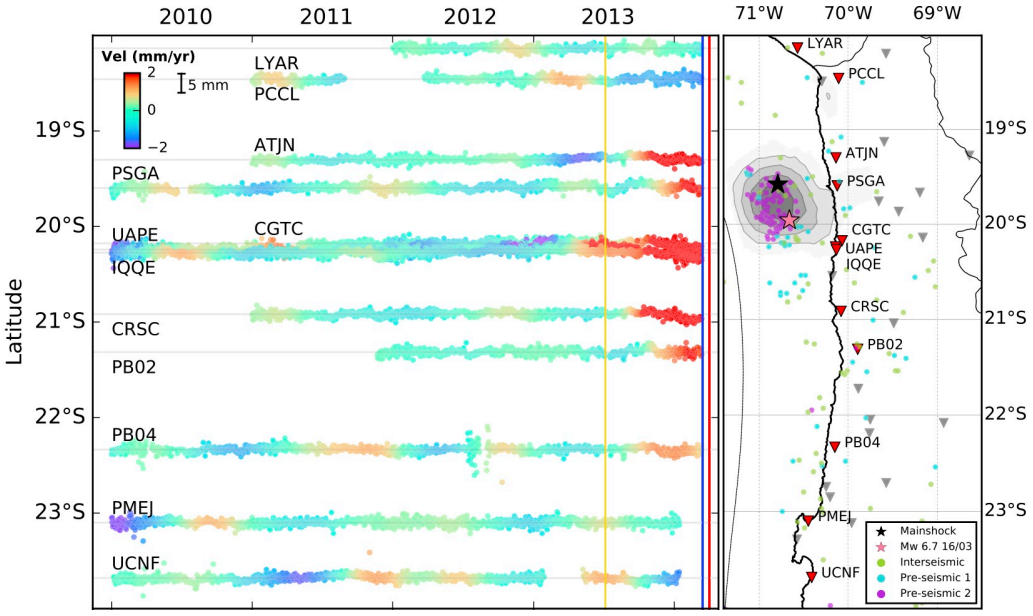

Figure 3.22 – [Socquet et al., 2017]

displacements of the order of 10mm at the coast (Fig. 3.22). Modeling suggests that an equivalent magnitude of M6.5 would be required to explain these displacements, although significant uncertainty likely prevails of this estimate. Unfortunately, once again, bursts of seismicity occurred during the same period, as reported by *Bouchon et al.* [2016], albeit with smaller maximum magnitude than during the March 2014 crisis (M5.8 on 4 January 2014, as opposed to M6.7 on 16 April 2014), which could suggest that part of this deformation may be due to regular earthquakes.

Nevertheless, as demonstrated by *Bouchon et al.* [2016], these long-term precursors were clustered in time, with a few shallow (<40 km) earthquakes occurring within a few days of much deeper (>80 km) events (Fig. 3.23). Such slightly delayed triggering of earthquakes has long been observed and numerous models have been used to explain them. The two most convincing mechanisms (in that they rely on a solid observational basis and are backed up by realistic mechanical modeling) are:

- static stress transfer from a nearby earthquake [*King et al.*, 1994].
- changes in pore fluid pressure due to passing waves (mostly Love surface waves) affecting the friction coefficient [*Pollitz et al.*, 2014; *Parsons et al.*, 2017]

Accordingly, these shallow aftershocks can influence each other by static stress transfer [*Herman et al.*, 2016]. However, the stress change due to a M<6 earthquake vanishes at very short range and cannot be invoked over distances of ∼100 km. This explanation fails to explain the synchronous occurrence of deep and shallow earthquakes. On the other hand, the maximum magnitude in the 3 days prior to the January 2014 bursts reported by [*Bouchon et al.*, 2016] was only M6.5 (2014/01/01, 16:03, Vanuatu) and M6.1 (2014/01/26, 13:55, Greece), none of which qualify as sufficiently energetic to be able to rise above the noise. As a consequence, an external cause for these nearly synchronous earthquakes cannot be found. Furthermore, *Kato and Nakagawa* [2014] reported the existence of repeating earthquakes (i.e. earthquakes producing nearly identical waveforms) during these periods. Repeating earthquake are interpreted as being

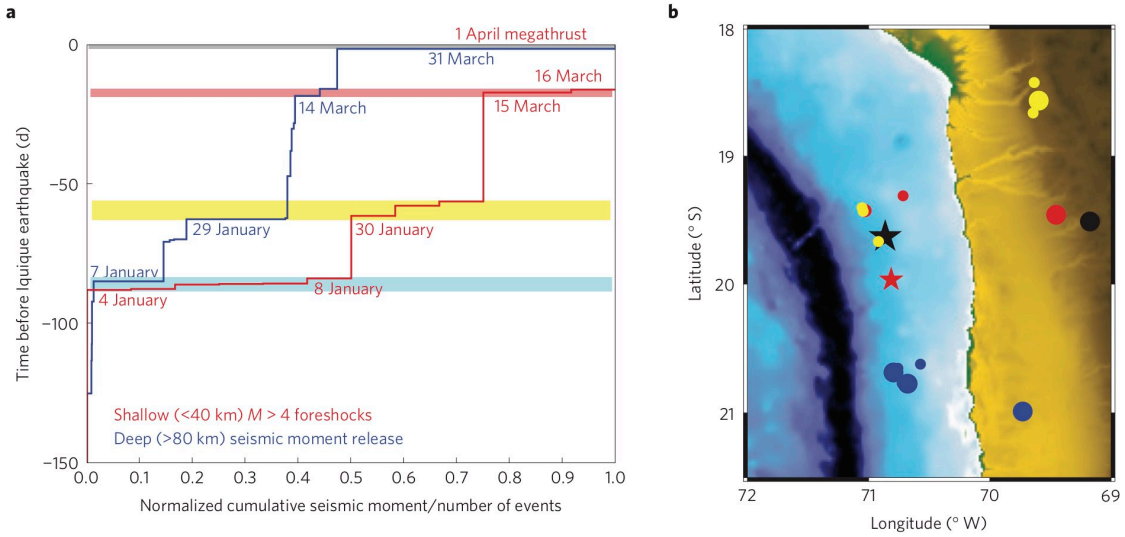

Figure 3.23 – [Bouchon et al., 2016]

compatible with rapid completion of a stick-slip cycle at local scale, presumably representing a diagnosis for an underlying fast slip of the interface.

Interestingly, one can draw a parallel between the events preceding the 2014 Iquique earthquake and other observations made in the weeks preceding the great M9.0 2011 Tohoku-Oki earthquake: (1) enhanced seismic activity both a shallow and intermediate depth, (2) foreshocks in the epicentral area of the incoming mainshock, (3) migration and acceleration of repeating earthquakes, (4) trenchward displacement of the upper plate [*Kato et al.*, 2012; *Mavrommatis et al.*, 2014, 2015; *Loveless and Meade*, 2016]. Overall, these findings strongly point to the existence of aseismic slip transients in subductions zones, or SSE (slow slip events), driving bursts of shallow and deep seismicity, causing repeated earthquakes, and eventually leading to the triggering of the mainshock.

On the negative side, direct evidence for these transients remains elusive in Chile. Furthermore, it is always worth mentioning that not all large earthquakes were preceded by seismic pre-

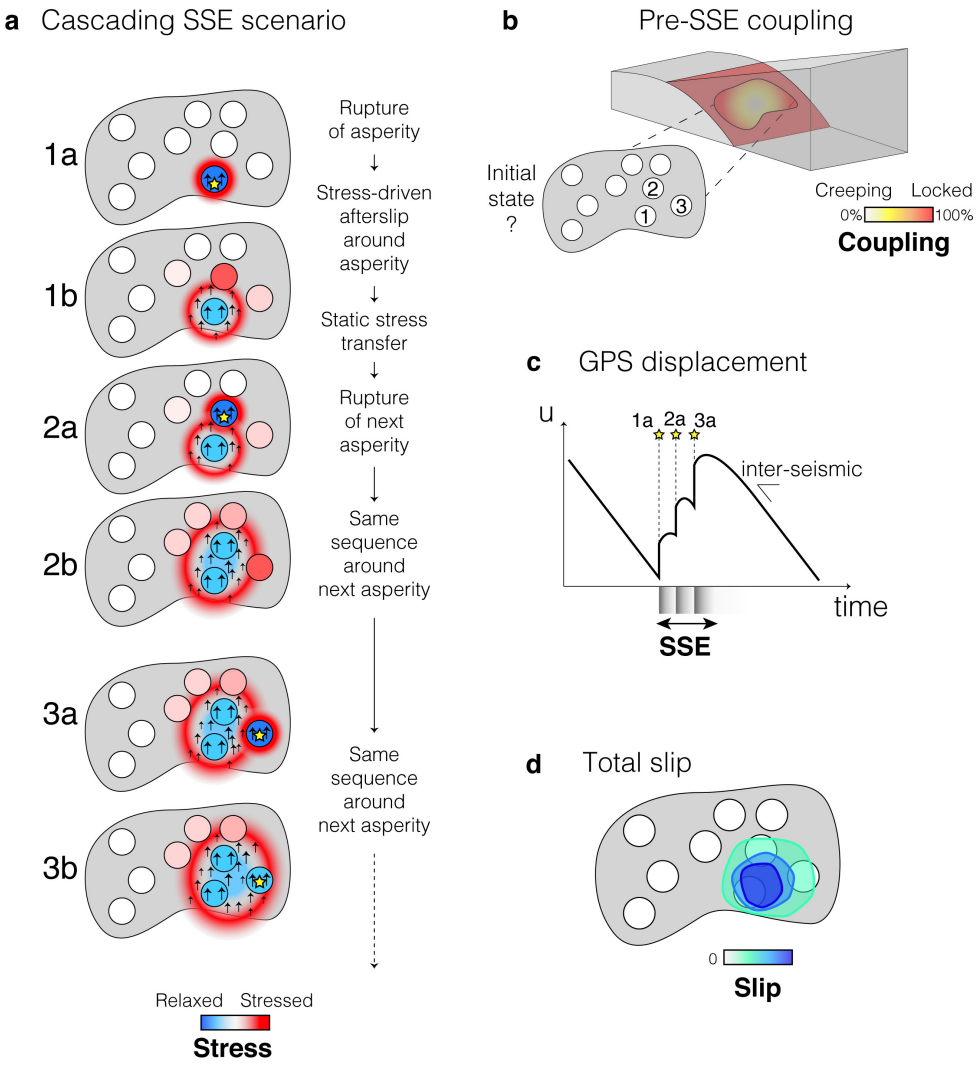

Figure 3.24 – Slow slip event (SSE) on a low-coupling region of the subduction interface.

cursors, and that seismic swarms are generally not followed by a large earthquakes [*Holtkamp et al.*, 2011]. As a consequence, although slip transients illuminate a peculiar behavior of seismogenic faults that is worth studying to better understand the mechanics of earthquakes, there is still a long way to go before these phenomena can be used for short-term seismic hazard assessment, not to mention earthquake prediction [*Bernard*, 2001].

On the positive side however, geodesy can place an upper bound on the equivalent magnitude for the aseismic slip that preceded the 2014 Iquique sequence. This magnitude can be conservatively estimated to be M<7. Therefore, contrary to the transients observed in Guerrero gap in Mexico [e.g. *Radiguet et al.*, 2012; *Bekaert et al.*, 2015a], these transients are unlikely to absorb a significant fraction of the relative plate motion accumulating during the interseismic period. Their importance in the slip budget of the megathrust is therefore relatively modest, and so is it of their static stress transfer potential. Triggering of a large earthquake during a SSE, as was recently observed in Mexico (2014 M7.3 Papanoa earthquake [e.g. *Radiguet et al.*, 2016]), is therefore unlikely, but not impossible, as suggested by the puzzling examples of Iquique and Tohoku.

3.3.3 Spatially- and temporally variable interseismic coupling

These observations suggest that the concept of interseismic coupling should be reconsidered. As progress is made in the accuracy of geodetic measurements, the recognition of a continuum between stick-slip and stable sliding behaviors is growing in popularity [e.g. *Meade and Loveless*, 2009]. This does not mean that the concept of full locking is obsolete (certainly the Gorkha earthquake falls in this category, as discussed in Section 3.1). Rather, these recent observations suggest that there likely exists a whole range of intermediate behaviors. For instance, slip may proceed at steady rate, explaining locally lower coupling, but this constant slip rate may be punctuated by occasional accelerations triggered by external factors. These external factors can include:

- stress change experienced when relatively "strong", small-scale asperities fail and transfer the load to their surroundings [*Vallée et al.*, 2013; *Rousset et al.*, 2016b] (Fig. 3.24). The slip transient may therefore go along with such a cascading failure, as "soft" regions surrounding the asperities are free to accelerate as they become unleashed. Such an interpretation would account for the discovery that some long-lasting (~6 months) SSEs in

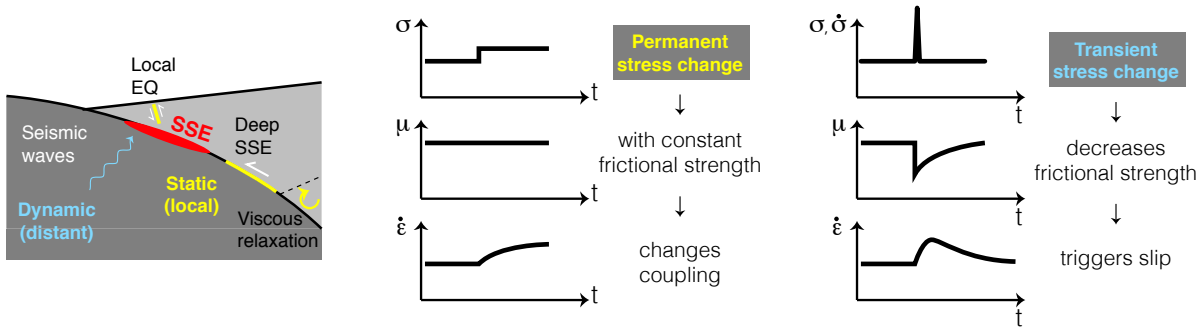

Figure 3.25 – Triggering of a SSE or of transient coupling change due to permanent / static (yellow) or transient / dynamic (blue) stress perturbations.

Mexico actually consist of a succession of smaller SSEs lasting only 1 or 2 days [*Frank et al.*, 2018].

- quasi-static stress transfer caused by rapid slip down-dip on the plate interface (as suggested by *Gardi et al.* [2006] to explain the July 1997 Coquimbo swarm and the unusual M7.6 15 October 1997 "slab-push" Punitaqui earthquake) or due to a nearby intraplate earthquake (as suggested by *Bie et al.* [2017] for the 2014 Iquique sequence, which may have been favored by the 2005 M7.8 Tarapacá earthquake), as shown in Fig. 3.25 (yellow).

- enhanced loading rate caused by viscous relaxation following a great earthquake rupturing a neighboring (along-strike) segment of the megathrust (Fig. 3.25, yellow), as inferred following the 2010 Maule earthquake, which increased the apparent loading rate by 15% in the area of the 2016 Illapel earthquake [*Ruiz et al.*, 2016].

- indirect destabilization by a nearby great earthquake, as a result of dynamic stress changes by passing seismic waves (Fig. 3.25, blue), as exemplified by the triggering of an SSE on the Hikurangi interface induced by the 2016 M7.8 Kaikōura earthquake [*Wallace et al.*, 2017].

3.3.4 Seafloor geodesy

In order to better understand these transient behaviors, and to better characterize the distribution of interseismic coupling (in particular at the trench), better measurements must be made. Indeed, the deceptive conclusions of the analysis of the Iquique precursors stem from the lack of resolution on offshore sources that can be achieved from onland geodetic measurements [*Tung and Masterlark*, 2018b]. Seafloor geodesy could represent a promising alternative to overcome this limitation [e.g. *Gagnon et al.*, 2005; *Ballu et al.*, 2013; *Hooper et al.*, 2013; *Yokota et al.*, 2016]. Recently, the combination of seafloor imaging and seafloor geodesy has allowed for the achievement of spectacular results to capture small-scale deformation signals (including transients) associated with rupture of the seabed due to shallow faulting in contexts of volcano submarine flank collapse [e.g. *Phillips et al.*, 2008; *Urlaub et al.*, 2018] or seafloor faulting associated with large ruptures on subduction megathrusts or strike-slip faulting [e.g. *Ito et al.*, 2011; *Kearse et al.*, 2018]. However, capturing large-scale deformation occurring at slow rates remains extremely challenging. Moreover, as the subduction interface gets shallower, seafloor measurements may start to suffer from the same limitation as near-fault onland geodetic measurements, namely the effect of heterogeneous resolution and departure from a purely elastic behavior (see Section 2.3). To balance this effect and achieve a homogeneous resolution in the mapping of the interface, a large number of sensors have to be installed – much greater than for distant onland networks –, which adds to the costs. Finally, and more fundamentally, it is unclear whether the frictional behavior of the interface near the trench can be inferred from the apparent coupling ratio, because slip at the trench can be seriously impeded by the stress shadow caused by absence of slip along its frictionally locked down-dip edge [*Almeida et al.*, 2018].

In any event, the impact of seafloor geodesy will remain limited until its actual implementation in the field, which is still uncertain due to the high cost and the limited accuracy [e.g. see *Bürgmann and Chadwell*, 2014, and references therein]. Recent technological progress in sea-bottom extensometry [e.g. *Yamamoto et al.*, 2019], shipborne sidescan multibeam sonar and coupled with GPS positiononing [*DeSanto and Sandwell*, 2019], fiber-optic interferometry

[e.g. *Jousset et al.*, 2018], coupling of borehole tiltmeters with remote fiber-optic sensing [e.g. *Chawah et al.*, 2015], drift controlled deepwater pressure gauges [e.g. *Sasagawa et al.*, 2016] have however been spectacular, which should bring back some hope.

This being said, when it comes to making pragmatic recommendation about short-term seismic hazard, the 2014 Iquique sequence illustrates a very common behavior of many fault zones on Earth: when a significant earthquake strikes, there is an increased probability for another significant earthquake to occur shortly after. The famous case the M9.5 1960 megathrust earthquake in Chile should always be recalled: although the earthquake may have been triggered by an aseismic slip transient [*Kanamori and Cipar*, 1974], the clearest harbinger of the incoming mega-quake was a M8.1 earthquake that occurred just a day before [*Cifuentes*, 1989]. In this context, adaptive forecasts based on short-term changes in seismicity rates [e.g. *Gerstenberger et al.*, 2005; *Helmstetter et al.*, 2006; *Shebalin et al.*, 2011; *Rundle et al.*, 2016] [see also *Tiampo and Shcherbakov*, 2012, and references thererin], although largely based on empirical assumptions, represent a perfectly reasonable approach.

3.4 2016 M5.8 Pawnee earthquake, Oklahoma

Welcome to the anthropocene!

3.4.1 Joint geodetic-seismological source inversion

The 3 September 2016 M5.8 Pawnee earthquake struck the northern part of the Oklahoma state, in the Central US (Fig. 3.26). This region is located far from plate boundaries, in an area where present-day strain rates are so small that they are below the detection of GPS ($\sim 10^{-9}$ yr^{-1}) [*Calais et al.*, 2006b]. The 2016 Pawnee earthquake therefore represents an opportunity to better characterize the strain and stress regime that prevails in this area.

At the time of writing, the 2016 Pawnee earthquake was and remains the largest of a series of moderate M>5 earthquakes that struck the US states of Oklahoma, Kansas, Arkansas and Texas between 2009 and 2017 (Fig. 3.26). These events are part of an overall increase in seismicity rate in the US midcontinent: more than 300 M>3 earthquakes were recorded between 2010 and 2012, compared to an average rate of 21 events per year from 1967 to 2000 [e.g. *Ellsworth*, 2013; *Hough*, 2014] (Fig. 3.26a). The cause of this spectacular increase in seismicity is now indisputably attributed to the injection of enormous volumes of wastewater produced by the oil industry [e.g. *Horton*, 2012; *Keranen et al.*, 2014; *Hornbach et al.*, 2015; *Weingarten et al.*, 2015; *Hincks et al.*, 2018]. Increased oil extraction started in 2007 when operators began to exploit new oil plays using unconventional extraction techniques, triggering anomalous earthquake activity. This particular situation further justifies the interest drawn by the 2016 Pawnee event in the earthquake geodesy community.

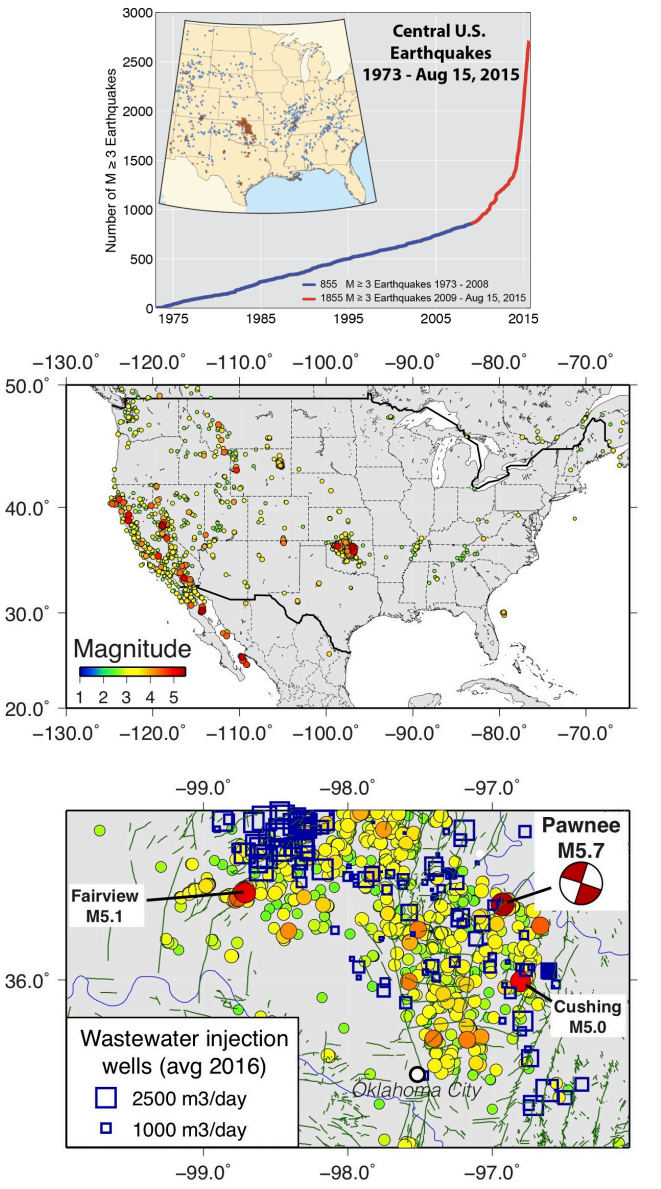

Figure 3.26 – Top: Earthquake count as a function of time in the US midcontinent [Rubinstein and Mahani, 2015]. Middle: Distribution of earthquakes in conterminous US for the year 2016 (source: USGS). Bottom: zoom on the area of anomalous seismicity in Oklahoma.

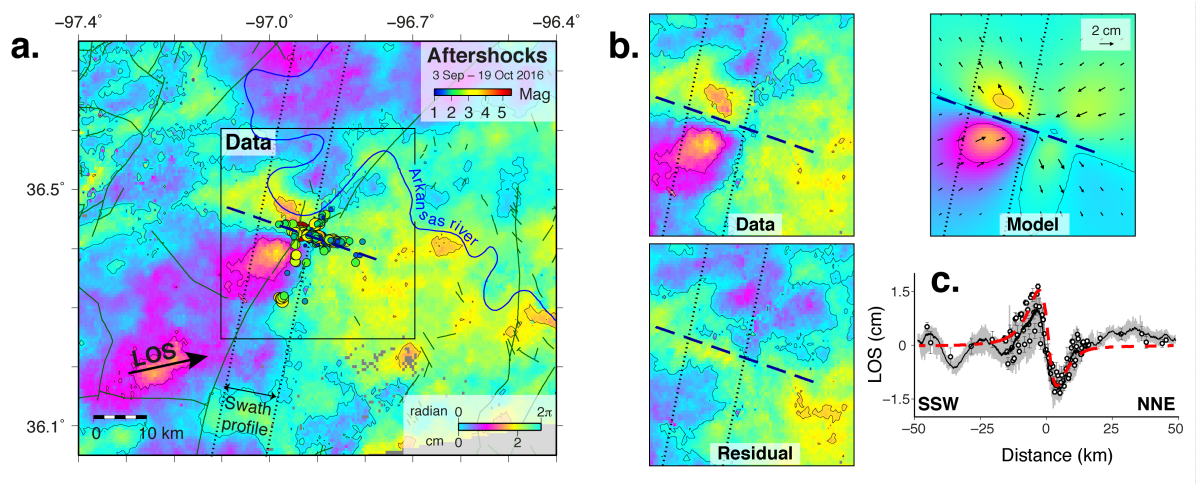

*Figure 3.27 – a: Coseismic deformation associated with the 3 September 2016 M5.8 Pawnee earthquake from Sentinel-1 time-series decomposition. b: Data, model and residual displacement maps. c: Swath profile perpendicular to the strike of the fault (dashed box in b). From **Grandin** et al. [2017].*

According to *Funning and Garcia* [2018], who conducted a systematic study of the detection capability of the Sentinel-1 system, the magnitude of completeness of the Sentinel-1-derived earthquake catalogue for events affecting emerged regions of the globe should be between M6.2 and M7.0. A magnitude 5.8 earthquake is close to the detection of the system, and can only be detected under favorable conditions in terms of coherence, atmospheric noise, source depth and focal mechanism.

In ***Grandin** et al.* [2017], we performed a time-series decomposition of Sentinel-1 data acquired every 12 days (Fig. 1.15), and estimated the spatial distribution of surface displacement (Fig. 1.16) using a simple model consisting of a step function in time for every pixel. This strategy allows for separating the fluctuations induced by atmospheric noise from the persistent spatial signature of coseismic deformation. The resulting surface displacement field shows the predicted pattern of deformation typical of a north-south or east-west trending strike-slip fault, consistent with the focal mechanism of the event (Fig. 3.27). The peak-to-peak surface displacement is as small as 3 centimeters, but can be clearly distinguished from the background noise.

Using a joint analysis of the Sentinel-1 interferogram and the seismic wavefield of the Pawnee earthquake (at regional and teleseismic distance), we were able to demonstrate that coseismic slip during the event was restricted to a unique patch measuring 10 km along-strike and 6 km down-dip, centered around a depth of $\sim$ 7 km. Furthermore, thanks to InSAR, it was possible to show that slip was restricted to depths greater than $\sim$ 3 km (Fig. 3.28). In contrast, wastewater injection in the vicinity of the epicenter (which is believed to be the main triggering mechanism for this earthquake, as discussed below) takes place at depths shallower than $\sim$ 2 km.

This single observation, which was confirmed independently by *Fielding et al.* [2017], indicates that wastewater injection, and, more broadly, human activity, is capable of triggering seismic slip on faults buried deep within the basement, including in areas of low tectonic strain. Therefore, the occurrence of the moderate-sized 2016 Pawnee earthquake has far reaching consequences.

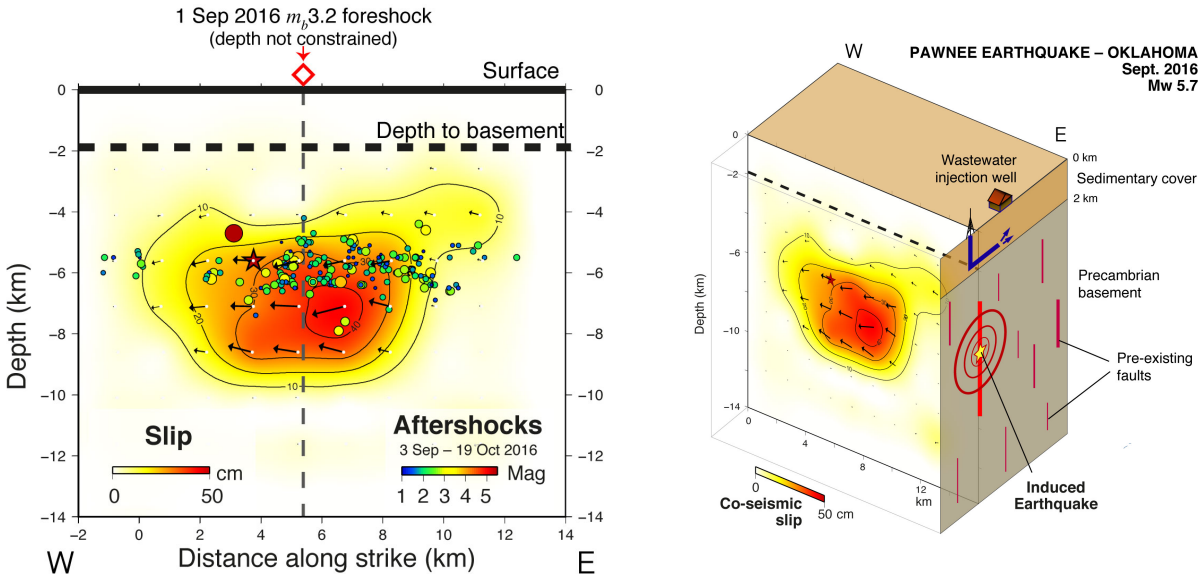

*Figure 3.28 – Left: Slip distribution of the 2016 Pawnee earthquake. Right: relationship between co-seismic slip and wastewater injection. [From **Grandin** et al., 2017].*

3.4.2 Increased seismic activity in Oklahoma

Oklahoma has a long history of oil exploitation, dating back to the end of the 19th century [*Clare*, 1963; *Boyd*, 2002, and references therein]. The all-time peak in exploitation was reached in the 1920s. Production then decayed until the 1950s, when secondary recovery techniques were first experimented, before their refinement in the 1970s and eventually their deployment elsewhere in the US and in the rest of the world. Today, advanced extraction techniques, also knows as enhanced oil recovery (EOR) techniques, allow for targeting unconventional formations, characterized by a low porosity and low permeability. These techniques include horizontal drilling, stimulation by injection of fluids of various chemical and physical compositions, and artificial increase of permeability by hydrofracturing [*Rubinstein and Mahani*, 2015]. Furthermore, experiments of microbial EOR techniques, which consist in injecting nutrients into reservoirs in order to enhance microbial activity and improve the recovery of oil, have been carried out in Oklahoma since at least the 1980s, with impressive success [*Safdel et al.*, 2017], which may suggest that these techniques are also employed today.

Unfortunately, a major drawback of these techniques is that large volumes of water-rich fluids are co-produced with the oil. Due to a high concentration of salt and heavy metals, these fluids are best described as brines. Contrary to common belief, these fluids do not originate from the injected material. Rather, they consist in water that has been trapped together with oil in low porosity, low permeability rocks for a long (geological) time. Cleansing or recycling these brines represents an exorbitant cost. As a result, these fluids are injected into other geological formations, often appositely called “disposal formations”. In Oklahoma, the most popular disposal formation is the Arbuckle formation, which consists in Cambrian-Ordovician ($\sim$ 500 Ma) dolomites [*Morgan and Murray*, 2015]. It is situated underneath the Carboniferous-age ($\sim$ 300 Ma) oil-bearing formations, but just above the basement, at depths of $\sim$ 2 km below the surface. These so-called “disposal formations” were not chosen for no reason, for they have the convenient characteristic of being underpressured, i.e. the fluid pressure is less than

hydrostatic. Underpressurization of a geological formations is thought to result (among other possibilities) from the action of long-term uplift and erosion [e.g. *Xie et al.*, 2003, and citations therein]. This would be compatible with the tectonic history of Oklahoma, which can be summarized as (1) an old orogen period in the Carboniferous, during which the Mississipian and Pennsylvanian oil reservoirs were formed, followed by (2) a long tectonic quiescence during the Mesozoic and (3) a recent, broad uplift in the early Tertiary as a result of the growth of the Rocky Mountains [*Johnson*, 2008].

The current episode of enhanced seismicity in Oklahoma includes two M>5.5 earthquakes in Prague (2011) and Pawnee (2016), which were widely felt by the population. A cluster of events also occurred just under the strategic oil storage facility in Cushing, while another significant event occurred in Fairview, well away from the area affected by fluid injection (Fig. 3.29). It is known for a fact that fluid injection is responsible for this anomalous seismicity, because the whole area was largely aseismic had prior to 2008. The two remaining important questions are :

- What is the link between fluid injection and earthquake occurrence?
- What is the hazard associated with this seismic upheaval?

3.4.3 Physical mechanisms of earthquake triggering

Seismic slip is believed to result from an instability caused by the sudden collapse of the frictional strength of faults that leads to the release of elastic strain energy stored prior to the event. The instability occurs when the resistance to slip on the fault becomes equal to the stress applied on the fault. The resistance to slip is often described by a friction law, which depends on the physical properties of the fault zone, as well as the slip rate and the stressing rate applied to

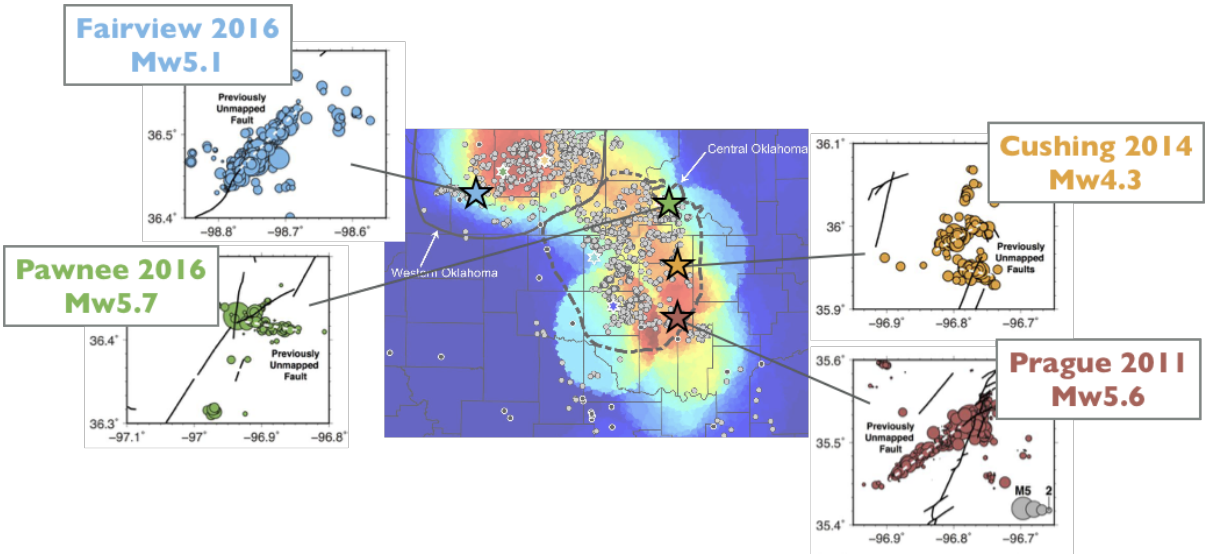

Figure 3.29 – Recent injection-induced earthquakes in Oklahoma [adapted from Langenbruch and Zoback, 2016; Yeck et al., 2017]. Alignment of aftershocks indicates that fault planes involved in the mainshocks are either oriented ESE-WNW or SW-NE, in agreement with the inferred background tectonic stress field.

the fault [*Scholz*, 1998; *Toda et al.*, 2002]. The main active fault zones on Earth are located along tectonic plate boundaries, which move steadily at relative velocities of the order of a fraction of or a few centimeters per years. After a more or less long period of tectonic loading, a certain threshold is reached, leading to an earthquake. This simple picture being sketched, it becomes necessary to immediately recall that a major complexity of earthquake phenomena arises from the fact that earthquakes tend to influence each other by mechanisms of static stress transfer, which leads to a collective behavior of earthquakes [e.g. see *Ben-Zion*, 2008, and references therein]. Furthermore, phenomena such as viscous relaxation and fluid flow can further complicate the identification of causal links between earthquakes, by introducing a time delay between the master and slave events [e.g. *Steacy et al.*, 2005]. Finally, fluids play an additional role in perturbing the pore pressure in the host rock, which is one of the ingredients of the strength of faults [*Segall and Rice*, 1995].

In the case of Oklahoma, where tectonic strain rates are essentially unmeasurably small, the increase in seismic activity is entirely due to wastewater injection. An open question is whether this seismicity is "*induced*" (i.e. generated directly by injection operations) or "*triggered*" (i.e. primarily driven by pre-existing stress, with injection only providing the last push that destabilizes the fault) [for a broader perspective of induced seismicity, see *Grigoli et al.*, 2017; *Foulger et al.*, 2018; *Keranen and Weingarten*, 2018]. In order to determine which category these earthquakes belong to, it is necessary to understand the effects of fluid injection. They can be divided in two distinct classes (Fig. 3.30): (a) increase in pore pressure, which leads to a weakening of faults and (b) increase in solid rock stress, which adds to the burden that is already sustained by faults.

The increase in pore pressure acts in the same way as a decrease in normal stress: when pore pressure increases, it tends to "unclamp" fault planes, thereby fostering slip. This phenomenon is well understood, and analytic solutions of Darcy's law are readily available to model the effect

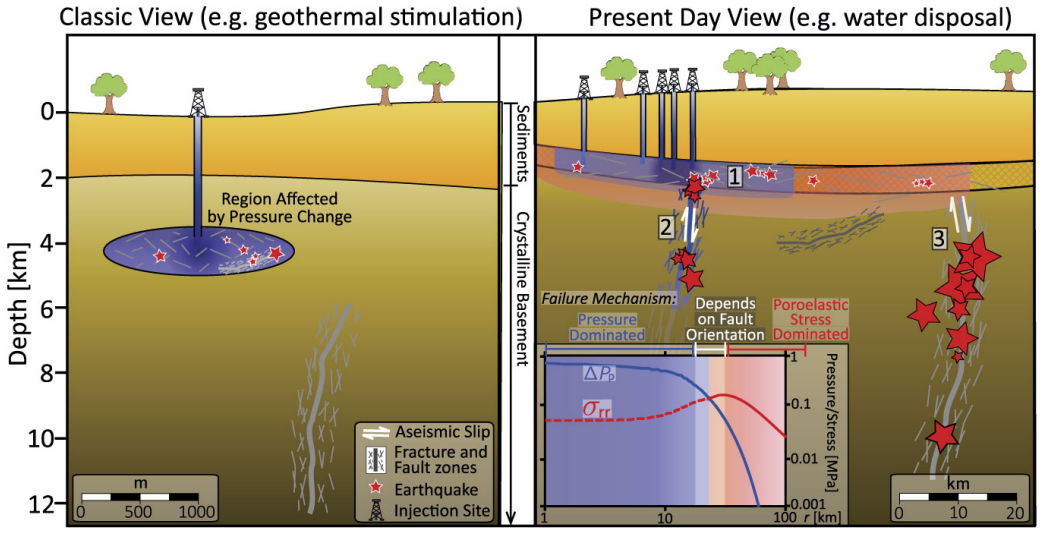

Figure 3.30 – Triggering of seismic activity by fluid injection due to direct pore pressure increase (left) or due to distant propagation of pore pressure and solid rock stress perturbations (right). Adapted from Goebel et al. [2017a].

of a pressure source embedded in a permeable medium. However, pore pressure perturbations can be greatly enhanced or reduced by the presence of highly permeable domains, which are capable of conveying fluids along preferential pathways [*Keranen et al.*, 2014]. The main unknown in these modeling attempts then becomes the actual geometry of the host medium, which may be highly stratified in terms of permeability, leading to a degeneration of the problem from 3D (isotropic) down to 2D (tabular) or even 1D (plane)[*Goebel et al.*, 2017a]. In any case, direct pore pressure effects tend to vanish rapidly, as they are limited by the distance traveled by the fluids.

On the other hand, the increase in solid rock stress can prevail at greater distance, as a result of poroelasticity [*Segall and Lu*, 2015]. Indeed, changes in fluid pressure induce deformation, which leads to stress changes, whose effect is to alter the stress gradients and eventually to influence the motion of fluids. In other words, pore pressure deforms rocks, but in return rock deformation squeezes the pores, and hence affects pore pressure. Hence, the equations governing solid rock stress and fluid flow are coupled [*Jaeger et al.*, 2009; *Segall*, 2010]. As a result of this coupling, the range of problems that can be solved analytically is reduced to a small number of idealized cases.

3.4.4 Short-term seismic hazard and regulator response

Whether the problem of induced seismicity should be solved analytically or numerically, the main limitation facing attempts to predict the effect of fluid injection on seismicity is the lack of knowledge of many ingredients of the model:

- injection parameters ;
- spatial distribution of permeability in the host rock ;
- spatial distribution of porosity in the host rock ;
- geometry of faults ;
- state of stress on faults ;
- frictional behavior of faults.

For instance, *Chang and Segall* [2016] have shown that the presence of a highly permeable plane in the vicinity of the injection point (such as a fault gouge), and even more, the connectivity of this permeable plane with the fluid reservoir, have a strong influence on the space-time evolution of pore pressure transients. Since the response of seismicity to changes in background pressure and stress is highly dependent on the *rate of change* of these quantities [*Toda et al.*, 2002, e.g.], the rate of change of injection parameters may thererfore have a strong effect on the probability of increasing or reducing seismicity. This phenomenon can produce rather counterintuitive effects, as shown by *Segall and Lu* [2015]: in low stress environment, a peak in induced seismicity can occur *after* the cessation of injection activity, especially if injection ceases abruptly, as a result of the propagation of poroelastic stress transients in the surrounding medium. This indicates that a mitigation of seismicity could be achieved by forcing injection parameters to vary smoothly with time. These first-order predictions are however modulated by the response of the medium, which likely depends on the geodynamic context. Paradoxically, an investigation of injection-induced seismicity in California and Oklahoma suggests a greater

sensitivity in the Oklahoma case, whereas, in California, seismicity rates seem to be comparatively little affected by changes in injection parameters [*Göbel*, 2015]. This is unfortunate, as our knowledge of active fault systems in Oklahoma is far less complete than in California.

The above-mentioned studies clearly suggest that predicting the effect of wastewater injection on the rate of seismicity is a difficult problem, because it depends on many unknown. In spite of this complexity, a few authors claim that earthquake hazard can be mitigated by carefully controlling injection operations, and have provided a few guidelines in this direction:

- advocates of the rapid response "traffic light" system propose a full methodology for enforcing a temporary decrease in injected volumes, in order to produce a certain level of intended short-term decrease in the seismicity [e.g. *Mignan et al.*, 2017].
- *McGarr* [2014] formulated a relationship to predict the maximum magnitude of earthquakes triggered in response to a certain volume of fluid injection. This study later led the authors to state that "hazard may be reduced by managing injection activities" [e.g. *McGarr et al.*, 2015].
- Similarly, *Walsh III and Zoback* [2016] proposed a probabilistic model of earthquake occurrence based on pore pressure modeling, accounting for the background tectonic stress and individual fault geometry.

In 2015, the population showed increasing concern as a result of widely-felt shaking[30]. In response, and following the regulation strategies proposed by scientists, the Oklahoma Corporate Commission (OCC) finally imposed in February 2016 a reduction of injected volumes by 40% in a wide area including most of the disposal wells[31]. These directives were further reinforced

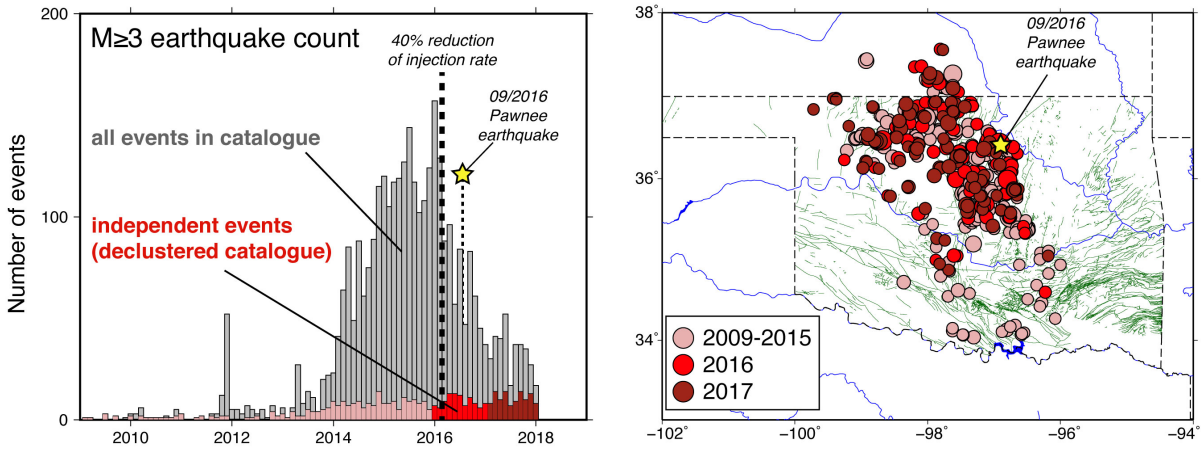

Figure 3.31 – Recent seismicity in Oklahoma [source: declustered catalogue of Petersen et al. 2018]. Grey symbols represent the full catalogue, whereas red-pink-maroon symbols only include the independent events after declustering of the catalogue.

[30] https://www.theguardian.com/us%2Dnews/2016/jan/01/oklahoma%2Dearthquakes%2Doil%2Dgas%2Dindustry%2Dwastewater%2Dinjection

[31] http://www.occeweb.com/News/2016/03%2D07%2D16ADVISORY%2DAOI%2C%20VOLUME%20REDUCTION.pdf

following the 3 September 2016 M5.8 Pawnee earthquake[32]. Since 2016, additional reductions were enforced on a case-by-case basis[33].

Shortly after this reduction of injected volumes of wastewater, a clear decrease in the rate of seismicity was noticed (Fig. 3.31). *Langenbruch and Zoback* [2016] were the first to analyze this sharp decrease in seismicity, and confidently predicted that "*the probability of potentially damaging larger events should (...) approach historic levels within a few years*" [*Langenbruch and Zoback*, 2016].

Nonetheless, a number of objections suggest that triumphalism should be tempered:

- [*Roach*, 2018] rightly pointed that the downturn in oil extraction activity has started well before regulatory actions taken by the OCC, and was in fact primarily driven by the collapse in oil prices on the global market in late 2014 – early 2015. In fact, the regulation issued by the OCC in February 2016 exactly coincides with an historic low in Brent Crude Oil Price (Fig. 3.32).

Figure 3.32 – Brent Crude Oil Prices: 10 Year Daily Chart. Source: `https://www.macrotrends.net/2480/brent-crude-oil-prices-10-year-daily-chart`.

- *Langenbruch and Zoback* [2016] recognized that the recent reduction in injected volumes would take time to produce its expected effect on seismicity, because long-lasting aftershock sequences will continue to produce an elevated rate of seismicity for many years. In other words, the earthquakes that occurred since the recent decrease of seismicity in 2016 still contain a significant number of aftershocks.

- *Petersen et al.* [2018] reported a slight increase in the number of independent earthquakes between 2016 and 2017 (i.e. after declustering the earthquake catalogue), from 100 to 122 events. Therefore, although total earthquake rates undeniably decreased since 2015, the rate of independent events remains at its maximum level (red histogram in Fig. 3.31), leading to maintaining hazard in Oklahoma at a high level[34]. Unfortunately, the last update in the declustered catalogue by USGS was published in March 2018 (`https://www.sciencebase.gov/catalog/item/5a85dc1de4b00f54eb36679d`), which precludes further scrutiny of this trend.

- *Ogwari et al.* [2018] demonstrated, on the basis of a detailed analysis of the Dallas-Fort Worth airport earthquake 2008–2015 sequence, that elevated rates of seismicity were still recorded 6 years after cessation of injection activity (which occurred in 2009 in the investigated area).

[32] `http://www.occeweb.com/News/2016/11%2D03%2D16PAWNEE%20POSTING.pdf`

[33] A summary of recent actions taken by the Oklahoma Corporate Commission can be found at: `http://www.occeweb.com/News/2018/05%2D30%2D18EARTHQUAKEACTIONSUMMARY.pdf` *(last accessed 5 October 2019).*

[34] See also `https://www.rms.com/blog/2018/04/18/earthquakes-in-oklahoma-an-update-on-induced-seismicity-hazard-and-risk-for-2018/`.

- in a comment to the *Langenbruch and Zoback* [2016] study, *Goebel et al.* [2017b] showed that choosing a different tuning of the parameters used by *Langenbruch and Zoback* [2016], while staying within the range of uncertainty on these parameters (in particular the p exponent in Omori's law and the b value), may increase the annual probability of exceedance of M>5 in 2025 from 5% to 40%.

- *Hornbach et al.* [2015] point that a proper understanding of the relationship between the concurrent decrease in injection and seismicity requires a systematic monitoring of seismic activity, which is currently lacking with available networks.

3.4.5 Looking ahead

Accordingly, although fluid injection has been shown to produce, at least in some occasions, a significant component of aseismic deformation [e.g. *Guglielmi et al.*, 2015], geodesy can only provide a modest contribution to a better understanding of the causal relationship between wastewater injection and seismicity. On the other hand, seismology certainly has a greater part to play. Detection of microearthquakes using dense seismic networks and template-matching techniques [e.g. *Meng and Ben-Zion*, 2017; *Ross et al.*, 2019] can bring a significant increase in the number of detected events, which is crucial for computing more robust statistics.

Notwithstanding current limitations of earthquake catalogues, short-term probabilistic seismic hazard forecasts of the USGS have attempted to accommodate the increased seismicity in Oklahoma in their short-term forecasts (1 year) [e.g. *Petersen et al.*, 2018]. In this case, instead of having recourse to sophisticated – and uncertain – physical models of fluid-fault interactions, these models generally rely on "classical" PSHA approaches exploiting seismic catalogues, disregarding of the details of fault geometries or fluid injection parameters.

Unfortunately, for regions with geodetic strain rates $< 10^{-9}$ yr^{-1}, historical seismic catalogues may be too short to contain the largest seismic events, i.e. those that released most of the seismic or geodetic moment [*Ward*, 1998], which makes this approach even more uncertain than in regions of elevated natural seismicity. The difficulty to assess the maximum magnitude M_{max} is indeed a major source of epistemic uncertainty in PSHA models [e.g. *Bommer and van Elk*, 2017]. What is more, a few studies have suggested that even the largest earthquakes reported in historical catalogues may have already been induced by oil-related activity, which started as early as the beginning of the 20th century, both in Oklahoma [*Hough and Page*, 2015], Texas [*Frohlich et al.*, 2016b; *Everley*, 2016; *Frohlich et al.*, 2016a] and California [*Hough and Bilham*, 2018], making M_{max} even more uncertain.

Furthermore, evidence for Holocene faulting on the Meers fault, outcropping in western Oklahoma [*Crone and Luza*, 1990], indicates that the area may have not been as seismically quiet as originally thought. In fact, a body of evidence suggests that seismicity in the intraplate region of the Central US (which includes Oklahoma) may be characterized by long intervals, separating moderate to large magnitude events, possibly clustered in time [*Calais et al.*, 2016; *Liu and Stein*, 2016]. These features are evidently difficult to assess from instrumental seismicity, especially during the present period of "anomalous" seismicity.

In recent years, a sustained global demand for oil and gas, combined with a increased quest for energy self-sufficiency, have pushed governments and operators to exploit new plays using unconventional techniques. This increase in extraction activity has generated a renewed interest for induced seismicity in geodynamically contrasted regions, such as the UK [*Hicks et al.*, 2019],

the Netherlands [*van Elk et al.*, 2017], Poland [*López-Comino et al.*, 2018] or the Sichuan basin in China [*Lei et al.*, 2017; *Chen et al.*, 2018]. In parallel, claims of an anthropic responsibility in the occurrence of a number of recent earthquakes are growing [see e.g. the online data base of *Wilson et al.*, 2017, available at `https://inducedearthquakes.org`]. The disagreement among scientist about the actual role of man in inducing earthquakes is more profound that it may seem. Indeed, the debate surrounding the issue of man-induced seismicity extends well beyond the academic sphere. In spite of a more limited societal impact, man-induced earthquakes give rise to arguments sharing many common features with a number of famous scientific controversies in the field of environmental science, including: (a) the controversy over the effects of tobacco on cancer and cardiovascular diseases in the 1970s-1980s, (b) the controversy over human responsibility in global warming in the 1990s-2000s, or (c) the controversy about the relationship between mass extinction of entomofauna and the widespread use of neonicotinoids in the 2000s-2010s. Indeed, these controversies involve similar ingredients: economic lobbies, denial, lack of political will, intended confusion between correlation and causality, contradiction between doubt (which generally prevails in the scientific method) and alarmism, tension between the tendency to think that technology will beat nature and the precautionary principle.

The collision between economic, political, societal and scientific interests will certainly keep induced seismicity a hot topic in the coming years, unless the recent decrease of seismicity leads to a shift of public interest to other urgent matters.

3.5 Reinterpretation of legacy geodetic data.

3.5.1 A digression about the 1954 Nevada earthquake sequence

As discussed in Section 1.3, when interpreting geodetic data spanning the time of occurrence of an earthquake, it is often convenient to display results in terms of vectors showing the horizontal components of the displacement field. This type of representation is useful to convey the result of the geodetic analysis in a comprehensive way, which makes it easier for the geologist to interpret the observations in terms static deformation due to faulting. However, the process by which vectors are deduced from raw geodetic observations requires an adjustment of observational errors across the network, which is achieved by means of a least-squares optimization procedure [e.g. *Bomford*, 1975]. In some cases, this process is computationally unstable because the number of observations is just enough to resolve internal strain in the network, but insufficient to robustly constrain broader deformation at the scale of the network. Furthermore, unless the survey is tied to a regional reference frame which is assumed to be unstrained, which is rarely the case, there is no way to determined the global translation and rotation of the whole network. As a result, it is often necessary to make a certain number of assumptions in order to stabilize the problem. These assumption generally take the form of forcing certain elements to be held fixed (e.g. station coordinate, vector direction, station-to-station angle). Unfortunately, these assumptions sometimes prove to be too stringent, or even completely wrong, as the understanding of actual deformation at the time of the processing may be incomplete.

The 1954 earthquake sequence of Nevada (USA) provides an instructive illustration of the possible caveats entailed by flawed assumptions during the processing of raw geodetic data (Fig. 3.33). The sequence started in July 1954 with an M_S6.6 earthquake on the Rainbow fault. By chance, a triangulation survey was being carried out at the same time in the area. Another earthquake struck during the course of the survey (23 August 1954, M_S6.8). After the survey was complete, the strongest shock of 16 December 1954 finally happened. This event was in fact a double one, consisting of a strong surface-breaking M_S7.2 "Fairview Peak" event, with an oblique focal mechanism (combining normal and strike-slip), followed 4 minutes later by the M_S6.8 "Dixie Valley" event, associated with pure normal-faulting. As a result of this extraordinary powerful sequence, it was decided to organize a post-earthquake geodetic survey, which was completed in 1955.

The horizontal displacement field shown in the top panel of Fig. 3.33 is the result of a least-squares adjustment and differencing of the two pre- and post-earthquake surveys. In order to stabilize the problem, a set of stations coordinates were held fixed [*Whitten*, 1957]. These reference points are indicated by blue crosses. Unfortunately, at the time when the data were processed, the importance of deformation in the area surrounding the Dixie Valley fault was overlooked, so that a fixed point was set right above the fault involved in the second event of the earthquake doublet. The reason for this underestimation of the importance of the second event may be plausibly attributed to a combination of factors, including (1) lack of control points further to the North, which means that the Dixie Valley earthquake was situated on the edge of the network, (2) lack of acknowledgement of surface ruptures along the Dixie Valley fault trace by the geodetic team, (3) smaller moment magnitude of the second event, which led to a mainly focusing the study on the stronger Fairview Peak event and (4) difficulty of seismologists at that time to model the second shock, which occurred four minutes only after the mainshock.

As a result of this erroneous assumption, the whole displacement field was distorted, so

Fairview Peak-Dixie Valley sequence, 1954

Original *[Whitten, 1957; Meister et al., 1968]*

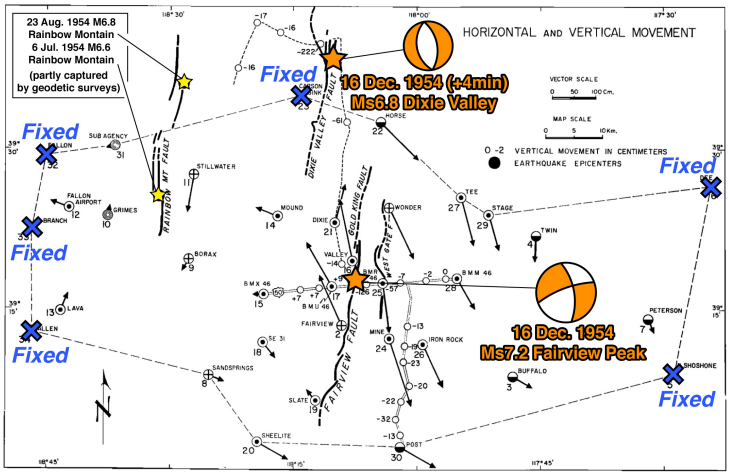

Re-interpreted *[Hodgkinson et al., 1996]*

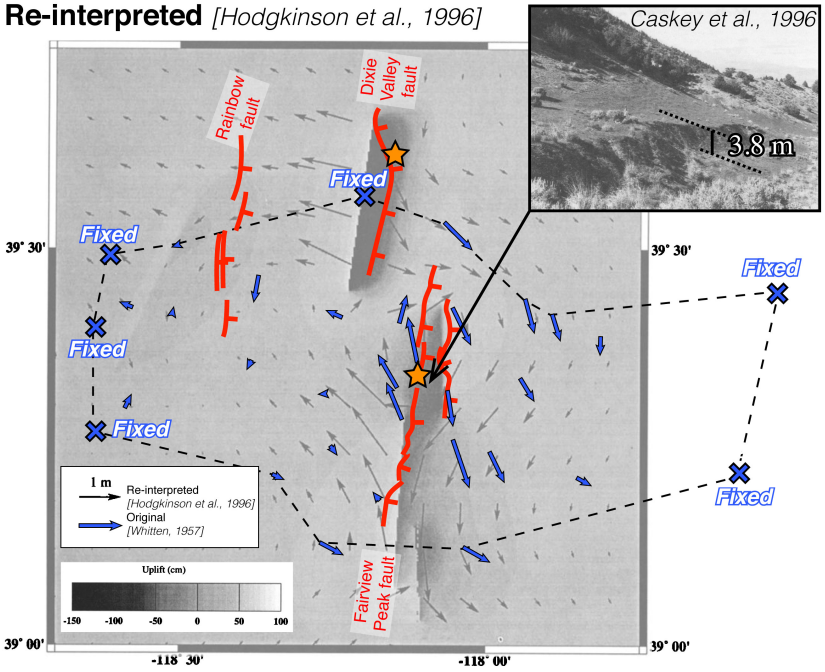

Figure 3.33 – Static displacement field of the Fairview Peak-Dixie Valley eathquake sequence (16 December 1954, M_S6.8 and M_S7.2). Top panel shows the horizontal vectors deduced from two triangulation surveys conducted in the summer of 1954 and in 1955, respectively [modified after Whitten, 1957; Meister et al., 1968]. Dashed polygon indicates the contour of the networks. Focal mechanisms are from Doser [1986]. Bottom panel shows the predicted displacement field from elastic modeling after re-interpretation of the geodetic data [modified from Hodgkinson et al., 1996]. Blue vectors are original vectors from upper panel rescaled for consistency. Inset shows surface rupture in the region of maximum surface deformation, as photographed in 1994 [from Caskey et al., 1996]. Blue crosses indicate the location of benchmarks whose coordinates were assumed to be fixed during the processing. Note that elastic modeling predicts substantial displacement at the benchmark located closest to the Dixie Valley fault.

that further analysis of the earthquake starting from the vector field of [*Whitten*, 1957] kept stumbling on apparent discrepancies between "observations" and predictions [e.g. *Meister et al.*, 1968; *Savage and Hastie*, 1969].

The Fairview example shows that incorrect coseismic vector fields can be the result of various sources of errors:

- measurement errors during the survey;
- instability in the compensation procedure;
- differences in network configuration between the surveys (e.g. before *versus* after earthquake);
- limited size of the network with respect to deformed region, leading to difficulty or impossibility to identify stable points;
- incorrect assumptions about fixed points / directions / angles between surveys caused.

As illustrated here, an improved understanding of the first-order features of the deformation, gained by accumulating observations of coseismic deformation over the past decades, has allowed for a re-interpretation of the original geodetic dataset, which made it possible to compute an updated, more robust source model of the 1954 earthquake sequence.

3.5.2 Geodetic strain in the Asal rift between 1978 and 2004

In this second example, we focus on the exceptional dataset acquired between 1972 and 2014 in the Asal rift, as part of a long-standing project carried out by Institut Géographique National (IGN), IPGP and other partners (including the IPG of Strasbourg). This dataset consists in trilateration and triangulation measurements that captured the 1978 Ardoukôba volcano-seismic crisis, exceptional event involving an eruption, a dike injection and spectacular normal faulting [*Ruegg et al.*, 1979]. A similar rifting episode was observed in the Krafla rift in Iceland in the 1970s-1980s [*Tryggvason*, 1984]. However, at that time, the details of the interaction between magma bodies and faults were not fully understood. Another event was captured by modern geodetic in Ethiopia from 2005 and 2011, and produced a wealth of results thanks, in particular, to InSAR [*Wright et al.*, 2006; ***Grandin** et al.*, 2009]. This recent Ethiopian event gave a new perspective on the previous 1978 Ardoukôba crisis, which motivated a re-interpretation of the old geodetic dataset gathered over the past decades in the Asal rift *Smittarello, **Grandin** et al.* [2016].

When the Asal rift network was originally designed in 1972, the broad area that would be affected by the 1978 rifting episode had not been fully anticipated. On the other hand, lack of surface manifestation of magma movement at depth made it difficult to recognize the existence of buried pressure sources, in particular in the vicinity of the Fieale volcano, at the center of the rift. As a result of this lack of information, assumptions made at that time about fixed points in the compensation procedure are subject to potential errors.

The effect of incorrect assumptions about fixed points in the compensation procedure of this previous dataset is further illustrated in the synthetic example of Fig. 3.34, extracted from *Smittarello, **Grandin** et al.* [2016]. Here, a synthetic analysis of trilateration data is developed, using the actual network configuration of the Asal rift (Djibouti) described by *Ruegg and Kasser* [1987]. The simulated data set consists in range measurements at two epochs, computed with the assumption that the network was affected by deformation from a pressure source indicated by the

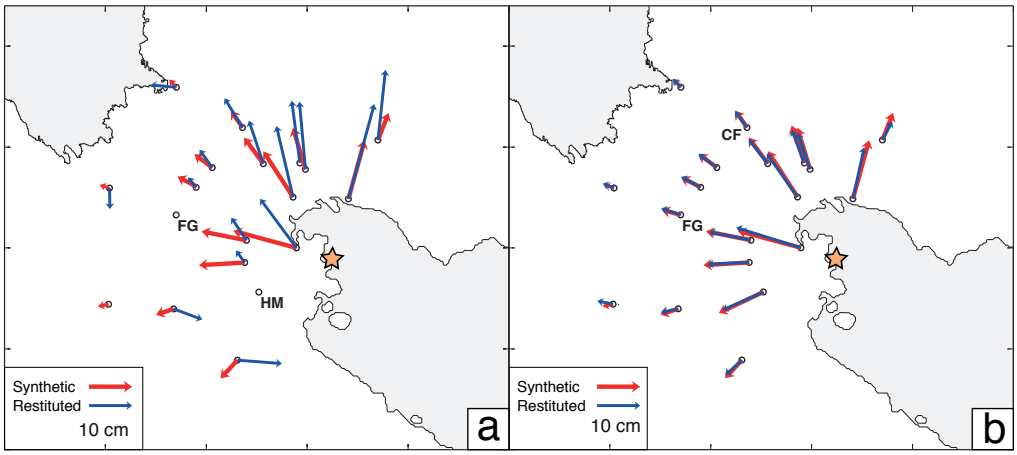

*Figure 3.34 – Asal rift (Djibouti) synthetic test. Left panel : FG and HM fixed during compensation. Right panel : FG fixed during compensation, then direction of relative motion between FG and CF is fixed a posteriori a posteriori [Smittarello, **Grandin** et al., 2016].*

orange star. Network compensation is first achieved under the assumption that the coordinates of two points are unchanged in the two surveys. The chosen points for this example are FG and HM, as in *Ruegg and Kasser* [1987]. At that time, it was thought that FG–HM being parallel to the rift, they would capture the block motion of one side of the rift with respect to the other. However, the role of pressure sources in creating a radial displacement field was overlooked.

Fig. 3.34a shows that the restituted vector field, in blue, differs significantly from the "true" vector field. Furthermore, the difference between the two vector fields does not display any simple pattern, at least to the untrained eye, which makes it difficult to understand what is going wrong. Severe deformation, including shearing and rotations, is caused by the assumption that points FG and HM are fixed, which is obviously not the case in the "true" vector field. Alternatively, one can retrieve the correct vector field by assuming that only one point remains fixed in the network compensation (here, FG). The resulting vector field (not shown) is contaminated with a residual global rotation around point FG, plus a residual global translation. Both of these unknowns can be estimated with reasonable success by assuming, *a posteriori* (i.e. after compensation) that the direction of relative displacement between points FG and CF remains parallel to the direction FG–CF (Fig. 3.34b).

The reason for this success is that the assumed source of deformation produces a symmetric displacement for points CF and FG, where symmetry is here meant with respect to a direction oriented NW-SE. This direction actually coincides with the direction of the plate boundary between Nubia and Arabia. Any source of deformation meeting this condition will be resolvable with this method. This includes any dike injection or pressure source, as long as they remain aligned along the plate boundary.

Coming back to the Fairview example, a more advanced analysis was proposed by *Hodgkinson et al.* [1996] in order to correct for the effect of poor network compensation (lower panel of Fig. 3.33). In this work, the raw geodetic data (i.e. angle and distance measurements) are directly used in a slip inversion of the earthquake, instead of inverting a potentially flawed set of vectors prior to the slip inversion. The vector field predicted by the inversion differs significantly from the vector field deduced from the original network compensation.

Accordingly, the above procedures (from *Hodgkinson et al.* [1996] and *Smittarello, **Grandin** et al.* [2016]) require that the geometry (and the nature) of the sources of deformation be already known *a priori*. Such an information may not be available at the time of surveying the networks, as progress is constantly made in our understanding of deformation processes affecting the lithosphere. But once sufficient knowledge is gained, re-interpretation of legacy geodetic data can prove extremely fruitful in constraining crucial information about the evolution of sources of deformation through time.

This is further illustrated in Fig. 3.35, where trilateration data spanning the period 1979–1984 is inverted to determine the evolution of inflation along and across the Asal rift. The modeled sources of deformation consist in a dike-like body lying along the plate boundary from the surface down to 4 km depth, and a Mogi-like pressure source centered on the dike, at 5 km depth. These sources simulate a transient magma influx to the rift following the seismic-volcanic crisis of Ardoukôba in 1978. Such an enhanced, transient magma supply underneath a rift recently affected by a dike injection originates from observations gained thanks to InSAR in

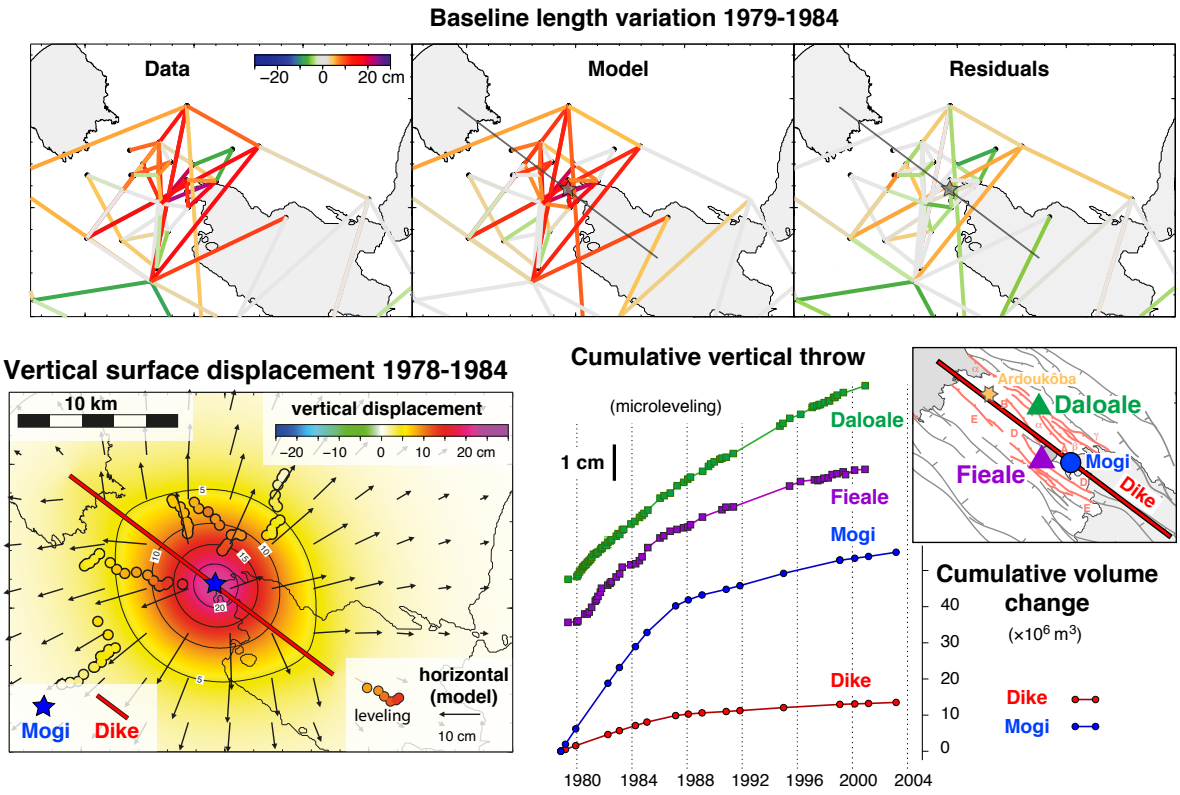

*Figure 3.35 – Top: observed, modeled and residual range changes from two trilateration surveys in 1979 and 1984, using a model consisting of a dike-like body and Mogi-like pressure source (see inset to the right). Bottom left: synthetic displacement field. Bottom right: evolution of the cumulative volume increase for the two sources of deformation (blue: dike; red: Mogi). Green and purple time-series show the evolution of vertical throw measured at short time intervals at two locations along the rift axis (not used in the inversion). Note the similarity of the Mogi source (blue) and the vertical throw at the nearby Fieale site (purple). Adapted from Smittarello, **Grandin** et al. [2016]. All data from Ruegg and Kasser [1987].*

the Manda Hararo rift during the 2005–2011 rifting episode [e.g ***Grandin** et al.*, 2010]. Using this model, trilateration data is fit with reasonable success, with residuals nowhere exceeding 10 centimeters. Furthermore, residual range changes are in general proportional to baseline length, which provides confidence in the absence of systematic residuals.

The assumption that deformation is caused by the same two sources throughout the 25 years following the 1979 survey suggests that the rift has expanded at a fast rate (i.e. faster than the steady-state rate during the post-2000 GPS era) in the $\sim$ 8 years after the Ardoukôba crisis (1978–1986). In 1986, a substantial slowdown of deformation is deduced from the same analysis of repeated trilateration surveys (Fig. 3.35). This abrupt change in the rate of deformation points to a magmatic source for the restituted deformation, as other processes such as viscous relaxation would predict a more gradual deceleration of deformation.

To conclude, the Ardoukôba and the Fairview Peak-Dixie Valley sequences illustrate the great value of old geodetic data [see also e.g. the reanalysis of the great 1923 Kanto earthquake in *Nyst et al.*, 2006]. Curation of geodetic data is essential to avoid the loss of information and an impossibility to reanalyze these "legacy" data in the light of the experience gained since their acquisition many decades ago.

Conclusion

Outlook

Based on the main conclusions identified in this report, a number of general prospective research directions are indicated in the following list.

- **Exploit geodetic data at high spatial and temporal resolution**, in particular space imagery:
  - High spatial resolution: modern space imagery, both optical and radar, is now able to deliver images with a spatial resolution better than 1 meter. This high spatial resolution, associated with state-of-the-art processing techniques, will improve our understanding of small-scale (short spatial wavelength) features of the displacement, the strain field, and the topography. Such information is extremely rich, especially for surface ruptures associated with large earthquakes. The full strain field associated with surface ruptures has recently revealed a high degree of variability along the ruptures, both due to a complex geometry of the fault trace, as well as along-strike fluctuations of the slip vector (e.g. Balochistan earthquake). The influence of gravity and dynamic stress changes starts to become apparent in these observations, which further complexifies the picture. On the other hand, near-fault deformation informs on the mechanical behavior of the fault zone, and allows for quantifying potential off-fault deformation and associated damage. More observations and better models need to be combined to understand the mechanisms that control this apparent complexity. As the natural variability of individual surface ruptures from outcrop scale to segment scale is quantified by analyzing a sufficient number of modern analogues, a re-interpretation of paleaoseismological observations could be undertaken. In particular, key assumptions behind seismic hazard assessment models (characteristic earthquake model, seismic cycle model, recurrence interval, segmentation) will become more and more testable. Furthermore,
  - High temporal resolution: on the other hand, high temporal resolution is instrumental in enabling a separation of processes that would otherwise be mixed, such as mainshocks and their aftershocks (e.g. Gorkha earthquake, Pedernales earthquake), or individual events in a given sequence (e.g. Norcia sequence, Kumamoto sequence). As more frequent acquisitions will become available, more complex phenomena will be discovered. High temporal resolution is also desirable to diminish the detection threshold of InSAR, as atmospheric corrections are facilitated by the availability of a greater number of independent interferograms (e.g. Oklahoma earthquake). Finally, transient signals can only be revealed if sufficient temporal

sampling is available. In combination with GPS, postseismic signals (relaxation, afterslip) will be better imaged and hence better understood.

- Large spatial scale: as explained above, high temporal resolution can only been achieved by wide-swath imaging modes. For conventional SAR imaging techniques, this objective comes at the expense of high spatial resolution, so that these two objectives cannot be met with a single system consisting of only a limited number of satellites (say, <5). Future SAR systems will overcome this limitation, allowing for high-resolution wide-swath (HRWS) imaging. Long spatial wavelength surface deformation will therefore be measurable, which will represent a new challenge, as large-scale atmospheric and ionospheric effects will have to be mitigated. Integration with GPS data will probably be required to provide a coherent reference frame, necessary to capture deformation at all spatial scales Once this objective is met, a better understanding of interseismic signals affecting continental fault systems will be possible, in particular the significance of the vertical component of deformation in contexts of tectonic compression (e.g. active orogens) or extension (e.g. continental rifting).
- Continuity: in order to study deformation over time scales of decades or more, a continuity of the measurements is desirable. Follow-up units as part of satellite missions such as Sentinel-1 will be essential to fulfill this objective. This fact should be recalled to the space agencies by the scientific community of earthquake geodesy.

- **Develop realistic mechanical models**: as more detailed observations of surface ruptures become available, the limits of simple linear elastic models become more and more exposed. These limitations likely arise from the peculiar behavior of fractured rocks at low confining pressure, which cannot be fully described by the simple models that reproduce satisfactorily deformation at large-scale. Furthermore, strong dynamic stress perturbations are suspected to lead to substantial off-fault damage in certain specific locations, leading to rock yield and thereby distorting the strain field at the surface. Such effects are inadequately modeled by classical tools used in most static slip inversions. Finite element methods are more adapted to model a complex geometry or a complex medium, but information often lacks to constrain the model parameters (fault geometry, distribution of elastic parameters, presence of pre-existing structures). Discrete element techniques may represent a possibility to reproduce rock deformation at shallow depth, but the computational cost of these techniques remains high. Boundary element methods are computationally efficient, but require a priori knowledge of fault geometry and careful meshing. In all cases, harnessing inversion strategies with computationally expensive forward models remains a major challenge. As the superiority of these complex mechanical models in explaining near- and on-fault observations in a consistent manner will become more and more apparent, efforts in this direction will certainly be fostered.

- **Foster joint inversions of geodetic, seismological and tsunami data**: geodetic data, and especially InSAR, provides crucial information about the geometry of the fault, as well as slip distribution. However, resolution on these two parameters decreases dramatically with depth. On the other hand, kinematic inversion of seismological records are often stabilized when the fault geometry and the final slip distribution are independently constrained. In the specific case of megathrust earthquakes, both geodetic and seismological

data may suffer from a poor resolution at the trench. Records of tsunami waves from offshore buoys can help filling this gap, but this requires the use of sophisticated numerical simulations of tsunami waves, in addition to the development of joint inversion techniques that can exploit at best the complementarity between the different data sets.

- **Develop seafloor instrumentation**: in the same line, onland measurements often lack resolution on processes occurring offshore. Seafloor instrumentation, in particular seafloor geodesy, has long been recognized as a promising path towards a better characterization of earthquake phenomena occurring at the ocean bottom. Our understanding of both subduction processes and mid-ocean ridge processes would benefit from seafloor geodesy. Technological progress in optical fiber and pressure sensors may soon bring this challenging objective into the real world.

- **Improve seismic (and aseismic) catalogues**: transient phenomena affecting tectonic faults can also be detected by carefully tracking seismic emissions on and near these faults. Subtle transients lead to tiny earthquakes, which can only be studied collectively provided a sufficiently complete seismic catalogue is available. To this end, automatic procedures to detect, classify, characterize and locate micro-earthquakes buried in seismological noise should be promoted. Such improved catalogues should benefit to the study of:

  - megathrust transients : by enabling the identification of slow-slip events, repeating quakes, and their potential space-time evolution;
  - injection-induced earthquakes : by tracking seismicity, a proxy for the diffusion of stress perturbations in the medium;
  - normal faulting sequences : by carefully locating seismicity in space, thereby illuminating potentially active satellite faults surrounding a master fault.

- **Expand paleaoseismological and tectonic studies**: the study of contemporary earthquakes using modern seismological and geodetic techniques should go along with a continued effort to document past historical and pre-historical earthquakes. Progress in paleoseismology can help recover information that is not accessible to modern observations. However, the study of recent events has shown the great spatial variability in the amount of surface slip along-strike, and the existence of repeated rupture of a single surface fault during the course of a single sequence has been clearly documented (e.g. the 2016 Norcia earthquake). Two-dimensional trenching and progress in dating techniques could help better deciphering the chronology of ruptures at the time scale of a full seismic cycle, while bringing refined information on the space-time distribution of slip during an event.

- **Improve communication and outreach**: In the event of a large earthquake, questions arise naturally among the general public about the short-term hazards to come. Feedback provided by earthquake scientists is crucial for helping citizens make the distinction between false theories and trusted information. However, models attempting to forecast earthquake hazard are subject to a great number of unknowns, which often makes it difficult to communicate the issues that populations face in the immediate aftermath of an earthquake. Better understanding how scientific speech can be perceived is essential to use the proper terms and gain a deeper impact. Recognition of the existence of multiple,

possibly coincidental hazards is also essential to better anticipate the worst-case scenarios (e.g. earthquake and triggered landslides, such as during the 2005 Kashmir earthquake [e.g. *Dunning et al.*, 2007]; volcano eruption and tropical storm, such as during the 1991 Pinatubo eruption [e.g. *Newhall and Punongbayan*, 1996]). In this respect, more interdisciplinary research is required at the interface between seismology, tectonics, meteorology and geomorphology, extending to information technology, communication studies, psychology and sociology.

Bibliography

Agnew, D. C., et al. (2002), History of seismology, *International handbook of earthquake and engineering seismology*, *81*, 3–11.

Agram, P., R. Jolivet, B. Riel, Y. Lin, M. Simons, E. Hetland, M.-P. Doin, and C. Lasserre (2013), New radar interferometric time series analysis toolbox released, *Eos, Transactions American Geophysical Union*, *94*(7), 69–70.

Aki, K., and P. G. Richards (1980), *Quantitative Seismology*, University Science Books.

Ali, S., K. Feigl, B. Carr, T. Masterlark, and F. Sigmundsson (2014), Geodetic measurements and numerical models of rifting in Northern Iceland for 1993–2008, *Geophysical Journal International*, *196*(3), 1267–1280.

Allen, T. I., D. J. Wald, P. S. Earle, K. D. Marano, A. J. Hotovec, K. Lin, and M. G. Hearne (2009), An Atlas of ShakeMaps and population exposure catalog for earthquake loss modeling, *Bulletin of Earthquake Engineering*, *7*(3), 701–718.

Allmann, B. P., and P. M. Shearer (2009), Global variations of stress drop for moderate to large earthquakes, *Journal of Geophysical Research: Solid Earth*, *114*(B1).

Almeida, R., E. O. Lindsey, K. Bradley, J. Hubbard, R. Mallick, and E. M. Hill (2018), Can the Updip Limit of Frictional Locking on Megathrusts Be Detected Geodetically? Quantifying the Effect of Stress Shadows on Near-Trench Coupling, *Geophysical Research Letters*, *45*(10), 4754–4763.

Ambraseys, N. (2009), *Earthquakes in the Mediterranean and Middle East: a multidisciplinary study of seismicity up to 1900*, Cambridge University Press.

Amoruso, A., L. Crescentini, and R. Scarpa (1998), Inversion of source parameters from near-and far-field observations: An application to the 1915 Fucino earthquake, central Apennines, Italy, *Journal of Geophysical Research: Solid Earth*, *103*(B12), 29,989–29,999.

Amoruso, A., L. Crescentini, and C. Fidani (2004), Effects of crustal layering on source parameter inversion from coseismic geodetic data, *Geophysical Journal International*, *159*(1), 353–364.

Ampuero, J.-P., and Y. Ben-Zion (2008), Cracks, pulses and macroscopic asymmetry of dynamic rupture on a bimaterial interface with velocity-weakening friction, *Geophysical Journal International*, *173*(2), 674–692.

Ampuero, J.-P., and F. Dahlen (2005), Ambiguity of the moment tensor, *Bulletin of the Seismological Society of America*, *95*(2), 390–400.

Anderson, E. M. (1936), The dynamics of the formation of cone-sheets, ring-dykes, and caldron-subsidences, *Proc. Roy. Soc. Edin.*, *56*, 128–157.

Armigliato, A., and S. Tinti (2003), Influence of topography on coseismic displacements induced by the Friuli 1976 and the Irpinia 1980 earthquakes (Italy) analyzed through a two-dimensional hybrid model, *Journal of Geophysical Research: Solid Earth*, *108*(B12).

Armijo, R., P. Tapponnier, J. Mercier, and T.-L. Han (1986), Quaternary extension in southern Tibet: Field observations and tectonic implications, *Journal of Geophysical Research: Solid Earth*, *91*(B14), 13,803–13,872.

Armijo, R., P. Tapponnier, and T. Han (1989), Late Cenozoic right-lateral strike-slip faulting in southern Tibet, *Journal of Geophysical Research: Solid Earth*, *94*(B3), 2787–2838.

Armijo, R., B. Meyer, G. King, A. Rigo, and D. Papanastassiou (1996), Quaternary evolution of the Corinth Rift and its implications for the Late Cenozoic evolution of the Aegean, *Geophysical Journal International*, *126*(1), 11–53.

Armstrong, M., and R. Jabin (1981), Variogram models must be positive-definite, *Mathematical Geology*, *13*(5), 455–459.

Arnadóttir, T., and P. Segall (1994), The 1989 Loma Prieta earthquake imaged from inversion of geodetic data, *Journal of Geophysical Research: Solid Earth*, *99*(B11), 21,835–21,855.

Arrowsmith, J. R., C. J. Crosby, A. M. Korzhenkov, E. Mamyrov, I. Povolotskaya, B. Guralnik, and A. Landgraf (2016), Surface rupture of the 1911 Kebin (Chon–Kemin) earthquake, Northern Tien Shan, Kyrgyzstan, *Geological Society, London, Special Publications*, *432*, SP432–10.

Ataeva, G., A. Shapira, and A. Hofstetter (2015), Determination of source parameters for local and regional earthquakes in Israel, *Journal of Seismology*, *19*(2), 389–401.

Atwater, B. F., M. P. Tuttle, E. S. Schweig, C. M. Rubin, D. K. Yamaguchi, and E. Hemphill-Haley (2003), Earthquake recurrence inferred from paleoseismology, *Developments in Quaternary Sciences*, *1*, 331–350.

Avouac, J.-P. (2015), Mountain Building: From earthquakes to geological deformation, *Treatise on geophysics*, *6*, 381–432.

Avouac, J.-P., and P. Tapponnier (1993), Kinematic model of active deformation in central Asia, *Geophysical Research Letters*, *20*(10), 895–898.

Backus, G., and F. Gilbert (1968), The resolving power of gross earth data, *Geophysical Journal of the Royal Astronomical Society*, *16*(2), 169–205.

Backus, G. E., and J. Gilbert (1967), Numerical applications of a formalism for geophysical inverse problems, *Geophysical Journal International*, *13*(1-3), 247–276.

Baillard, C., H. Lyon-Caen, L. Bollinger, A. Rietbrock, J. Letort, and L. B. Adhikari (2017), Automatic analysis of the Gorkha earthquake aftershock sequence: evidences of structurally segmented seismicity, *Geophysical Journal International*, *209*(2), 1111–1125.

Bak, P., and C. Tang (1989), Earthquakes as a self-organized critical phenomenon, *Journal of Geophysical Research: Solid Earth*, *94*(B11), 15,635–15,637.

Ballu, V., P. Bonnefond, S. Calmant, M.-N. Bouin, B. Pelletier, O. Laurain, W. Crawford, C. Baillard, and O. De Viron (2013), Using altimetry and seafloor pressure data to estimate vertical deformation offshore: Vanuatu case study, *Advances in Space Research*, *51*(8), 1335–1351.

Bamler, R., and P. Hartl (1998), Synthetic aperture radar interferometry, *Inverse problems*, *14*(4), R1.

Bao, H., J.-P. Ampuero, L. Meng, E. J. Fielding, C. Liang, C. W. D. Milliner, T. Feng, and H. Huang (2019), Early and persistent supershear rupture of the 2018 magnitude 7.5 Palu earthquake, *Nature Geoscience*, *12*(1), s41,561–018–0297–z.

Barbot, S., Y. Fialko, and D. Sandwell (2008), Effect of a compliant fault zone on the inferred earthquake slip distribution, *Journal of Geophysical Research: Solid Earth*, *113*(B6).

Barbot, S., Y. Hamiel, and Y. Fialko (2008), Space geodetic investigation of the coseismic and postseismic deformation due to the 2003 M_w7.2 Altai earthquake: Implications for the local lithospheric rheology, *J. Geophys. Res.*, *113*(B3), doi:10.1029/2007JB005063.

Barbot, S., Y. Fialko, and D. Sandwell (2009), Three-dimensional models of elastostatic deformation in heterogeneous media, with applications to the Eastern California Shear Zone, *Geophysical Journal International*, *179*(1), 500–520.

Barnhart, W., and R. Lohman (2010), Automated fault model discretization for inversions for coseismic slip distributions, *Journal of Geophysical Research: Solid Earth*, *115*(B10).

Båth, M. (1965), Lateral inhomogeneities of the upper mantle, *Tectonophysics*, *2*(6), 483–514.

Bawden, G. W. (2001), Source parameters for the 1952 Kern County earthquake, California: A joint inversion of leveling and triangulation observations, *Journal of Geophysical Research: Solid Earth*, *106*(B1), 771–785.

Beauducel, F., P. Briole, and J.-L. Froger (2000), Volcano-wide fringes in ERS synthetic aperture radar interferograms of Etna (1992–1998): Deformation or tropospheric effect?, *Journal of Geophysical Research: Solid Earth*, *105*(B7), 16,391–16,402.

Bechor, N. B. D., and H. A. Zebker (2006), Measuring two-dimensional movements using a single InSAR pair, *Geophys. Res. Lett.*, *33*, 16,311–+, doi:10.1029/2006GL026883.

Bedford, J., M. Moreno, B. Schurr, M. Bartsch, and O. Oncken (2015), Investigating the final seismic swarm before the Iquique-Pisagua 2014 Mw 8.1 by comparison of continuous GPS and seismic foreshock data, *Geophysical Research Letters*, *42*(10), 3820–3828.

Béjar-Pizarro, M., D. Carrizo, A. Socquet, R. Armijo, S. Barrientos, F. Bondoux, S. Bonvalot, J. Campos, D. Comte, J. De Chabalier, et al. (2010), Asperities and barriers on the seismogenic zone in North Chile: state-of-the-art after the 2007 M w 7.7 Tocopilla earthquake inferred by GPS and InSAR data, *Geophysical Journal International*, *183*(1), 390–406.

Bekaert, D., A. Hooper, and T. Wright (2015a), Reassessing the 2006 Guerrero slow-slip event, Mexico: Implications for large earthquakes in the Guerrero Gap, *Journal of Geophysical Research: Solid Earth*, *120*(2), 1357–1375.

Bekaert, D., R. Walters, T. Wright, A. Hooper, and D. Parker (2015b), Statistical comparison of InSAR tropospheric correction techniques, *Remote Sensing of Environment*, *170*, 40–47.

Ben-Menahem, A. (1995), A concise history of mainstream seismology: Origins, legacy, and perspectives, *Bulletin of the Seismological Society of America*, *85*(4), 1202–1225.

Ben-Zion, Y. (2008), Collective behavior of earthquakes and faults: Continuum-discrete transitions, progressive evolutionary changes, and different dynamic regimes, *Reviews of Geophysics*, *46*(4).

Benoit, A., B. Pinel-Puysségur, R. Jolivet, and C. Lasserre (2019), PhaCo: an algorithm based on phase closure for the correction of unwrapping errors in SAR interferometry, https://hal.archives-ouvertes.fr/hal-02152196

Berardino, P., G. Fornaro, R. Lanari, and E. Sansosti (2002), A new algorithm for surface deformation monitoring based on small baseline differential SAR interferograms, *IEEE Transactions on Geoscience and Remote Sensing*, *40*, 2375–2383, doi:10.1109/TGRS.2002.803792.

Bernard, P. (2001), From the search of "precursors" to the research on "crustal transients", *Tectonophysics*, *338*(3-4), 225–232.

Besse, J., V. Courtillot, J. Pozzi, M. Westphal, and Y. Zhou (1984), Palaeomagnetic estimates of crustal shortening in the Himalayan thrusts and Zangbo suture, *Nature*, *311*(5987), 621.

Biamonte, J., P. Wittek, N. Pancotti, P. Rebentrost, N. Wiebe, and S. Lloyd (2017), Quantum machine learning, *Nature*, *549*(7671), 195.

Bie, L., I. Ryder, and M. Métois (2017), Deep postseismic viscoelastic relaxation excited by an intraslab normal fault earthquake in the Chile subduction zone, *Tectonophysics*, *712*, 729–735.

Biggs, J., T. Wright, Z. Lu, and B. Parsons (2007), Multi-interferogram method for measuring interseismic deformation: Denali Fault, Alaska, *Geophysical Journal International*, *170*(3), 1165–1179.
Biggs, J., S. Ebmeier, W. Aspinall, Z. Lu, M. Pritchard, R. Sparks, and T. Mather (2014), Global link between deformation and volcanic eruption quantified by satellite imagery, *Nature communications*, *5*, 3471.
Bilham, R. (2019), Himalayan earthquakes: a review of historical seismicity and early 21st century slip potential, *Geological Society, London, Special Publications*, *483*, SP483–16.
Bilham, R., and N. Ambraseys (2005), Apparent Himalayan slip deficit from the summation of seismic moments for Himalayan earthquakes, 1500–2000, *Current science*, pp. 1658–1663.
Bilham, R., and P. England (2001), Plateau "pop-up" in the great 1897 Assam earthquake, *Nature*, *410*(6830), 806.
Bilham, R., and E. Fielding (2013), Remote sensing and the search for surface rupture, Haiti 2010, *Natural hazards*, *68*(1), 213–217.
Bilham, R., and S. Hough (2006), Future earthquakes on the Indian subcontinent: inevitable hazard, preventable risk, *South Asian Journal*, *12*(5), 1–9.
Bilham, R., K. Larson, and J. Freymueller (1997), GPS measurements of present-day convergence across the Nepal Himalaya, *Nature*, *386*(6620), 61.
Bilham, R., D. Mencin, R. Bendick, and R. Bürgmann (2017), Implications for elastic energy storage in the Himalaya from the Gorkha 2015 earthquake and other incomplete ruptures of the Main Himalayan thrust, *Quaternary International*, *462*, 3–21.
Bird, P., D. D. Jackson, Y. Y. Kagan, C. Kreemer, and R. Stein (2015), GEAR1: A global earthquake activity rate model constructed from geodetic strain rates and smoothed seismicity, *Bulletin of the Seismological Society of America*, *105*(5), 2538–2554.
Blaikie, P., T. Cannon, I. Davis, and B. Wisner (2005), *At risk: natural hazards, people's vulnerability and disasters*, Routledge.
Blewitt, G., M. B. Heflin, F. H. Webb, U. J. Lindqwister, and R. P. Malla (1992), Global coordinates with centimeter accuracy in the International Terrestrial Reference Frame using GPS, *Geophysical Research Letters*, *19*(9), 853–856.
Blewitt, G., M. B. Heflin, K. J. Hurst, D. C. Jefferson, F. H. Webb, and J. F. Zumberge (1993), Absolute far-field displacements from the 28 June 1992 Landers earthquake sequence, *Nature*, *361*(6410), 340.
Bock, Y., D. C. Agnew, P. Fang, J. F. Genrich, B. H. Hager, T. A. Herring, K. W. Hudnut, R. W. King, S. Larsen, J.-B. Minster, et al. (1993), Detection of crustal deformation from the Landers earthquake sequence using continuous geodetic measurements, *Nature*, *361*(6410), 337.
Bock, Y., S. Wdowinski, P. Fang, J. Zhang, S. Williams, H. Johnson, J. Behr, J. Genrich, J. Dean, M. v. Domselaar, et al. (1997), Southern California Permanent GPS Geodetic Array: Continuous measurements of regional crustal deformation between the 1992 Landers and 1994 Northridge earthquakes, *Journal of Geophysical Research: Solid Earth*, *102*(B8), 18,013–18,033.
Bodart, O., V. Cayol, S. Court, and J. Koko (2016), XFEM-Based Fictitious Domain Method for Linear Elasticity Model with Crack, *SIAM Journal on Scientific Computing*, *38*(2), B219–B246.
Bodin, P., and J. N. Brune (1996), On the scaling of slip with rupture length for shallow strike-slip earthquakes: quasi-static models and dynamic rupture propagation, *Bulletin of the Seismological Society of America*, *86*(5), 1292–1299.
Bollinger, L., J. Avouac, R. Cattin, and M. Pandey (2004), Stress buildup in the Himalaya, *Journal of Geophysical Research: Solid Earth*, *109*(B11).
Bollinger, L., S. N. Sapkota, P. Tapponnier, Y. Klinger, M. Rizza, J. Van Der Woerd, D. Tiwari, R. Pandey, A. Bitri, and S. Bes de Berc (2014), Estimating the return times of great Himalayan earthquakes in eastern Nepal: Evidence from the Patu and Bardibas strands of the Main Frontal Thrust, *Journal of Geophysical Research: Solid Earth*, *119*(9), 7123–7163.
Bollinger, L., P. Tapponnier, S. Sapkota, and Y. Klinger (2016), Slip deficit in central Nepal: Omen for a repeat of the 1344 AD earthquake?, *Earth, Planets and Space*, *68*(1), 12.
Bomford, G. (1975), Geodesy., *Geodesy., by Bomford, G.. 3rd edition. Oxford (UK): Clarendon Press, 10+ 731 p.*
Bommer, J. J., and J. van Elk (2017), Comment on ?The maximum possible and the maximum expected earthquake magnitude for production-induced earthquakes at the gas field in Groningen, The Netherlands? by Gert Zöller and Matthias Holschneider, *Bulletin of the Seismological Society of America*, *107*(3), 1564–1567.
Bossu, R., S. Gilles, G. Mazet-Roux, F. Roussel, L. Frobert, and L. Kamb (2012), Flash sourcing, or rapid detection and characterization of earthquake effects through website traffic analysis, *Annals of Geophysics*, *54*(6).
Bouchon, M., and K. Aki (1980), Simulation of long-period, near-field motion for the great California earthquake of 1857, *Bulletin of the Seismological Society of America*, *70*(5), 1669–1682.
Bouchon, M., V. Durand, D. Marsan, H. Karabulut, and J. Schmittbuhl (2013), The long precursory phase of most large interplate earthquakes, *Nature geoscience*, *6*(4), 299.
Bouchon, M., D. Marsan, V. Durand, M. Campillo, H. Perfettini, R. Madariaga, and B. Gardonio (2016), Potential slab deformation and plunge prior to the Tohoku, Iquique and Maule earthquakes, *Nature Geoscience*, *9*(5), 380.
Boudin, F., P. Bernard, L. Longuevergne, N. Florsch, C. Larmat, C. Courteille, P.-A. Blum, T. Vincent, and M. Kammentaler (2008), A silica long base tiltmeter with high stability and resolution, *Review of Scientific Instruments*, *79*(3), 034,502.
Boyd, D. T. (2002), Oklahoma oil: Past, present, and future, *Oklahoma Geol. Notes*, *62*(3), 97–106.
Boyd, S., and L. Vandenberghe (2004), *Convex optimization*, Cambridge university press.
Bro, R., and S. De Jong (1997), A fast non-negativity-constrained least squares algorithm, *Journal of chemometrics*, *11*(5), 393–401.
Brodsky, E. E., J. J. Gilchrist, A. Sagy, and C. Collettini (2011), Faults smooth gradually as a function of slip, *Earth and Planetary Science Letters*, *302*(1-2), 185–193.
Bruhat, L., S. Barbot, and J.-P. Avouac (2011), Evidence for postseismic deformation of the lower crust following the 2004 Mw6. 0 Parkfield earthquake, *Journal of Geophysical Research: Solid Earth*, *116*(B8).
Brune, J. N. (1968), Seismic moment, seismicity, and rate of slip along major fault zones, *Journal of Geophysical Research*, *73*(2), 777–784.
Budnitz, R. J., G. Apostolakis, and D. M. Boore (1997), Recommendations for probabilistic seismic hazard analysis: guidance on uncertainty and use of experts, *Tech. rep.*, Nuclear Regulatory Commission, Washington, DC (United States). Div. of Engineering Technology; Lawrence Livermore National Lab., CA (United States); Electric Power Research Inst., Palo Alto, CA (United States); USDOE, Washington, DC (United States).
Bufe, C. G., P. W. Harsh, and R. O. Burford (1977), Steady-state seismic slip–A precise recurrence model, *Geophysical Research Letters*, *4*(2), 91–94.
Bürgmann, R., and D. Chadwell (2014), Seafloor geodesy, *Annual Review of Earth and Planetary Sciences*, *42*, 509–534.
Bürgmann, R., D. D. Pollard, and S. J. Martel (1994), Slip distributions on faults: effects of stress gradients, inelastic deformation, heterogeneous host-rock stiffness, and fault interaction, *Journal of Structural Geology*, *16*(12), 1675–1690.
Burridge, R., and L. Knopoff (1964), Body force equivalents for seismic dislocations, *Bulletin of the Seismological Society of America*, *54*(6A), 1875–1888.
Byrne, D. E., L. R. Sykes, and D. M. Davis (1992), Great thrust earthquakes and aseismic slip along the plate boundary of the Makran subduction zone, *Journal of Geophysical Research: Solid Earth*, *97*(B1), 449–478.
Çakir, Z., J.-B. d. Chabalier, R. Armijo, B. Meyer, A. Barka, and G. Peltzer (2003), Coseismic and early post-seismic slip associated with the 1999 Izmit earthquake (Turkey), from SAR interferometry and tectonic field observations, *Geophysical Journal International*, *155*(1), 93–110.
Calabrese, D., F. Carnevale, A. Croce, I. Rana, G. Spera, R. Venturini, C. Germani, F. Spadoni, F. Bagaglini, R. Roscigno, et al. (2015), New concepts and innovative solutions of the COSMO-SkyMed ?Seconda Generazione? system, in *Geoscience and Remote Sensing Symposium (IGARSS), 2015 IEEE International*, pp. 223–226, IEEE.
Calais, E., L. Dong, M. Wang, Z. Shen, and M. Vergnolle (2006a), Continental deformation in Asia from a combined GPS solution, *Geophysical Research Letters*, *33*(24).
Calais, E., J. Han, C. DeMets, and J. Nocquet (2006b), Deformation of the North American plate interior from a decade of continuous GPS measurements, *Journal of geophysical research: solid earth*, *111*(B6).
Calais, E., A. Freed, G. Mattioli, F. Amelung, S. Jónsson, P. Jansma, S.-H. Hong, T. Dixon, C. Prépetit, and R. Momplaisir (2010), Transpressional rupture of an unmapped fault during the 2010 Haiti earthquake, *Nature Geoscience*, *3*(11), 794.
Calais, E., T. Camelbeeck, S. Stein, M. Liu, and T. Craig (2016), A new paradigm for large earthquakes in stable continental plate interiors, *Geophysical Research Letters*, *43*(20), 10–621.
Caskey, S., S. Wesnousky, P. Zhang, and D. Slemmons (1996), Surface faulting of the 1954 Fairview Peak (MS 7.2) and Dixie Valley (MS 6.8) earthquakes, central Nevada, *Bulletin of the Seismological Society of America*, *86*(3), 761–787.
Catalán, P. A., R. Aránguiz, G. González, T. Tomita, R. Cienfuegos, J. González, M. N. Shrivastava, K. Kumagai, C. Mokrani, P. Cortés, et al. (2015), The 1 April 2014 Pisagua tsunami: observations and modeling, *Geophysical Research Letters*, *42*(8), 2918–2925.
Cattin, R., P. Briole, H. Lyon-Caen, P. Bernard, and P. Pinettes (1999), Effects of superficial layers on coseismic displacements for a dip-slip fault and geophysical implications, *Geophysical Journal International*, *137*(1), 149–158.
Causse, M., G. Cultrera, L. Moreau, A. Herrero, E. Schiappapietra, and F. Courboulex (2017), Bayesian rupture imaging in a complex medium: The 29 May 2012 Emilia, Northern Italy, earthquake, *Geophysical Research Letters*, *44*(15), 7783–7792.
Cavalié, O., and S. Jónsson (2014), Block-like plate movements in eastern Anatolia observed by InSAR, *Geophysical Research Letters*, *41*(1), 26–31.
Cavalié, O., M.-P. Doin, C. Lasserre, and P. Briole (2007), Ground motion measurement in the Lake Mead area, Nevada, by differential synthetic aperture radar interferometry time series analysis: Probing the lithosphere rheological structure, *Journal of Geophysical Research: Solid Earth*, *112*(B3).
Cavalié, O., C. Lasserre, M.-P. Doin, G. Peltzer, J. Sun, X. Xu, and Z.-K. Shen (2008), Measurement of interseismic strain across the Haiyuan fault (Gansu, China), by InSAR, *Earth and Planetary Science Letters*, *275*(3-4), 246–257.
Cavalié, O., E. Pathier, M. Radiguet, M. Vergnolle, N. Cotte, A. Walpersdorf, V. Kostoglodov, and F. Cotton (2013), Slow slip event in the Mexican subduction zone: Evidence of shallower slip in the Guerrero seismic gap for the 2006 event revealed by the joint inversion of InSAR and GPS data, *Earth and Planetary Science Letters*, *367*, 52–60.
Cayol, V., and F. H. Cornet (1998), Effects of topography on the interpretation of the deformation field of prominent volcanoes?Application to Etna, *Geophysical Research Letters*, *25*(11), 1979–1982.
Cayol, V., T. Catry, L. Michon, M. Chaput, V. Famin, O. Bodart, J.-L. Froger, and C. Romagnoli (2014), Sheared sheet intrusions as mechanism for lateral flank displacement on basaltic volcanoes: Applications to Réunion Island volcanoes, *Journal of Geophysical Research: Solid Earth*, *119*(10), 7607–7635.
Champenois, J., Y. Klinger, R. **Grandin**, et al. (2017), Surface rupture and slip distribution of the 2016 Mw7. 8 Kaikōura earthquake (New Zealand) from optical satellite image correlation using MicMac, in *EGU General Assembly Conference Abstracts*, vol. 19, p. 16421.
Chang, K., and P. Segall (2016), Injection-induced seismicity on basement faults including poroelastic stressing, *Journal of Geophysical Research: Solid Earth*, *121*(4), 2708–2726.
Chawah, P., J. Chéry, F. Boudin, M. Cattoen, H. C. Seat, G. Plantier, F. Lizion, A. Sourice, P. Bernard, C. Brunet, et al. (2015), A simple pendulum borehole tiltmeter based on a triaxial optical-fibre displacement sensor, *Geophysical Journal International*, *203*(2), 1026–1038.
Cheloni, D., V. De Novellis, M. Albano, A. Antonioli, M. Anzidei, S. Atzori, A. Avallone, C. Bignami, M. Bonano, S. Calcaterra, et al. (2017), Geodetic model of the 2016 Central Italy earthquake sequence inferred from InSAR and GPS data, *Geophysical Research Letters*, *44*(13), 6778–6787.

Chen, A. C., and H. A. Zebker (2014), Reducing ionospheric effects in InSAR data using accurate coregistration, *IEEE Transactions on Geoscience and Remote Sensing*, *52*(1), 60–70.
Chen, C. W., and H. A. Zebker (2001), Two-dimensional phase unwrapping with use of statistical models for cost functions in nonlinear optimization, *JOSA A*, *18*(2), 338–351.
Chen, H., X. Meng, F. Niu, Y. Tang, C. Yin, and F. Wu (2018), Microseismic monitoring of stimulating shale gas reservoir in SW China: 2. Spatial clustering controlled by the preexisting faults and fractures, *Journal of Geophysical Research: Solid Earth*, *123*(2), 1659–1672.
Chen, W.-P., and P. Molnar (1977), Seismic moments of major earthquakes and the average rate of slip in central Asia, *Journal of Geophysical Research*, *82*(20), 2945–2969.
Chéry, J. (2008), Geodetic strain across the San Andreas fault reflects elastic plate thickness variations (rather than fault slip rate), *Earth and Planetary Science Letters*, *269*(3-4), 352–365.
Chéry, J., S. Carretier, and J.-F. Ritz (2001), Postseismic stress transfer explains time clustering of large earthquakes in Mongolia, *Earth and Planetary Science Letters*, *194*(1-2), 277–286.
Chlieh, M., P. Mothes, J.-M. Nocquet, P. Jarrin, P. Charvis, D. Cisneros, Y. Font, J.-Y. Collot, J.-C. Villegas-Lanza, F. Rolandone, et al. (2014), Distribution of discrete seismic asperities and aseismic slip along the Ecuadorian megathrust, *Earth and Planetary Science Letters*, *400*, 292–301.
Choi, J.-H., Y. Klinger, M. Ferry, J.-F. Ritz, R. Kurtz, M. Rizza, L. Bollinger, B. Davaasambuu, N. Tsend-Ayush, and S. Demberel (2018), Geologic Inheritance and Earthquake Rupture Processes: The 1905 M? 8 Tsetserleg-Bulnay Strike-Slip Earthquake Sequence, Mongolia, *Journal of Geophysical Research: Solid Earth*, *123*(2), 1925–1953.
Christodoulidis, D. C., D. E. Smith, R. Kolenkiewicz, S. Klosko, M. Torrence, and P. Dunn (1985), Observing tectonic plate motions and deformations from satellite laser ranging, *Journal of Geophysical Research: Solid Earth*, *90*(B11), 9249–9263.
Cifuentes, I. L. (1989), The 1960 Chilean earthquakes, *Journal of Geophysical Research: Solid Earth*, *94*(B1), 665–680.
Clare, P. H. (1963), *Petroleum geology of Pawnee County, Oklahoma*, University of Oklahoma.
Clarke, P., D. Paradissis, P. Briole, P. England, B. Parsons, H. Billiris, G. Veis, and J.-C. Ruegg (1997), Geodetic investigation of the 13 May 1995 Kozani-Grevena (Greece) earthquake, *Geophysical Research Letters*, *24*(6), 707–710.
Cloud, J. (2001), Imaging the World in a Barrel: CORONA and the Clandestine Convergence, *Social Studies of Science*, *31*, 231–251.
Cloude, S. R., and E. Pottier (1996), A review of target decomposition theorems in radar polarimetry, *IEEE transactions on geoscience and remote sensing*, *34*(2), 498–518.
Comninou, M., and J. Dundurs (1975), The angular dislocation in a half space, *Journal of Elasticity*, *5*(3-4), 203–216.
Converse, G., and M. Comninou (1975), Dependence on the elastic constants of surface deformation due to faulting, *Bulletin of the Seismological Society of America*, *65*(5), 1173–1176.
Crone, A. J., and K. V. Luza (1990), Style and timing of Holocene surface faulting on the Meers fault, southwestern Oklahoma, *Geological Society of America Bulletin*, *102*(1), 1–17.
Crone, A. J., M. N. Machette, M. G. Bonilla, J. J. Lienkaemper, K. L. Pierce, W. E. Scott, and R. C. Bucknam (1987), Surface faulting accompanying the Borah Peak earthquake and segmentation of the Lost River fault, central Idaho, *Bulletin of the Seismological Society of America*, *77*(3), 739–770.
Cumming, I. G., and F. H. Wong (2005), Digital processing of synthetic aperture radar data, *Artech house*, *1*(2), 3.
Curlander, J. C., and R. N. McDonough (1991), *Synthetic aperture radar*, vol. 396, John Wiley & Sons New York, NY, USA.
Daout, S., M.-P. Doin, G. Peltzer, A. Socquet, and C. Lasserre (2017), Large-scale InSAR monitoring of permafrost freeze-thaw cycles on the Tibetan Plateau, *Geophysical Research Letters*, *44*(2), 901–909.
Daout, S., M.-P. Doin, G. Peltzer, C. Lasserre, A. Socquet, M. Volat, and H. Sudhaus (2018), Strain partitioning and present-day fault kinematics in NW Tibet from Envisat SAR interferometry, *Journal of Geophysical Research: Solid Earth*, *123*(3), 2462–2483.
De Guidi, G., A. Vecchio, F. Brighenti, R. Caputo, F. Carnemolla, A. Di Pietro, M. Lupo, M. Maggini, S. Marchese, D. Messina, et al. (2017), Brief communication: Co-seismic displacement on 26 and 30 October 2016 (M w= 5.9 and 6.5)–earthquakes in central Italy from the analysis of a local GNSS network, *Natural Hazards and Earth System Sciences*, *17*(11), 1885.
De Natale, G., and F. Pingue (1991), A variable slip fault model for the 1908 Messina Straits (Italy) earthquake, by inversion of levelling data, *Geophysical Journal International*, *104*(1), 73–84.
De Zan, F., and A. M. Guarnieri (2006), TOPSAR: Terrain observation by progressive scans, *IEEE Transactions on Geoscience and Remote Sensing*, *44*(9), 2352–2360.
De Zan, F., M. Zonno, and P. López-Dekker (2015), Phase inconsistencies and multiple scattering in SAR interferometry, *IEEE Transactions on Geoscience and Remote Sensing*, *53*(12), 6608–6616.
Deledalle, C.-A., L. Denis, G. Poggi, F. Tupin, and L. Verdoliva (2014), Exploiting patch similarity for SAR image processing: the nonlocal paradigm, *IEEE Signal Processing Magazine*, *31*(4), 69–78.
Delorme, A., R. **Grandin**, Y. Klinger, et al. (2019), Complex deformation at shallow depth during the 30 October 2016 Mw6.5 Norcia earthquake: interference between tectonic and gravity processes, *Tectonics, in revision*.
Delouis, B., D. Giardini, P. Lundgren, and J. Salichon (2002), Joint inversion of InSAR, GPS, teleseismic, and strong-motion data for the spatial and temporal distribution of earthquake slip: Application to the 1999 Izmit mainshock, *Bulletin of the Seismological Society of America*, *92*(1), 278–299.
DeMets, C., R. G. Gordon, D. Argus, and S. Stein (1990), Current plate motions, *Geophysical journal international*, *101*(2), 425–478.
Denolle, M. A., W. Fan, and P. M. Shearer (2015), Dynamics of the 2015 M7. 8 Nepal earthquake, *Geophysical Research Letters*, *42*(18), 7467–7475.
DeSanto, J. B., and D. T. Sandwell (2019), Meter-scale seafloor geodetic measurements obtained from repeated multibeam sidescan surveys, *Marine Geodesy*, pp. 1–10.
Dixon, T. H., G. Gonzalez, S. Lichten, D. Tralli, G. Ness, and J. Dauphin (1991), Preliminary determination of Pacfic-North America relative motion in the southern Gulf of Calfornia using the Global Positioning System, *Geophysical Research Letters*, *18*(5), 861–864.
Dixon, T. H., F. Farina, C. DeMets, P. Jansma, P. Mann, and E. Calais (1998), Relative motion between the Caribbean and North American plates and related boundary zone deformation from a decade of GPS observations, *Journal of Geophysical Research: Solid Earth*, *103*(B7), 15,157–15,182.
Doin, M.-P., C. Lasserre, G. Peltzer, O. Cavalié, and C. Doubre (2009), Corrections of stratified tropospheric delays in SAR interferometry: Validation with global atmospheric models, *Journal of Applied Geophysics*, *69*(1), 35–50.
Doin, M.-P., S. Guillaso, R. Jolivet, C. Lasserre, F. Lodge, G. Ducret, and R. **Grandin** (2011), Presentation of the small baseline NSBAS processing chain on a case example: the Etna deformation monitoring from 2003 to 2010 using Envisat data, in *Proceedings of the Fringe Symposium*, pp. 3434–3437, ES.
Doin, M.-P., C. Twardzik, G. Ducret, C. Lasserre, S. Guillaso, and S. Jianbao (2015), InSAR measurement of the deformation around Siling Co Lake: inferences on the lower crust viscosity in central Tibet, *Journal of Geophysical Research: Solid Earth*, *120*(7), 5290–5310.
Dolan, J. F., and B. D. Haravitch (2014), How well do surface slip measurements track slip at depth in large strike-slip earthquakes? The importance of fault structural maturity in controlling on-fault slip versus off-fault surface deformation, *Earth and Planetary Science Letters*, *388*, 38–47.
Dong, J., W. Sun, X. Zhou, and R. Wang (2014), Effects of Earth's layered structure, gravity and curvature on coseismic deformation, *Geophysical Journal International*, *199*(3), 1442–1451.
Doser, D. I. (1986), Earthquake processes in the Rainbow Mountain-Fairview Peak-Dixie Valley, Nevada, region 1954–1959, *Journal of Geophysical Research: Solid Earth*, *91*(B12), 12,572–12,586.
Doubre, C., and G. Peltzer (2007), Fluid-controlled faulting process in the Asal Rift, Djibouti, from 8 yr of radar interferometry observations, *Geology*, *35*, 69, doi:10.1130/G23022A.1.
Doubre, C., A. Deprez, F. Masson, A. Socquet, E. Lewi, R. **Grandin**, A. Nercessian, P. Ulrich, J.-B. De Chabalier, I. Saad, et al. (2016), Current deformation in Central Afar and triple junction kinematics deduced from GPS and InSAR measurements, *Geophysical Journal International*, *208*(2), 936–953.
Doyon, M., J. Smyth, G. Kroupnik, C. Carrie, M. Sauvageau, J.-F. Levesque, F. Babiker, V. Abbasi, C. Giguere, S. Côté, et al. (2018), RADARSAT CONSTELLATION MISSION: Toward launch and operations, in *2018 SpaceOps Conference*, p. 2605.
Du, Y., A. Aydin, and P. Segall (1992), Comparison of various inversion techniques as applied to the determination of a geophysical deformation model for the 1983 Borah Peak earthquake, *Bulletin of the Seismological Society of America*, *82*(4), 1840–1866.
Du, Y., P. Segall, and H. Gao (1994), Dislocations in inhomogeneous media via a moduli perturbation approach: General formulation and two-dimensional solutions, *Journal of Geophysical Research: Solid Earth*, *99*(B7), 13,767–13,779.
Ducret, G., M.-P. Doin, R. **Grandin**, C. Lasserre, and S. Guillaso (2014), DEM corrections before unwrapping in a small baseline strategy for InSAR time series analysis, *IEEE Geoscience and Remote Sensing Letters*, *11*(3), 696–700.
Dumont, S., Y. Klinger, A. Socquet, J. Escartín, R. **Grandin**, E. Jacques, S. Medynski, and C. Doubre (2019), Rifting Processes at a Continent-Ocean Transition Rift Revealed by Fault Analysis: Example of Dabbahu-Manda-Hararo Rift (Ethiopia), *Tectonics*, *38*(1), 190–214, doi:10.1029/2018TC005141.
Dunning, S., W. Mitchell, N. Rosser, and D. Petley (2007), The Hattian Bala rock avalanche and associated landslides triggered by the Kashmir Earthquake of 8 October 2005, *Engineering Geology*, *93*(3-4), 130–144.
Duputel, Z., P. S. Agram, M. Simons, S. E. Minson, and J. L. Beck (2014), Accounting for prediction uncertainty when inferring subsurface fault slip, *Geophysical Journal International*, *197*(1), 464–482.
Duputel, Z., J. Jiang, R. Jolivet, M. Simons, L. Rivera, J.-P. Ampuero, B. Riel, S. E. Owen, A. W. Moore, S. V. Samsonov, et al. (2015), The Iquique earthquake sequence of April 2014: Bayesian modeling accounting for prediction uncertainty, *Geophysical Research Letters*, *42*(19), 7949–7957.
Duquesnoy, T., E. Barrier, M. Kasser, M. Aurelio, R. Gaulon, R. Punongbayan, and C. Rangin (1994), Detection of creep along the Philippine fault: First results of geodetic measurements on Leyte island, central Philippine, *Geophysical Research Letters*, *21*(11), 975–978.
Dvorak, J. J., and D. Dzurisin (1997), Volcano geodesy: The search for magma reservoirs and the formation of eruptive vents, *Reviews of Geophysics*, *35*(3), 343–384.
Earle, P. (2010), Earthquake twitter, *Nature Geoscience*, *3*(4), 221.
Ebmeier, S., J. Biggs, T. Mather, and F. Amelung (2013), Applicability of InSAR to tropical volcanoes: insights from Central America, *Geological Society, London, Special Publications*, *380*(1), 15–37.
Ebmeier, S., B. Andrews, M. Araya, D. Arnold, J. Biggs, C. Cooper, E. Cottrell, M. Furtney, J. Hickey, J. Jay, et al. (2018), Synthesis of global satellite observations of magmatic and volcanic deformation: implications for volcano monitoring & the lateral extent of magmatic domains, *Journal of Applied Volcanology*, *7*(1), 2.
Elliott, J., R. Jolivet, P. González, J.-P. Avouac, J. Hollingsworth, M. Searle, and V. Stevens (2016), Himalayan megathrust geometry and relation to topography revealed by the Gorkha earthquake, *Nature Geoscience*, *9*(2), 174.
Elliott, J. R., J. Biggs, B. Parsons, and T. J. Wright (2008), InSAR slip rate determination on the Altyn Tagh Fault, northern Tibet, in the presence of topographically correlated atmospheric delays, *Geophys. Res. Lett.*, *35*, 12,309–+, doi:10.1029/2008GL033659.
Ellouz-Zimmermann, N., E. Deville, C. Müller, S. Lallemant, A. Subhani, and A. Tabreez (2007), Impact of sedimentation on convergent margin tectonics: Example of the Makran accretionary prism (Pakistan), in *Thrust Belts and Foreland Basins*, pp. 327–350, Springer.
Ellsworth, W. L. (2013), Injection-induced earthquakes, *Science*, *341*(6142), 1225,942.

Engdahl, E. R. (2002), Global seismicity: 1900-1999, *International handbook of earthquake and engineering seismology*, pp. 665–690.
Engelen, S., M. Oever, P. Mahapatra, P. Sundaramoorthy, E. Gill, R. Meijer, and C. Verhoeven (2012), NanoSAR-Case study of synthetic aperture radar for nano-satellites, in *63rd International Astronautical Congress 2012, IAC 2012, 1 October 2012 through 5 October 2012, Naples, 10, 8159-8164*.
European Commission, Joint Research Centre (JRC); Columbia University, Center for International Earth Science Information Network - CIESIN (2015), *GHS population grid, derived from GPW4, multitemporal (1975, 1990, 2000, 2015)*, http://data.europa.eu/89h/jrc-ghsl-ghs_pop_gpw4_globe_r2015a
Evans, E. L., and B. J. Meade (2012), Geodetic imaging of coseismic slip and postseismic afterslip: Sparsity promoting methods applied to the great Tohoku earthquake, *Geophysical Research Letters*, *39*(11).
Everley, S. (2016), Comment on "A Historical Review of Induced Earthquakes in Texas"ĂŹ by Cliff Frohlich, Heather DeShon, Brian Stump, Chris Hayward, Matt Hornbach, and Jacob I. Walter, *Seismological Research Letters*, *87*(6), 1378, doi:10.1785/0220160122.
Fan, W., and P. M. Shearer (2015), Detailed rupture imaging of the 25 April 2015 Nepal earthquake using teleseismic P waves, *Geophysical Research Letters*, *42*(14), 5744–5752.
Fattahi, H., F. Amelung, E. Chaussard, and S. Wdowinski (2015), Coseismic and postseismic deformation due to the 2007 M5. 5 Ghazaband fault earthquake, Balochistan, Pakistan, *Geophysical Research Letters*, *42*(9), 3305–3312.
Fattahi, H., P. Agram, and M. Simons (2017), A network-based enhanced spectral diversity approach for TOPS time-series analysis, *IEEE Transactions on Geoscience and Remote Sensing*, *55*(2), 777–786.
Feigl, K. L., D. C. Agnew, Y. Bock, D. Dong, A. Donnellan, B. H. Hager, T. A. Herring, D. D. Jackson, T. H. Jordan, R. W. King, et al. (1993), Space geodetic measurement of crustal deformation in central and southern California, 1984–1992, *Journal of Geophysical Research: Solid Earth*, *98*(B12), 21,677–21,712.
Ferretti, A., C. Prati, and F. Rocca (2001), Permanent scatterers in SAR interferometry, *IEEE Transactions on Geoscience and Remote Sensing*, *39*, 8–20, doi:10.1109/36.898661.
Ferretti, A., A. Fumagalli, F. Novali, C. Prati, F. Rocca, and A. Rucci (2011), A new algorithm for processing interferometric data-stacks: SqueeSAR, *IEEE Transactions on Geoscience and Remote Sensing*, *49*(9), 3460–3470.
Ferry, M., M. Meghraoui, N. Abou Karaki, M. Al-Taj, and L. Khalil (2011), Episodic behavior of the Jordan Valley section of the Dead Sea fault inferred from a 14-ka-long integrated catalog of large earthquakes, *Bulletin of the Seismological Society of America*, *101*(1), 39–67.
Fialko, Y. (2004), Probing the mechanical properties of seismically active crust with space geodesy: Study of the coseismic deformation due to the 1992 Mw7. 3 Landers (southern California) earthquake, *Journal of Geophysical Research: Solid Earth*, *109*(B3).
Fialko, Y. (2006), Interseismic strain accumulation and the earthquake potential on the southern San Andreas fault system, *Nature*, *441*(7096), 968.
Fialko, Y., M. Simons, and D. Agnew (2001), The complete (3-D) surface displacement field in the epicentral area of the 1999 Mw7. 1 Hector Mine earthquake, California, from space geodetic observations, *Geophysical Research Letters*, *28*(16), 3063–3066.
Fialko, Y., D. Sandwell, M. Simons, and P. Rosen (2005), Three-dimensional deformation caused by the Bam, Iran, earthquake and the origin of shallow slip deficit, *Nature*, *435*, 295–299, doi:10.1038/nature03425.
Fialko, Y., A. Gonzalez, J. Gonzalez-Garcia, S. Barbot, S. Leprince, D. Sandwell, and D. Agnew (2010), Static rupture model of the 2010 M7. 2 El Mayor-Cucapah earthquake from ALOS, ENVISAT, SPOT and GPS data, in *AGU Fall Meeting Abstracts*.
Fielding, E. J., S. S. Sangha, D. P. Bekaert, S. V. Samsonov, and J. C. Chang (2017), Surface deformation of north-central Oklahoma related to the 2016 M w 5.8 Pawnee earthquake from SAR interferometry time series, *Seismological Research Letters*, *88*(4), 971–982.
Foulger, G. R., M. P. Wilson, J. G. Gluyas, B. R. Julian, and R. J. Davies (2018), Global review of human-induced earthquakes, *Earth-Science Reviews*, *178*, 438–514.
Franceschetti, G., and R. Lanari (1999), *Synthetic aperture radar processing*, CRC press.
Frank, W. B. (2016), Slow slip hidden in the noise: The intermittence of tectonic release, *Geophysical Research Letters*, *43*(19).
Frank, W. B., B. Rousset, C. Lasserre, and M. Campillo (2018), Revealing the cluster of slow transients behind a large slow slip event, *Science advances*, *4*(5), eaat0661.
Frankel, A. (2013), Comment on ?Why earthquake hazard maps often fail and what to do about it? by S. Stein, R. Geller, and M. Liu, *Tectonophysics*, *592*, 200–206.
Freeman, A., G. Krieger, P. Rosen, M. Younis, W. T. Johnson, S. Huber, R. Jordan, and A. Moreira (2009), SweepSAR: Beam-forming on receive using a reflector-phased array feed combination for spaceborne SAR, in *Radar Conference, 2009 IEEE*, pp. 1–9, IEEE.
Freund, L., and D. Barnett (1976), A two-dimensional analysis of surface deformation due to dip-slip faulting, *Bulletin of the Seismological Society of America*, *66*(3), 667–675.
Frohlich, C., H. DeShon, B. Stump, C. Hayward, M. Hornbach, and J. I. Walter (2016a), Reply to "Comment on "A Historical Review of Induced Earthquakes in Texas"ĂŹ by Cliff Frohlich, Heather DeShon, Brian Stump, Chris Hayward, Matt Hornbach, and Jacob I. Walter" by Steve Everley, *Seismological Research Letters*, *87*(6), 1381, doi:10.1785/0220160148.
Frohlich, C., H. DeShon, B. Stump, C. Hayward, M. Hornbach, and J. I. Walter (2016b), A historical review of induced earthquakes in Texas, *Seismological Research Letters*, *87*(4), 1022, doi:10.1785/0220160016.
Fu, Y., and J. T. Freymueller (2012), Seasonal and long-term vertical deformation in the Nepal Himalaya constrained by GPS and GRACE measurements, *Journal of Geophysical Research: Solid Earth*, *117*(B3).
Fujiwara, S., T. Nishimura, M. Murakami, H. Nakagawa, M. Tobita, and P. A. Rosen (2000), 2.5-D surface deformation of M6. 1 earthquake near Mt Iwate detected by SAR interferometry, *Geophysical research letters*, *27*(14), 2049–2052.
Fukahata, Y., and T. J. Wright (2008), A non-linear geodetic data inversion using ABIC for slip distribution on a fault with an unknown dip angle, *Geophysical Journal International*, *173*(2), 353–364.
Fukuda, J., and K. M. Johnson (2010), Mixed linear – non-linear inversion of crustal deformation data: Bayesian inference of model, weighting and regularization parameters, *Geophysical Journal International*, *181*(3), 1441–1458.
Fukushima, Y., V. Cayol, and P. Durand (2005), Finding realistic dike models from interferometric synthetic aperture radar data: The February 2000 eruption at Piton de la Fournaise, *Journal of Geophysical Research: Solid Earth*, *110*(B3).
Funning, G., and A. Garcia (2017), A systematic study of earthquake detectability using Sentinel-1 Interferometric Wide-Swath data, doi:10.17605/OSF.IO/9WG8S.
Funning, G. J., and A. Garcia (2018), A systematic study of earthquake detectability using Sentinel-1 Interferometric Wide-Swath data, *Geophysical Journal International*, *216*(1), 332–349.
Funning, G. J., B. Parsons, T. J. Wright, J. A. Jackson, and E. J. Fielding (2005), Surface displacements and source parameters of the 2003 Bam (Iran) earthquake from Envisat advanced synthetic aperture radar imagery, *Journal of Geophysical Research: Solid Earth*, *110*(B9).
Funning, G. J., B. Parsons, and T. J. Wright (2007), Fault slip in the 1997 Manyi, Tibet earthquake from linear elastic modelling of InSAR displacements, *Geophysical Journal International*, *169*(3), 988–1008.
Gagnon, K., C. D. Chadwell, and E. Norabuena (2005), Measuring the onset of locking in the Peru–Chile trench with GPS and acoustic measurements, *Nature*, *434*(7030), 205.
Galetzka, J., D. Melgar, J. F. Genrich, J. Geng, S. Owen, E. O. Lindsey, X. Xu, Y. Bock, J.-P. Avouac, L. B. Adhikari, et al. (2015), Slip pulse and resonance of the Kathmandu basin during the 2015 Gorkha earthquake, Nepal, *Science*, *349*(6252), 1091–1095.
Gallovič, F., and J.-P. Ampuero (2015), A new strategy to compare inverted rupture models exploiting the eigenstructure of the inverse problem, *Seismological Research Letters*, *86*(6), 1679–1689.
Gao, H., D. A. Schmidt, and R. J. Weldon (2012), Scaling relationships of source parameters for slow slip events, *Bulletin of the Seismological Society of America*, *102*(1), 352–360.
Gardi, A., A. Lemoine, R. Madariaga, and J. Campos (2006), Modeling of stress transfer in the Coquimbo region of central Chile, *Journal of Geophysical Research: Solid Earth*, *111*(B4).
Garrett, E., I. Shennan, E. Watcham, and S. Woodroffe (2013), Reconstructing paleoseismic deformation, 1: modern analogues from the 1960 and 2010 Chilean great earthquakes, *Quaternary Science Reviews*, *75*, 11–21.
Gatelli, F., A. M. Guamieri, F. Parizzi, P. Pasquali, C. Prati, and F. Rocca (1994), The wavenumber shift in SAR interferometry, *IEEE Transactions on Geoscience and Remote Sensing*, *32*(4), 855–865.
Gebert, N., G. Krieger, and A. Moreira (2009), Digital beamforming on receive: Techniques and optimization strategies for high-resolution wide-swath SAR imaging, *IEEE Transactions on Aerospace and Electronic Systems*, *45*(2).
Geller, R. J., D. D. Jackson, Y. Y. Kagan, and F. Mulargia (1997), Earthquakes cannot be predicted, *Science*, *275*(5306), 1616–1616.
Gerstenberger, M. C., S. Wiemer, L. M. Jones, and P. A. Reasenberg (2005), Real-time forecasts of tomorrow's earthquakes in California, *Nature*, *435*(7040), 328.
Geudtner, D., R. Torres, P. Snoeij, M. Davidson, and B. Rommen (2014), Sentinel-1 system capabilities and applications, in *Geoscience and Remote Sensing Symposium (IGARSS), 2014 IEEE International*, pp. 1457–1460, IEEE.
Ghiglia, D. C., and L. A. Romero (1994), Robust two-dimensional weighted and unweighted phase unwrapping that uses fast transforms and iterative methods, *JOSA A*, *11*(1), 107–117.
Gilbert, F. (1971), Ranking and winnowing gross Earth data for inversion and resolution, *Geophysical Journal of the Royal Astronomical Society*, *23*(1), 125–128.
Giudici, D., D. Mapelli, M. van den Oever, E. De Witte, V. Boccia, and B. Rommen (2018), Performance Analysis of a Multi-static SAR mission concept enhancing Sentinel-1 capabilities, in *EUSAR 2018; 12th European Conference on Synthetic Aperture Radar*, pp. 1–6, VDE.
Göbel, T. (2015), A comparison of seismicity rates and fluid-injection operations in Oklahoma and California: Implications for crustal stresses, *The Leading Edge*, *34*(6), 640–648.
Goebel, T., M. Weingarten, X. Chen, J. Haffener, and E. Brodsky (2017a), The 2016 Mw5. 1 Fairview, Oklahoma earthquakes: Evidence for long-range poroelastic triggering at> 40 km from fluid disposal wells, *Earth and Planetary Science Letters*, *472*, 50–61.
Goebel, T. H., J. I. Walter, K. Murray, and E. E. Brodsky (2017b), Comment on ?How will induced seismicity in Oklahoma respond to decreased saltwater injection rates?? by C. Langenbruch and MD Zoback, *Science advances*, *3*(8), e1700,441.
Goitom, B., C. Oppenheimer, J. O. Hammond, R. **Grandin**, et al. (2015), First recorded eruption of Nabro volcano, Eritrea, 2011, *Bulletin of volcanology*, *77*(10), 85.
Goldstein, R. M., and C. L. Werner (1998), Radar interferogram filtering for geophysical applications, *Geophysical research letters*, *25*(21), 4035–4038.
Goldstein, R. M., H. A. Zebker, and C. L. Werner (1988), Satellite radar interferometry: Two-dimensional phase unwrapping, *Radio science*, *23*(4), 713–720.
Gomba, G., A. Parizzi, F. De Zan, M. Eineder, and R. Bamler (2015), Toward operational compensation of ionospheric effects in SAR interferograms: The split-spectrum method, *IEEE Transactions on Geoscience and Remote Sensing*, *54*(3), 1446–1461.
Gomba, G., F. R. González, and F. De Zan (2017), Ionospheric phase screen compensation for the Sentinel-1 TOPS and ALOS-2 ScanSAR modes, *IEEE Transactions on Geoscience and Remote Sensing*, *55*(1), 223–235.
Gómez Ferreras, F. (2017), Study of Earth Observation business models by means of CANVAS methodology, Master's thesis, Universitat Politècnica de Catalunya.

Gong, W., F. J. Meyer, S. Liu, and R. F. Hanssen (2015), Temporal filtering of InSAR data using statistical parameters from NWP models, *IEEE Transactions on geoscience and remote sensing*, *53*(7), 4033–4044.
Gonzalez-Ortega, A., Y. Fialko, D. Sandwell, F. Alejandro Nava-Pichardo, J. Fletcher, J. Gonzalez-Garcia, B. Lipovsky, M. Floyd, and G. Funning (2014), El Mayor-Cucapah (Mw 7.2) earthquake: Early near-field postseismic deformation from InSAR and GPS observations, *Journal of Geophysical Research: Solid Earth*, *119*(2), 1482–1497.
Grandin, R., A. Socquet, R. Binet, Y. Klinger, E. Jacques, J. B. de Chabalier, G. C. P. King, C. Lasserre, S. Tait, P. Tapponnier, D. A., and P. P. (2009), September 2005 Manda Hararo-Dabbahu rifting event, Afar (Ethiopia): Constraints provided by geodetic data, *J. Geophys. Res.*, *114*(B12), doi:10.1029/2008JB005843.
Grant, L. B., and A. Donnellan (1994), 1855 and 1991 surveys of the San Andreas fault: Implications for fault mechanics, *Bulletin of the Seismological Society of America*, *84*(2), 241–246.
Gray, A. L., K. E. Mattar, and G. Sofko (2000), Influence of ionospheric electron density fluctuations on satellite radar interferometry, *Geophysical Research Letters*, *27*(10), 1451–1454.
Grigoli, F., S. Cesca, E. Priolo, A. P. Rinaldi, J. F. Clinton, T. A. Stabile, B. Dost, M. G. Fernandez, S. Wiemer, and T. Dahm (2017), Current challenges in monitoring, discrimination, and management of induced seismicity related to underground industrial activities: A European perspective, *Reviews of Geophysics*, *55*(2), 310–340.
Grollimund, B., and M. D. Zoback (2001), Did deglaciation trigger intraplate seismicity in the New Madrid seismic zone?, *geology*, *29*(2), 175–178.
Guarnieri, A. M., and C. Prati (1996), ScanSAR focusing and interferometry, *IEEE Transactions on Geoscience and Remote Sensing*, *34*(4), 1029–1038.
Guglielmi, Y., F. Cappa, J.-P. Avouac, P. Henry, and D. Elsworth (2015), Seismicity triggered by fluid injection–induced aseismic slip, *Science*, *348*(6240), 1224–1226, doi:10.1126/science.aab0476.
Gutenberg, B., and C. F. Richter (1944), Frequency of earthquakes in California, *Bulletin of the Seismological Society of America*, *34*(4), 185–188.
Haeussler, P. J., D. P. Schwartz, T. E. Dawson, H. D. Stenner, J. J. Lienkaemper, B. Sherrod, F. R. Cinti, P. Montone, P. A. Craw, A. J. Crone, et al. (2004), Surface rupture and slip distribution of the Denali and Totschunda faults in the 3 November 2002 M 7.9 earthquake, Alaska, *Bulletin of the Seismological Society of America*, *94*(6B), S23–S52.
Hamling, I. J., S. Hreinsdóttir, K. Clark, J. Elliott, C. Liang, E. Fielding, N. Litchfield, P. Villamor, L. Wallace, T. J. Wright, et al. (2017), Complex multifault rupture during the 2016 M w 7.8 Kaikōura earthquake, New Zealand, *Science*, *356*(6334), eaam7194.
Hamlyn, J., T. Wright, R. Walters, C. Pagli, E. Sansosti, F. Casu, S. Pepe, M. Edmonds, B. M. Kilbride, D. Keir, et al. (2018), What causes subsidence following the 2011 eruption at Nabro (Eritrea)?, *Progress in Earth and Planetary Science*, *5*(1), 31.
Hanks, T. C., and W. H. Bakun (2008), M-log A observations for recent large earthquakes, *Bulletin of the Seismological Society of America*, *98*(1), 490–494.
Hanks, T. C., and H. Kanamori (1979), A moment magnitude scale, *Journal of Geophysical Research: Solid Earth*, *84*(B5), 2348–2350.
Hanssen, R. F. (2001), *Radar interferometry: data interpretation and error analysis*, vol. 2, Springer Science & Business Media.
Hanssen, R. F., F. van Leijen, N. Pierdicca, N. Floury, and U. Wegmuller (2015), L-band multistatic radar interferometry for 3D deformation vector decomposition, in *Geoscience and Remote Sensing Symposium (IGARSS), 2015 IEEE International*, pp. 4057–4060, IEEE.
Harris, R. A., and P. Segall (1987), Detection of a locked zone at depth on the Parkfield, California, segment of the San Andreas fault, *Journal of Geophysical Research: Solid Earth*, *92*(B8), 7945–7962.
Harris, R. A., and R. W. Simpson (1996), In the shadow of 1857-the effect of the great Ft. Tejon earthquake on subsequent earthquakes in southern California, *Geophysical Research Letters*, *23*(3), 229–232.
Hartzell, S. H., and T. H. Heaton (1983), Inversion of strong ground motion and teleseismic waveform data for the fault rupture history of the 1979 Imperial Valley, California, earthquake, *Bulletin of the Seismological Society of America*, *73*(6A), 1553–1583.
Hayford, J., and A. Baldwin (1908), Geodetic measurements of Earth movements, in *The California Earthquake of April 18, 1906, Report of the State Earthquake Investigation Commission, Volume 1*, pp. 114–145, Carnegie Institution of Washington, Washington, DC.
Hearn, E. H., and R. Bürgmann (2005), The effect of elastic layering on inversions of GPS data for coseismic slip and resulting stress changes: Strike-slip earthquakes, *Bulletin of the Seismological Society of America*, *95*(5), 1637–1653.
Heaton, T. H., and R. E. Heaton (1989), Static deformations from point forces and force couples located in welded elastic Poissonian half-spaces: Implications for seismic moment tensors, *Bulletin of the seismological society of America*, *79*(3), 813–841.
Helmstetter, A., Y. Y. Kagan, and D. D. Jackson (2006), Comparison of short-term and time-independent earthquake forecast models for southern California, *Bulletin of the Seismological Society of America*, *96*(1), 90–106.
Hensley, S., P. A. Rosen, and E. Gurrola (2000), Topographic map generation from the Shuttle Radar Topography Mission C-band SCANSAR interferometry, in *Microwave Remote Sensing of the Atmosphere and Environment II*, vol. 4152, pp. 179–190, International Society for Optics and Photonics.
Herbert, J. W., M. L. Cooke, and S. T. Marshall (2014), Influence of fault connectivity on slip rates in southern California: Potential impact on discrepancies between geodetic derived and geologic slip rates, *Journal of Geophysical Research: Solid Earth*, *119*(3), 2342–2361.
Herman, M. W., K. P. Furlong, G. P. Hayes, and H. M. Benz (2016), Foreshock triggering of the 1 April 2014 Mw 8.2 Iquique, Chile, earthquake, *Earth and Planetary Science Letters*, *447*, 119–129.
Herring, T., I. Shapiro, T. Clark, C. Ma, J. Ryan, B. Schupler, C. Knight, G. Lundqvist, D. Shaffer, N. Vandenberg, et al. (1986), Geodesy by radio interferometry: evidence for contemporary plate motion, *Journal of Geophysical Research: Solid Earth*, *91*(B8), 8341–8347.
Hicks, S., J. Verdon, B. Baptie, R. Luckett, Z. Mildon, and T. Gernon (2019), A shallow earthquake swarm close to hydrocarbon activities: discriminating between natural and induced causes for the 2018–19 Surrey, UK earthquake sequence, *EarthArXiv*, https://eartharxiv.org/b2ypu/.
Hincks, T., W. Aspinall, R. Cooke, and T. Gernon (2018), Oklahoma's induced seismicity strongly linked to wastewater injection depth, *Science*, *359*(6381), 1251–1255.
Hodgkinson, K. M., R. S. Stein, and G. Marshall (1996), Geometry of the 1954 Fairview Peak-Dixie Valley earthquake sequence from a joint inversion of leveling and triangulation data, *Journal of Geophysical Research: Solid Earth*, *101*(B11), 25,437–25,457.
Hoffman, M. D., and A. Gelman (2014), The No-U-Turn sampler: adaptively setting path lengths in Hamiltonian Monte Carlo., *Journal of Machine Learning Research*, *15*(1), 1593–1623.
Hollingsworth, J., S. Leprince, F. Ayoub, and J.-P. Avouac (2012), Deformation during the 1975–1984 Krafla rifting crisis, NE Iceland, measured from historical optical imagery, *Journal of Geophysical Research: Solid Earth*, *117*(B11).
Holtkamp, S. G., M. Pritchard, and R. Lohman (2011), Earthquake swarms in south america, *Geophysical Journal International*, *187*(1), 128–146.
Holzner, J., and R. Bamler (2002), Burst-mode and ScanSAR interferometry, *IEEE transactions on geoscience and remote sensing*, *40*(9), 1917–1934.
Hooper, A. (2008), A multi-temporal InSAR method incorporating both persistent scatterer and small baseline approaches, *Geophys. Res. Lett.*, *35*(16), 16,302–+, doi:10.1029/2008GL034654.
Hooper, A., and H. A. Zebker (2007), Phase unwrapping in three dimensions with application to InSAR time series, *JOSA A*, *24*(9), 2737–2747.
Hooper, A., P. Segall, and H. Zebker (2007), Persistent scatterer interferometric synthetic aperture radar for crustal deformation analysis, with application to Volcán Alcedo, Galápagos, *Journal of Geophysical Research: Solid Earth*, *112*(B7).
Hooper, A., D. Bekaert, K. Spaans, and M. Arıkan (2012), Recent advances in SAR interferometry time series analysis for measuring crustal deformation, *Tectonophysics*, *514*, 1–13.
Hooper, A., J. Pietrzak, W. Simons, H. Cui, R. Riva, M. Naeije, A. T. van Scheltinga, E. Schrama, G. Stelling, and A. Socquet (2013), Importance of horizontal seafloor motion on tsunami height for the 2011 Mw= 9.0 Tohoku-Oki earthquake, *Earth and Planetary Science Letters*, *361*, 469–479.
Hornbach, M. J., H. R. DeShon, W. L. Ellsworth, B. W. Stump, C. Hayward, C. Frohlich, H. R. Oldham, J. E. Olson, M. B. Magnani, C. Brokaw, et al. (2015), Causal factors for seismicity near Azle, Texas, *Nature communications*, *6*, 6728.
Hornblow, S., M. Quigley, A. Nicol, R. Van Dissen, and N. Wang (2014), Paleoseismology of the 2010 Mw 7.1 Darfield (Canterbury) earthquake source, Greendale fault, New Zealand, *Tectonophysics*, *637*, 178–190.
Horton, S. (2012), Disposal of hydrofracking waste fluid by injection into subsurface aquifers triggers earthquake swarm in central Arkansas with potential for damaging earthquake, *Seismological Research Letters*, *83*(2), 250–260.
Hough, S. E. (2014), Shaking from injection-induced earthquakes in the central and eastern United States, *Bulletin of the Seismological Society of America*, *104*(5), 2619–2626.
Hough, S. E. (2016), *Predicting the unpredictable: the tumultuous science of earthquake prediction*, Princeton University Press.
Hough, S. E., and R. Bilham (2018), Poroelastic stress changes associated with primary oil production in the Los Angeles Basin, California, *The Leading Edge*, *37*(2), 108–116.
Hough, S. E., and R. G. Bilham (2005), *After the Earth Quakes: Elastic Rebound on an Urban Planet*, Oxford University Press.
Hough, S. E., and M. Page (2015), A century of induced earthquakes in Oklahoma?, *Bulletin of the Seismological Society of America*, *105*(6), 2863–2870.
Hubbard, J., R. Almeida, A. Foster, S. N. Sapkota, P. Bürgi, and P. Tapponnier (2016), Structural segmentation controlled the 2015 Mw 7.8 Gorkha earthquake rupture in Nepal, *Geology*, *44*(8), 639–642.
Hussain, E., A. Hooper, T. J. Wright, R. J. Walters, and D. P. Bekaert (2016), Interseismic strain accumulation across the central North Anatolian Fault from iteratively unwrapped InSAR measurements, *Journal of Geophysical Research: Solid Earth*, *121*(12), 9000–9019.
Hussain, E., T. J. Wright, R. J. Walters, D. P. Bekaert, R. Lloyd, and A. Hooper (2018), Constant strain accumulation rate between major earthquakes on the North Anatolian Fault, *Nature communications*, *9*(1), 1392.
Husson, L., T. Bodin, G. Spada, G. Choblet, and C. Kreemer (2018), Bayesian surface reconstruction of geodetic uplift rates: Mapping the global fingerprint of Glacial Isostatic Adjustment, *Journal of Geodynamics*, *122*, 25–40.
Ide, S., G. C. Beroza, D. R. Shelly, and T. Uchide (2007), A scaling law for slow earthquakes, *Nature*, *447*(7140), 76.
Ikari, M. J., Y. Ito, K. Ujiie, and A. J. Kopf (2015), Spectrum of slip behaviour in Tohoku fault zone samples at plate tectonic slip rates, *Nature Geoscience*, *8*(11), 870.
Imamura, A. (1930), On the block movement accompanying and following the Great Kwanto earthquake of 1923, *Proceedings of the Imperial Academy*, *6*(10), 415–418.
Ito, Y., T. Tsuji, Y. Osada, M. Kido, D. Inazu, Y. Hayashi, H. Tsushima, R. Hino, and H. Fujimoto (2011), Frontal wedge deformation near the source region of the 2011 Tohoku-Oki earthquake, *Geophysical Research Letters*, *38*(7).
Jackson, D. D. (1972), Interpretation of inaccurate, insufficient and inconsistent data, *Geophysical Journal International*, *28*(2), 97–109.
Jacques, E., T. Kidane, P. Tapponnier, I. Manighetti, Y. Gaudemer, B. Meyer, J. Ruegg, L. Audin, and R. Armijo (2011), Normal faulting during the August 1989 earthquakes in central Afar: Sequential triggering and propagation of rupture along the Dōbi Graben, *Bulletin of the Seismological Society of America*, *101*(3), 994–1023.
Jaeger, J. C., N. G. Cook, and R. Zimmerman (2009), *Fundamentals of rock mechanics*, John Wiley & Sons.
Jiang, H., G. Feng, T. Wang, and R. Bürgmann (2017), Toward full exploitation of coherent and incoherent information in Sentinel-1 TOPS data for retrieving surface displacement: Application to the 2016 Kumamoto (Japan) earthquake, *Geophysical Research Letters*, *44*(4), 1758–1767.

Johnson, K. (2008), Geologic history of Oklahoma: Educational publication: Oklahoma Geological Survey.
Johnson, K., and P. Segall (2004), Viscoelastic earthquake cycle models with deep stress-driven creep along the San Andreas fault system, *Journal of Geophysical Research: Solid Earth*, *109*(B10).
Johnson, K. M., R. Burgmann, and K. Larson (2006), Frictional properties on the San Andreas fault near Parkfield, California, inferred from models of afterslip following the 2004 earthquake, *Bulletin of the Seismological Society of America*, *96*(4B), S321–S338.
Johnston, A. C. (1996), Seismic moment assessment of earthquakes in stable continental regions – III. New Madrid 1811–1812, Charleston 1886 and Lisbon 1755, *Geophysical Journal International*, *126*(2), 314–344.
Jolivet, R., and M. Simons (2018), A multipixel time series analysis method accounting for ground motion, atmospheric noise, and orbital errors, *Geophysical Research Letters*, *45*(4), 1814–1824.
Jolivet, R., R. Cattin, N. Chamot-Rooke, C. Lasserre, and G. Peltzer (2008), Thin-plate modeling of interseismic deformation and asymmetry across the Altyn Tagh fault zone, *Geophysical Research Letters*, *35*(2).
Jolivet, R., R. Bürgmann, and N. Houlié (2009), Geodetic exploration of the elastic properties across and within the northern San Andreas Fault zone, *Earth and Planetary Science Letters*, *288*(1-2), 126–131.
Jolivet, R., R. **Grandin**, C. Lasserre, M.-P. Doin, and G. Peltzer (2011), Systematic InSAR tropospheric phase delay corrections from global meteorological reanalysis data, *Geophysical Research Letters*, *38*(17).
Jolivet, R., C. Lasserre, M.-P. Doin, S. Guillaso, G. Peltzer, R. Dailu, J. Sun, Z.-K. Shen, and X. Xu (2012), Shallow creep on the Haiyuan fault (Gansu, China) revealed by SAR interferometry, *Journal of Geophysical Research: Solid Earth*, *117*(B6).
Jolivet, R., Z. Duputel, B. Riel, M. Simons, L. Rivera, S. Minson, H. Zhang, M. Aivazis, F. Ayoub, S. Leprince, et al. (2014), The 2013 M w 7.7 Balochistan earthquake: Seismic potential of an accretionary wedge, *Bulletin of the Seismological Society of America*, *104*(2), 1020–1030.
Jolivet, R., M. Simons, P. Agram, Z. Duputel, and Z.-K. Shen (2015), Aseismic slip and seismogenic coupling along the central San Andreas Fault, *Geophysical Research Letters*, *42*(2), 297–306.
Jónsson, S., H. Zebker, P. Segall, and F. Amelung (2002), Fault Slip Distribution of the 1999 M_w 7.1 Hector Mine, California, Earthquake, Estimated from Satellite Radar and GPS Measurements, *Bull. Seismol. Soc. Am.*, *92*(4), 1377–1389, doi:10.1785/0120000922.
Jordan, T. H., and J. N. Franklin (1971), Optimal solutions to a linear inverse problem in geophysics, *Proceedings of the National Academy of Sciences*, *68*(2), 291–293.
Jousset, P., T. Reinsch, T. Ryberg, H. Blanck, A. Clarke, R. Aghayev, G. P. Hersir, J. Henninges, M. Weber, and C. M. Krawczyk (2018), Dynamic strain determination using fibre-optic cables allows imaging of seismological and structural features, *Nature communications*, *9*(1), 2509.
Juhel, K., J.-P. Ampuero, M. Barsuglia, P. Bernard, E. Chassande-Mottin, D. Fiorucci, J. Harms, J.-P. Montagner, M. Vallée, and B. Whiting (2018), Earthquake early warning using future generation gravity strainmeters, *Journal of Geophysical Research: Solid Earth*, *123*(12), 10–889.
Jung, H.-S., J.-S. Won, and S.-W. Kim (2009), An improvement of the performance of multiple-aperture SAR interferometry (MAI), *IEEE Transactions on Geoscience and Remote Sensing*, *47*(8), 2859–2869.
Jungels, P. H., and G. A. Frazier (1973), Finite element analysis of the residual displacements for an earthquake rupture: Source parameters for the San Fernando earthquake, *Journal of Geophysical Research*, *78*(23), 5062–5083.
Just, D., and R. Bamler (1994), Phase statistics of interferograms with applications to synthetic aperture radar, *Applied optics*, *33*(20), 4361–4368.
Kääb, A., B. Altena, and J. Mascaro (2017), Coseismic displacements of the 14 November 2016 M w 7.8 Kaikōura, New Zealand, earthquake using the Planet optical cubesat constellation, *Natural Hazards and Earth System Sciences*, *17*(5), 627.
Kagan, Y., and D. Jackson (1995), New seismic gap hypothesis: Five years after, *Journal of Geophysical Research: Solid Earth*, *100*(B3), 3943–3959.
Kagan, Y. Y. (1996), Comment on "The Gutenberg-Richter or characteristic earthquake distribution, which is it?" by Steven G. Wesnousky, *Bulletin of the Seismological Society of America*, *86*(1A), 274–285.
Kampes, B. M., R. F. Hanssen, and Z. Perski (2003), Radar interferometry with public domain tools, in *Proceedings of FRINGE*, vol. 3.
Kanamori, H. (2008), Earthquake physics and real-time seismology, *Nature*, *451*(7176), 271.
Kanamori, H., and C. R. Allen (1986), Earthquake repeat time and average stress drop, in *Earthquake Source Mechanics. Geophysical monograph*, vol. 37, pp. 227–235, American Geophysical Union.
Kanamori, H., and D. L. Anderson (1975), Theoretical basis of some empirical relations in seismology, *Bulletin of the seismological society of America*, *65*(5), 1073–1095.
Kanamori, H., and J. J. Cipar (1974), Focal process of the great Chilean earthquake May 22, 1960, *Physics of the Earth and Planetary Interiors*, *9*(2), 128–136.
Kaneko, Y., and Y. Fialko (2011), Shallow slip deficit due to large strike-slip earthquakes in dynamic rupture simulations with elasto-plastic off-fault response, *Geophysical Journal International*, *186*(3), 1389–1403.
Kato, A., and S. Nakagawa (2014), Multiple slow-slip events during a foreshock sequence of the 2014 Iquique, Chile Mw 8.1 earthquake, *Geophysical Research Letters*, *41*(15), 5420–5427.
Kato, A., K. Obara, T. Igarashi, H. Tsuruoka, S. Nakagawa, and N. Hirata (2012), Propagation of slow slip leading up to the 2011 Mw 9.0 Tohoku-Oki earthquake, *Science*, p. 1215141.
Kato, T., G. El-Fiky, E. N. Oware, and S. Miyazaki (1998), Crustal strains in the Japanese islands as deduced from dense GPS array, *Geophysical research letters*, *25*(18), 3445–3448.
Kaula, W. M. (1966), *Theory of satellite geodesy: applications of satellites to geodesy*, 2013 Courier Corporation, Reprint of Blaisdell Publishing Company, Waltham, Massachusetts, 1966 edition.
Kearse, J., T. A. Little, R. J. Van Dissen, P. M. Barnes, R. Langridge, J. Mountjoy, W. Ries, P. Villamor, K. J. Clark, A. Benson, et al. (2018), Onshore to offshore ground-surface and seabed rupture of the Jordan–Kekerengu–Needles fault network during the 2016 M w 7.8 Kaikōura earthquake, New Zealand, *Bulletin of the Seismological Society of America*.
Keranen, K. M., and M. Weingarten (2018), Induced seismicity, *Annual Review of Earth and Planetary Sciences*, *46*, 149–174.
Keranen, K. M., M. Weingarten, G. A. Abers, B. A. Bekins, and S. Ge (2014), Sharp increase in central Oklahoma seismicity since 2008 induced by massive wastewater injection, *Science*, *345*(6195), 448–451.
King, G. C., and S. G. Wesnousky (2007), Scaling of fault parameters for continental strike-slip earthquakes, *Bulletin of the Seismological Society of America*, *97*(6), 1833–1840.
King, G. C., R. S. Stein, and J. Lin (1994), Static stress changes and the triggering of earthquakes, *Bulletin of the Seismological Society of America*, *84*(3), 935–953.
Klein, E., L. Fleitout, C. Vigny, and J. Garaud (2016), Afterslip and viscoelastic relaxation model inferred from the large-scale post-seismic deformation following the 2010 M w 8.8 Maule earthquake (Chile), *Geophysical Journal International*, *205*(3), 1455–1472.
Klein, E., C. Vigny, L. Fleitout, R. **Grandin**, R. Jolivet, E. Rivera, and M. Métois (2017), A comprehensive analysis of the Illapel 2015 Mw8. 3 earthquake from GPS and InSAR data, *Earth and Planetary Science Letters*, *469*, 123–134.
Klinger, Y. (2010), Relation between continental strike-slip earthquake segmentation and thickness of the crust, *Journal of Geophysical Research: Solid Earth*, *115*(B7).
Klinger, Y., L. Rivera, H. Haessler, and J.-C. Maurin (1999), Active faulting in the Gulf of Aqaba: new knowledge from the Mw 7.3 earthquake of 22 November 1995, *Bulletin of the Seismological Society of America*, *89*(4), 1025–1036.
Klinger, Y., K. Sieh, E. Altunel, A. Akoglu, A. Barka, T. Dawson, T. Gonzalez, A. Meltzner, and T. Rockwell (2003), Paleoseismic evidence of characteristic slip on the western segment of the North Anatolian fault, Turkey, *Bulletin of the Seismological Society of America*, *93*(6), 2317–2332.
Klinger, Y., X. Xu, P. Tapponnier, J. Van der Woerd, C. Lasserre, and G. King (2005), High-resolution satellite imagery mapping of the surface rupture and slip distribution of the M w 7.8, 14 November 2001 Kokoxili earthquake, Kunlun fault, northern Tibet, China, *Bulletin of the Seismological Society of America*, *95*(5), 1970–1987.
Klinger, Y., R. Michel, and G. C. P. King (2006), Evidence for an earthquake barrier model from Mw ~ 7.8 Kokoxili (Tibet) earthquake slip-distribution, *Earth. Planet. Sci. Lett.*, *242*, 354–364, doi:10.1016/j.epsl.2005.12.003.
Klinger, Y., M. Etchebes, P. Tapponnier, and C. Narteau (2011), Characteristic slip for five great earthquakes along the Fuyun fault in China, *Nature Geoscience*, *4*(6), 389.
Klinger, Y., K. Okubo, A. Vallage, J. Champenois, A. Delorme, E. Rougier, Z. Lei, E. E. Knight, A. Munjiza, C. Satriano, et al. (2018), Earthquake damage patterns resolve complex rupture processes, *Geophysical Research Letters*, *45*(19), 10–279.
Knopoff, L. (1958), Energy release in earthquakes, *Geophysical Journal International*, *1*(1), 44–52.
Kobayashi, R., and K. Koketsu (2005), Source process of the 1923 Kanto earthquake inferred from historical geodetic, teleseismic, and strong motion data, *Earth, planets and space*, *57*(4), 261–270.
Kolawole, F., E. A. Atekwana, S. Malloy, D. S. Stamps, R. **Grandin**, M. G. Abdelsalam, K. Leseane, and E. M. Shemang (2017), Aeromagnetic, gravity, and Differential Interferometric Synthetic Aperture Radar analyses reveal the causative fault of the 3 April 2017 Mw 6.5 Moiyabana, Botswana, earthquake, *Geophysical Research Letters*, *44*(17), 8837–8846.
Kossobokov, V., and A. Nekrasova (2012), Global seismic hazard assessment program maps are erroneous, *Seismic instruments*, *48*(2), 162–170.
Kostrov, V. (1974), Seismic moment and energy of earthquakes, and seismic flow of rock, *Izv. Acad. Sci. USSR Phys. Solid Earth*, *1*, 23–44.
Kraus, T., B. Bräutigam, J. Mittermayer, S. Wollstadt, and C. Grigorov (2016), TerraSAR-X staring spotlight mode optimization and global performance predictions, *IEEE Journal of Selected Topics in Applied Earth Observations and Remote Sensing*, *9*(3), 1015–1027.
Kreemer, C., W. E. Holt, and A. J. Haines (2003), An integrated global model of present-day plate motions and plate boundary deformation, *Geophysical Journal International*, *154*(1), 8–34.
Kreemer, C., G. Blewitt, and F. Maerten (2006), Co-and postseismic deformation of the 28 March 2005 Nias Mw 8.7 earthquake from continuous GPS data, *Geophysical Research Letters*, *33*(7).
Kreemer, C., G. Blewitt, and E. C. Klein (2014), A geodetic plate motion and Global Strain Rate Model, *Geochemistry, Geophysics, Geosystems*, *15*(10), 3849–3889.
Krieger, G. (2014), MIMO-SAR: Opportunities and pitfalls, *IEEE Transactions on Geoscience and Remote Sensing*, *52*(5), 2628–2645.
Krieger, G., and A. Moreira (2003), Potential of digital beamforming in bi-and multistatic SAR, in *Geoscience and Remote Sensing Symposium, 2003. IGARSS'03. Proceedings. 2003 IEEE International*, vol. 1, pp. 527–529, IEEE.
Kumar, S., S. G. Wesnousky, T. K. Rockwell, R. W. Briggs, V. C. Thakur, and R. Jayangondaperumal (2006), Paleoseismic evidence of great surface rupture earthquakes along the Indian Himalaya, *Journal of Geophysical Research: Solid Earth*, *111*(B3).
Kurtz, R., Y. Klinger, M. Ferry, and J.-F. Ritz (2018), Horizontal surface-slip distribution through several seismic cycles: The Eastern Bogd fault, Gobi-Altai, Mongolia, *Tectonophysics*, *734*, 167–182.
Kurushin, R. (1997), *The surface rupture of the 1957 Gobi-Altay, Mongolia, earthquake*, vol. 320, Geological Society of America.

Labarre, S., S. Jacquemoud, C. Ferrari, A. Delorme, A. Derrien, R. **Grandin**, M. Jalludin, F. Lemaître, M. Métois, M. Pierrot-Deseilligny, et al. (2019), Retrieving soil surface roughness with the Hapke photometric model: Confrontation with the ground truth, *Remote sensing of environment*, *225*, 1–15.
Lacassin, R., and S. Lavelle (2016), The crisis of a paradigm. A methodological interpretation of Tohoku and Fukushima catastrophe, *Earth-science reviews*, *155*, 49–59.
Langenbruch, C., and M. D. Zoback (2016), How will induced seismicity in Oklahoma respond to decreased saltwater injection rates?, *Science advances*, *2*(11), e1601,542.
Larson, K. M., J. T. Freymueller, and S. Philipsen (1997), Global plate velocities from the Global Positioning System, *Journal of Geophysical Research: Solid Earth*, *102*(B5), 9961–9981.
Larson, K. M., P. Bodin, and J. Gomberg (2003), Using 1-Hz GPS data to measure deformations caused by the Denali fault earthquake, *Science*, *300*(5624), 1421–1424.
Lasserre, C., P.-H. Morel, Y. Gaudemer, P. Tapponnier, F. Ryerson, G. King, F. Metivier, M. Kasser, M. Kashgarian, B. Liu, et al. (1999), Postglacial left slip rate and past occurrence of M? 8 earthquakes on the western Haiyuan fault, Gansu, China, *Journal of Geophysical Research: Solid Earth*, *104*(B8), 17,633–17,651.
Lasserre, C., G. Peltzer, F. Crampé, Y. Klinger, J. Van Der Woerd, and P. Tapponnier (2005), Coseismic deformation of the 2001 Mw= 7.8 Kokoxili earthquake in Tibet, measured by synthetic aperture radar interferometry, *Journal of Geophysical Research: Solid Earth*, *110*(B12408).
Lauer, B., R. **Grandin**, and Y. Klinger (2019), Fault geometry and slip distribution of the 2013 Mw 7.7 Balochistan earthquake from non-linear and linear inversions of SAR and optical data, *Journal of Geophysical Research, submitted*.
Lavé, J., and J. Avouac (2001), Fluvial incision and tectonic uplift across the Himalayas of central Nepal, *Journal of Geophysical Research: Solid Earth*, *106*(B11), 26,561–26,591.
Lavé, J., D. Yule, S. Sapkota, K. Basant, C. Madden, M. Attal, and R. Pandey (2005), Evidence for a great medieval earthquake (˜ 1100 AD) in the central Himalayas, Nepal, *Science*, *307*(5713), 1302–1305.
Lawrence, R., R. Yeats, S. Khan, A. Farah, and K. DeJong (1981), Thrust and strike slip fault interaction along the Chaman transform zone, Pakistan, *Geological Society, London, Special Publications*, *9*(1), 363–370.
Lawson, C. L., and R. J. Hanson (1974), *Solving least squares problems*, vol. 15, Siam.
Le Beon, M., Y. Klinger, A. Q. Amrat, A. Agnon, L. Dorbath, G. Baer, J.-C. Ruegg, O. Charade, and O. Mayyas (2008), Slip rate and locking depth from GPS profiles across the southern Dead Sea Transform, *Journal of Geophysical Research: Solid Earth*, *113*(B11).
Le Pichon, X., C. Kreemer, and N. Chamot-Rooke (2005), Asymmetry in elastic properties and the evolution of large continental strike-slip faults, *Journal of Geophysical Research: Solid Earth*, *110*(B3).
Lee, J.-S., S. R. Cloude, K. P. Papathanassiou, M. R. Grunes, and I. H. Woodhouse (2003), Speckle filtering and coherence estimation of polarimetric SAR interferometry data for forest applications, *IEEE Transactions on Geoscience and Remote Sensing*, *41*(10), 2254–2263.
Lefevre, M., Y. Klinger, M. Al-Qaryouti, M. Le Béon, and K. Moumani (2018), Slip deficit and temporal clustering along the Dead Sea fault from paleoseismological investigations, *Scientific reports*, *8*(1), 4511.
Lei, X., D. Huang, J. Su, G. Jiang, X. Wang, H. Wang, X. Guo, and H. Fu (2017), Fault reactivation and earthquakes with magnitudes of up to Mw4. 7 induced by shale-gas hydraulic fracturing in Sichuan Basin, China, *Scientific reports*, *7*(1), 7971.
Lemoine, A., D. Bertil, A. Roullé, and P. Briole (2019), The volcano-tectonic crisis of 2018 east of Mayotte, Comoros islands, *EarthArXiv*, https://eartharxiv.org/d46xj.
León-Ríos, S., S. Ruiz, A. Maksymowicz, F. Leyton, A. Fuenzalida, and R. Madariaga (2016), Diversity of the 2014 Iquique?s foreshocks and aftershocks: clues about the complex rupture process of a Mw 8.1 earthquake, *Journal of Seismology*, *20*(4), 1059–1073.
Leonard, M. (2010), Earthquake fault scaling: Self-consistent relating of rupture length, width, average displacement, and moment release, *Bulletin of the Seismological Society of America*, *100*(5A), 1971–1988.
Leão, J. W., and J. B. Silva (1989), Discrete linear transformations of potential field data, *Geophysics*, *54*(4), 497–507.
Li, Z., J.-P. Muller, P. Cross, and E. J. Fielding (2005), Interferometric synthetic aperture radar (InSAR) atmospheric correction: GPS, Moderate Resolution Imaging Spectroradiometer (MODIS), and InSAR integration, *Journal of Geophysical Research: Solid Earth*, *110*(B3).
Liang, C., Q. Zeng, J. Jia, J. Jiao, et al. (2013), ScanSAR interferometric processing using existing standard InSAR software for measuring large scale land deformation, *Computers & geosciences*, *51*, 439–448.
Liang, C., P. Agram, M. Simons, and E. J. Fielding (2019), Ionospheric Correction of InSAR Time Series Analysis of C-band Sentinel-1 TOPS Data, doi:10.31223/osf.io/atxr7.
Lisowski, M. (2007), Analytical volcano deformation source models, in *Volcano deformation*, pp. 279–304, Springer.
Liu, M., and S. Stein (2016), Mid-continental earthquakes: Spatiotemporal occurrences, causes, and hazards, *Earth-Science Reviews*, *162*, 364–386.
Liu-Zeng, J., Y. Shao, Y. Klinger, K. Xie, D. Yuan, and Z. Lei (2015), Variability in magnitude of paleoearthquakes revealed by trenching and historical records, along the Haiyuan fault, China, *Journal of Geophysical Research: Solid Earth*, *120*(12), 8304–8333.
Lohman, R. B., and M. Simons (2005), Some thoughts on the use of InSAR data to constrain models of surface deformation: Noise structure and data downsampling, *Geochemistry, Geophysics, Geosystems*, *6*(1).
López-Comino, J., S. Cesca, J. Jarosławski, N. Montcoudiol, S. Heimann, T. Dahm, S. Lasocki, A. Gunning, P. Capuano, and W. L. Ellsworth (2018), Induced seismicity response of hydraulic fracturing: results of a multidisciplinary monitoring at the Wysin site, Poland, *Scientific reports*, *8*(1), 8653.
López-Quiroz, P., M.-P. Doin, F. Tupin, P. Briole, and J.-M. Nicolas (2009), Time series analysis of Mexico City subsidence constrained by radar interferometry, *Journal of Applied Geophysics*, *69*(1), 1–15.
Loveless, J. P., and B. J. Meade (2016), Two decades of spatiotemporal variations in subduction zone coupling offshore Japan, *Earth and Planetary Science Letters*, *436*, 19–30.
Lyon-Caen, H. e. a., R. Armijo, J. Drakopoulos, J. Baskoutass, N. Delibassis, R. Gaulon, V. Kouskouna, J. Latoussakis, K. Makropoulos, P. Papadimitriou, et al. (1988), The 1986 Kalamata (South Peloponnesus) earthquake: Detailed study of a normal fault, evidences for east-west extension in the Hellenic Arc, *Journal of Geophysical Research: Solid Earth*, *93*(B12), 14,967–15,000.
Lyons, S., and D. Sandwell (2003), Fault creep along the southern San Andreas from interferometric synthetic aperture radar, permanent scatterers, and stacking, *Journal of Geophysical Research: Solid Earth*, *108*(B1).
Ma, X., and N. Kusznir (1994), Effects of rigidity layering, gravity and stress relaxation on 3-D subsurface fault displacement fields, *Geophysical Journal International*, *118*(1), 201–220.
Madariaga, R. (1979), On the relation between seismic moment and stress drop in the presence of stress and strength heterogeneity, *Journal of Geophysical Research: Solid Earth*, *84*(B5), 2243–2250.
Maerten, F., P. Resor, D. Pollard, and L. Maerten (2005), Inverting for slip on three-dimensional fault surfaces using angular dislocations, *Bulletin of the Seismological Society of America*, *95*(5), 1654–1665.
Maerten, F., L. Maerten, and M. Cooke (2010), Solving 3D boundary element problems using constrained iterative approach, *Computational Geosciences*, *14*(4), 551–564.
Manighetti, I., G. King, and C. G. Sammis (2004), The role of off-fault damage in the evolution of normal faults, *Earth and Planetary Science Letters*, *217*(3-4), 399–408.
Manighetti, I., M. Campillo, S. Bouley, and F. Cotton (2007), Earthquake scaling, fault segmentation, and structural maturity, *Earth and Planetary Science Letters*, *253*(3-4), 429–438.
Mansfield, C., and J. Cartwright (1996), High resolution fault displacement mapping from three-dimensional seismic data: evidence for dip linkage during fault growth, *Journal of Structural Geology*, *18*(2-3), 249–263.
Mansinha, L., and D. Smylie (1971), The displacement fields of inclined faults, *Bulletin of the Seismological Society of America*, *61*(5), 1433–1440.
Marti, É. (2018), Estimation des taux de séismes le long de la faille du Levant (Israël/Jordanie) à partir des données publiées, Master's thesis, Institut de Physique du Globe de Paris.
Martin, S. S., S. E. Hough, and C. Hung (2015), Ground motions from the 2015 M w 7.8 Gorkha, Nepal, earthquake constrained by a detailed assessment of macroseismic data, *Seismological Research Letters*, *86*(6), 1524–1532.
Maruyama, T. (1964), Statical elastic dislocations in an infinite and semi-infinite medium, *Bull. Earthq. Res. Inst., Univ. Tokyo*, *42*, 289–368.
Massonnet, D., and J.-C. Souyris (2008), *Imaging with synthetic aperture radar*, CRC Press.
Massonnet, D., M. Rossi, C. Carmona, F. Adragna, G. Peltzer, K. Feigl, and T. Rabaute (1993), The displacement field of the Landers earthquake mapped by radar interferometry, *Nature*, *364*, 138–142, doi:10.1038/364138a0.
Masterlark, T. (2003), Finite element model predictions of static deformation from dislocation sources in a subduction zone: sensitivities to homogeneous, isotropic, Poisson-solid, and half-space assumptions, *Journal of Geophysical Research: Solid Earth*, *108*(B11).
Masterlark, T., and K. L. Hughes (2008), Next generation of deformation models for the 2004 M9 Sumatra-Andaman earthquake, *Geophysical Research Letters*, *35*(19).
Masuti, S. S., S. Barbot, and N. Kapre (2014), Relax-Miracle: GPU parallelization of semi-analytic fourier-domain solvers for earthquake modeling, in *High Performance Computing (HiPC), 2014 21st International Conference on*, pp. 1–10, IEEE.
Matsu'ura, M. (1977a), Inversion of geodetic data. Part I. Mathematical Formulation, *Journal of Physics of the Earth*, *25*, 69–90.
Matsu'ura, M. (1977b), Inversion of geodetic data. Part II. Optimal model of conjugate fault system for the 1927 Tango earthquake, *Journal of Physics of the Earth*, *25*(3), 233–255.
Matsuzawa, T., H. Hirose, B. Shibazaki, and K. Obara (2010), Modeling short-and long-term slow slip events in the seismic cycles of large subduction earthquakes, *Journal of Geophysical Research: Solid Earth*, *115*(B12).
Maurer, J., P. Segall, and A. M. Bradley (2017), Bounding the moment deficit rate on crustal faults using geodetic data: Methods, *Journal of Geophysical Research: Solid Earth*.
Mavko, G. M. (1981), Mechanics of motion on major faults, *Annual Review of Earth and Planetary Sciences*, *9*(1), 81–111.
Mavrommatis, A. P., P. Segall, and K. M. Johnson (2014), A decadal-scale deformation transient prior to the 2011 Mw 9.0 Tohoku-oki earthquake, *Geophysical Research Letters*, *41*(13), 4486–4494.
Mavrommatis, A. P., P. Segall, N. Uchida, and K. M. Johnson (2015), Long-term acceleration of aseismic slip preceding the Mw 9 Tohoku-oki earthquake: Constraints from repeating earthquakes, *Geophysical Research Letters*, *42*(22), 9717–9725.
McCann, W., S. Nishenko, L. Sykes, and J. Krause (1979), Seismic gaps and plate tectonics: seismic potential for major boundaries, in *Earthquake Prediction and Seismicity Patterns*, pp. 1082–1147, Springer.
McClusky, S., S. Balassanian, A. Barka, C. Demir, S. Ergintav, I. Georgiev, O. Gurkan, M. Hamburger, K. Hurst, H. Kahle, et al. (2000), Global Positioning System constraints on plate kinematics and dynamics in the eastern Mediterranean and Caucasus, *Journal of Geophysical Research: Solid Earth*, *105*(B3), 5695–5719.
McCormick Kilbride, B., M. Edmonds, and J. Biggs (2016), Observing eruptions of gas-rich compressible magmas from space, *Nature communications*, *7*, 13,744.
McGarr, A. (2014), Maximum magnitude earthquakes induced by fluid injection, *Journal of Geophysical Research: solid earth*, *119*(2), 1008–1019.

McGarr, A., B. Bekins, N. Burkardt, J. Dewey, P. Earle, W. Ellsworth, S. Ge, S. Hickman, A. Holland, E. Majer, et al. (2015), Coping with earthquakes induced by fluid injection, *Science*, *347*(6224), 830–831.
McHugh, S., and M. J. Johnston (1977), An analysis of coseismic tilt changes from an array in central California, *Journal of Geophysical Research*, *82*(36), 5692–5698.
McTigue, D., and P. Segall (1988), Displacements and tilts from dip-slip faults and magma chambers beneath irregular surface topography, *Geophysical Research Letters*, *15*(6), 601–604.
McTigue, D. F. (1987), Elastic stress and deformation near a finite spherical magma body: Resolution of the point source paradox, *J. Geophys. Res.*, *92*, 12,931–12,940, doi:10.1029/JB092iB12p12931.
McTigue, D. F., and C. C. Mei (1981), Gravity-induced stresses near topography of small slope, *Journal of Geophysical Research: Solid Earth*, *86*(B10), 9268–9278.
Mctigue, D. F., and R. S. Stein (1984), Topographic amplification of tectonic displacement: implications for geodetic measurement of strain changes, *Journal of Geophysical Research: Solid Earth*, *89*(B2), 1123–1131.
Meade, B. J. (2007), Algorithms for the calculation of exact displacements, strains, and stresses for triangular dislocation elements in a uniform elastic half space, *Computers & geosciences*, *33*(8), 1064–1075.
Meade, B. J., and J. P. Loveless (2009), Predicting the geodetic signature of Mw≥8 slow slip events, *Geophysical Research Letters*, *36*(1).
Meertens, C. M., and J. M. Wahr (1986), Topographic effect on tilt, strain, and displacement measurements, *Journal of Geophysical Research: Solid Earth*, *91*(B14), 14,057–14,062.
Meister, L. J., R. O. Burford, G. A. Thompson, and R. L. Kovach (1968), Surface strain changes and strain energy release in the Dixie Valley-Fairview Peak Area, Nevada, *Journal of Geophysical Research*, *73*(18), 5981–5994.
Meng, H., and Y. Ben-Zion (2017), Detection of small earthquakes with dense array data: example from the San Jacinto fault zone, southern California, *Geophysical Journal International*, *212*(1), 442–457, doi:10.1093/gji/ggx404.
Meng, L., J.-P. Ampuero, A. Sladen, and H. Rendon (2012), High-resolution backprojection at regional distance: Application to the Haiti M7. 0 earthquake and comparisons with finite source studies, *Journal of Geophysical Research: Solid Earth*, *117*(B4).
Menke, W. (1989), *Geophysical data analysis: Discrete inverse theory*, International Geophysics Series, New York: Academic Press, 1989, Rev.ed.
Métivier, L., O. de Viron, C. P. Conrad, S. Renault, M. Diament, and G. Patau (2009), Evidence of earthquake triggering by the solid earth tides, *Earth and Planetary Science Letters*, *278*(3-4), 370–375.
Métois, M., A. Socquet, and C. Vigny (2012), Interseismic coupling, segmentation and mechanical behavior of the central Chile subduction zone, *Journal of Geophysical Research: Solid Earth*, *117*(B3).
Métois, M., M. Benjelloun, C. Lasserre, R. **Grandin**, L. Barrier, E. Dushi, and R. Koçi (2019), Subsidence associated with oil extraction, measured from time-series analysis of Sentinel-1 data: case study of the Patos-Marinza oil field, Albania., *Solid Earth Discuss., in review*, doi:10.5194/se-2019-12.
Meyer, F., R. Bamler, N. Jakowski, and T. Fritz (2006), The potential of low-frequency SAR systems for mapping ionospheric TEC distributions, *IEEE Geoscience and Remote Sensing Letters*, *3*(4), 560–564.
Michel, R., J.-P. Avouac, and J. Taboury (1999), Measuring ground displacements from SAR amplitude images: Application to the Landers earthquake, *Geophysical Research Letters*, *26*(7), 875–878.
Mignan, A., M. Broccardo, S. Wiemer, and D. Giardini (2017), Induced seismicity closed-form traffic light system for actuarial decision-making during deep fluid injections, *Scientific reports*, *7*(1), 13,607.
Miller, M. M., D. J. Johnson, C. M. Rubin, H. Dragert, K. Wang, A. Qamar, and C. Goldfinger (2001), GPS-determination of along-strike variation in Cascadia margin kinematics: Implications for relative plate motion, subduction zone coupling, and permanent deformation, *Tectonics*, *20*(2), 161–176.
Minson, S., M. Simons, and J. Beck (2013), Bayesian inversion for finite fault earthquake source models I – Theory and algorithm, *Geophysical Journal International*, *194*(3), 1701–1726.
Miranda, N. (2014), Definition of the TOPS SLC deramping function for products generated by the S-1 IPF, *Eur. Space Agency, Paris, France, Tech. Rep*.
Miyashita, K., and M. Matsu'ura (1978), Inversion analysis of static displacement data associated with the Alaska earthquake of 1964, *Journal of Physics of the Earth*, *26*(4), 333–349.
Mogi, K. (1958), Relations between the Eruptions of Various Volcanoes and the Deformations of the Ground Surfaces around them., *Earthquake research institute*, *36*, 99–134.
Mogi, K. (1958), Relations between the eruptions of various volcanoes and the deformations of the ground surfaces around them, *Bull. Earthq. Res. Inst.*, *36*, 99–134.
Molnar, P., and P. Tapponnier (1975), Cenozoic tectonics of Asia: effects of a continental collision, *science*, *189*(4201), 419–426.
Montagner, J.-P., K. Juhel, M. Barsuglia, J. P. Ampuero, E. Chassande-Mottin, J. Harms, B. Whiting, P. Bernard, E. Clévédé, and P. Lognonné (2016), Prompt gravity signal induced by the 2011 Tohoku-Oki earthquake, *Nature communications*, *7*, 13,349.
Moore, C., T. J. Wright, A. J. Hooper, and J. Biggs (2018), InSAR Observations of Long-Term Extension in the Build-Up to the January 2017 Eruption of Erta ?Ale volcano, Afar, Ethiopia., in *AGU Fall Meeting Abstracts*.
Moreira, A., P. Prats-Iraola, M. Younis, G. Krieger, I. Hajnsek, and K. P. Papathanassiou (2013), A tutorial on synthetic aperture radar, *IEEE Geoscience and remote sensing magazine*, *1*(1), 6–43.
Morgan, B. C., and K. E. Murray (2015), Characterizing small-scale permeability of the Arbuckle Group, Oklahoma, *Okla. Geol. Surv. Open-File Rept. OF2-2015*, pp. 1–12.
Mosegaard, K., and M. Sambridge (2002), Monte Carlo analysis of inverse problems, *Inverse problems*, *18*(3), R29.
Mosegaard, K., and A. Tarantola (1995), Monte Carlo sampling of solutions to inverse problems, *Journal of Geophysical Research: Solid Earth*, *100*(B7), 12,431–12,447.
Motohka, T., Y. Kankaku, S. Miura, and S. Suzuki (2018), Overview of the Advanced Land Observing Satellite-4 (ALOS-4) mission, in *Japan Geoscience Union Meeting 2018*, STT48-06.
Mulargia, F., P. B. Stark, and R. J. Geller (2017), Why is probabilistic seismic hazard analysis (PSHA) still used?, *Physics of the Earth and Planetary Interiors*, *264*, 63–75.
Natawidjaja, D. H., K. Sieh, M. Chlieh, J. Galetzka, B. W. Suwargadi, H. Cheng, R. L. Edwards, J.-P. Avouac, and S. N. Ward (2006), Source parameters of the great Sumatran megathrust earthquakes of 1797 and 1833 inferred from coral microatolls, *Journal of Geophysical Research: Solid Earth*, *111*(B6).
Neumann, M., L. Ferro-Famil, and A. Reigber (2009), Estimation of forest structure, ground, and canopy layer characteristics from multibaseline polarimetric interferometric SAR data, *IEEE Transactions on Geoscience and Remote Sensing*, *48*(3), 1086–1104.
Newhall, C. G., and R. Punongbayan (1996), *Fire and mud: eruptions and lahars of Mount Pinatubo, Philippines*, Philippine Institute of Volcanology and Seismology Quezon City.
Nikkhoo, M., and T. R. Walter (2015), Triangular dislocation: an analytical, artefact-free solution, *Geophysical Journal International*, *201*(2), 1119–1141.
Nikkhoo, M., T. R. Walter, P. R. Lundgren, and P. Prats-Iraola (2016), Compound dislocation models (CDMs) for volcano deformation analyses, *Geophysical Journal International*, p. ggw427.
Nocquet, J. (2018), Stochastic static fault slip inversion from geodetic data with non-negativity and bound constraints, *Geophysical Journal International*, *214*(1), 366–385.
Nocquet, J.-M., P. Jarrin, M. Vallée, P. Mothes, R. **Grandin**, et al. (2017), Supercycle at the Ecuadorian subduction zone revealed after the 2016 Pedernales earthquake, *Nature Geoscience*, *10*(2), 145.
Nyst, M., T. Nishimura, F. Pollitz, and W. Thatcher (2006), The 1923 Kanto earthquake reevaluated using a newly augmented geodetic data set, *Journal of Geophysical Research: Solid Earth*, *111*(B11).
Ogwari, P. O., H. R. DeShon, and M. J. Hornbach (2018), The Dallas-Fort Worth airport earthquake sequence: Seismicity beyond injection period, *Journal of Geophysical Research: Solid Earth*, *123*(1), 553–563.
Okada, Y. (1985), Surface deformation due to shear and tensile faults in a half space, *Bull. Seismol. Soc. Am.*, *75*(4), 1135–1154.
Oldham, R. D. (1900), *Report on the Great Earthquake of 12th June 1897*, Office of the Geological survey.
Omori, F. (1916), Chapter VII. Level change and horizontal displacement of the ground caused by the Sakura-Jima eruption of 1914, in *The Sakura-Jima eruption and earthquakes*, vol. 8, pp. 152–179, Bulletin of the Imperial Earthquake Investigation Committee.
Oskin, M. E., J. R. Arrowsmith, A. H. Corona, A. J. Elliott, J. M. Fletcher, E. J. Fielding, P. O. Gold, J. J. G. Garcia, K. W. Hudnut, J. Liu-Zeng, et al. (2012), Near-field deformation from the El Mayor–Cucapah earthquake revealed by differential LIDAR, *Science*, *335*(6069), 702–705.
Page, M. T., S. Custódio, R. J. Archuleta, and J. Carlson (2009), Constraining earthquake source inversions with GPS data: 1. Resolution-based removal of artifacts, *Journal of Geophysical Research: Solid Earth*, *114*(B1).
Parker, R. L. (1977), Understanding Inverse Theory, *Annual Review of Earth and Planetary Sciences*, *5*, 35–+, doi:10.1146/annurev.ea.05.050177.000343.
Parsons, T., L. Malagnini, and A. Akinci (2017), Nucleation speed limit on remote fluid-induced earthquakes, *Science advances*, *3*(8), e1700,660.
Peacock, D. (2002), Propagation, interaction and linkage in normal fault systems, *Earth-Science Reviews*, *58*(1-2), 121–142.
Peary, B. D., R. Shaw, and Y. Takeuchi (2012), Utilization of social media in the east Japan earthquake and tsunami and its effectiveness, *Journal of Natural Disaster Science*, *34*(1), 3–18.
Peltzer, G., K. W. Hudnut, and K. L. Feigl (1994), Analysis of coseismic surface displacement gradients using radar interferometry: New insights into the Landers earthquake, *Journal of Geophysical Research: Solid Earth*, *99*(B11), 21,971–21,981.
Peltzer, G., P. Rosen, F. Rogez, and K. Hudnut (1998), Poroelastic rebound along the Landers 1992 earthquake surface rupture, *Journal of Geophysical Research: Solid Earth*, *103*(B12), 30,131–30,145.
Peltzer, G., F. Crampé, S. Hensley, and P. Rosen (2001), Transient strain accumulation and fault interaction in the Eastern California shear zone, *Geology*, *29*, 975–+, doi:10.1130/0091-7613(2001)029<0975:TSAAFI>2.0.CO;2.
Peng, Z., and J. Gomberg (2010), An integrated perspective of the continuum between earthquakes and slow-slip phenomena, *Nature Geoscience*, *3*(9), 599.
Petersen, M. D., C. S. Mueller, M. P. Moschetti, S. M. Hoover, K. S. Rukstales, D. E. McNamara, R. A. Williams, A. M. Shumway, P. M. Powers, P. S. Earle, et al. (2018), 2018 One-Year Seismic Hazard Forecast for the Central and Eastern United States from Induced and Natural Earthquakes, *Seismological Research Letters*, *89*(3), 1049–1061.
Philip, H., and M. Meghraoui (1983), Structural analysis and interpretation of the surface deformations of the El Asnam earthquake of October 10, 1980, *Tectonics*, *2*(1), 17–49.
Phillips, K. A., C. D. Chadwell, and J. A. Hildebrand (2008), Vertical deformation measurements on the submerged south flank of Kīlauea volcano, Hawai'i reveal seafloor motion associated with volcanic collapse, *Journal of Geophysical Research: Solid Earth*, *113*(B5).
Pinel, V., A. Hooper, S. De la Cruz-Reyna, G. Reyes-Davila, M. Doin, and P. Bascou (2011), The challenging retrieval of the displacement field from InSAR data for andesitic stratovolcanoes: Case study of Popocatepetl and Colima Volcano, Mexico, *Journal of Volcanology and Geothermal Research*, *200*(1-2), 49–61.
Pinel-Puysségur, B., R. Michel, and J.-P. Avouac (2012), Multi-link InSAR time series: Enhancement of a wrapped interferometric database, *IEEE Journal of Selected Topics in Applied Earth Observations and Remote Sensing*, *5*(3), 784–794.

Pinel-Puysségur, B., R. **Grandin**, L. Bollinger, et al. (2014), Multifaulting in a tectonic syntaxis revealed by InSAR: the case of the Ziarat earthquake sequence (Pakistan), *Journal of Geophysical Research: Solid Earth*, *119*(7), 5838–5854.
Pollitz, F. F. (1996), Coseismic deformation from earthquake faulting on a layered spherical Earth, *Geophysical Journal International*, *125*(1), 1–14.
Pollitz, F. F., and I. S. Sacks (1994), Fault model of the 1891 Nobi earthquake from historic triangulation and leveling, *Journal of Physics of the Earth*, *42*(1), 1–43.
Pollitz, F. F., B. Brooks, X. Tong, M. G. Bevis, J. H. Foster, R. Bürgmann, R. Smalley Jr, C. Vigny, A. Socquet, J.-C. Ruegg, et al. (2011), Coseismic slip distribution of the February 27, 2010 Mw 8.8 Maule, Chile earthquake, *Geophysical Research Letters*, *38*(9).
Pollitz, F. F., R. Bürgmann, R. S. Stein, and V. Sevilgen (2014), The profound reach of the 11 April 2012 M 8.6 Indian Ocean earthquake: Short-term global triggering followed by a longer-term global shadow, *Bulletin of the Seismological Society of America*, *104*(2), 972–984.
Pondard, N., R. Armijo, G. C. King, B. Meyer, and F. Flerit (2007), Fault interactions in the Sea of Marmara pull-apart (North Anatolian Fault): earthquake clustering and propagating earthquake sequences, *Geophysical Journal International*, *171*(3), 1185–1197.
Prats, P., R. Scheiber, J. Mittermayer, A. Meta, and A. Moreira (2010), Processing of sliding spotlight and TOPS SAR data using baseband azimuth scaling, *IEEE Transactions on geoscience and remote sensing*, *48*(2), 770–780.
Prats-Iraola, P., R. Scheiber, L. Marotti, S. Wollstadt, and A. Reigber (2012), TOPS interferometry with TerraSAR-X, *IEEE Transactions on geoscience and remote sensing*, *50*(8), 3179–3188.
Prawirodirdjo, L., Y. Bock, J. Genrich, S. Puntodewo, J. Rais, C. Subarya, and S. Sutisna (2000), One century of tectonic deformation along the Sumatran fault from triangulation and Global Positioning System surveys, *Journal of Geophysical Research: Solid Earth*, *105*(B12), 28,343–28,361.
Price, E. J., and D. T. Sandwell (1998), Small-scale deformations associated with the 1992 Landers, California, earthquake mapped by synthetic aperture radar interferometry phase gradients, *Journal of Geophysical Research: Solid Earth*, *103*(B11), 27,001–27,016.
Pritchard, M., M. Simons, P. Rosen, S. Hensley, and F. Webb (2002), Co-seismic slip from the 1995 July 30 Mw= 8. 1 Antofagasta, Chile, earthquake as constrained by InSAR and GPS observations, *Geophys. J. Int*, *150*, 362–376.
Queiroz de Almeida, F. (2018), Multichannel Staggered SAR for High-Resolution Wide-Swath Imaging, Ph.D. thesis, Karlsruher Instituts für Technologie (KIT).
Rabus, B., M. Eineder, A. Roth, and R. Bamler (2003), The shuttle radar topography mission?a new class of digital elevation models acquired by spaceborne radar, *ISPRS journal of photogrammetry and remote sensing*, *57*(4), 241–262.
Radiguet, M., F. Cotton, M. Vergnolle, M. Campillo, B. Valette, V. Kostoglodov, and N. Cotte (2011), Spatial and temporal evolution of a long term slow slip event: the 2006 Guerrero Slow Slip Event, *Geophysical Journal International*, *184*(2), 816–828.
Radiguet, M., F. Cotton, M. Vergnolle, M. Campillo, A. Walpersdorf, N. Cotte, and V. Kostoglodov (2012), Slow slip events and strain accumulation in the Guerrero gap, Mexico, *Journal of Geophysical Research: Solid Earth*, *117*(B4).
Radiguet, M., H. Perfettini, N. Cotte, A. Gualandi, B. Valette, V. Kostoglodov, T. Lhomme, A. Walpersdorf, E. C. Cano, and M. Campillo (2016), Triggering of the 2014 Mw 7.3 Papanoa earthquake by a slow slip event in Guerrero, Mexico, *Nature Geoscience*, *9*(11), 829.
Ragon, T., A. Sladen, Q. Bletery, M. Vergnolle, O. Cavalié, and A. Avallone (2018a), Joint inversion of co-seismic and early post-seismic slip: Application to the 2009 Mw6.3 L'Aquila earthquake, Central Italy, doi:10.31223/osf.io/urkga.
Ragon, T., A. Sladen, and M. Simons (2018b), Accounting for uncertain fault geometry in earthquake source inversions–I: theory and simplified application, *Geophysical Journal International*, *214*(2), 1174–1190.
Reid, H. (1910), Permanent displacements of the ground, in *The California Earthquake of April 18, 1906, Report of the State Earthquake Investigation Commission, Volume 2, The mechanics of the earthquake*, pp. 16–28, Carnegie Institution of Washington, Washington, DC.
Reid, H. F. (1913), Sudden Earth-movements in Sumatra in 1892, *Bulletin of the Seismological Society of America*, *3*(2), 72–79.
Reitherman, R. (2006), Earthquakes that have initiated the development of earthquake engineering, *Bulletin of the New Zealand Society for Earthquake Engineering*, *39*(3), 145–157.
Ren, Z., Z. Zhang, T. Chen, S. Yan, J. Yin, P. Zhang, W. Zheng, H. Zhang, and C. Li (2016), Clustering of offsets on the Haiyuan fault and their relationship to paleoearthquakes, *Bulletin*, *128*(1-2), 3–18.
Roach, T. (2018), Oklahoma earthquakes and the price of oil, *Energy policy*, *121*, 365–373.
Rodriguez-Cassola, M., P. Prats, D. Schulze, N. Tous-Ramon, U. Steinbrecher, L. Marotti, M. Nannini, M. Younis, P. López-Dekker, M. Zink, et al. (2012), First bistatic spaceborne SAR experiments with TanDEM-X, *IEEE Geoscience and Remote Sensing Letters*, *9*(1), 33–37.
Rodriguez-Cassola, M., P. Prats-Iraola, F. De Zan, R. Scheiber, A. Reigber, D. Geudtner, and A. Moreira (2015), Doppler-related distortions in TOPS SAR images, *IEEE Transactions on Geoscience and Remote Sensing*, *53*(1), 25–35.
Rogers, G., and H. Dragert (2003), Episodic tremor and slip on the Cascadia subduction zone: The chatter of silent slip, *Science*, *300*(5627), 1942–1943.
Rolandone, F., J.-M. Nocquet, P. A. Mothes, P. Jarrin, M. Vallée, N. Cubas, S. Hernandez, M. Plain, S. Vaca, and Y. Font (2018), Areas prone to slow slip events impede earthquake rupture propagation and promote afterslip, *Science advances*, *4*(1), eaao6596.
Romanowicz, B., and L. Ruff (2002), On moment-length scaling of large strike slip earthquakes and the strength of faults, *Geophysical Research Letters*, *29*(12), 45–1.
Rosen, P. A., S. Henley, G. Peltzer, and M. Simons (2004), Updated Repeat Orbit Interferometry Package Released, *Eos Trans. AGU*, *85*(5), 47–47, doi:10.1029/2004EO050004.
Rosen, P. A., E. Gurrola, G. F. Sacco, and H. Zebker (2012), The InSAR scientific computing environment, in *Synthetic Aperture Radar, 2012. EUSAR. 9th European Conference on*, pp. 730–733, VDE.
Rosich, B., A. Monti-Guarnieri, D. D?Aria, I. Navas, B. Duesmann, C. Cafforio, P. Guccione, S. Vazzana, O. Barois, O. Colin, et al. (2007), ASAR wide swath mode interferometry: Optimisation of the scan pattern synchronisation, in *Proceedings of the Envisat Symposium, SP*, vol. 636, Citeseer.
Ross, Z. E., D. T. Trugman, E. Hauksson, and P. M. Shearer (2019), Searching for hidden earthquakes in Southern California, *Science*, *364*(6442), 767–771.
Rott, H., P. López-Dekker, S. Solberg, L. Ulander, T. Nagler, G. Krieger, P. Prats, M. Rodriguez, M. Zonno, and A. Moreira (2017), SESAME: A single-pass interferometric SEntinel-1 companion SAR mission for monitoring GEO-and biosphere dynamics, in *Geoscience and Remote Sensing Symposium (IGARSS), 2017 IEEE International*, pp. 107–110, IEEE.
Rousset, B., R. Jolivet, M. Simons, C. Lasserre, B. Riel, P. Milillo, Z. Çakir, and F. Renard (2016a), An aseismic slip transient on the North Anatolian Fault, *Geophysical Research Letters*, *43*(7), 3254–3262.
Rousset, B., C. Lasserre, N. Cubas, S. Graham, M. Radiguet, C. DeMets, A. Socquet, M. Campillo, V. Kostoglodov, E. Cabral-Cano, et al. (2016b), Lateral variations of interplate coupling along the mexican subduction interface: Relationships with long-term morphology and fault zone mechanical properties, *Pure and Applied Geophysics*, *173*(10-11), 3467–3486.
Rousset, B., M. Campillo, C. Lasserre, W. Frank, N. Cotte, A. Walpersdorf, A. Socquet, and V. Kostoglodov (2017), A geodetic matched filter search for slow slip with application to the Mexico subduction zone, *Journal of Geophysical Research: Solid Earth*, *122*, 10,498–10,514.
Roux-Mallouf, L., M. Ferry, J.-F. Ritz, T. Berthet, R. Cattin, D. Drukpa, et al. (2016), First paleoseismic evidence for great surface-rupturing earthquakes in the Bhutan Himalayas, *Journal of Geophysical Research: Solid Earth*, *121*(10), 7271–7283.
Rubin, A. M. (2008), Episodic slow slip events and rate-and-state friction, *Journal of Geophysical Research: Solid Earth*, *113*(B11).
Rubinstein, J. L., and A. B. Mahani (2015), Myths and facts on wastewater injection, hydraulic fracturing, enhanced oil recovery, and induced seismicity, *Seismological Research Letters*, *86*(4), 1060–1067.
Ruegg, J., P. Briole, K. Feigl, A. Orsoni, C. Vigny, M. A. Abdallah, O. Bellier, J.-B. de Chabalier, P. Huchon, E. Jacques, et al. (1993), First epoch geodetic GPS measurements across the Afar plate boundary zone, *Geophysical research letters*, *20*(18), 1899–1902.
Ruegg, J., M. Olcay, and D. Lazo (2001), Co-, post-and pre (?)-seismic displacements associated with the Mw 8.4 Southern Peru earthquake of 23 June 2001 from continuous GPS measurements, *Seismological Research Letters*, *72*(6), 673–678.
Ruegg, J., J. Campos, R. Madariaga, E. Kausel, J. De Chabalier, R. Armijo, D. Dimitrov, I. Georgiev, and S. Barrientos (2002), Interseismic strain accumulation in south central Chile from GPS measurements, 1996–1999, *Geophysical research letters*, *29*(11).
Ruegg, J. C., and M. Kasser (1987), Deformation across the Asal-Ghoubbet rift, Djibouti, uplift and crustal extension 1979-1986, *Geophys. Res. Lett.*, *14*, 745–748, doi:10.1029/GL014i007p00745.
Ruegg, J.-C., M. Kasser, J.-C. Lépine, and A. Tarantola (1979), Geodetic measurements of rifting associated with a seismo-volcanic crisis in afar, *Geophys. Res. Lett.*, *6*(11), 817–820.
Ruiz, S., and R. Madariaga (2011), Determination of the friction law parameters of the Mw 6.7 Michilla earthquake in northern Chile by dynamic inversion, *Geophysical Research Letters*, *38*(9).
Ruiz, S., R. **Grandin**, et al. (2013), The Constitución earthquake of 25 March 2012: a large aftershock of the Maule earthquake near the bottom of the seismogenic zone, *Earth and Planetary Science Letters*, *377*, 347–357.
Ruiz, S., M. Metois, A. Fuenzalida, J. Ruiz, F. Leyton, R. **Grandin**, C. Vigny, R. Madariaga, and J. Campos (2014), Intense foreshocks and a slow slip event preceded the 2014 Iquique Mw 8.1 earthquake, *Science*, *345*(6201), 1165–1169.
Ruiz, S., E. Klein, F. del Campo, E. Rivera, P. Poli, M. Metois, V. Christophe, J. C. Baez, G. Vargas, F. Leyton, et al. (2016), The seismic sequence of the 16 September 2015 M w 8.3 Illapel, Chile, earthquake, *Seismological Research Letters*, *87*(4), 789–799.
Rundle, J. B., D. Turcotte, A. Donnellan, L. Grant Ludwig, M. Luginbuhl, and G. Gong (2016), Nowcasting earthquakes, *Earth and Space Science*, *3*(11), 480–486.
Runge, H., M. Werner, M. Eineder, H. Breit, S. Suchandt, and D. Massonnet (2002), Advanced synthetic aperture RADAR observations with clusters of SAR satellites, in *ISPRS Workshop, High Resolution Mapping from Space, Hannover, Germany*, pp. 179–188.
Rupnik, E., M. P. Deseilligny, A. Delorme, and Y. Klinger (2016), Refined satellite image orientation in the free open-source photogrammetric tools APERO/MICMAC, *ISPRS Annals of the Photogrammetry, Remote Sensing and Spatial Information Sciences*, *3*, 83.
Russo, G., G. Giberti, and G. Sartoris (1997), Numerical modeling of surface deformation and mechanical stability of Vesuvius volcano, Italy, *Journal of Geophysical Research: Solid Earth*, *102*(B11), 24,785–24,800.
Rybicki, K. (1971), The elastic residual field of a very long strike-slip fault in the presence of a discontinuity, *Bulletin of the Seismological Society of America*, *61*(1), 79–92.
Saar, M. O., and M. Manga (2003), Seismicity induced by seasonal groundwater recharge at Mt. Hood, Oregon, *Earth and Planetary Science Letters*, *214*(3-4), 605–618.
Safdel, M., M. A. Anbaz, A. Daryasafar, and M. Jamialahmadi (2017), Microbial enhanced oil recovery, a critical review on worldwide implemented field trials in different countries, *Renewable and Sustainable Energy Reviews*, *74*, 159–172.
Sagiya, T. (1999), Interplate coupling in the Tokai district, central Japan, deduced from continuous GPS data, *Geophysical Research Letters*, *26*(15), 2315–2318.

Saint Fleur, N., N. Feuillet, R. **Grandin**, et al. (2015), Seismotectonics of southern Haiti: A new faulting model for the 12 January 2010 M7. 0 earthquake, *Geophysical Research Letters*, *42*(23).
Saito, H., P. R. Akbar, H. Watanabe, V. Ravindra, J. Hirokawa, K. Ura, and P. Budhaditya (2017), Compact X-band Synthetic Aperture Radar for 100kg Class Satellite, *IEICE Transactions on Communications*, *100*(9), 1653–1660.
Sambridge, M. (1999), Geophysical inversion with a neighbourhood algorithm?II. Appraising the ensemble, *Geophysical Journal International*, *138*(3), 727–746.
Sambridge, M., K. Gallagher, A. Jackson, and P. Rickwood (2006), Trans-dimensional inverse problems, model comparison and the evidence, *Geophysical Journal International*, *167*(2), 528–542.
Sandwell, D., R. Mellors, X. Tong, M. Wei, and P. Wessel (2011), Open radar interferometry software for mapping surface deformation, *Eos, Transactions American Geophysical Union*, *92*(28), 234–234.
Sapkota, S., L. Bollinger, Y. Klinger, P. Tapponnier, Y. Gaudemer, and D. Tiwari (2013), Primary surface ruptures of the great Himalayan earthquakes in 1934 and 1255, *Nature Geoscience*, *6*(1), 71.
Sapkota, S. N., L. Bollinger, and F. Perrier (2016), Fatality rates of the Mw8.2, 1934, Bihar–Nepal earthquake and comparison with the April 2015 Gorkha earthquake, *Earth, Planets and Space*, *68*(1), 40.
Sasagawa, G., M. Cook, and M. Zumberge (2016), Drift-corrected seafloor pressure observations of vertical deformation at Axial Seamount 2013–2014, *Earth and Space Science*, *3*(9), 381–385.
Savage, J. (1998), Displacement field for an edge dislocation in a layered half-space, *Journal of Geophysical Research: Solid Earth*, *103*(B2), 2439–2446.
Savage, J., and L. Hastie (1969), A dislocation model for the Fairview Peak, Nevada, earthquake, *Bulletin of the Seismological Society of America*, *59*(5), 1937–1948.
Savage, J., and R. Simpson (1997), Surface strain accumulation and the seismic moment tensor, *Bulletin of the Seismological Society of America*, *87*(5), 1345–1353.
Savage, J. C., and L. Hastie (1966), Surface deformation associated with dip-slip faulting, *Journal of Geophysical Research*, *71*(20), 4897–4904.
Scales, J. A., and R. Snieder (1997), To Bayes or not to Bayes?, *Geophysics*, *62*(4), 1045–1046.
Scheiber, R., and A. Moreira (2000), Coregistration of interferometric SAR images using spectral diversity, *IEEE Transactions on Geoscience and Remote Sensing*, *38*(5), 2179–2191.
Schlögel, R., C. Doubre, J.-P. Malet, and F. Masson (2015), Landslide deformation monitoring with ALOS/PALSAR imagery: A D-InSAR geomorphological interpretation method, *Geomorphology*, *231*, 314–330.
Schmidt, D. A., and R. Bürgmann (2003), Time-dependent land uplift and subsidence in the Santa Clara valley, California, from a large interferometric synthetic aperture radar data set, *Journal of Geophysical Research: Solid Earth*, *108*(B9).
Scholz, C. H. (1982), Scaling laws for large earthquakes: consequences for physical models, *Bulletin of the Seismological Society of America*, *72*(1), 1–14.
Scholz, C. H. (1998), Earthquakes and friction laws, *Nature*, *391*(6662), 37.
Scholz, C. H., C. Aviles, and S. G. Wesnousky (1986), Scaling differences between large interplate and intraplate earthquakes, *Bulletin of the Seismological Society of America*, *76*(1), 65–70.
Schurr, B., G. Asch, S. Hainzl, J. Bedford, A. Hoechner, M. Palo, R. Wang, M. Moreno, M. Bartsch, Y. Zhang, et al. (2014), Gradual unlocking of plate boundary controlled initiation of the 2014 Iquique earthquake, *Nature*, *512*(7514), 299.
Schwartz, D. P., and K. J. Coppersmith (1984), Fault behavior and characteristic earthquakes: Examples from the Wasatch and San Andreas fault zones, *Journal of Geophysical Research: Solid Earth*, *89*(B7), 5681–5698.
Segall, P. (2010), *Earthquake and volcano deformation*, Princeton University Press.
Segall, P., and R. Harris (1986), Slip deficit on the San Andreas fault at Parkfield, California, as revealed by inversion of geodetic data, *Science*, *233*(4771), 1409–1413.
Segall, P., and R. Harris (1987), Earthquake deformation cycle on the San Andreas fault near Parkfield, California, *Journal of Geophysical Research: Solid Earth*, *92*(B10), 10,511–10,525.
Segall, P., and S. Lu (2015), Injection-induced seismicity: Poroelastic and earthquake nucleation effects, *Journal of Geophysical Research: Solid Earth*, *120*(7), 5082–5103.
Segall, P., and J. R. Rice (1995), Dilatancy, compaction, and slip instability of a fluid-infiltrated fault, *Journal of Geophysical Research: Solid Earth*, *100*(B11), 22,155–22,171.
Shaw, B. E. (2011), Surface-slip gradients of large earthquakes, *Bulletin of the Seismological Society of America*, *101*(2), 792–804.
Shaw, B. E., and C. H. Scholz (2001), Slip-length scaling in large earthquakes: Observations and theory and implications for earthquake physics, *Geophysical Research Letters*, *28*(15), 2995–2998.
Shaw, B. E., and S. G. Wesnousky (2008), Slip-length scaling in large earthquakes: The role of deep-penetrating slip below the seismogenic layer, *Bulletin of the Seismological Society of America*, *98*(4), 1633–1641.
Shebalin, P., C. Narteau, M. Holschneider, and D. Schorlemmer (2011), Short-Term Earthquake Forecasting Using Early Aftershock StatisticsShort-Term Earthquake Forecasting Using Early Aftershock Statistics, *Bulletin of the Seismological Society of America*, *101*(1), 297–312, doi:10.1785/0120100119.
Shimazaki, K., and T. Nakata (1980), Time-predictable recurrence model for large earthquakes, *Geophysical Research Letters*, *7*(4), 279–282.
Shirzaei, M. (2015), A seamless multitrack multitemporal InSAR algorithm, *Geochemistry, Geophysics, Geosystems*, *16*(5), 1656–1669.
Shreve, T., R. **Grandin**, et al. (2019), From major caldera subsidence to quiescence at the world's top volcanic degassing source, Ambrym, Vanuatu: the influence of regional tectonics, *Scientific Reports, in revision*, doi:10.31223/osf.io/c8d5v.
Sibson, R. H. (2006), Charles Lyell and the 1855 Wairarapa, New Zealand Earthquake: Recognition of Fault Rupture Accompanying an Earthquake, *Seismological Research Letters*, *77*(3), 359.
Sieh, K. (1996), The repetition of large-earthquake ruptures, *Proceedings of the National Academy of Sciences*, *93*(9), 3764–3771.
Sieh, K. E. (1978a), Central California foreshocks of the great 1857 earthquake, *Bulletin of the Seismological Society of America*, *68*(6), 1731–1749.
Sieh, K. E. (1978b), Slip along the San Andreas fault associated with the great 1857 earthquake, *Bulletin of the Seismological Society of America*, *68*(5), 1421–1448.
Silcock, D. M., and J. Beavan (2001), Geodetic constraints on coseismic rupture during the 1990 Ms 7.8 Luzon, Philippines, earthquake, *Geochemistry, Geophysics, Geosystems*, *2*(7).
Simons, M., and P. A. Rosen (2007), Interferometric Synthetic Aperture Radar, in *Treatise on Geophysics*, vol. 3, edited by G. Schubert, pp. 391–446, Elsevier, Amsterdam.
Simons, M., Y. Fialko, and L. Rivera (2002), Coseismic Deformation from the 1999 M_w 7.1 Hector Mine, California, Earthquake as Inferred from InSAR and GPS Observations, *Bull. Seismol. Soc. Am.*, *92*(4), 1390–1402, doi:10.1785/0120000933.
Simons, W., B. Ambrosius, R. Noomen, D. Angermann, P. Wilson, M. Becker, E. Reinhart, A. Walpersdorf, and C. Vigny (1999), Observing plate motions in SE Asia: Geodetic results of the GEODYSSEA project, *Geophysical Research Letters*, *26*(14), 2081–2084.
Smith-Konter, B. R., D. T. Sandwell, and P. Shearer (2011), Locking depths estimated from geodesy and seismology along the San Andreas Fault System: Implications for seismic moment release, *Journal of Geophysical Research: Solid Earth*, *116*(B6).
Smittarello, D., R. **Grandin**, et al. (2016), Transient deformation in the Asal-Ghoubbet Rift (Djibouti) since the 1978 diking event: Is deformation controlled by magma supply rates?, *Journal of Geophysical Research: Solid Earth*, *121*(8), 6030–6052.
Sneddon, I. N. (1946), The distribution of stress in the neighbourhood of a crack in an elastic solid, *Proc. R. Soc. Lond. A*, *187*(1009), 229–260.
Socquet, A., J. P. Valdes, J. Jara, F. Cotton, A. Walpersdorf, N. Cotte, S. Specht, F. Ortega-Culaciati, D. Carrizo, and E. Norabuena (2017), An 8 month slow slip event triggers progressive nucleation of the 2014 Chile megathrust, *Geophysical Research Letters*, *44*(9), 4046–4053.
Socquet, A., J. Hollingsworth, E. Pathier, and M. Bouchon (2019), Evidence of supershear during the 2018 magnitude 7.5 Palu earthquake from space geodesy, *Nature Geoscience*, *12*(1), s41,561–018–0296–0.
Song, S. G., G. C. Beroza, and P. Segall (2008), A unified source model for the 1906 San Francisco earthquake, *Bulletin of the Seismological Society of America*, *98*(2), 823–831.
Soudarin, L., and A. Cazenave (1995), Large-scale tectonic plate motions measured with the DORIS Space Geodesy System, *Geophysical research letters*, *22*(4), 469–472.
Souriau, A., A. Cazenave, R. B. G. Balmino, K. Dominh, P. Mazzega, J. Lemoine, J. Ruegg, C. Boucher, P. Willis, M. Kasser, et al. (1991), Present-Day Plate Motions: Retrieval From The TOPEX/POSEIDON Orbitography Network (DORIS System).
Steacy, S., J. Gomberg, and M. Cocco (2005), Introduction to special section: Stress transfer, earthquake triggering, and time-dependent seismic hazard, *Journal of Geophysical Research: Solid Earth*, *110*(B5).
Stein, R., and M. W. Stirling (2015), Seismic hazard assessment: Honing the debate, testing the models, *Eos, Earth and Space Science News*.
Stein, S. (2006), Limitations of a Young Science, *Seismological Research Letters*, *77*(3), 351–353, doi:10.1785/gssrl.77.3.351.
Stein, S., R. J. Geller, and M. Liu (2012), Why earthquake hazard maps often fail and what to do about it, *Tectonophysics*, *562*, 1–25.
Stevens, V., and J. Avouac (2015), Interseismic coupling on the main Himalayan thrust, *Geophysical Research Letters*, *42*(14), 5828–5837.
Stevens, V., and J.-P. Avouac (2016), Millenary Mw> 9.0 earthquakes required by geodetic strain in the Himalaya, *Geophysical Research Letters*, *43*(3), 1118–1123.
Stirling, M., D. Rhoades, and K. Berryman (2002), Comparison of earthquake scaling relations derived from data of the instrumental and preinstrumental era, *Bulletin of the Seismological Society of America*, *92*(2), 812–830.
Stirling, M. W., S. G. Wesnousky, and K. Shimazaki (1996), Fault trace complexity, cumulative slip, and the shape of the magnitude-frequency distribution for strike-slip faults: A global survey, *Geophysical Journal International*, *124*(3), 833–868.
Storchak, D. A., D. Di Giacomo, I. Bondár, E. R. Engdahl, J. Harris, W. H. Lee, A. Villaseñor, and P. Bormann (2013), Public release of the ISC–GEM global instrumental earthquake catalogue (1900–2009), *Seismological Research Letters*, *84*(5), 810–815.
Strader, A., M. Werner, J. Bayona, P. Maechling, F. Silva, M. Liukis, and D. Schorlemmer (2018), Prospective Evaluation of Global Earthquake Forecast Models: 2 Yrs of Observations Provide Preliminary Support for Merging Smoothed Seismicity with Geodetic Strain Rates, *Seismological Research Letters*.
Sudhaus, H., and J. Sigurjón (2009), Improved source modelling through combined use of InSAR and GPS under consideration of correlated data errors: application to the June 2000 Kleifarvatn earthquake, Iceland, *Geophysical Journal International*, *176*(2), 389–404.
Sun, J., K. M. Johnson, Z. Cao, Z. Shen, R. Bürgmann, and X. Xu (2011), Mechanical constraints on inversion of coseismic geodetic data for fault slip and geometry: Example from InSAR observation of the 6 October 2008 Mw 6.3 Dangxiong-Yangyi (Tibet) earthquake, *Journal of Geophysical Research: Solid Earth*, *116*(B1).
Sun, R. J. (1969), Theoretical size of hydraulically induced horizontal fractures and corresponding surface uplift in an idealized medium, *J. Geophys. Res.*, *74*(25), 5995–6011.
Symithe, S. J., E. Calais, J. S. Haase, A. M. Freed, and R. Douilly (2013), Coseismic slip distribution of the 2010 M 7.0 Haiti earthquake and resulting stress changes on regional faults, *Bulletin of the Seismological Society of America*, *103*(4), 2326–2343.

Szeliga, W., R. Bilham, D. M. Kakar, and S. H. Lodi (2012), Interseismic strain accumulation along the western boundary of the Indian subcontinent, *Journal of Geophysical Research: Solid Earth*, *117*(B8).
Tapponnier, P., G. Peltzer, A. Le Dain, R. Armijo, and P. Cobbold (1982), Propagating extrusion tectonics in Asia: New insights from simple experiments with plasticine, *Geology*, *10*(12), 611–616.
Tarantola, A. (1987), *Inverse Problem Theory*, Elsevier, Amsterdam, The Netherlands.
Tarantola, A. (2006), Popper, Bayes and the inverse problem, *Nature physics*, *2*(8), 492.
Tarantola, A., and B. Valette (1982a), Generalized Nonlinear Inverse Problems Solved Using the Least Squares Criterion, *Rev. Geophys.*, *20*, 219–232.
Tarantola, A., and B. Valette (1982b), Inverse Problems = Quest for Information, *J. Geophys.*, *50*, 159–170.
Tarantola, A., J.-C. Ruegg, and J.-C. Lépine (1979), Geodetic evidence for rifting in Afar: a brittle-elastic model of the behaviour of the lithosphere, *Earth. Planet. Sci. Lett.*, *45*, 435–444, doi:10.1016/0012-821X(79)90142-0.
Tarantola, A., J.-C. Ruegg, and J.-C. Lépine (1979), Geodetic evidence for rifting in Afar a brittle-elastic model of the behaviour of the lithosphere, *Earth and Planetary Science Letters*, *45*(2), 435–444.
Temtime, T., J. Biggs, E. Lewi, I. Hamling, T. Wright, and A. Ayele (2018), Spatial and temporal patterns of deformation at the Tendaho geothermal prospect, Ethiopia, *Journal of Volcanology and Geothermal Research*, *357*, 56–67.
Grandin, R. (2014), TerraSAR-X ScanSAR interferometry in practice, unpublished report.
Grandin, R. (2015), Interferometric processing of SLC Sentinel-1 TOPS data, in *FRINGE'15: Advances in the Science and Applications of SAR Interferometry and Sentinel-1 InSAR Workshop, Frascati, Italy, 23-27 March 2015*.
Grandin, R., J. F. Borges, M. Bezzeghoud, B. Caldeira, and F. Carrilho (2007a), Simulations of strong ground motion in SW Iberia for the 1969 February 28 (M s= 8.0) and the 1755 November 1 (M 8.5) earthquakes-II. Strong ground motion simulations, *Geophysical Journal International*, *171*(2), 807–822.
Grandin, R., J. F. Borges, M. Bezzeghoud, B. Caldeira, and F. Carrilho (2007b), Simulations of strong ground motion in SW Iberia for the 1969 February 28 (Ms= 8.0) and the 1755 November 1 (M 8.5) earthquakes–I. Velocity model, *Geophysical Journal International*, *171*(3), 1144–1161.
Grandin, R., A. Socquet, M.-P. Doin, E. Jacques, J.-B. de Chabalier, and G. King (2010), Transient rift opening in response to multiple dike injections in the Manda Hararo rift (Afar, Ethiopia) imaged by time-dependent elastic inversion of interferometric synthetic aperture radar data, *Journal of Geophysical Research: Solid Earth*, *115*(B9).
Grandin, R., M.-P. Doin, L. Bollinger, B. Pinel-Puysségur, G. Ducret, R. Jolivet, and S. N. Sapkota (2012a), Long-term growth of the Himalaya inferred from interseismic InSAR measurement, *Geology*, *40*(12), 1059–1062.
Grandin, R., A. Socquet, C. Doubre, E. Jacques, and G. C. King (2012b), Elastic thickness control of lateral dyke intrusion at mid-ocean ridges, *Earth and Planetary Science Letters*, *319*, 83–95, doi:10.1016/j.epsl.2011.12.011.
Grandin, R., M. Vallée, C. Satriano, R. Lacassin, Y. Klinger, M. Simoes, and L. Bollinger (2015), Rupture process of the Mw= 7.9 2015 Gorkha earthquake (Nepal): insights into Himalayan megathrust segmentation, *Geophysical Research Letters*, *42*(20), 8373–8382.
Grandin, R., E. Klein, M. Métois, and C. Vigny (2016), Three-dimensional displacement field of the 2015 Mw8.3 Illapel earthquake (Chile) from across-and along-track Sentinel-1 TOPS interferometry, *Geophysical Research Letters*, *43*(6), 2552–2561.
Grandin, R., M. Vallée, and R. Lacassin (2017), Rupture Process of the Mw 5.8 Pawnee, Oklahoma, Earthquake from Sentinel-1 InSAR and Seismological Data, *Seismological Research Letters*, *88*(4), 994–1004.
Grandin, R., F. Beauducel, A. Peltier, V. Ballu, K. Chanard, P. Valty, P. Bonnefond, J.-B. de Chabalier, T. Shreve, F. Koudogbo, A. Urdiroz, A. Filatov, F. Novali, P. Durand, and J.-C. Komorowski (2019), Surface deformation during the 2018-19 Mayotte seismo-volcanic crisis from GNSS, Synthetic Aperture Radar and seafloor geodesy, in *AGU Fall Meeting Abstracts*.
Thatcher, W. (1975), Strain accumulation and release mechanism of the 1906 San Francisco earthquake, *Journal of Geophysical Research*, *80*(35), 4862–4872.
Thatcher, W., and T. C. Hanks (1973), Source parameters of southern California earthquakes, *Journal of geophysical research*, *78*(35), 8547–8576.
Thatcher, W., G. Marshall, and M. Lisowski (1997), Resolution of fault slip along the 470-km-long rupture of the great 1906 San Francisco earthquake and its implications, *Journal of Geophysical Research: Solid Earth*, *102*(B3), 5353–5367.
Thayer, G. D. (1974), An improved equation for the radio refractive index of air, *Radio Science*, *9*(10), 803–807.
Thompson, A. A. (2015), Overview of the RADARSAT constellation mission, *Canadian Journal of Remote Sensing*, *41*(5), 401–407.
Thompson, T. B., and B. J. Meade (2018), Topography and the shallow slip deficit inference, doi:10.31223/osf.io/puz84.
Tiampo, K., and R. Shcherbakov (2012), Seismicity-based earthquake forecasting techniques: Ten years of progress, *Tectonophysics*, *522-523*, 89–121.
Tiampo, K., J. Rundle, J. Fernandez, and J. Langbein (2000), Spherical and ellipsoidal volcanic sources at Long Valley caldera, California, using a genetic algorithm inversion technique, *Journal of Volcanology and Geothermal Research*, *102*(3-4), 189–206.
Tibshirani, R. (1996), Regression shrinkage and selection via the lasso, *Journal of the Royal Statistical Society. Series B (Methodological)*, pp. 267–288.
Tinti, S., and A. Armigliato (2002), A 2-D hybrid technique to model the effect of topography on coseismic displacements. Application to the Umbria-Marche (central Italy) 1997 earthquake sequence, *Geophysical Journal International*, *150*(2), 542–557.
Toda, S., R. S. Stein, and T. Sagiya (2002), Evidence from the AD 2000 Izu islands earthquake swarm that stressing rate governs seismicity, *Nature*, *419*(6902), 58.
Tong, X., D. Sandwell, and B. Smith-Konter (2013), High-resolution interseismic velocity data along the San Andreas fault from GPS and InSAR, *Journal of Geophysical Research: Solid Earth*, *118*(1), 369–389.
Tong, X., D. T. Sandwell, and B. Smith-Konter (2015), An integral method to estimate the moment accumulation rate on the Creeping Section of the San Andreas Fault, *Geophysical Journal International*, *203*(1), 48–62.
Trasatti, E., C. Giunchi, and M. Bonafede (2003), Effects of topography and rheological layering on ground deformation in volcanic regions, *Journal of Volcanology and Geothermal Research*, *122*(1-2), 89–110.
Tryggvason, E. (1984), Widening of the Krafla fissure swarm during the 1975–1981 volcano-tectonic episode, *Bul. Volc.*, *47*(1), 47–69, doi:10.1007/BF01960540.
Tsuji, H., Y. Hatanaka, T. Sagiya, and M. Hashimoto (1995), Coseismic crustal deformation from the 1994 Hokkaido-Toho-Oki earthquake monitored by a nationwide continuous GPS array in Japan, *Geophysical Research Letters*, *22*(13), 1669–1672.
Tung, S., and T. Masterlark (2016), Coseismic slip distribution of the 2015 Mw7. 8 Gorkha, Nepal, earthquake from joint inversion of GPS and InSAR data for slip within a 3-D heterogeneous Domain, *Journal of Geophysical Research: Solid Earth*, *121*(5), 3479–3503.
Tung, S., and T. Masterlark (2018a), Resolving source geometry of the 24 August 2016 Amatrice, central Italy, earthquake from InSAR data and 3D finite-element modeling, *Bulletin of the Seismological Society of America*, *108*(2), 553–572.
Tung, S., and T. Masterlark (2018b), Sensitivities of Near-field Tsunami Forecasts to Megathrust Deformation Predictions, *Journal of Geophysical Research: Solid Earth*, *123*(2), 1711–1735.
Twardzik, C., M. Vergnolle, A. Sladen, and A. Avallone (2019), Unravelling the contribution of early postseismic deformation using sub-daily GNSS positioning, *Scientific reports*, *9*(1), 1775.
Ulaby, F. T., and C. Elachi (1990), Radar polarimetry for geoscience applications, *Norwood, MA, Artech House, Inc., 1990, 376 p. No individual items are abstracted in this volume.*
Urlaub, M., F. Petersen, F. Gross, A. Bonforte, G. Puglisi, F. Guglielmino, S. Krastel, D. Lange, and H. Kopp (2018), Gravitational collapse of Mount Etna?s southeastern flank, *Science Advances*, *4*(10), eaat9700.
Vallage, A., Y. Klinger, R. **Grandin**, et al. (2015), Inelastic surface deformation during the 2013 Mw 7.7 Balochistan, Pakistan, earthquake, *Geology*, *43*(12), 1079–1082.
Vallée, M. (2013), Source time function properties indicate a strain drop independent of earthquake depth and magnitude, *Nature communications*, *4*, 2606.
Vallée, M., J.-M. Nocquet, J. Battaglia, Y. Font, M. Segovia, M. Regnier, P. Mothes, P. Jarrin, D. Cisneros, S. Vaca, et al. (2013), Intense interface seismicity triggered by a shallow slow slip event in the Central Ecuador subduction zone, *Journal of Geophysical Research: Solid Earth*, *118*(6), 2965–2981.
Vallée, M., J. P. Ampuero, K. Juhel, P. Bernard, J.-P. Montagner, and M. Barsuglia (2017), Observations and modeling of the elastogravity signals preceding direct seismic waves, *Science*, *358*(6367), 1164–1168.
Van der Woerd, J., A.-S. Meriaux, Y. Klinger, F. Ryerson, Y. Gaudemer, and P. Tapponnier (2002), The 14 November 2001, Mw= 7.8 Kokoxili earthquake in northern Tibet (Qinghai Province, China), *Seismological Research Letters*, *73*(2), 125–135.
van Elk, J., D. Doornhof, J. J. Bommer, S. J. Bourne, S. J. Oates, R. Pinho, and H. Crowley (2017), Hazard and risk assessments for induced seismicity in Groningen, *Netherlands Journal of Geosciences*, *96*(5), s259–s269.
Van Puymbroeck, N., R. Michel, R. Binet, J.-P. Avouac, and J. Taboury (2000), Measuring earthquakes from optical satellite images, *Applied Optics*, *39*(20), 3486–3494.
Vergnolle, M., F. Pollitz, and E. Calais (2003), Constraints on the viscosity of the continental crust and mantle from GPS measurements and postseismic deformation models in western Mongolia, *Journal of Geophysical Research: Solid Earth*, *108*(B10).
Vergnolle, M., A. Walpersdorf, V. Kostoglodov, P. Tregoning, J. Santiago, N. Cotte, and S. Franco (2010), Slow slip events in Mexico revised from the processing of 11 year GPS observations, *Journal of Geophysical Research: Solid Earth*, *115*(B8).
Villano, M., G. Krieger, and A. Moreira (2014), Staggered SAR: High-resolution wide-swath imaging by continuous PRI variation, *IEEE Transactions on Geoscience and Remote Sensing*, *52*(7), 4462–4479.
Vosoughi, S., D. Roy, and S. Aral (2018), The spread of true and false news online, *Science*, *359*(6380), 1146–1151.
Wald, D. J., and T. H. Heaton (1994), Spatial and temporal distribution of slip for the 1992 Landers, California, earthquake, *Bulletin of the Seismological Society of America*, *84*(3), 668–691.
Wald, D. J., and P. G. Somerville (1995), Variable-slip rupture model of the great 1923 Kanto, Japan, earthquake: Geodetic and body-waveform analysis, *Bulletin of the Seismological Society of America*, *85*(1), 159–177.
Wallace, L. M., Y. Kaneko, S. Hreinsdóttir, I. Hamling, Z. Peng, N. Bartlow, E. D?Anastasio, and B. Fry (2017), Large-scale dynamic triggering of shallow slow slip enhanced by overlying sedimentary wedge, *Nature Geoscience*, *10*(10), 765.
Walsh III, F. R., and M. D. Zoback (2016), Probabilistic assessment of potential fault slip related to injection-induced earthquakes: Application to north-central Oklahoma, USA, *Geology*, *44*(12), 991–994.

Wang, H., T. J. Wright, J. Liu-Zeng, and L. Peng (2019a), Strain Rate Distribution in South-Central Tibet From Two Decades of InSAR and GPS, *Geophysical Research Letters*, *46*(10), 5170–5179.
Wang, K., and Y. Fialko (2015), Slip model of the 2015 Mw 7.8 Gorkha (Nepal) earthquake from inversions of ALOS-2 and GPS data, *Geophysical Research Letters*, *42*(18), 7452–7458.
Wang, K., X. Xu, and Y. Fialko (2017), Improving Burst Alignment in TOPS Interferometry With Bivariate Enhanced Spectral Diversity, *IEEE Geoscience and Remote Sensing Letters*, *14*(12), 2423–2427.
Wang, S., W. Xu, C. Xu, Z. Yin, R. Bürgmann, L. Liu, and G. Jiang (2019b), Changes in Groundwater Level Possibly Encourage Shallow Earthquakes in Central Australia: The 2016 Petermann Ranges Earthquake, *Geophysical Research Letters*, *46*(6), 3189–3198, doi:10.1029/2018GL080510.
Ward, S. N. (1994), A multidisciplinary approach to seismic hazard in southern California, *Bulletin of the Seismological Society of America*, *84*(5), 1293–1309.
Ward, S. N. (1998), On the consistency of earthquake moment rates, geological fault data, and space geodetic strain: the United States, *Geophysical Journal International*, *134*(1), 172–186.
Ward, S. N., and S. E. Barrientos (1986), An inversion for slip distribution and fault shape from geodetic observations of the 1983, Borah Peak, Idaho, earthquake, *Journal of Geophysical Research: Solid Earth*, *91*(B5), 4909–4919.
Ward, S. N., and G. R. Valensise (1989), Fault parameters and slip distribution of the 1915 Avezzano, Italy, earthquake derived from geodetic observations, *Bulletin of the Seismological Society of America*, *79*(3), 690–710.
Wedmore, L., J. F. Walker, G. P. Roberts, P. Sammonds, K. McCaffrey, and P. Cowie (2017), A 667 year record of coseismic and interseismic Coulomb stress changes in central Italy reveals the role of fault interaction in controlling irregular earthquake recurrence intervals, *Journal of Geophysical Research: Solid Earth*, *122*(7), 5691–5711.
Weingarten, M., S. Ge, J. W. Godt, B. A. Bekins, and J. L. Rubinstein (2015), High-rate injection is associated with the increase in US mid-continent seismicity, *Science*, *348*(6241), 1336–1340.
Wells, D. L., and K. J. Coppersmith (1994), New empirical relationships among magnitude, rupture length, rupture width, rupture area, and surface displacement, *Bulletin of the seismological Society of America*, *84*(4), 974–1002.
Wenzel, H.-G. (1996), The nanogal software: Earth tide data processing package ETERNA 3.30, *Bull. Inf. Marées Terrestres*, *124*, 9425–9439.
Wesnousky, S. G. (1994), The Gutenberg-Richter or characteristic earthquake distribution, which is it?, *Bulletin of the Seismological Society of America*, *84*(6), 1940–1959.
Wesnousky, S. G. (1996), Reply to Yan Kagan's comment on ?The Gutenberg-Richter or characteristic earthquake distribution, which is it??, *Bulletin of the Seismological Society of America*, *86*(1A), 286–291.
Wesnousky, S. G. (2008), Displacement and geometrical characteristics of earthquake surface ruptures: Issues and implications for seismic-hazard analysis and the process of earthquake rupture, *Bulletin of the Seismological Society of America*, *98*(4), 1609–1632.
Wesnousky, S. G., Y. Kumahara, D. Chamlagain, I. K. Pierce, A. Karki, and D. Gautam (2017), Geological observations on large earthquakes along the Himalayan frontal fault near Kathmandu, Nepal, *Earth and Planetary Science Letters*, *457*, 366–375.
Whipple, K. X., M. Shirzaei, K. V. Hodges, and J. R. Arrowsmith (2016), Active shortening within the Himalayan orogenic wedge implied by the 2015 Gorkha earthquake, *Nature Geoscience*, *9*(9), 711.
Whitten, C. (1957), Geodetic measurements in the Dixie Valley area, *Bulletin of the Seismological Society of America*, *47*(4), 321–325.
Wiggins, R. A. (1972), The general linear inverse problem: Implication of surface waves and free oscillations for earth structure, *Reviews of Geophysics*, *10*(1), 251–285.
Williams, C. A., and G. Wadge (1998), The effects of topography on magma chamber deformation models: Application to Mt. Etna and radar interferometry, *Geophysical Research Letters*, *25*(10), 1549–1552.
Wilson, M., G. Foulger, J. Gluyas, R. Davies, and B. Julian (2017), HiQuake: The human-induced earthquake database, *Seismological Research Letters*, *88*(6), 1560–1565.
Wright, T., E. Fielding, and B. Parsons (2001a), Triggered slip: observations of the 17 August 1999 Izmit (Turkey) earthquake using radar interferometry, *Geophysical Research Letters*, *28*(6), 1079–1082.
Wright, T., B. Parsons, and E. Fielding (2001b), Measurement of interseismic strain accumulation across the North Anatolian Fault by satellite radar interferometry, *Geophysical Research Letters*, *28*(10), 2117–2120.
Wright, T. J., Z. Lu, and C. Wicks (2004a), Constraining the slip distribution and fault geometry of the M w 7.9, 3 November 2002, Denali fault earthquake with Interferometric Synthetic Aperture Radar and Global Positioning System data, *Bulletin of the Seismological Society of America*, *94*(6B), S175–S189.
Wright, T. J., B. Parsons, P. C. England, and E. J. Fielding (2004b), InSAR observations of low slip rates on the major faults of western Tibet, *Science*, *305*(5681), 236–239.
Wright, T. J., B. E. Parsons, and Z. Lu (2004), Toward mapping surface deformation in three dimensions using InSAR, *Geophys. Res. Lett.*, *31*(1), 1607, doi:10.1029/2003GL018827.
Wright, T. J., C. Ebinger, J. Biggs, A. Ayele, G. Yirgu, D. Keir, and A. Stork (2006), Magma-maintained rift segmentation at continental rupture in the 2005 Afar dyking episode, *Nature*, *442*(7100), 291.
Wright, T. J., N. Houlié, M. Hildyard, and T. Iwabuchi (2012), Real-time, reliable magnitudes for large earthquakes from 1 Hz GPS precise point positioning: The 2011 Tohoku-Oki (Japan) earthquake, *Geophysical research letters*, *39*(12).
Wu, Y., Z. Jiang, H. Liang, L. Chang, C. Chen, S. Zhu, J. Zhao, and J. Du (2016), Coseismic deformations of the 2015 Mw 7.8 Gorkha earthquake and interseismic strain accumulation in the Himalayan tectonic belt and Tibetan plateau, *Tectonophysics*, *670*, 144–154.
Wyatt, F. K. (1988), Measurements of coseismic deformation in southern California: 1972–1982, *Journal of Geophysical Research: Solid Earth*, *93*(B7), 7923–7942.
Wye, L., and S. Lee (2016), SRI CubeSat imaging radar for earth science (SRI-CIRES), in *Earth Science Technology Office Forum (June 2015)*.
Wyss, M. (2017), Report estimated quake death tolls to save lives, *Nature*, *545*, 151–153.
Wyss, M., and J. N. Brune (1968), Seismic moment, stress, and source dimensions for earthquakes in the California-Nevada region, *Journal of Geophysical Research*, *73*(14), 4681–4694.
Xie, X., J. J. Jiao, Z. Tang, and C. Zheng (2003), Evolution of abnormally low pressure and its implications for the hydrocarbon system in the southeast uplift zone of Songliao basin, China, *AAPG bulletin*, *87*(1), 99–119.
Xu, X., G. Yu, Y. Klinger, P. Tapponnier, and J. Van Der Woerd (2006), Reevaluation of surface rupture parameters and faulting segmentation of the 2001 Kunlunshan earthquake (Mw7. 8), northern Tibetan Plateau, China, *Journal of Geophysical Research: Solid Earth*, *111*(B5).
Xu, X., X. Tong, D. T. Sandwell, C. W. Milliner, J. F. Dolan, J. Hollingsworth, S. Leprince, and F. Ayoub (2016), Refining the shallow slip deficit, *Geophysical Journal International*, *204*(3), 1867–1886.
Xu, X., D. T. Sandwell, and D. Bassett (2017), A spectral expansion approach for geodetic slip inversion: implications for the downdip rupture limits of oceanic and continental megathrust earthquakes, *Geophysical Journal International*, *212*(1), 400–411.
Yabuki, T., and M. Matsu'Ura (1992), Geodetic data inversion using a Bayesian information criterion for spatial distribution of fault slip, *Geophysical Journal International*, *109*(2), 363–375.
Yagi, Y., and Y. Fukahata (2011), Introduction of uncertainty of Green's function into waveform inversion for seismic source processes, *Geophysical Journal International*, *186*(2), 711–720.
Yagüe-Martínez, N., P. Prats-Iraola, F. R. Gonzalez, R. Brcic, R. Shau, D. Geudtner, M. Eineder, and R. Bamler (2016), Interferometric processing of Sentinel-1 TOPS data, *IEEE Transactions on Geoscience and Remote Sensing*, *54*(4), 2220–2234.
Yamamoto, R., M. Kido, Y. Ohta, N. Takahashi, Y. Yamamoto, A. Pinar, D. Kalafat, H. Özener, and Y. Kaneda (2019), Seafloor geodesy revealed partial creep of the North Anatolian Fault submerged in the Sea of Marmara, *Geophysical Research Letters*, *46*(3), 1268–1275.
Yan, Y., M.-P. Doin, P. Lopez-Quiroz, F. Tupin, B. Fruneau, V. Pinel, and E. Trouvé (2012), Mexico City subsidence measured by InSAR time series: Joint analysis using PS and SBAS approaches, *IEEE Journal of Selected Topics in Applied Earth Observations and Remote Sensing*, *5*(4), 1312–1326.
Yan, Y., V. Pinel, E. Trouvé, E. Pathier, J. Perrin, P. Bascou, and F. Jouanne (2013), Coseismic displacement field and slip distribution of the 2005 Kashmir earthquake from SAR amplitude image correlation and differential interferometry, *Geophysical Journal International*, *193*(1), 29–46.
Yang, X., and P. M. Davis (1988), Deformation from inflation of a dipping finite prolate spheroid in an elastic half?space as a model for volcanic stressing, *J. Geophys. Res.*, *93*(B5), 4249–4257.
Yeck, W., G. Hayes, D. E. McNamara, J. L. Rubinstein, W. Barnhart, P. Earle, and H. M. Benz (2017), Oklahoma experiences largest earthquake during ongoing regional wastewater injection hazard mitigation efforts, *Geophysical Research Letters*, *44*(2), 711–717.
Yokota, Y., T. Ishikawa, S.-i. Watanabe, T. Tashiro, and A. Asada (2016), Seafloor geodetic constraints on interplate coupling of the Nankai Trough megathrust zone, *Nature*, *534*(7607), 374.
Youngs, R. R., and K. J. Coppersmith (1985), Implications of fault slip rates and earthquake recurrence models to probabilistic seismic hazard estimates, *Bulletin of the Seismological society of America*, *75*(4), 939–964.
Yu, C., Z. Li, N. T. Penna, and P. Crippa (2018), Generic atmospheric correction model for Interferometric Synthetic Aperture Radar observations, *Journal of Geophysical Research: Solid Earth*, *123*(10), 9202–9222.
Yun, S., P. Segall, and H. Zebker (2006), Constraints on magma chamber geometry at Sierra Negra Volcano, Galápagos Islands, based on InSAR observations, *Journal of Volcanology and geothermal research*, *150*(1-3), 232–243.
Zadro, M., and C. Braitenberg (1999), Measurements and interpretations of tilt–strain gauges in seismically active areas, *Earth-Science Reviews*, *47*(3-4), 151–187.
Zebker, H. A., and Y. Lu (1998), Phase unwrapping algorithms for radar interferometry: residue-cut, least-squares, and synthesis algorithms, *JOSA A*, *15*(3), 586–598.
Zebker, H. A., and J. Villasenor (1992), Decorrelation in interferometric radar echoes, *IEEE Transactions on geoscience and remote sensing*, *30*(5), 950–959.
Zebker, H. A., P. A. Rosen, and S. Hensley (1997), Atmospheric effects in interferometric synthetic aperture radar surface deformation and topographic maps, *Journal of Geophysical Research: Solid Earth*, *102*(B4), 7547–7563.
Zhao, B., R. Bürgmann, D. Wang, K. Tan, R. Du, and R. Zhang (2017), Dominant Controls of Downdip Afterslip and Viscous Relaxation on the Postseismic Displacements Following the Mw7.9 Gorkha, Nepal, Earthquake, *Journal of Geophysical Research: Solid Earth*, *122*(10), 8376–8401.
Zhou, X., W. Sun, B. Zhao, G. Fu, J. Dong, and Z. Nie (2012), Geodetic observations detecting coseismic displacements and gravity changes caused by the Mw= 9.0 Tohoku-Oki earthquake, *Journal of Geophysical Research: Solid Earth*, *117*(B5).
Zhou, Y., J. R. Elliott, B. Parsons, and R. T. Walker (2015), The 2013 Balochistan earthquake: An extraordinary or completely ordinary event?, *Geophysical Research Letters*, *42*(15), 6236–6243.
Zhou, Y., R. T. Walker, J. Hollingsworth, M. Talebian, X. Song, and B. Parsons (2016), Coseismic and postseismic displacements from the 1978 Mw 7.3 Tabas-e-Golshan earthquake in eastern Iran, *Earth and Planetary Science Letters*, *452*, 185–196.
Zhu, L., and L. A. Rivera (2002), A note on the dynamic and static displacements from a point source in multilayered media, *Geophysical Journal International*, *148*(3), 619–627.
Zielke, O., J. R. Arrowsmith, L. G. Ludwig, and S. O. Akciz (2012), High-Resolution Topography-Derived Offsets along the 1857 Fort Tejon Earthquake Rupture Trace, San Andreas FaultHigh-Resolution Topography-Derived Offsets along the 1857 Fort Tejon Rupture, San Andreas Fault, *Bulletin of the Seismological Society of America*, *102*(3), 1135–1154.

Zielke, O., Y. Klinger, and J. R. Arrowsmith (2015), Fault slip and earthquake recurrence along strike-slip faults?Contributions of high-resolution geomorphic data, *Tectonophysics*, *638*, 43–62.
Zink, M., M. Bachmann, B. Brautigam, T. Fritz, I. Hajnsek, A. Moreira, B. Wessel, and G. Krieger (2014), TanDEM-X: the new global DEM takes shape, *IEEE Geoscience and Remote Sensing Magazine*, *2*(2), 8–23.
Ziv, A., M.-P. Doin, and R. **Grandin** (2013), What can be learned from underdetermined geodetic slip inversions: the Parkfield GPS network example, *Geophysical Journal International*, *194*(3), 1900–1908.